Ultrafast Spin Dynamics in Magnetic Thin Films and Heterostructures

Thesis submitted for the degree of

Doctor of Philosophy (Science)

In

Physics (Experimental)

By

Surya Narayan Panda

Department of Physics

University of Calcutta

2022

DEDICATED TO ALL MY RESPECTED TEACHERS. . . . . .

Abstract

An in-depth understanding of ultrafast magnetization dynamics and its efficient control over a broad timescale in magnetic thin films and heterostructures have gained huge interest among scientific communities lately because of its potential applications in modern-day data storage and memory devices. In this doctoral thesis, we have investigated ultrafast magnetization dynamics in different ferromagnetic thin films and heterostructures from femtosecond to nanosecond timescale. The influence of various internal and external factors, such as film thickness, laser fluence, external magnetic field, crystal structure, spin-orbit coupling and pure spin current transport on this magnetization dynamics have been studied thoroughly. We have measured ultrafast spin dynamics by employing time-resolved magneto-optical Kerr effect magnetometry based on an amplified femtosecond laser system. Ultrafast demagnetization results are analysed by a phenomenological three-temperature model while the damped precessional oscillations are modelled by macrospin formalism-based Landau-Lifshitz-Gilbert torque equation. Different static characterization techniques like X-ray diffraction, X-ray reflectivity, micro-Raman spectroscopy, atomic force microscopy, static magneto-optical Kerr effect magnetometry, vibrating sample magnetometry, etc. have been used to study the crystalline property, layer thickness, interface quality, two-dimensional nature, surface topography and static and quasi-static magnetic properties of our samples.

The studied problems in this doctoral thesis can be broadly categorized into three parts:

I) Investigation of the effect of spin pumping in thin film heterostructures: By utilizing an all-optical excitation and detection technique, we have demonstrated spin pumping-induced interfacial spin transparency in technologically important β-Ta/CoFeB/SiO_2 and W/CoFeB/SiO_2 (in both α and β phases of W) interfaces. Other than interfacial spin transparency, we have also extracted parameters like spin-diffusion length, spin-mixing conductance, spin-flip probability and spin backflow factor in these heterostructures. Additional effects like spin memory loss, two-magnon scattering etc., which could affect the extent of spin transport, have been examined in these systems. Also, we have investigated the magnetization dynamics in the single layer graphene (SLG)/CoFeB/SiO_2 heterostructure and separated the contribution of spin pumping from other defect-induced contributions like two-magnon scattering and established spin pumping-induced spin transport as a dominant contributor to ultrafast demagnetization mechanism.

II) Fluence-dependent magnetization dynamics in permalloy thin films: We have studied the ultrafast spin dynamics in permalloy thin films of different thicknesses to realize the modulation of ultrafast demagnetization time, fast remagnetization time, precessional frequency, temporal chirp parameter and Gilbert damping parameter of both uniform Kittel mode and bulk perpendicular standing spin wave modes with film thickness and laser pump fluence.

III) Effect of spin-orbit coupling on the magnetization dynamics: To underpin the effect of spin-orbit coupling (SOC) on the magnetization dynamics of ferromagnetic CoFeB, we have used different nonmagnetic underlayers (such as Ta/Ru/Ta, Ta, W, Pt and Cu) that differ in SOC strength. We have observed that higher SOC strength of the underlayer leads to higher damping, faster ultrafast demagnetization, faster remagnetization and more efficient spin transport through the interfaces which decrease the interfacial spin accumulation.

List of publications

A. Published/Submitted in journals

☐ Included in the thesis

1. "*All-optical Detection of Interfacial Spin Transparency from Spin Pumping in β-Ta/CoFeB Thin Films*", **S. N. Panda**, S. Mondal, J. Sinha, S. Choudhury and A. Barman, *Science Advances*, **5**, eaav7200 (2019).

2. "*Structural Phase-Dependent Giant Interfacial Spin Transparency in W/CoFeB Thin Film Heterostructures*", **S. N. Panda**, S. Majumder, A. Bhattacharyya, S. Dutta, S. Choudhury and A. Barman, *ACS Applied Materials & Interfaces*, **17**, 20875–20884 (2021).

3. "*Femtosecond Laser-Induced Spin Dynamics in Single Layer Graphene/CoFeB Thin Films*", **S. N. Panda**, S. Majumder, S. Choudhury, A. Bhattacharya, S. Sinha, A. Barman, *Nanoscale*, **13**, 13709-13718 (2021).

4. "*Role of Spin-Orbit Coupling on Ultrafast Spin Dynamics in Nonmagnet/Ferromagnet Heterostructures*", **S. N. Panda**, B. Rana, Y. C. Otani and A. Barman, *Advanced Quantum Technologies*, 2200016 (2022).

5. "*All-Optical Observation of Nearly 100% Spin Transparency of Single Layer Graphene/CoFeB Interface*", **S. N. Panda**, S. Majumder, S. Choudhury, A. Bhattacharya, S. Sinha and A. Barman (*Manuscript under preparation*).

6. "*Fluence-Dependent Ultrafast Magnetization Dynamics in Permalloy Thin Films with Different Thicknesses*", **S. N. Panda**, S. Mondal and A. Barman (*Manuscript under preparation*).

☐ Not included in the thesis

1. "*Nanochannels for Spin Wave Manipulation in* $Ni_{80}Fe_{20}$ *Nanodot Arrays", * S. Sahoo, **S. N. Panda**, S. Barman, Y. Otani and A. Barman, *Journal of Magnetism and Magnetic Materials*, **522**, 167550 (2020).

2. "*Ultrafast Spin Dynamics of Electrochemically Grown Heusler Alloy Films*" M. R. Karim, A. Adhikari, **S. N. Panda**, P. Sharangi, S. Kayal, G. Manna, P. S. A. Kumar, S. Bedanta, A. Barman and I. Sarkar, *Journal of Physical Chemistry C*, **125**, 10483-10492 (2021).

3. "*Ultrafast Demagnetization in Ultrathin Film Magnetic Multilayers*" S. Pan, F. Ganss, **S. N. Panda**, G. Sellge, C. Banerjee, J. Sinha, O. Hellwig and A. Barman, *Journal of Materials Science,* 57, 6212–6222 (2022).

4. "*Strain-induced structural ordering of Heusler nanoparticles with high heating rate for magneto-thermal application*", M. R. Karim, **S. N. Panda**, A. Barman and I. Sarkar, *Nanotechnology,* **33**, 235701 (2022).

5. "*Magnetic Configuration Driven Femtosecond Spin Dynamics in Synthetic Antiferromagnets*", A. De, S. Arekapudi, L. Koch, F. Samad, **S. N. Panda**, B. Böhm, O. Hellwig and A. Barman, *ACS Applied Materials & Interfaces*, **14**, 13970–13979 (2022).

6. "*Role of defect density and Rashba shift on interfacial Dzyaloshinskii-Moriya interaction and spin pumping in single layer graphene/$Co_{20}Fe_{60}B_{20}$ heterostructures*", A. K. Mondal, S. Majumder, S. Sahoo, **S. N. Panda**, S. Sinha and A. Barman, *ACS Applied Nano Materials,* **5**, 5056–5063 (2022).

7. "*All-Optical Detection of Spin Pumping and Giant Interfacial Spin Transparency in $Co_2Fe_{0.4}Mn_{0.6}Si$/Pt Heterostructure*", K. Dutta, **S. N. Panda**, T. Seki, S. Pan, K. Takanashi and A. Barman, *Advanced Quantum Technologies*, 2200033 (2022).

8. "*Femtosecond Laser-Induced Ultrafast Spin Dynamics in Ferromagnetic Thin Films: Comparative Study Using Two Theoretical Models*", S. Mukhopadhyay, S. Majumder, **S.N. Panda** and A. Barman (*Manuscript Submitted*).

9. "*Role of Spin Transport on Ultrafast Demagnetization in β-Ta/$Co_{20}Fe_{60}B_{20}$ Bilayers*", S. Dutta, **S.N. Panda**, J. Sinha, S. Choudhury and A. Barman (*Manuscript Submitted*).

B. Conference presentations

1. "*Detection of interfacial spin transparency by spin pumping in CoFeB/β-Ta thin films***"**, **S.N. Panda** *et al.* in "Bose Tagore National Advanced Workshop on Recent Advances in Condensed Matter Physics: Theory and Experiment **(**NAWCMP-2018), India".

2. "*Study of spin pumping-induced interfacial spin transparency in CoFeB/β-Ta thin films***"**, **S.N. Panda** *et al.* in "International Conference on Complex and Functional Materials (ICCFM-2018), India".

3. "*Ultrafast all-optical detection of interfacial spin transparency for pure spin current transport in CoFeB/β-Ta thin films*", **S.N. Panda** *et al.* in "Ultrafast Sciences (UFS 2019), India".

4. "*All-optical detection of interfacial spin transparency by spin pumping-induced modulation of damping in CoFeB/β-Ta thin films*", **S. N. Panda** *et al.* in "XXth International Workshop on Physics of Semiconductor Devices (IWPSD 2019), India".

5. "*Study of Ultrafast Magnetization Dynamics in Ferrimagnetic* $Gd_x Fe_{1-x}$ *Thin Films*", **S. N. Panda** *et al.* in "Symposium on Science, Technology and applications of Rare Earths (STAR-2019), India".

6. "*Study of Magnetization Dynamics in CoFeB Thin Films Grown on Single Layer Graphene*", **S.N. Panda** *et al.* in "International Conference on Nanoscience and Technology (ICONSAT-2020), India".

7. "*Ultrafast Detection of Interfacial Spin Transparency in CoFeB/β-Ta Thin Film Heterostructures by Pure Spin Current Transport*", **S. N. Panda** *et al.* in "International Conference on Emerging Electronics (IEEE-ICEE 2020), India".

8. "*Ultrafast Detection of Crystal Structure Dependent Interfacial Spin Transparency in W/CoFeB Thin Films*", **S. N. Panda** *et al.* in "International Conference on Current Trends in Materials Science and Engineering (CTMSE-2021), India".

9. "*All-optical detection of crystal structure-dependent interfacial spin transparency in W/CoFeB heterostructures*", **S. N. Panda** *et al.* in "MagIC+ Magnetism, Interactions and Complexity online workshop-2021, Poznan, Poland".

10. "*Crystal Structure Dependent Interfacial Spin Transparency in W/CoFeB Thin Films*", **S. N. Panda** *et al.* in "Bose Fest-2021, India".

11. "*Correlation between Femtosecond Laser-Induced Spin Current and Spin Dynamics at the Single Layer Graphene/CoFeB thin films*", **S. N. Panda** *et al.* in "Joint MMM-Intermag Conference-2022, New Orleans, LA, United States".

Acknowledgement

My journey at S. N. Bose National Centre for Basic Sciences (SNBNCBS) started on 3rd August 2015, as an integrated PhD (IPhD) student. Although I had an aim to do something unique for my society in the field of Physics, but I had no idea how to do it. SNBNCBS have provided me that real exposure to do research in the field of experimental physics. My journey from a small village called Sankorkor near Cuttack city in Orissa to a reputed institute like SNBNCBS was indeed a memorable one. There were lots of ups and downs during this journey which help me to shape myself from a common student to an independent research scholar. All these moments, which I shared with a lot of extraordinary people on the course of this long journey irrespective of good or bad, will be remembered by me forever.

Firstly, I want to convey my sincere gratitude to my PhD supervisor Prof. Anjan Barman for his constant support and excellent guidance throughout my PhD tenure and also when I was a project intern under him. I still remember those days when he carefully listens to all the works presented by me in his group meeting and give his most valuable feedback. Also, he allows me to learn different research methodologies and teach me how to present research work. The efforts he gives to maintain his world-class laboratory, are simply exceptional. That’s why he is always critical about my mistakes as he expects the same effort from me too. Other than being a good researcher, he is an extraordinary person who values his family the most. Overall, he is the perfect blend of discipline, dedication, vision and emotion. I am forever indebted to him for showing faith in me and providing me with an opportunity to explore the field of Spintronics.

I am thankful to Prof. Jaivardhan Sinha for sharing his in-depth understanding of different spin-based phenomena, characterization tools and for helping me in the interpretation of some of my experimental results. I thank Dr Sucheta Mondal for her continuous guidance during my initial days in the lab. She introduced me to the time-resolved magneto-optical Kerr effect set-up and taught me its alignment procedures. I thank my past senior group members Prof. Bivas Rana, Prof. Susmita Saha, Dr Ruma Mandal, Dr Semanti Pal, Dr Bipul Kumar Mahato, Dr Dheeraj Kumar, Dr Debanjan Polley, Dr Arnab Ganguly, Dr Kallol Mukherjee, Prof. Arabinda Haldar, Dr Sandeep Agarwal, Dr Rakhi Acharya and Dr Sumona Sinha for their inspirations whenever I met them. I also thank my senior colleagues-cum-friends Dr Chandrima Banerjee, Dr Samiran Choudhury, Dr Santanu Pan, Dr Avinash Kumar Chaurasiya, Dr Arpan

Bhattacharyya, Mrs Anulekha De and Mr Sourav Sahoo for their support, inspiration and valuable discussions during my PhD tenure. I am thankful to all my lab batchmates Mr Sudip Majumder, Mr Amrit Kumar Mondal, Ms Arundhati Adhikari and Mr Koustuv Dutta for helping me in various experimental work in the lab. Also, I thank my junior colleagues Mr Pratap Kumar Pal, Ms Soma Dutta, Ms Sreya Pal, Ms Suchetana Mukhopadhyay and Mr Chandan Kumar for designing a very friendly and cheerful environment in the lab. The presence of project research students like Mr Gaurav Patel, Mr Shubham Shukla, Mr Anuj Kumar Dhiman, Mr Biswajit Sahoo, Mr Gyandeep Pradhan, Ms Daisy Gogoi, Ms Kajal Tiwari, Mr Abhilash Mishra, Mr Rajdwip Bhar and Mr Gaurav Kanu was also very blissful.

My heartiest thanks to my IPhD batchmates Mr Anupam Gorai, Ms Swarnali Hait, Mr Atul Rathor, Mr Shashank Gupta and Mr Santanu Mukherjee for helping me a lot to get settled in Kolkata. I express my thanks to all my juniors, seniors and colleagues of SNBNCBS institute for creating a homely environment inside the campus. I also express my gratitude to all the members of the technical cell, academic section, account section and purchase section of SNBNCBS for their help and support which make my life much easier in this centre. I acknowledge SNBNCBS for providing me with financial support and all the basic research facilities inside the campus. I am thankful to the SNB-mess cooking team for providing a healthy meal every day. Also, I thank institute canteen members for the evening meal and for the utmost care they have provided to me during the COVID-19 pandemic. I thank all the local shops: Vai da shop, Dulal da shop, Ranjan restaurant, Lakhan da shop, Big Bazaar etc. and online food delivery apps like Swiggy, Zomato, Jio mart etc. for making my living comfortable here without worrying about food.

Although this short paragraph will not be sufficient to describe the contribution of my family to my life success, still, my heartiest thanks to all my family members (Mr Sangram Panda, Mr Bikram Panda, Mr Sanjay Dash, Mrs Sarojini Panda, Mrs Sushree Sangeeta Dash and Mr Subrat Dash) for all their unconditional love, sacrifices and encouragement that make my life so much easier. They have never complained even though I could not go home on any occasion during my PhD. I received lots of love and care from all my sisters and brothers during this period which encourages me a lot. My deepest respect to my grandparents for their unconditional love throughout my life. At last, I am extremely grateful to all my teachers who trained me according to my potential and tried to ignite in me that curiosity to know more about this world which has made me more inclined towards doing research. This thesis is a tribute to all of them.

Surya Narayan Panda

S. N. Bose National Centre for Basic Sciences

Kolkata, India

Table of Contents

Chapter-1

Introduction

The electronics industry has observed a boom since the invention of transistors in 1947 which brings continuous improvement in semiconductor-based microprocessor technology [1]. It has followed the Moore's Law [2] successfully for decades, where the number of transistors almost doubled on a fixed chip area every two years. The data storage density and information processing speed have also increased by many folds during this time while decreasing the external power dissipation and manufacturing cost. This technological revolution has affected almost every aspect of our life. The introduction of advanced electronic products such as smartphones, laptops, modern automobiles, high-definition cameras, advanced manufacturing instruments, medical implants etc., is driving our economy these days. With every passing day, these devices are also becoming much more cheap, fast and more powerful which not only broadens our economy but also increases the quality of our life. Nowadays we mostly find people working on their computers, surfing the internet through the worldwide web, or communicating through mobile phones. In general, this astounding development in modern electronic devices has transformed our daily life by making it much more oriented towards technological innovations.

However, further advancement in this semiconductor-based technology is projected to face lots of hindrances in near future due to several constraints imposed by the laws of physics. For example, "5 nm process" technology is used by the data storage industry nowadays where transistors of 5 nm average size, are used to store one bit of information. It has been observed that further downscaling of this transistor size is much tougher as its size approaches the atomic limit [3]. This bottleneck has already taken effect in some devices by increasing the power consumption, reducing the processing speed, causing a larger heating effect and shortening the battery life in these devices [4]. This has led to an urgent global search for finding different alternatives to semiconductor-based electronics to keep the development of electronics at the pace of the Moore's Law.

Spintronics (an acronym for spin-based electronics) is one of the promising fields to solve the above-mentioned drawbacks arising from semiconductor-based electronics [5, 6]. The central idea behind spintronics is to utilize the spin degrees of freedom of a magnetic material to process and store information. Spin is mainly connected to the magnetization of a material. This was first experimentally observed in 1922 by Stern and Gerlach [7] and theorized by Uhlenbeck and Goudsmit in 1926 [8]. The spin can be imagined to be the self-rotation of a particle around its axis. This rotation can either be clockwise (assumed to be the spin-down configuration) or anticlockwise (known to be the spin-up configuration) which can store one “bit” of data if used in a storage device. Exploration of spin-based properties in different magnetic thin films and heterostructures has led to several scientific discoveries. Among all these discoveries, the observation of giant magnetoresistance (GMR) in ferromagnetic/nonmagnetic/ferromagnetic type spin-valve heterostructures was a milestone [9, 10]. The mechanism involved behind this observation is the less resistive spin-polarized current (a current involving an imbalance between spin-up and spin-down states) transport between different ferromagnetic layers with parallel magnetic orientation. GMR technology had direct industrial application as small magnetic field sensor in the read head of a hard disk drive (HDD) which was able to enhance the data storage density by decreasing the magnetic bit-size. This successful commercialization of GMR had established the field of spintronics among the scientific community and led to the Nobel prize (Physics) in 2007 to Albert Fert and Peter Grünberg. Further advances in this field also led to the discovery of tunnel magnetoresistance (TMR) in ferromagnetic/insulator/ferromagnetic heterostructures [11]. In recent times, magnetic read heads based on TMR technology are widely used in our laptops and desktops. Other than this, TMR is also used in magnetoresistive random-access memory (MRAM) which can lead to high density non-volatile memory devices. These spin-based devices show some distinct advantages over conventional charge-based electronic devices due to their longer thermal stability, faster information processing speed, higher storage capacity and more energy efficiency [12]. Although many spin-based applications can be envisioned in the modern era but there are several challenges that need to be addressed to achieve these applications in reality. For instance, spin-based technological advancement requires an in-depth understanding of fundamental phenomena involved behind spin manipulation mechanisms over a broad timescale in magnetic systems, which need experimental investigation of static and dynamic magnetic properties in a wide range of magnetic materials.

In the upcoming sections, an overview of the significant advancements in the field of spintronics mainly the spin dynamics along with their potential applications will be presented which has motivated us to carry out this doctoral thesis work.

1.1 Importance of magnetic thin films and heterostructures

The significant improvement in the growth facilities of ultrathin films of sub-nanometre thickness has led to the discovery of several interesting new phenomena in present times. Especially use of GMR and TMR in magnetic read heads of HDD and controlled ultrafast magnetization switching [13] has revolutionized this research area. The evolution of this technology has enabled the achievement of 1 TB/inch^2 areal density in modern-day HDD devices which was 2 kB/inch^2 in 1956 as developed by IBM [14]. Initially, people were using magnetic tapes, drums and disks to store the data in the devices. In these devices, information was stored in magnetic domains depending upon their magnetization orientation and the reading and writing of information were done using GMR or TMR-based magnetic read heads [15-17]. Subsequently, longitudinal recording media [18, 19] were used to store information. These media used in-plane magnetized domains to store individual bits which were further retrieved by using GMR and TMR-based read heads. With the ever-increasing demand for enhanced storage capacity, scientists were forced to decrease the domain size of longitudinal recording media which led to two main drawbacks. One was the difficulty to sense magnetic signals from these very small storage areas which was partly solved by using much more sensitive read heads. Another challenge was to thermally stabilize magnetic moments in these tiny magnetic domains by avoiding the superparamagnetic effect [20]. In the presence of superparamagnetic effect, thermal vibration arising at room temperature is also able to randomize the magnetic moments of the domains which limit their further downscaling. This superparamagnetic limit can be partially avoided by using a pinning layer of antiferromagnetic material for exchange biasing the ferromagnetic layer [21]. Later, magnetic thin film heterostructures with large perpendicular magnetic anisotropy (PMA) strength (such as Co/Pd, Co/Pt, Fe/Pt etc.) were investigated and found to be both magnetically and thermally more stable than longitudinal recording media devices [22-25]. Also, the use of soft and hard ferromagnetic materials in a spin-valve structure helps scientists to avoid antiferromagnetic pinning in these devices [26]. In magnetic thin films and multilayers, PMA arises mainly due to the SOC of the layers. Hence, high SOC strength materials such as Pt, Pd, W, Ta etc., are mostly used for device applications. Besides, the PMA strongly depends upon the film thickness and amount of defects, initial growth conditions (such as annealing temperature, doping concentration etc.) of the ferromagnetic layer, heavy metal layer (due to high SOC strength) and capping layer (such as MgO, HfO_2, SiO_2) which allows its efficient control and fine tunability [27, 28]. Changing these external conditions can also affect various static and dynamic magnetic properties such as coercivity, saturating field, saturation magnetization, magnetic anisotropy energy, Curie temperature, Gilbert damping parameter, spin relaxation time, spin transport etc., which have a direct impact on magnetic data storage and memory industry. Therefore, it is important to investigate these static and dynamic magnetic properties systematically in different thin film heterostructures by varying these external conditions.

Although thermal stability of very small magnetic domains and subsequent detection of these small magnetic moments are achieved using various new technologies but for increasing data processing speed it is also important to switch these stable moments effectively in a very short timescale. Various switching mechanisms were proposed over the years such as magnetic field-induced switching [29], precessional switching [30, 31], charge current-induced switching [32], spin current-induced switching [33], all-optical switching (AOS) [13], strain-induced switching [34], domain-wall switching [35], voltage controlled switching [36] etc. Among all these switching mechanisms femtosecond laser-induced AOS is the fastest one. The first complete magnetization reversal using a femtosecond laser pulse was achieved in 2007 by Stanciu *et al*. in a GdFeCo ferrimagnetic alloy [13]. Two mechanisms are primarily involved in this switching process. The first one is the laser-induced heating effect that leads to the ultrafast demagnetization process [37] and the other one is the inverse Faraday effect [38]. Initial studies showed that the AOS process depends on the helicity of the laser beam which is why it is commonly known as all-optical helicity-dependent switching (AO-HDS) [39]. AO-HDS has further been observed in various thin films of synthetic ferrimagnets [39], ferromagnets [40], granular films [40], antiferromagnets [41] etc. Furthermore, recent studies have shown that in some materials this switching can also be helicity independent [42]. The proposal to control data bits through ultrafast laser pulse by the AOS process motivates the scientific community to investigate various underlying mechanisms such as ultrafast demagnetization that are involved in this switching process. The excitation by ultrafast laser pulse can also tune the magnetization switching time just by changing excitation fluence, pulse width, wavelength and spot size of the laser beam. This tunability has significant potential to be used in heat-assisted magnetic recording (HAMR) devices [43].

The above fundamental developments and promising potential applications have motivated us to investigate laser-induced ultrafast processes in different magnetic thin films and heterostructures.

1.1.1 Nonmagnetic/Ferromagnetic thin film heterostructures

A nonmagnetic (NM) layer placed next to a ferromagnetic (FM) layer has attracted immense attention lately because of its potential applications in energy-efficient magnetic data storage and memory devices. If the NM layer has high SOC strength, then these heterostructures can show significant spin-orbit effects like spin pumping [44], spin Hall effect [45], inverse spin Hall effect [46], spin caloric effects [47], Rashba-Edelstein effect [48], inverse Rashba-Edelstein effect [49], interfacial Dzyaloshinskii-Moriya interaction [50] etc., which are vital in developing spin-orbitronic devices. These spin-based effects can generate and utilize pure spin current [51] to store and process information where the net flow of charge vanishes. Devices based on pure spin current have very low unwanted power loss arising from Joule heating and the Oersted field effect, which is why these devices are considered to be more efficient and less power-consuming [52]. For utilizing pure spin current in an electronic circuit, one needs to create a source of spin imbalance (which can be called the spin battery), a dissipation-free conductor, an external manipulator and a detector. In 2002, A. Brataas *et al*. proposed the concept of "spin battery" where the pure spin current can be generated from the magnetization precession in a FM layer and transported to the adjacent NM layer due to the chemical potential differences developed in these heterostructures [53]. This mechanism is known as "spin pumping". The detailed theoretical demonstration and experimental validation of the spin pumping mechanism were further given by Y. Tserkovnyak *et al*. in the same year [44]. Spin pumping is a well-studied and efficient mechanism for the generation of pure spin current in NM/FM heterostructures. This method is devoid of net flow of charge across the NM/FM interface, which makes it free from impedance mismatch problems [54, 55].

Co, Fe, Ni, CoFe, $Co_{20}Fe_{60}B_{20}$ (CoFeB hereafter), Permalloy ($Ni_{80}Fe_{20}$, Py hereafter), ferromagnetic Heusler alloys etc., are a few popular FMs that have been regularly used alongside different NMs for the generation of pure spin current through spin pumping. Among those, CoFeB and Py are very highly used materials due to their low coercivity, negligible magnetostriction, small magnetic anisotropy, high spin polarization and large tunnel magnetoresistance, which make them suitable candidates for magnetic recording head sensors as well as high-frequency transformers [56, 57]. Also, a broad range of NM materials such as heavy metals [58], two-dimensional (2D) materials (such as graphene, transition metal dichalcogenides etc.) [59], semiconductors [60], topological insulators [61], metal oxides [62], superconductors [63] etc., have been investigated for spin pumping based applications. Pt, Pd, W, Ta, Cu, Ru, Ag, Au etc. are a few extensively studied heavy metals for spin pumping study. Among all these, W and Ta have attracted greater attention due to their relatively high SOC strength combined with lower cost in comparison to most commonly used materials like Pt, Au and Ag. Also, W and Ta exhibit thickness-dependent structural phase transition from a tetragonal crystal structure (β-phase) to a body-centred cubic structure (α-phase) [64, 65]. The β-phase is a higher resistive phase with stronger SOC, but its stabilization and cut-off thickness depend upon various initial deposition conditions such as argon pressure, annealing temperature etc. This phase-transition influences pure spin current generation in them which is also evident from different spin Hall angles in two different phases [66]. However, the effect of this structural phase transition on the efficiency of interfacial spin transport across the interfaces is not been extensively studied so far.

The pure spin current generated in NM/FM heterostructures through spin pumping is actively used in spin-torque-based devices, leading to a new sub-field of spintronics called spin-orbitronics [67]. However, the efficiency of the spin-orbit torque (SOT) depends strongly on NM/FM interface quality which can be characterized through parameters such as interfacial spin transparency, spin-mixing conductance, spin backflow factor etc. [68] The interface controls the spin current transport from one layer to another. Various other effects like spin memory loss [69], interfacial spin-orbit coupling [70], interfacial band hybridization [71], two-magnon scattering [72], proximity-induced effects [73], Rashba effect [48] etc. may appear in NM/FM interfaces which can also affect the spin current transport. However, for efficient spin current-based device fabrication, it is important to increase the efficiency of spin transfer across the NM/FM interfaces by minimizing the interfacial losses. The dissipation of pure spin current applies a torque on the magnetization precession of the FM layer which eventually modulates the Gilbert damping parameter of the composite system. If the NM/FM interface is not transparent then the extent of damping modulation can get affected significantly due to the interfacial losses. Hence, NM/FM interface plays a vital role in the efficient transport of pure spin current for being utilized in SOT devices.

Interfacial spin transparency (*T*) can effectively quantify the efficiency of interfacial spin current transfer through the NM/FM interface [68, 74]. *T* determines the extent of electronic band matching at the interfaces and depends on various intrinsic and extrinsic factors such as interfacial defects, spin-mixing conductance, charge conductivity, spin-flip probability, layer thickness etc. For a suitable device application, it is desired that NM/FM interface must have a high *T*-value. This compulsion has ignited the investigation of *T* in different NM/FM heterostructures for different SOT-based applications. Recent studies have shown that overlooking the effect of this *T*-value leads to an underestimation of the magnitude of SOT and spin Hall angle [74]. A major portion of this doctoral thesis is focused on the quantification of *T* through spin pumping and the effect of crystal structure on the *T*-value in Ta/CoFeB and W/CoFeB heterostructures.

So far, primarily electrical excitation and detection techniques such as the non-local spin injection in lateral spin valves, spin-torque ferromagnetic resonance (ST-FMR), spin Hall magnetoresistance, second-harmonic generation, inverse spin Hall effect measurement etc., have been used for the investigation of spin pumping effect and quantification of *T*. These electrical detection techniques need delicate sample fabrication techniques, which may cause various artefacts arising from electrical contacts, impurity scattering centres and large area averaging. Values of different dynamic parameters such as the Gilbert damping parameter are often over-estimated amid the presence of these external artefacts. More recently, all-optical time-resolved magneto-optical Kerr effect (TR-MOKE) [75] technique has emerged as a reliable and non-invasive technique for unambiguous determination of Gilbert damping parameter, which has been effectively used to study the spin pumping-induced pure spin current transport in NM/FM bilayers [75]. Here, the Gilbert damping parameter can be extracted directly from the decay profile of the damped precessional oscillation, giving an edge of this method over other electrical techniques. Besides, TR-MOKE is a local technique which minimizes the contributions arising from defects and inhomogeneities through large area averaging. Throughout, this doctoral thesis work we will use the all-optical TR-MOKE technique to probe the ultrafast magnetization dynamics from femtosecond to nanosecond timescale in various NM/FM heterostructures.

1.1.2 Graphene/Ferromagnet thin films

To build efficient spin-based devices with reduced power consumption, the selection of material is very critical. As spin current is dissipative in nature, long-distance transfer of information requires materials in such devices to have a long spin lifetime [76] and long spin diffusion length [77]. Graphene, a 2D honeycomb lattice of carbon, is a promising material in spintronics owing to the attainment of long spin diffusion length of several micrometres and long spin lifetime of few microseconds at room temperature [78]. These are possible due to the negligible intrinsic SOC strength [79], high electron mobility [80] and low resistivity [81] of graphene. Moreover, other interesting properties like long spin coherence length [82], gate-voltage controlled spin transport [83], large magnetoresistance [84], defect and proximity-induced spin-orbit coupling [85], linear dispersion [86] and weak hyperfine interaction [87] promote graphene to be a suitable material for spin-based complex networking devices. Graphene has a 2D flat surface which violates the energy conservation law of thermodynamics and makes it very unstable at room temperature. However, it can be stabilized in presence of different out-of-plane distortions like ripples, wrinkles, crumples etc. [88] These distortions can be engineered via oxidation [89], hybridization [90], adsorption [91], fluorination [92] and proximity effects [93]. Such engineered graphene can have enhanced SOC strength, band-gap opening (between the graphene occupied and unoccupied bands) and induced localized states around the Fermi level, making it further interesting for spin-based studies.

Among different graphene-based materials, the Graphene/FM hybrid heterostructure is the most vital one from the spintronics point of view. When graphene is deposited in proximity to FM, the pπ-states of graphene hybridize with the d-states of FM at the Graphene/FM interface [93]. The main reasons behind this interfacial band hybridization are the symmetry matching of both the bands and spatial overlap between their orbitals. This hybridization causes an upward shift of FM bands and a downward shift of the graphene bands which significantly alter various magnetic and transport properties of the FM. There is also a charge transfer across the Graphene/FM interface which induces spin polarization in graphene and causes anomalous softening of phonons. Also, this mutual transfer of atoms across the Graphene/FM interface decreases the net spin polarization and magnetic moment of the FM [93]. Recent observations of the spin Hall effect [94], inverse spin Hall effect [59], anomalous Hall effect [95], PMA [96], spin-dependent Klein tunnelling [97], Rashba effect [98], spin pumping [59] and interfacial Dzyaloshinskii-Moriya interaction [99] in these heterostructures prove its potential to be used in spintronic devices. Furthermore, wide-range controllability of defect-induced extrinsic SOC in Graphene/FM thin films via deposition conditions of the FM thin film and gating make these heterostructures a unique material with a broad range of applications.

The non-local spin injection has been the most popular technique to inject and transport spin current in graphene. Here, the spin current is transferred across the Graphene/FM interface by a charge transport mechanism. The difference in resistance of Graphene and FM hinders this charge transport significantly. This problem is widely known as the impedance mismatch problem and it decreases the efficiency of spin transport (smaller than 10%). Although by inserting a thin insulating layer we can avoid this impedance mismatch problem partially but yet the maximum spin transport efficiency achieved so far is only about 30%. A recent demonstration of the spin pumping in Graphene/FM, which is free from any charge current transport, can easily solve this impedance mismatch problem. Due to the presence of out-of-plane distortions in graphene, there is a finite contribution from the two-magnon scattering to the spin transport alongside spin pumping. However, the exact contribution of both spin pumping and two-magnon scattering to the spin transport in Graphene/FM hybrid heterostructures has not been investigated till date. This motivates us to systematically investigate the magnetization dynamics in Graphene/FM heterostructures over a broad range of timescale from femtosecond to nanosecond range capturing various dynamic magnetic phenomena.

1.2 Femtosecond laser-induced ultrafast demagnetization

The magnetization of a magnetic material can be manipulated via different mechanisms. Among these, fundamental exchange interaction is the fastest dynamic process followed by optical inter-site spin transfer and ultrafast demagnetization [75]. These are followed by some relatively slower phenomena such as damped precessional dynamics, spin wave propagation, magnetic vortex dynamics and domain-wall dynamics which can effectively manipulate the system magnetization [75]. In this doctoral thesis work, we are mainly focused on studying ultrafast demagnetization and damped precessional dynamics of various magnetic thin films and heterostructures.

The ultrafast demagnetization mechanism was first demonstrated in 1996 by Beaurepaire *et al.* in ferromagnetic nickel thin film [37]. In this article, it was observed that after being excited by a 60-femtosecond laser pulse the remanent magnetization of the system dropped very rapidly within a few hundreds of femtoseconds followed by subsequent recovery. This rapid drop in the magnetic moment of the system was called ultrafast demagnetization. This magnetization drop is of an exponential type having a time constant which is termed as the ultrafast demagnetization time. In the initial years after its discovery, ultrafast demagnetization was interpreted to be a consequence of spin temperature rise which is correlated with the electron temperature of a magnetic system. A three-temperature model was proposed as an extension to the two-temperature model [100] by adding the spin degree of freedom to the existing electron and lattice system. Although in this assumption the process of energy transfer from the femtosecond laser pulse to magnetic degrees of freedom has remained an enigma. Also, the consideration of instantaneous rise in electron temperature without any properly defined angular momentum transfer mechanism makes this model even more debatable. This debate was intensified even further when an ultrafast demagnetization time of around 50 femtosecond was achieved by Gudde *et al.*, which raised questions about the concept of energy exchange mechanisms [101]. To solve this conundrum, several other models such as the microscopic three-temperature model [102], four-temperature model [103], super-diffusive spin transport model [104] etc., have been proposed over the last two decades to understand the underlying mechanisms behind the ultrafast demagnetization mechanism. Besides, different mechanisms have been proposed to explain the angular momentum transfer process during this sudden drop in magnetization, including Elliott-Yafet type spin-flip scattering [105], Coulomb exchange spin-flip scattering [106], electron-magnon spin-flip scattering [107], SOC [108], spin current transport [104], transport of non-thermal electrons [109] etc. Later, ultrafast demagnetization was also found to be an important phenomenon involved in the AOS process which can revolutionize ultrafast data storage technology by optical manipulation of magnetic bits [13]. One can also estimate the spin polarization of a material quantitatively from ultrafast demagnetization measurement [110]. The high value of spin polarization can result in a high TMR value of a composite magnetic structure which is mandatory for efficient magnetic storage and memory devices. Furthermore, understanding the mechanisms behind this phenomenon will be helpful for understanding sub-picosecond non-equilibrium spin dynamics which is of utmost importance for spintronics applications.

1.3 Correlation between ultrafast demagnetization time and Gilbert damping parameter

Although various models and mechanisms are been proposed to understand this ultrafast demagnetization process but the exact microscopic mechanisms involved in this magnetization loss remained elusive to the scientific community. Detailed calculations correlating the different phenomena occurring at distinct time scales of magnetization dynamics have been performed by interconnecting different models. As a result of these studies, it has been found that although the timescale of magnetic damping (approximately nanosecond) and ultrafast demagnetization (approximately femtosecond) differ by several orders of magnitude, the underlying mechanism involved behind these two processes can be very similar. Therefore, the correlation between the ultrafast demagnetization time and Gilbert damping parameter was thought to be a potent method for probing the dominant microscopic contribution to the ultrafast demagnetization process. As a first step toward this direction, Koopmans *et al.* suggested an inversely proportional relationship between the ultrafast demagnetization time and Gilbert damping parameter in 2005 based on a quantum mechanical assumption that there are two different magnetic fields (i.e., exchange field and applied external magnetic field) that dominate at two different timescales (i.e., femtosecond and nanosecond) [111]. However, this model revealed several drawbacks due to over-simplified assumptions, such as negligence of band structure variation, inapplicability to rare-earth metals and lack of experimental validation [112]. Later by using density-functional theory, Fahnle *et al.* suggested that the ultrafast demagnetization time and Gilbert damping parameter can be either directly or inversely proportional to each other depending on governing microscopic mechanism in damping [113]. The proportional dependence suggests a major conductivity-like contribution to damping governed by the intra-band scattering mechanism, whereas an inverse dependency confirms a dominant resistivity-like contribution to damping through the inter-band scattering mechanism. This model also had a few drawbacks as it does not include the effect of spin transport in the ultrafast demagnetization process. More recently, Zhang *et al.* have shown experimentally that in Co/Ni heterostructures the Gilbert damping parameter shows a proportional dependency on the ultrafast demagnetization time due to dominant spin-flip scattering contribution to the ultrafast demagnetization mechanism [114]. They have suggested an inverse correlation between Gilbert damping parameter and ultrafast demagnetization time may occur due to major spin transport contribution via spin pumping effect mechanism in metallic thin film heterostructures. Further experiments suggest that depending upon the choice of materials and the nature of the interaction between the laser pulse and magnetic system, there are predominantly two contributions to the ultrafast demagnetization process [115]. The first one comes from spin-flip scattering and the other contribution comes from spin current transport. In this thesis work, we will explore how different microscopic contributions dominate the ultrafast magnetization dynamics in several potentially important thin films by correlating their ultrafast demagnetization time with the Gilbert damping parameter.

1.4 Objectives of this thesis

The main objective of this doctoral research work is to elucidate the ultrafast spin dynamics spanning over a long timescale ranging from femtoseconds to nanoseconds in different ferromagnetic thin films and heterostructures. It aims to focus on some of the leading problems in the field of spintronics, such as the correlation between different microscopic processes involved with ultrafast magnetization dynamics modulated by laser fluence and film thickness in ferromagnetic thin films, reliable probing of all-optical laser-induced spin pumping effect and determination of interfacial spin transparency (T) in technologically important NM/FM heterostructures, the effect of crystal structure on spin pumping-induced T, the mechanisms involved in spin transport through single layer graphene (SLG)/FM heterostructure and the role of spin-orbit coupling on the magnetization dynamics and interfacial spin transport. The objective can be more precisely described as understanding the effects of film thickness, laser fluence, external magnetic field, crystal structure, spin-orbit coupling strength and spin-torque on the ultrafast magnetization dynamics of ferromagnetic thin films and heterostructures.

The samples for these studies have been prepared by ultrahigh vacuum RF/DC magnetron sputtering techniques. The structural, morphological and elemental properties of the samples have been characterized by atomic force microscopy, X-ray reflectivity, X-ray diffraction and micro-Raman spectroscopy. The static magnetic properties have been studied by the static magneto-optical Kerr effect magnetometry and vibrating sample magnetometry. The magnetization dynamics have been studied using custom-built TR-MOKE magnetometry based on an amplified femtosecond laser system. The ultrafast demagnetization data have been modelled by a phenomenological three-temperature model, the precessional data have been modelled by solving the Landau Lifshitz Gilbert equation and the interfacial spin transport has been modelled by both ballistic and diffusive transport theories.

The studied systems in this thesis can be classified as follows:

1.4.1 Investigation of the effect of spin pumping in NM/FM thin film heterostructures

By utilizing an all-optical excitation and detection technique, we have demonstrated spin pumping-induced interfacial spin transparency in technologically important β-Ta/CoFeB/SiO_2 and W/CoFeB/SiO_2 (in both α and β phases of W) heterostructures. Other than interfacial spin transparency, we have also extracted parameters like spin-diffusion length, spin-mixing conductance, spin-flip probability and spin backflow factor in these heterostructures. Additional effects like spin memory loss, interfacial band hybridization, two-magnon scattering etc., which may affect the Gilbert damping, have also been examined in these systems.

1.4.2 Investigation of the effect of spin pumping on spin dynamics in single layer graphene (SLG)/FM thin film heterostructures

We have investigated the magnetization dynamics in the SLG/CoFeB/SiO_2 heterostructure and isolated the contribution of spin pumping from other contributions like spin memory loss and two-magnon scattering and established spin pumping-induced spin transport as the dominant contributor to ultrafast demagnetization mechanism. An inverse correlation between ultrafast demagnetization time and Gilbert damping parameter is been established due to interfacial spin accumulation at the SLG/CoFeB interface and spin pumping-induced pure spin currents transport.

1.4.3 Fluence-dependent magnetization dynamics in Py thin films

The study of pump fluence-dependent ultrafast magnetization dynamics in Py thick films having different thicknesses has been conducted by using TR-MOKE magnetometry. The effect of increasing laser pump fluence on various dynamic parameters, such as ultrafast demagnetization time, fast remagnetization time, electron temperature, spin temperature and lattice temperature have been comprehensively studied and explained. Also, the modulation of precessional frequency, temporal chirp parameter and Gilbert damping parameter with film thickness and laser pump fluence have been carefully studied for both uniform Kittel mode and bulk perpendicular standing spin wave modes.

1.4.4 Effect of SOC strength on ultrafast magnetization dynamics

To underpin the effect of SOC on the magnetization dynamics of ferromagnetic CoFeB, we have used different nonmagnetic underlayers (such as Ta/Ru/Ta, Ta, W, Pt, Cu and Si/SiO_2 (i.e., no underlayer)) that differ in SOC strength. We establish an intercorrelation between ultrafast demagnetization time, fast remagnetization time, Gilbert damping parameter and SOC strength. We have also utilized the SOC strength of NM layers to control other important parameters like effective spin-mixing conductance and spin chemical potential which are of paramount importance for spin-based device fabrication. It has been observed that the higher the SOC strength of the underlayer, the higher the Gilbert damping, the faster the ultrafast demagnetization and remagnetization and more efficient the spin transport through the interface and the smaller the interfacial spin accumulation.

All these studies can open up new pathways for the construction of future spintronics and spin-orbitronics devices.

References

1. J. Bardeen and W. H. Brattain, Phys. Rev. **75**, 1208-1225 (1949).
2. G. E. Moore, IEEE Solid-State Circuits Society Newsletter **11**, 33-35 (2006).
3. Moore's deviation, Nat. Nanotechnol. **12**, 1105 (2017).
4. F. Peper, New Gener. Comput. **35**, 253-269 (2017).
5. A. Hirohata, K. Yamada, Y. Nakatani, I. L. Prejbeanu, B. Dieny, P. Pirro and B. Hillebrands, J. Magn. Magn. Mater. **509**, 166711 (2020).
6. S. M. Yakout, J. Supercond. Nov. Magn. **33**, 2557-2580 (2020).
7. W. Gerlach and O. Stern, Z. Phys. **9**, 349-352 (1922).

8. G. E. Uhlenbeck and S. Goudsmit, Nature **117**, 264-265 (1926).

9. M. N. Baibich, J. M. Broto, A. Fert, F. N. Van Dau, F. Petroff, P. Etienne, G. Creuzet, A. Friederich and J. Chazelas, Phys. Rev. Lett. **61**, 2472-2475 (1988).

10. G. Binasch, P. Grünberg, F. Saurenbach and W. Zinn, Phys. Rev. B **39**, 4828-4830 (1989).

11. M. Julliere, Phys. Lett. A **54**, 225-226 (1975).

12. P. Barla, V. K. Joshi and S. Bhat, J. Comput. Electron. **20**, 805-837 (2021).

13. C. D. Stanciu, F. Hansteen, A. V. Kimel, A. Kirilyuk, A. Tsukamoto, A. Itoh and T. Rasing, Phys. Rev. Lett. **99**, 047601 (2007).

14. E. Grochowski, The Continuing Evolution of Magnetic Hard Disk Drives. In Holographic Data Storage (Springer: Berlin, 2000).

15. S. Ikeda, J. Hayakawa, Y. Ashizawa, Y. M. Lee, K. Miura, H. Hasegawa, M. Tsunoda, F. Matsukura and H. Ohno, Appl. Phys. Lett. **93**, 082508 (2008).

16. S. S. P. Parkin, C. Kaiser, A. Panchula, P. M. Rice, B. Hughes, M. Samant and S. H. Yang, Nat. Mater. **3**, 862-867 (2004).

17. J. S. Moodera, L. R. Kinder, T. M. Wong and R. Meservey, Phys. Rev. Lett. **74**, 3273-3276 (1995).

18. H. N. Bertram, H. Zhou and R. Gustafson, IEEE Trans. Magn. **34**, 1845-1847 (1998).

19. A. Moser and D. Weller, IEEE Trans. Magn. **35**, 2808-2813 (1999).

20. S. H. Charap, L. P. Ling and H. Yanjun, IEEE Trans. Magn. **33**, 978-983 (1997).

21. R. L. Stamps, J. Phys. D: Appl. Phys. **33**, R247-R268 (2000).

22. M. Albrecht, C. T. Rettner, A. Moser, M. E. Best and B. D. Terris, Appl. Phys.Lett. **81**, 2875-2877 (2002).

23. S. Iwasaki, IEEE Trans. Magn. **16**, 71-76 (1980).

24. D. Weller and A. Moser, IEEE Trans. Magn. **35**, 4423-4439 (1999).

25. J. Moritz, S. Landis, J. C. Toussaint, R. Bayle-Guillemaud, B. Rodmacq, G. Casali, A. Lebib, Y. Chen, J. P. Nozires and B. Dieny, IEEE Trans. Magn. **38**, 1731-1736 (2002).

26. I. A. Iusipova and A. I. Popov, Semiconductors **55**, 1008-1020 (2021).

27. B. Dieny and M. Chshiev, Rev. Mod. Phys. **89**, 025008 (2017).

28. B. Tudu and A. Tiwari, Vacuum **146**, 329-341 (2017).

29. C. H. Back, D. Weller, J. Heidmann, D. Mauri, D. Guarisco, E. L. Garwin and H. C. Siegmann, Phys. Rev. Lett. **81**, 3251 (1998).

30. T. Gerrits, H. A. Van Den Berg, J. Hohlfeld, L. Bär and T. Rasing, Nature **418**, 509-12 (2002).

31. T. M. Crawford, P. Kabos and T. J. Silva, Appl. Phys. Lett. **76**, 2113-2115 (2000).

32. H. An, T. Ohno, Y. Kanno, Y. Kageyama, Y. Monnai, H. Maki, J. Shi and K. Ando, Sci. Adv. **4**, eaar2250 (2018).

33. L. Liu, C. F. Pai, Y. Li, H. W. Tseng, D. C. Ralph and R. A. Buhrman, Science **336**, 555-558 (2012).

34. A. K. Biswas, H. Ahmad, J. Atulasimha and S. Bandyopadhyay, Nano Lett. **17**, 3478-3484 (2017).

35. M. Yamanouchi, D. Chiba, F. Matsukura and H. Ohno, Nature **428**, 539-542 (2004).

36. A. Chen, Y. Zhao, P. Li, X. Zhang, R. Peng, H. Huang, L. Zou, X. Zheng, S. Zhang, P. Miao, Y. Lu, J. Cai and C. W. Nan, Adv. Mater. **28**, 363-369 (2016).

37. E. Beaurepaire, J. C. Merle, A. Daunois and J. Y. Bigot, Phys. Rev. Lett. **76**, 4250-4253 (1996).

38. A. V. Kimel, A. Kirilyuk, P. A. Usachev, R. V. Pisarev, A. M. Balbashov and T. Rasing, Nature **435**, 655-657 (2005).

39. J. W. Liao, P. Vallobra, L. O'Brien, U. Atxitia, V. Raposo, D. Petit, T. Vemulkar, G. Malinowski, M. Hehn, E. Martínez, S. Mangin and R. P. Cowburn, Adv. Sci. **6**, 1901876 (2019).
40. C. H. Lambert, S. Mangin, B. S. Varaprasad, Y. K. Takahashi, M. Hehn, M. Cinchetti, G. Malinowski, K. Hono, Y. Fainman, M. Aeschlimann and E. E. Fullerton, Science **345**, 1337-1340 (2014).
41. T. Dannegger, M. Berritta, K. Carva, S. Selzer, U. Ritzmann, P. M. Oppeneer and U. Nowak, Phys. Rev. B **104**, L060413 (2021).
42. J. Wei, B. Zhang, M. Hehn, W. Zhang, G. Malinowski, Y. Xu, W. Zhao and S. Mangin, Phys. Rev. Appl. **15**, 054065 (2021).
43. L. Pan and D. B. Bogy, Nat. Photonics **3**, 189-190 (2009).
44. Y. Tserkovnyak, A. Brataas and G. E. W. Bauer, Phys. Rev. Lett. **88**, 117601 (2002).
45. J. Sinova, S. O. Valenzuela, J. Wunderlich, C. H. Back and T. Jungwirth, Rev. Mod. Phys. **87**, 1213-1260 (2015).
46. E. Saitoh, M. Ueda, H. Miyajima and G. Tatara, Appl. Phys. Lett. **88**, 182509 (2006).
47. W. Lin, M. Hehn, L. Chaput, B. Negulescu, S. Andrieu, F. Montaigne and S. Mangin, Nat. Commun. **3**, 744 (2012).
48. J. C. R. Sánchez, L. Vila, G. Desfonds, S. Gambarelli, J. P. Attané, J. M. De Teresa, C. Magén and A. Fert, Nat. Commun. **4**, 2944 (2013).
49. K. Shen, G. Vignale and R. Raimondi, Phys. Rev. Lett. **112**, 096601 (2014).
50. A. K. Chaurasiya, C. Banerjee, S. Pan, S. Sahoo, S. Choudhury, J. Sinha and A. Barman, Sci. Rep. **6**, 32592 (2016).
51. A. Hoffmann, Phys. Status Solidi C **4**, 4236-4241 (2007).
52. S. A. Wolf, D. D. Awschalom, R. A. Buhrman, J. M. Daughton, S. von Molnár, M. L. Roukes, A. Y. Chtchelkanova and D. M. Treger, Science **294**, 1488-95 (2001).
53. A. Brataas, Y. Tserkovnyak, G. E. W. Bauer and B. I. Halperin, Phys. Rev. B **66**, 060404 (2002).
54. G. Schmidt, D. Ferrand, L. W. Molenkamp, A. T. Filip and B. J. van Wees, Phys. Rev. B **62**, R4790-R4793 (2000).
55. K. Ando, S. Takahashi, J. Ieda, H. Kurebayashi, T. Trypiniotis, C. H. Barnes, S. Maekawa and E. Saitoh, Nat. Mater. **10**, 655-9 (2011).
56. J. S. Kim, G. Kim, J. Jung, K. Jung, J. Cho, W. Y. Kim and C. Y. You, Sci. Rep. **12**, 4549 (2022).
57. G. Nahrwold, J. M. Scholtyssek, S. Motl-Ziegler, O. Albrecht, U. Merkt and G. Meier, J. Appl. Phys. **108**, 013907 (2010).
58. A. Brataas, Y. Tserkovnyak, G. E. W. Bauer and P. J. Kelly, Spin pumping and spin transfer, (Oxford University Press, United Kingdom, 2017).
59. Z. Tang, E. Shikoh, H. Ago, K. Kawahara, Y. Ando, T. Shinjo and M. Shiraishi, Phys. Rev. B **87**, 140401 (2013).
60. R. Adhikari, M. Matzer, A. T. Martín-Luengo, M. C. Scharber and A. Bonanni, Phys. Rev. B **94**, 085205 (2016).
61. M. Jamali, J. S. Lee, J. S. Jeong, F. Mahfouzi, Y. Lv, Z. Zhao, B. K. Nikolić, K. A. Mkhoyan, N. Samarth and J.-P. Wang, Nano Lett. **15**, 7126-7132 (2015).
62. B. Sahoo, K. Roy, P. Gupta, A. Mishra, B. Satpati, B. B. Singh and S. Bedanta, Adv. Quantum Technol. **4**, 2000146 (2021).
63. K. R. Jeon, C. Ciccarelli, A. J. Ferguson, H. Kurebayashi, L. F. Cohen, X. Montiel, M. Eschrig, J. W. A. Robinson and M. G. Blamire, Nat. Mater. **17**, 499-503 (2018).

64. J. Liu, T. Ohkubo, S. Mitani, K. Hono and M. Hayashi, Appl. Phys. Lett. **107**, 232408 (2015).
65. J. Torrejon, J. Kim, J. Sinha, S. Mitani, M. Hayashi, M. Yamanouchi and H. Ohno, Nat. Commun. **5**, 4655 (2014).
66. S. Mondal, S. Choudhury, N. Jha, A. Ganguly, J. Sinha and A. Barman, Phys. Rev. B **96**, 054414 (2017).
67. A. Soumyanarayanan, N. Reyren, A. Fert and C. Panagopoulos, Nature **539**, 509-517 (2016).
68. C. F. Pai, Y. Ou, L. H. Vilela-Leão, D. C. Ralph and R. A. Buhrman, Phys. Rev. B **92**, 064426 (2015).
69. J. C. Rojas-Sánchez, N. Reyren, P. Laczkowski, W. Savero, J. P. Attané, C. Deranlot, M. Jamet, J. M. George, L. Vila and H. Jaffrès, Phys. Rev. Lett. **112**, 106602 (2014).
70. V. P. Amin and M. D. Stiles, Phys. Rev. B **94**, 104419 (2016).
71. N. Nakajima, T. Koide, T. Shidara, H. Miyauchi, H. Fukutani, A. Fujimori, K. Iio, T. Katayama, M. Nývlt and Y. Suzuki, Phys. Rev. Lett. **81**, 5229-5232 (1998).
72. M. J. Hurben and C. E. Patton, J. Appl. Phys. **83**, 4344-4365 (1998).
73. K. Nagata, S. Y. Matsushita, X. C. Pan, K. K. Huynh and K. Tanigaki, Phys. Rev. Mater. **5**, 024208 (2021).
74. W. Zhang, W. Han, X. Jiang, S. H. Yang and S. S. P. Parkin, Nat. Phys. **11**, 496-502 (2015).
75. A. Barman and J. Sinha, Spin Dynamics and Damping in Ferromagnetic Thin Films and Nanostructures (Springer: Switzerland, 2018).
76. T. Y. Yang, J. Balakrishnan, F. Volmer, A. Avsar, M. Jaiswal, J. Samm, S. R. Ali, A. Pachoud, M. Zeng, M. Popinciuc, G. Güntherodt, B. Beschoten and B. Özyilmaz, Phys. Rev. Lett. **107**, 047206 (2011).
77. N. Tombros, C. Jozsa, M. Popinciuc, H. T. Jonkman and B. J. van Wees, Nature **448**, 571-574 (2007).
78. K. S. Novoselov, A. K. Geim, S. V. Morozov, D. Jiang, Y. Zhang, S. V. Dubonos, I. V. Grigorieva and A. A. Firsov, Science **306**, 666-669 (2004).
79. D. Huertas-Hernando, F. Guinea and A. Brataas, Phys. Rev. B **74**, 155426 (2006).
80. A. K. Geim and K. S. Novoselov, Nat. Mater. **6**, 183-191 (2007).
81. Y. Liu, H. Tsunoyama, T. Akita and T. Tsukuda, J. Phys. Chem. C **113**, 13457-13461 (2009).
82. C. Berger, Z. Song, X. Li, X. Wu, N. Brown, C. Naud, D. Mayou, T. Li, J. Hass, A. N. Marchenkov, E. H. Conrad, P. N. First and W. A. de Heer, Science **312**, 1191-1196 (2006).
83. S. Das Sarma, S. Adam, E. H. Hwang and E. Rossi, Rev. Mod. Phys. **83**, 407-470 (2011).
84. V. M. Karpan, G. Giovannetti, P. A. Khomyakov, M. Talanana, A. A. Starikov, M. Zwierzycki, J. van den Brink, G. Brocks and P. J. Kelly, Phys. Rev. Lett. **99**, 176602 (2007).
85. S. Sinha, S. Pan, S. Choudhury, J. Sinha and A. Barman, J. Phys. Chem. C **121**, 17442-17449 (2017).
86. A. H. Castro Neto, F. Guinea, N. M. R. Peres, K. S. Novoselov and A. K. Geim, Rev. Mod. Phys. **81**, 109-162 (2009).
87. J. Fischer, B. Trauzettel and D. Loss, Phys. Rev. B **80**, 155401 (2009).
88. S. Deng and V. Berry, Mater. Today **19**, 197-212 (2016).
89. A. M. Dimiev and J. M. Tour, ACS Nano **8**, 3060-3068 (2014).
90. S. Chae, T. H. Le, C. S. Park, Y. Choi, S. Kim, U. Lee, E. Heo, H. Lee, Y. A. Kim, O. S. Kwon and H. Yoon, Nanoscale **12**, 13351-13359 (2020).
91. F. Mehmood, R. Pachter, W. Lu and J. J. Boeckl, J. Phys. Chem. C **117**, 10366-10374 (2013).

92. S. K. Padamata, A. Yasinskiy, S. Stopic and B. Friedrich, J. Fluor. Chem. **255-256**, 109964 (2022).
93. A. Dahal and M. Batzill, Nanoscale **6**, 2548-2562 (2014).
94. A. Avsar, J. Y. Tan, T. Taychatanapat, J. Balakrishnan, G. K. W. Koon, Y. Yeo, J. Lahiri, A. Carvalho, A. S. Rodin, E. C. T. O’Farrell, G. Eda, A. H. Castro Neto and B. Özyilmaz, Nat. Commun. **5**, 4875 (2014).
95. Z. Wang, C. Tang, R. Sachs, Y. Barlas and J. Shi, Phys. Rev. Lett. **114**, 016603 (2015).
96. N. Rougemaille, A. T. N'Diaye, J. Coraux, C. Vo-Van, O. Fruchart and A. K. Schmid, Appl. Phys. Lett. **101**, 142403 (2012).
97. M. H. Liu, J. Bundesmann and K. Richter, Phys. Rev. B **85**, 085406 (2012).
98. O. Rader, A. Varykhalov, J. Sánchez-Barriga, D. Marchenko, A. Rybkin and A. M. Shikin, Phys. Rev. Lett. **102**, 057602 (2009).
99. A. K. Chaurasiya, A. Kumar, R. Gupta, S. Chaudhary, P. K. Muduli and A. Barman, Phys. Rev. B **99**, 035402 (2019).
100. B. L. K. S. I. Anisimov and T. L. Perel'man, Sov. Phys. JETP **39**, 375 (1974).
101. J. Güdde, U. Conrad, V. Jähnke, J. Hohlfeld and E. Matthias, Phys. Rev. B **59**, R6608-R6611 (1999).
102. B. Koopmans, G. Malinowski, F. Dalla Longa, D. Steiauf, M. Fähnle, T. Roth, M. Cinchetti and M. Aeschlimann, Nat. Mater. **9**, 259-265 (2010).
103. A. Mekonnen, A. R. Khorsand, M. Cormier, A. V. Kimel, A. Kirilyuk, A. Hrabec, L. Ranno, A. Tsukamoto, A. Itoh and T. Rasing, Phys. Rev. B **87**, 180406 (2013).
104. M. Battiato, K. Carva and P. M. Oppeneer, Phys. Rev. Lett. **105**, 027203 (2010).
105. A. Born, R. Decker, R. Büchner, R. Haverkamp, K. Ruotsalainen, K. Bauer, A. Pietzsch and A. Föhlisch, Sci. Rep. **11**, 1883 (2021).
106. M. Krauß, T. Roth, S. Alebrand, D. Steil, M. Cinchetti, M. Aeschlimann and H. C. Schneider, Phys. Rev. B **80**, 180407 (2009).
107. E. Carpene, E. Mancini, C. Dallera, M. Brenna, E. Puppin and S. De Silvestri, Phys. Rev. B **78**, 174422 (2008).
108. G. P. Zhang and W. Hübner, Phys. Rev. Lett. **85**, 3025-3028 (2000).
109. J. H. Shim, A. A. Syed, J. I. Kim, H. G. Piao, S. H. Lee, S. Y. Park, Y. S. Choi, K. M. Lee, H. J. Kim, J.R. Jeong, J. I. Hong, D. E. Kim and D. H. Kim, Sci. Rep. **10**, 6355-6355 (2020).
110. A. Mann, J. Walowski, M. Münzenberg, S. Maat, M. J. Carey, J. R. Childress, C. Mewes, D. Ebke, V. Drewello, G. Reiss and A. Thomas, Phys. Rev. X **2**, 041008 (2012).
111. B. Koopmans, J. J. M. Ruigrok, F. D. Longa and W. J. M. D. Jonge, Phys. Rev. Lett. **95**, 267207 (2005).
112. J. Walowski, G. Müller, M. Djordjevic, M. Münzenberg, M. Kläui, C. A. F. Vaz and J. A. C. Bland, Phys. Rev. Lett. **101**, 237401 (2008).
113. M. Fähnle, J. Seib and C. Illg, Phys. Rev. B **82**, 144405 (2010).
114. W. Zhang, W. He, X. Q. Zhang, Z. H. Cheng, J. Teng and M. Fähnle, Phys. Rev. B **96**, 220415 (2017).
115. W. Zhang, Q. Liu, Z. Yuan, K. Xia, W. He, Q. F. Zhan, X. Q. Zhang and Z. H. Cheng, Phys. Rev. B **100**, 104412 (2019).

Chapter-2

Theoretical background

2.1 Ferromagnetism

Magnetic materials in a magnetic field (H) develop a net magnetic moment. The amount of magnetic moment per unit volume is known as the magnetization (M) of that system. The relation between M and H can be given by:

$$M = \chi H \tag{2.1}$$

Here, χ is the magnetic susceptibility of the material. The dependency of χ on H and temperature (T) determines the magnetic ordering of the system. Based on this dependency magnetic systems can be classified into five groups called diamagnetic, paramagnetic, ferromagnetic, ferrimagnetic and antiferromagnetic. Diamagnetic materials have a negative susceptibility which is independent of H and T. This dependency can be explained by Langevin's theory of diamagnetism [1, 2] assuming only the orbital angular momentum of the electron. Paramagnetic susceptibility is independent of H but shows an inverse dependency on the T [3]. This variation can be explained by Curie's law of paramagnetism [4]. The susceptibility of FM materials shows a similar inverse dependency on T. However, the uniqueness of these materials is that below a critical temperature (called Curie temperature (T_c)) these materials show some finite magnetization, which is known as spontaneous magnetization. Susceptibility of these materials is given by Curie-Weiss law as [5, 6]:

$$\chi_f = \frac{C}{T - T_c} \tag{2.2}$$

Here, C is a constant (given as $Ng^2J(J+1)\mu_B^2/3k_B$ where N is the number of atoms per unit volume, g is the Lande g-factor, J is the total angular momentum quantum number, μ_B is the Bohr magneton and k_B is the Boltzmann's constant). To explain this spontaneous magnetization, Weiss assumed that an inherent molecular field always exists inside a FM. Later, Heisenberg theoretically established that this molecular field comes from the fundamental exchange interaction by assuming both orbital and spin degrees of freedom of the electron [7]. For FMs, the exchange integral is positive which favours parallel alignment of neighbouring spins. This exchange integral is negative for antiferromagnetic materials leading to an antiparallel alignment of adjacent spins which resulted in a net-zero magnetic moment. In the case of ferrimagnets, although neighbouring spins are antiparallel but they possess different magnitudes which leads to a non-zero magnetic moment at low temperature. In this doctoral thesis, we have investigated different FMs such as CoFeB and Py.

2.2 Magnetization dynamics

As discussed in the previous section, consideration of spin degrees of freedom of a material is mandatory for the realization of magnetization in a ferromagnetic material. Thus, to get an in-depth insight into the different magnetic properties of a material, we need to understand both static and dynamic spin-based properties of that material. Ultrafast magnetization dynamics cover a wide spectrum of phenomena ranging over femtosecond (fs) to microsecond (μs) timescale. The faster dynamic phenomena are fundamental exchange interaction (~ few fs), optical inter-site spin transfer (~ 10s fs), spin-orbit coupling (~ 10s fs - few picosecond (ps)) and ultrafast demagnetization (~ 100s fs - few ps). The comparatively slower dynamic phenomena are precessional dynamics (~ few ps - few nanosecond (ns)), damping (~ 100s ps - few ns), vortex core switching (~ 10s ps - few ns), magnetic writing via spin reversal (~ few ps - 100s ps), propagation of the spin wave (~ 100s ps - 10s ns) and domain-wall motion (~ few ns - few μs) [8].

During laser-based TR-MOKE measurements, a short laser pulse (~ 10s fs pulse width) excites the magnetic material. The coherent interaction of laser photon with electron and spin degrees of freedom of magnetic material leads to instantaneous thermalization of these electrons and spins which causes a sudden loss in magnetization of the material. This phenomenon is known as ultrafast demagnetization [9]. Ultrafast demagnetization is followed by a two-step recovery of the disordered magnetic system through fast remagnetization (occurs within 10s ps due to the flow of energy from electron and spin system to lattice) and slow remagnetization (occurs within 100s ps due to the energy dissipation from lattice to surroundings or substrate). The slow remagnetization process is superimposed with a damped precessional oscillation around an effective magnetic field direction within the time range of a few ns.

2.2.1 Ultrafast demagnetization

Before the 1990s, the use of ferromagnetic films for data writing applications through Curie-point writing was an interesting idea [10]. The time taken for recovery of magnetization in ferromagnetic materials after excitation by femtosecond laser pulse sets the limitation in data processing speed. This limitation is based on the fact that after the excitation by a laser pulse, hot electron gas is created above the Fermi level which further thermalizes magnetic and non-magnetic systems within 1 ps. However, the exact mechanisms involved in the interactions of electron gas with other systems (such as spin and lattice) which cause modulation of magnetization, were unknown. It was assumed that in the states involving the hot electrons, the spins are excited by spin-dependent electron scattering through electron-magnon interaction. However, the lack of experimental facilities to probe these transient hot electron states in femtosecond timescale created an open research field. Active research in this field was further ignited in 1996 when the ultrafast demagnetization was first observed by Beaurepaire *et al.* in an in-plane magnetized Ni foil using the optical pump-probe technique [9]. They observed an instantaneous drop in remanent magnetization within a few hundreds of fs after excitation by a 60 fs pulsed laser beam. This first observation of ultrafast demagnetization was described by a simple theoretical argument based on a phenomenological three-temperature model. With time, several stand-alone theories were proposed to explain different experimental observations on ultrafast demagnetization [11-14]. Despite all those proposed models and mechanisms, the exact underlying microscopic processes involved in this ultrafast loss of magnetization have remained debatable.

2.2.1.1 Three-temperature model

The ultrafast demagnetization process was first explained phenomenologically by using the 'three-temperature (3T) model'. It was an expansion of a well-studied "two-temperature (2T) model" which was proposed by Anisimov in 1974 based on electron-lattice energy distribution [15]. In 3T-model, it was assumed that electron, spin and lattice are three coupled heat baths that inherently exist inside a FM material. These heat baths have their specific heats and temperatures. Also, they can exchange energy among themselves at any given time to bring the whole system into equilibrium.

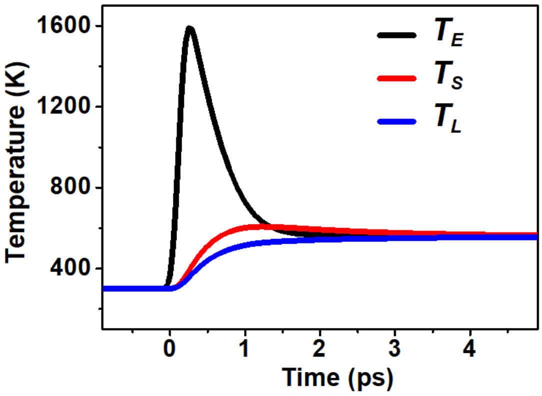

Figure 2.1: Temperature evolution of electron (E), spin (S) and lattice (L) heat baths after laser excitation.

According to this model, after the pump laser pulse excitation, the photon energy of the laser beam is absorbed by the electron heat reservoir and creates hot electrons above the Fermi level. This is also evident from the sudden increase in the electron temperature in Figure 2.1. During this electron temperature rise, the total spin angular momentum of the system remains conserved due to dipole approximation. Further, redistribution of majority and minority spins through scattering leads to an increase in spin temperature after a certain time delay. This rise in spin temperature causes rapid magnetization loss in the sample. Then, energy from electron and spin baths is dissipated in the lattice leading to a fast remagnetization. After a few ps, all three heat baths come into an equilibrium. Figure 2.2 portray the sequence of events after laser excitation as proposed by the 3T-model. According to this model, the temperature evolutions of the electron, spin and lattice heat baths can be expressed by three coupled differential equations given as:

$$C_E(T_E)\frac{dT_E}{dt} = -G_{EL}(T_E - T_L) - G_{ES}(T_E - T_S) + P(t) \tag{2.3}$$

$$C_S(T_S)\frac{dT_S}{dt} = -G_{ES}(T_S - T_E) - G_{SL}(T_S - T_L) \tag{2.4}$$

$$C_L(T_L)\frac{dT_L}{dt} = -G_{EL}(T_L - T_E) - G_{SL}(T_L - T_S) \tag{2.5}$$

where the temperatures of the electron, spin and lattice baths are denoted by T_E, T_S and T_L, respectively. C_E, C_S and C_L are the specific heat capacity of the electron, spin and lattice baths and G_{ES}, G_{EL} and G_{SL} are the electron-spin, electron-lattice and spin-lattice coupling parameters, respectively. $P(t)$ is the laser excitation term which is likely to be Gaussian in nature. C_E is considered to be proportional to the T_E, *i.e.*, $C_E = \gamma T_E$, where γ is determined by the electron density of states around the Fermi level. The magnetization of a system at any particular delay time can be extracted by solving equation (2.3-2.5) combined with the mean-field theory of ferromagnet. From this solution, the evolution of electron, spin and lattice temperature with the delay time is obtained along with the values of specific heats and coupling constants. The 3T-model was further solved analytically by Dalla Longa *et al.* in 2007 [16] under specific boundary conditions, such as negligible specific heat, instantaneous increase in electron temperature after laser excitation etc. This analytical solution is widely used among the scientific community to determine the ultrafast demagnetization time and fast remagnetization time from the ultrafast demagnetization data.

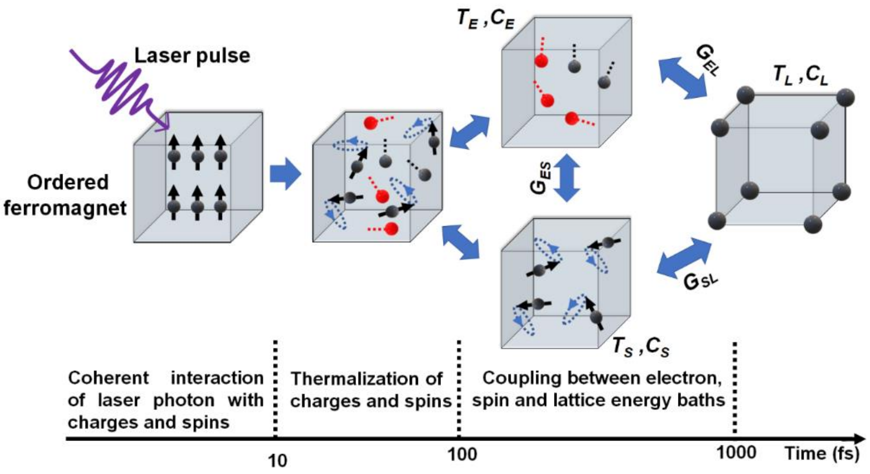

Figure 2.2: Ultrafast demagnetization and relaxation mechanisms according to the three-temperature model.

2.2.2 Mechanisms involved behind ultrafast demagnetization

Although the 3T-model could phenomenologically explain the ultrafast demagnetization and subsequent fast recovery process, this model also has a few drawbacks as below.

1. It does not take into consideration the underlying microscopic mechanisms involved in the ultrafast demagnetization phenomenon such as the energy transfer process from laser photons to ordered ferromagnetic system, angular momentum transfer mechanisms between different heat baths etc.
2. This model could not explain the reason behind the two-step demagnetization (a sub-ps demagnetization followed by a slow few ps magnetization loss) process observed in rare-earth ferrimagnets.

Several microscopic mechanisms were proposed over time to solve these discrepancies in the 3T-model. We have discussed these mechanisms in the following sections.

2.2.2.1 Elliot-Yafet scattering

In 2010, Koopman *et al.* proposed a microscopic model based upon phonon-mediated Elliott-Yafet scattering to explain the ultrafast demagnetization mechanism [11]. This model could also explain both the fast sub-picosecond single-step demagnetization process in transition metals ferromagnets (Type-I demagnetization) and the slow two-step demagnetization process of rare earth ferrimagnets (Type-II demagnetization). In this model, it was assumed that there is a finite probability for a spin to get flipped via a scattering event. This probability is called the spin-flip probability. When a scattering event takes place, electrons transfer some of their angular momenta to the phonons. This angular momentum transfer results in band-mixing of minority spin-down and majority spin-up states with similar spin-states near the Fermi level and also changes the probability of finding the scattered electron in its previous spin state (either spin-up or spin-down). According to this theory, spin-mixing due to the phonon-mediated spin-flip scattering depends upon the number of minority spin-down and majority spin-up states at the Fermi level. According to this model, the temperature evolution of electron, lattice and magnetization can be expressed by three coupled differential equations given by:

$$C_E(T_E)\frac{dT_E}{dt} = \nabla_z(k\nabla_z T_E) + G_{EL}(T_L - T_E) \qquad (2.6)$$

$$C_L\frac{dT_L}{dt} = G_{EL}(T_E - T_L) \qquad (2.7)$$

$$\frac{dm}{dt} = Rm\frac{T_L}{T_C}\left(1 - m\,coth\left(\frac{mT_C}{T_E}\right)\right) \tag{2.8}$$

Here, m (= M/M_s) represents the normalized magnetization and T_L, T_E and T_C are the lattice, electron and Curie temperature respectively. R is the Koopmans parameter which determines whether ultrafast demagnetization is type-I or type-II. R can be expressed as:

$$R = \frac{8k_B T_c^2 V_{at}}{(\mu_{at}/\mu_B)E_D^2}\,a_{sf}G_{EL} \tag{2.9}$$

Here, a_{sf}, V_{at}, μ_{at}, E_D and G_{EL} represent the spin-flip probability, atomic volume, atomic magnetic moment, Debye energy and electron-lattice coupling parameter, respectively. Whereas, μ_B and k_B are the Bohr magneton and Boltzmann constant. It has been observed that R is very small for rare earth materials (like Tb, Gd etc.) while it is much higher for transition metals (like Ni, Fe etc.). These observations allow researchers to claim that a smaller R-value can lead to two-step slow demagnetization with a significant contribution of spin-lattice relaxation to the demagnetization process.

2.2.2.2 Spin-orbit coupling

Zhang and Hübner argued that ultrafast demagnetization is a cooperative effect of the laser field and the spin-orbit coupling (SOC) of a magnetic material [17]. They found that in the absence of SOC femtosecond laser pulse alone can not demagnetize a ferromagnetic sample. In the presence of SOC, the spin angular momentum of a magnetic material induces a finite orbital angular momentum. This orbital angular momentum is very much sensitive to lattice fluctuations and deformations. This leads to a loss in spin angular momentum as electrons are unable to follow the motion of spins, resulting in ultrafast demagnetization. Also, in the presence of SOC, both singlet and triplet states intermix and lose their identity. This intermixing can convert various forbidden spin states into allowed states. Further, different laser-induced spin transitions explore these allowed states leading to a sudden decrease in system magnetization.

2.2.2.3 Coulomb interaction

In large SOC strength materials, electron-electron scattering mediated through Coulomb interaction can be a reason for ultrafast loss of magnetization [18]. In this scattering process, the available phase space for the transition of an electron from minority spin bands to majority spin bands is comparatively much higher than in the electron-phonon scattering process. During this process, the excitation by ultrashort laser pulse creates a nonequilibrium electron distribution and these excited electrons go through both inter-band and intra-band Coulomb scattering. Ultrafast demagnetization is followed by fast remagnetization due to energy transfer to the lattice heat bath. Recent studies have also demonstrated that the presence of these electron-electron scattering is mandatory for the ultrafast demagnetization process to occur [18].

2.2.2.4 Electron-magnon interaction

In materials with high SOC strength, electron-magnon interaction can cause a significant reduction in the spin angular momentum of the system. This loss was first proposed by Carpene *et al.* in 2008 [19]. Here, it was assumed that electron-magnon interaction can lead to spin-flip scattering which is analogous to phonon-mediated Elliot-Yafet scattering, with magnons behaving as the absorber of spin angular momentum. Due to the L-S coupling, loss of spin angular momentum leads to an increase in the orbital angular momentum of the system. This decrease in the spin angular momentum can contribute to the ultrafast demagnetization process and is explained by electron-magnon interaction.

2.2.2.5 Relativistic spin-photon interaction

In 2009, Bigot *et al.* proposed a theory based on relativistic spin-photon interaction that can explain the ultrafast demagnetization mechanism [20]. As per this theory, there is a coupling between electron spin and electromagnetic laser pulse via relativistic terms coming from the Dirac Hamiltonian. Due to this coupling, the coherent interaction between the femtosecond laser pulse and ferromagnetic spins is a relativistic quantum electrodynamic process. This process modifies the angular momentum of the light nonlinearly. Following this, electrons and spins get thermalized via incoherent interaction and lose their phase memory *w.r.t.* the excitation which leads to ultrafast demagnetization.

2.2.2.6 Phonon-phonon interaction

Dornes *et al*. observed a spin angular momentum loss in the ferromagnetic iron sample due to the generation of a transverse strain wave and its subsequent propagation from surface to bulk [21]. They tried to understand this in terms of conversion of spin angular momentum to mechanical angular momentum via magnetic field-induced magnetization reversal. This effect is also popularly known as the Einstein-de Haas effect. They finally concluded that the laser-induced ultrafast demagnetization phenomenon can be significantly affected via the interaction of lattices.

2.2.2.7 Terahertz emission

In recent times, it has been observed that the ultrafast demagnetization mechanism is associated with the emission of terahertz pulses [22]. After excitation by pump laser, different spin-flip scattering events occur inside a magnetic system due to its SOC. However, these scattering events are not sufficient to completely demagnetize the sample. Simultaneous to these spin-flip events, there are few spin relaxations between the majority and minority bands. This relaxation process is mediated via the emission of THz photons, which consequently contributes to the demagnetization mechanism.

2.2.2.8 Optical inter-site spin transfer

Optical inter-site spin transfer (OISTR) is a newly proposed mechanism that can manipulate spins of a magnetic material by effectively redistributing these spins between different sublattices [23, 24]. It has been shown that within 20 fs after the laser pulse excitation, the entire ultrafast spin dynamics is driven by this OISTR effect. This effect is also observed in NM/FM heterostructures where spins at the interface have majority spin-orientation flow towards the NM and minority spins transferred to a FM. Their minority spins later undergo spin-orbit-induced spin-flip scattering to become demagnetized. In multi-sublattice materials, the OISTR effect dominates the initial (within about 20 fs) spin dynamics and leads to a faster and more efficient ultrafast demagnetization.

2.2.2.9 Phonon-magnon interaction

Phonon-magnon scattering [25] occurs at a much slower timescale on the order of a few 10s of ps. This scattering mechanism is believed to be very slow for contributing significantly to the demagnetization process of normal ferromagnets. However, it is a possible mechanism involved in the two-step demagnetization process in rare-earth ferrimagnets.

2.2.2.10 Super-diffusive spin current transport

Most of the theories developed to understand ultrafast demagnetization focused on the angular momentum transfer process. These proposals are based on the assumption that the femtosecond laser directly interacts with perfectly aligned spins and opens up different channels for angular momentum dissipation. None of these models takes into consideration any spin transport phenomenon to explain the ultrafast demagnetization mechanism. However, in 2008 Malinowski *et al.* observed that the spin transport of hot electrons inside a synthetic antiferromagnet accelerates its demagnetization process [26]. Following this experimental observation, Battiato *et al.* proposed a semiclassical model in 2010 to underpin the role of spin transport in the demagnetization process [14]. In this model, they demonstrated that the laser-induced demagnetization process can be explained without assuming the creation of any spin-flip channels, but simply through super-diffusive spin transport theory. According to this theory, there exists a spin-dependent transport of electrons inside a magnetic system where the electrons with majority up-spin orientation cause faster diffusion into the substrate in comparison to the electrons with minority down-spin orientation. After laser excitation, electrons in d-bands are excited by absorbing energy from the laser photons to the s-bands or p-bands that exist above the Fermi level. The mobility of these excited s-bands and p-bands is much larger in comparison to the initial d-bands which makes these electrons extremely mobile. These mobile electrons travel at a very high velocity in some random direction and experience various spin-conserving scattering events. These continuous scattering events create a torrent of hot electrons. The electron flux generated through laser excitation can be given by the transport equation:

$$\frac{\partial n^{tot}}{\partial t} + \frac{n^{tot}}{\tau} = \left(-\frac{\partial}{\partial z}\hat{\phi} + \hat{I}\right)\left(\hat{S}n^{tot} + S^{ext}\right) \tag{2.10}$$

Here, n^{tot}, τ and S^{ext} represent the density of electron, spin lifetime and electron source term respectively. $\hat{\phi}$ and $\hat{I}$ are flux and identity operators. $\hat{S}$ can be defined as $\hat{S}n^{[1]} = S^{[2]}$ where $n^{[1]}$ and $S^{[2]}$ are the density of first-generation electrons and second-generation excitation term. Here, the lifetime of electrons with the majority and minority spins are different which results in the gradual decrease in the majority spins in the magnetic layer. This loss in majority carriers leads to a reduction of the net magnetization of the system that causes ultrafast demagnetization. The standard diffusive motion of particles can be characterized by the variance of the displacement (σ^2). For a particle distribution with diffusive transport, σ^2 can be expressed as $\sigma^2 \propto t^n$, with $n = 1$. Whereas, for the Ballistic transport $n = 2$, *i.e.* $\sigma^2 \propto t^2$. Super diffusive spin transport is neither ballistic nor diffusive. Here, n is time-dependent and varies from $n = 2$ for a shorter lifetime to $n = 1$ for a longer lifetime.

2.2.3 Precessional dynamics

In the absence of an applied magnetic field, the electron spins inside a magnetic material are randomly oriented. However, when a large enough magnetic field is applied then all spins try to get aligned along the magnetic field direction to minimize the total energy of the system (as shown in Figure 2.3(a)). The minimum energy state of the system where all spins are directed along the effective magnetic field direction is called the ground state spin configuration. The whole system can be considered to be a giant macrospin with a high net magnetic moment (vector sum of magnetic moments of all the individual spin). Here, the total energy of the system is the sum of different energies like Zeeman, anisotropy, magnetoelastic and exchange energy which also corresponds to different applied magnetic field values. The vector that sums up all these fields is called the effective magnetic field. Before any external perturbation, this macrospin of a magnetic material is in equilibrium and oriented in the effective magnetic field direction. The perturbation by a femtosecond laser pulse or RF microwave field modifies this effective magnetic field leading to it being directed along a non-equilibrium direction (as shown in Figures 2.3(b) and 2.3(c)). The macrospin will try to return to its initial equilibrium position by exerting a torque along the direction of the initial effective magnetic field direction. This triggers a damped spiral rotation of magnetization around the effective magnetic field which is known as the precessional dynamics. This rotational motion can be explained by a phenomenological theory based upon Landau-Lifshitz-Gilbert (LLG) equation [27]. The LLG torque equation was first proposed by Landau and Lifshitz in 1935 [28] and further modified by Gilbert who inserted a modified damping term [29]. The theoretical formulation of LLG-equation is briefly discussed below:

The relation between the torque (τ) experienced by a particle rotating at an orbital angular momentum L can be written as:

$$\tau = \frac{dL}{dt} \tag{2.11}$$

If we incorporate quantum mechanical concepts such as spin angular momentum (S) instead of classical orbital angular momentum, then a similar equation also can be written as:

$$\tau = \frac{dS}{dt} \tag{2.12}$$

The magnetic moment M of a magnetic material is connected to S via the relation:

$$M = -\gamma S \tag{2.13}$$

where γ is the gyromagnetic ratio of the electron. When an effective magnetic field of H_{eff} is applied to a material of net magnetic moment M then it experiences a torque of amount:

$$\tau = M \times H_{eff} \tag{2.14}$$

In equation 2.12, if we substitute the value of M and τ from equation 2.13 and equation 2.14, we will obtain:

$$\frac{dM}{dt} = -\gamma\left(M \times H_{eff}\right) \tag{2.15}$$

Where H_{eff} is the effective magnetic field composed of the applied external magnetic field, dipolar field, exchange field and anisotropy field. The physical meaning of this equation is that the magnetization precesses around H_{eff} at a constant amplitude and frequency (also called Larmor frequency = γH_{eff}) without any energy dissipation. However, in a practical scenario, the precessional amplitude gradually decreases with time. So, to match the real precessional dynamics, introduction of an additional damping term is mandatory. Thus, Landau and Lifshitz (LL) suggested a dynamic equation incorporating a damping term along with the precessional torque term. This LL-equation is expressed as:

$$\frac{dM}{dt} = -\gamma\left(M \times H_{eff}\right) + \frac{\lambda}{M_S^2} M \times \left(M \times H_{eff}\right) \tag{2.16}$$

Here, the $\frac{\lambda}{M_s^2} M \times (M \times H_{eff})$ term represents the contribution of damping of magnetization dynamics, M_s is the saturation magnetization and λ is the Landau damping parameter with a dimension of second^{-1}. The LL-damping could not take into consideration the large non-eddy current-induced damping contributions. To get rid of this limitation, Gilbert reformulated this theory which was more consistent and took into consideration of other significant damping contributions. The modified LL-equation, also known as the LLG-equation can be written as:

$$\frac{dM}{dt} = -\gamma\left(M \times H_{eff}\right) + \frac{\alpha}{M_s}\left(M \times \frac{dM}{dt}\right) \tag{2.17}$$

Here the first term denotes the precessional torque term, while the second term is the damping term. The directions of these torques are shown in Figure 2.3 (d). Here, the dimensionless coefficient α is called the Gilbert damping parameter which is analogous to the Rayleigh energy dissipation function. Also, α is related to λ via the relation, $\alpha = \frac{\lambda}{\gamma M_s}$.

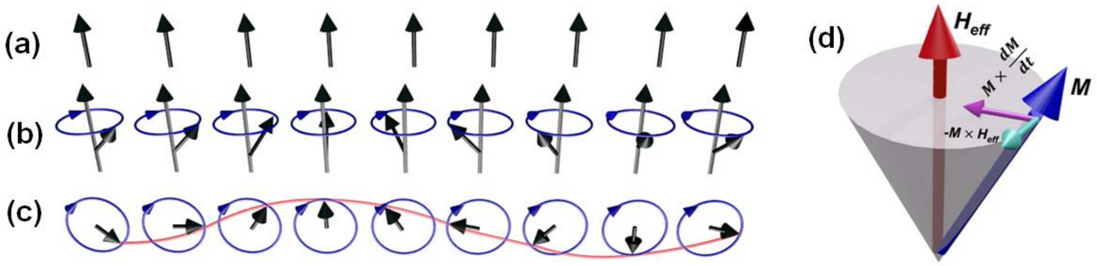

Figure 2.3: Spin configuration at the (a) ground state, (b) incoherent precessional state and (c) coherent precessional state. (d) The magnetization precession around an effective magnetic field (H_{eff}).

2.2.3.1 Kittel equation

The foundation of precessional dynamics is based upon the concept of ferromagnetic resonance. When a FM material is placed in a static bias magnetic field and a RF magnetic field is also applied perpendicular to the bias field, then an energy absorption takes place from the RF magnetic field when the resonance condition is met, *i.e.* the frequency of the RF field is equal to the precessional frequency of the FM material at that bias field value. This is known as ferromagnetic resonance (FMR) and the frequency at which this resonance occurs is called FMR frequency (ω). In general, the resonance occurs at a much higher frequency than that of the Larmor frequency. In 1948, C. Kittel derived the resonance condition by solving the equation of motion after explicitly defining the role played by the demagnetizing field [30]. The ω obtained from this solution can be expressed as:

$$\omega = \mu_0\gamma\sqrt{[H + (N_y - N_z)M_s][H + (N_x - N_z)M_s]} \qquad (2.18)$$

Here, N_x, N_y and N_z are x, y and z components of the demagnetizing field tensor. The values of the components of demagnetizing field tensor and corresponding resonance frequency for a few popular shapes are:

1. For a sphere, N_x= N_y= N_z= 1/3 and $\omega = \mu_0\gamma H$.

2. For a plane, N_x= N_y= 0, N_z=1 and $\omega = \mu_0\gamma\sqrt{H(H + M_s)}$.

2. For an infinite circular cylinder, N_x= N_y= 1/2, N_z= 0 and $\omega = \mu_0\gamma\left(H + \frac{M_s}{2}\right)$.

Other than the demagnetizing field, the magnetic anisotropy of a system also affects the resonance frequency of a material. The equation (2.18) for resonance frequency can be modified by incorporating different magnetic anisotropy terms. Few expressions for resonance frequency with some anisotropies are:

1. For in-plane magnetized samples with uniaxial anisotropy (K_1 = uniaxial anisotropy constant):

$$\omega = \mu_0\gamma\sqrt{\left[H + 4\pi M_s + \frac{2K_1}{M_s}\right]\left[H + \frac{2K_1}{M_s}\right]} \qquad (2.19)$$

2. For in-plane magnetized samples with cubic anisotropy (K_2 = cubic anisotropy constant):

$$\omega = \mu_0\gamma\sqrt{\left[H + 4\pi M_s + \frac{2K_1}{M_s}\right]\left[H + \frac{2K_1}{M_s} + \frac{2K_2}{M_s}\right]} \qquad (2.20)$$

3. For out-of-plane magnetized samples ($K_\perp$ = out-of-plane magnetic anisotropy constant):

$$\omega = \mu_0\gamma\left(H + 4\pi M_s + \frac{2K_\perp}{M_s}\right) \qquad (2.21)$$

2.2.3.2 Spin wave

In 1930, F. Bloch have introduced the concept of spin waves to understand the decrease in saturation magnetization with system temperature [31]. Before external perturbation electron spins are aligned parallel to each other and directed along the effective magnetic field direction. The excitation of magnetic material increases the temperature in the excitation area which can flip an electron spin. As spins in a ferromagnet are connected via exchange interaction, flipping of a single spin triggers the flipping of the neighbouring spins with a finite phase difference between adjacent spins. To minimize the exchange energy cost, this phase difference propagates in a magnetic system as a wave. This wave is known as spin wave. The quanta of the spin wave are called magnons [32]. For uniform precessional motion, exchange coupled spins precess around the effective magnetic field at the same phase. Hence, the wavelength (λ) of the spin wave of uniform precessional mode is nearly infinity and the corresponding wavevector (k) tends to zero. In the case of non-uniform precession, there is a finite propagation of phase difference which results in a finite λ and a non-zero k-value of the spin wave.

Depending upon the range of interaction and wavelength, spin waves can be divided into two types, *i.e.* a) exchange spin waves and b) dipolar spin waves [33]. Exchange-dominated spin waves are short-wavelength spin waves dominated by exchange interaction. Similarly, dipolar interaction dominated and longer wavelength spin waves are identified as dipolar spin waves. Furthermore, there are some spin wave modes where both exchange interaction and dipolar interaction play equal roles in their appearances. These modes generally appear at a wavelength similar to the exchange length. The resonance frequency for such dipole-exchange dominated spin waves for a FM system of infinite thickness can be expressed as:

$$\omega = \mu_0\gamma\sqrt{\left[H + \frac{2A}{M_s}k^2\right]\left[H + 4\pi M_s sin^2\theta + \frac{2A}{M_s}k^2\right]} \tag{2.22}$$

Here, k is the wavevector, A is the exchange-stiffness constant and θ is the angle between the magnetization and the magnetic easy axis of the sample.

In a FM material, the exchange-dominated spin waves can also travel across the film thickness to create standing waves. The spin wave modes that appear in the spectrum due to these standing waves are called perpendicular standing spin wave (PSSW) modes. Here, the resonance frequency can be given as:

$$\omega = \mu_0\gamma\sqrt{\left[H + \frac{2A}{M_s}\left(\frac{n\pi}{d}\right)^2\right]\left[H + 4\pi M_s + \frac{2A}{M_s}\left(\frac{n\pi}{d}\right)^2\right]} \tag{2.23}$$

Here, n is the order of the PSSW mode and d is the thickness of the sample.

Control over different spin waves via external excitation such as femtosecond laser, spin-torque or external bias magnetic field may lead to various structural engineering of magnon-based information processing devices. In this doctoral thesis, we have mainly studied the uniform precessional motion ($k \approx 0$) and PSSW modes of different order in magnetic thin films and heterostructures.

2.2.4 Magnetic damping

During the magnetization precession, there is always some finite dissipation of spin angular momentum through the lattice which causes a gradual decrease in precessional amplitude with time. This mechanism of known as magnetic damping. The efficient control over the magnetic damping parameter has huge importance in the magnetic data storage industry as it allows to accelerate magnetization recovery to the equilibrium in the magnetization reversal process. In addition, understanding the underlying mechanisms behind magnetic damping and its sufficient modulation via external means are essential for designing advanced spintronics devices. High magnetic damping materials are desirable to eliminate the 'ringing' of magnetization (precession) during the data-writing process in MRAM devices. Whereas, low damping materials are equally important in the spintronics community as they are helpful to reduce the write-current in spin-torque-based MRAM devices and long-distance spin wave propagation in magnonic devices.

Magnetic damping is classified into indirect and direct magnetic damping based on the direction of energy transfer [34]. If the energy within the magnetic system is conserved, then the damping is indirect (e.g. damping of the spin waves by Stoner excitation, damping due to the mode conversion etc.). In direct damping, energy is transferred from the magnetic system to the adjacent nonmagnetic system. Direct damping is categorised into two classes: intrinsic and extrinsic damping [35]. Scattering from phonons is unavoidable in a magnetic system and can not be reduced to zero, which determines the intrinsic damping as it can not be controlled externally. Extrinsic damping arises due to the additional magnon scattering from the phonons, which depends on various extrinsic factors such as defect density, magnetic anisotropy, external temperature, sample geometry, growth quality etc. Different damping contributions can also be tuned via spin current [36], phonon-drag [37], eddy current [38], doping [39], capping [40], introduction of strain [41], inversion-symmetry breaking at interfaces [42] etc. In the following section, we will describe briefly the mechanisms involved in both intrinsic and extrinsic damping.

2.2.4.1 Intrinsic damping

Mechanisms such as intrinsic spin-orbit coupling of FMs, eddy current, phonon drag mechanisms etc. are a few governing factors involved in intrinsic damping.

A. Intrinsic spin-orbit coupling

The coupling between an electron's spin and orbital angular momentum is called spin-orbit coupling (SOC). This coupling plays a vital role in determining the electronic and magnetic properties of that material via controlling the electron flow, spin-flip scattering, magnetic anisotropy, spin relaxation time and dissipation rate of the spin current in these devices. In the presence of SOC in a material, the spin magnetic moment is converted into orbital magnetic moments which are very sensitive to lattice fluctuations. This leads to a certain loss in the total magnetic moment of the system which eventually causes finite magnetic damping. Detailed theoretical calculation of the dependency of intrinsic damping on the SOC strength was given by V. Kambersky in 1976 through the torque-correlation model [43]. According to this model, there are two processes that contribute significantly to SOC-induced magnetic damping, *i.e.* i) phonon-mediated spin-flip scattering (explained by s-d exchange interaction) and ii) ordinary scattering (explained by breathing Fermi surface model).

I. Phonon-mediated spin-flip scattering

Through the scattering theory approach, Elliott and Yafet proposed a phonon-mediated spin-flip scattering mechanism in 1954 for energy dissipation in ferromagnetic metals [44, 45]. In 1956, its mathematical formulation was given by Kittel and Mitchel based upon the s-d relaxation mechanism [46]. According to this model, the SOC of a material unfolds a possibility of spin-flip scattering via phonons between two spin sub-bands. Always in these materials, the localized d-electrons are coupled to itinerant s-electrons via s-d exchange interaction which helps to transfer the spin angular momentum from d-electrons to s-electrons. This leads to an incoherent spin-flip scattering (where the total spin angular momentum is not conserved) of both s- and d-electrons. The extracted α-value from this model can be written as:

$$\alpha = D_F \left[\frac{\gamma\hbar^2(\delta g)^2}{4\tau M_s}\right] \tag{2.24}$$

Here, τ^{-1}, D_F and δg represent electron-phonon collision frequency, density of states in the Fermi level and deviation in the electronic g-factor, respectively. α and D_F shows a proportional relationship indicating that a denser Fermi level will help to enhance the damping.

II. Ordinary scattering

The theory of the ordinary scattering mechanism was given as the breathing Fermi surface model [47, 48]. According to this model, spin sub-bands with different wave vectors are considered to be non-identical in the presence of SOC. Scattering within these sub-bands has some finite contribution to the damping process. During the precessional motion, magnetization orientation changes continuously and the energy states of the different spin bands vary randomly. As a consequence, a spin state at one side of the Fermi level at a certain delay time can experience a transition to the other side of the Fermi level at another delay time. This transition can create an electron-hole pair and results in faster dissipation of spin angular momentum. The damping contribution according to this model can be written as:

$$\alpha = \left[\frac{\gamma\xi^2 D_F \tau(\delta g)^2}{4M_s}\right] \tag{2.25}$$

Here, ξ is the SOC strength of the material. It was found later that the breathing Fermi surface model has not taken into consideration the effect of electron scattering that comes from temperature variation in the system which may lead to underestimation of the α. Later, it was found that there can be two types of contribution to damping depending upon the generation of electron-hole pair [49]:

a. Intra-band electron-hole pair generation: Both electron and hole occur in the same band. Damping has a major conductivity-like contribution (as it varies directly proportional to the material's conductivity) and varies proportionally to ξ^3. This is mostly valid at low temperatures.

b. Inter-band electron-hole pair generation: Electron and hole appear in different bands. Damping has a major resistivity-like contribution (as it varies directly proportional to the material's resistivity) and varies as ξ^2. It is mainly valid at high temperatures.

B. Phonon-drag mechanism

In 1998, H. Suhl proposed a magnon-phonon scattering mechanism that can enhance the damping process in magnetostrictive materials [50]. There are two ways excited phonons can dissipate their energy:

a. Direct energy dissipation to the lattice from uniform precessional oscillation.

b. Indirect energy dissipation via non-uniform spin wave excitation.

The direct energy dissipation process is also known as the phonon-drag mechanism. The damping that arises due to this mechanism can be given as:

$$\alpha = \frac{2\zeta\gamma}{M_S}\left[\frac{B(1+\sigma)}{Y}\right]^2 \tag{2.26}$$

Here σ, Y, B and ζ represent the Poisson's ratio, Young's modulus, magnetoelastic shear constant and phonon viscosity of the system, respectively. The phonon-drag mechanism is only present in the materials where the ferromagnetic resonance frequency is driven along the film thickness by the elastic waves.

C. Eddy current mechanism

As per Faraday's law, an electromotive force (emf) will be generated due to the time-dependent magnetic field. This emf will oppose any further change in the applied magnetic field. The magnetization precession in a FM material is similar to the time-dependent magnetic field, that can produce an emf. This emf can induce a finite current in that FM material which is known as Eddy current. Following Faraday's law, this Eddy current opposes any change in the magnetization orientation *w.r.t.* the external magnetic field which leads to damping enhancement. The Eddy current contribution to damping is more prominent for highly conducting FMs of higher thickness which is close to or even higher than the skin depth of the microwave excitation field [51]. The damping modulation that arises due to this mechanism can be expressed as:

$$\alpha = \frac{(\gamma M_S)^2}{6}\left(\frac{4\pi}{c}\right)2\sigma d^2 \tag{2.27}$$

where σ is the electrical conductivity of the FM material, c is the light speed in the vacuum and d is the thickness of the FM material.

2.2.4.2 Extrinsic damping

Few external factors can affect the damping parameter significantly in a magnetic system. This additional damping contribution is known as extrinsic damping. It can have both local and nonlocal contributions. In local damping, the energy gets dissipated within the phonon and electron system of the magnetic material itself. For example, if there are defects and inhomogeneities in the sample then it can generate non-uniform resonance modes in addition to the uniform ones, which can enhance the damping of the composite system. In a magnetic material, nonlocal extrinsic damping arises when another magnetic or nonmagnetic material is present adjacent to it. This additional damping arises due to spin-torques on the magnetic system generated due to spin current (via different spin-orbit effects) or transfer of spin angular momentum out of the magnetic system (also known as spin pumping). The additional nonlocal damping is strongly influenced by the layer thicknesses, SOC strength of materials and nature of the interface. Here, we present an overview of the popular extrinsic mechanisms that can affect the damping of the uniformly precessing spins.

A. Inhomogeneous magnetic anisotropy

In presence of magnetic anisotropy in a material, the magnetization of the system prefers a few specific directions over others [52]. In presence of sufficiently high magnetic anisotropy in the sample, the precessional dynamics can be modified which could enhance the magnetic damping of that material significantly. This damping enhancement is more prominent in the lower applied fields as spins are loosely bound along the magnetic field direction and hence are easier to be perturbed through the anisotropy field. The stronger the anisotropy field in comparison to the external magnetic field higher is the value of α. With a decrease in the external magnetic field, α increases exponentially which shows a peak at the anisotropy field.

B. Magnetic impurity

In a magnetic material, any defect or impurity centre can act as a scattering point for the precessing spins. The scattering process is inelastic in nature. These scattering centres lead to dephasing of the precessional oscillation leading to a loss of energy from the magnetic system and an ensuing enhancement of α. This contribution to magnetic damping can be controlled by decreasing the defect density of the sample.

C. Two-magnon scattering

The presence of magnetic defects and inhomogeneities in the ultra-thin magnetic films can cause scattering of the uniform precessional mode ($k = 0$) by non-uniform modes ($k \neq 0$). This process is commonly known as two-magnon scattering (TMS) [53, 54]. It is an inelastic scattering mechanism where energy is conserved but magnon momentum is not conserved. There are mainly three factors that influence the TMS contribution to precessional dynamics, namely i) precessional frequency, ii) angle between the easy axis of the sample and the external applied magnetic field and iii) magnetic film thickness.

The number of degenerate magnons that are available for scattering increases with increasing precessional frequency. This also indicates that the magnon-magnon scattering probability increases with increasing frequency. With an increase in the angle between the easy axis of the sample and the external applied magnetic field, magnon degeneracy decreases gradually. Finally, the degeneracy vanishes when the sample magnetization is directed perfectly along the out-of-plane direction. The TMS contribution to the α shows an inverse square dependency on the FM layer thickness.

D. Spin memory loss

Spin memory loss causes partial depolarization of spin current generated by the FMR method at the interfaces. This loss was first proposed in 1993 by T. Valet *et al.* in the study of current-perpendicular-to-plane GMR [55]. According to this proposal, if $\boldsymbol{J_s}$ is the amount of spin current generated on the FM side after excitation, then only $(1-\delta)\boldsymbol{J_s}$ can cross the NM/FM interface (where δ is the spin memory loss coefficient) while $\delta\boldsymbol{J_s}$ is absorbed in the interface due to the interfacial spin-orbit coupling or defects. Different theoretical calculations and experimental studies have confirmed that a current discontinuity arises at the NM/FM interface due to spin memory loss where the interface acts as a perfect spin sink [56-58]. This loss affects the spin transport and increases the α-value of a composite system by decreasing the transparency of the interface. For spin-based device fabrication, it is recommended to minimize this effect in a composite structure by creating a transparent, sharp and defect-free interface.

E. Spin current-induced torque

Magnetic damping of a FM material can be significantly altered by spin current injection via different interesting spin-orbit effects, like the spin Hall effect (SHE) [59], Rashba-Edelstein effect (REE) [60], different spin caloric effects [61] etc. The injected spin current applies a torque on the precessing spins and modulates their energy dissipation process. If charge current is applied to a high SOC strength NM material, then spin polarization is developed along its transverse direction due to spin-dependent scattering. This phenomenon is known as the SHE. This spin polarization flows as pure spin current and is transferred to the adjacent FM layer through the NM/FM interface and exerts a torque on the precessing magnetization of the FM, which can either increase (damping like torque) or decrease (anti-damping like torque) the α of the composite NM/FM system. REE is another spin-charge conversion mechanism, which appears in the presence of spin-polarized surface states. When the charge current passes through these spin-polarized surface states, then a finite spin accumulation appears at the interfaces. This spin accumulation flows as a spin current and exerts a torque on the magnetization dynamics. Similar to SHE and REE, there are a few spin caloric effects such as the spin Seebeck effect, spin Nernst effect and spin Peltier effect that could inter-convert between thermal and spin current. Here the temperature gradient can generate spin current and modulate α significantly.

F. Spin pumping

In an NM/FM heterostructure, an external excitation causes magnetization precession because of which spin angular momentum is transferred from the FM layer to the NM layer in the form of pure spin current. This effect is known as the spin pumping effect as it is analogous to the physical pumping mechanism. As a result, the amplitude of precession suffers a faster decay leading to an enhancement of α. This effect in NM/FM layered systems was first proposed in 1988 by Hurdequint *et al.* to interpret the results of a spin resonance experiment [62]. Here, the authors argued that the precessing magnetization is the source of a nonequilibrium spin accumulation that diffuses out of the NM/FM interfaces into the adjacent NM layer where it is dissipated by spin-flip processes. The spin pumping-induced enhancement in α was further discussed in 1996 by Berger *et al.* in NM/FM/NM type spin-valve structures [63]. Their expression for the modulation of α scales as a function of the layer thickness and a few material parameters. However, this modulation does not vanish with vanishing exchange splitting which makes its validity very doubtful. In 2002, Y. Tserkovnyak and A. Brataas theoretically demonstrated this damping enhancement in NM/FM heterostructures by employing the time-dependent adiabatic scattering theory which got widely accepted among the scientific community [36, 64, 65]. In their study, they predicted that in presence of a NM layer adjacent to the FM layer, spin current will be pumped from the FM layer to the NM layer and get partially or fully absorbed. The pumped spin current (I_S^{pump}) from the FM layer to the NM layer due to spin pumping effect can be expressed as:

$$I_s^{pump} = \frac{\hbar}{4\pi}\left(g_r^{\uparrow\downarrow} M \times \frac{dM}{dt} - g_i^{\uparrow\downarrow}\frac{dM}{dt}\right) \qquad (2.28)$$

Here $g_i^{\uparrow\downarrow}$ and $g_r^{\uparrow\downarrow}$are the imaginary and real parts of the spin-mixing conductance. The presence of a large but finite NM reservoir attached to one side of the FM is expected to induce a non-vanishing spin accumulation at the NM/FM interface. The chemical potential difference between spin-up and spin-down states acts as a perturbation to pump these accumulated spins out from the NM/FM interface and allow them to relax through spin-flip scattering. For a slow enough variation of magnetization, this spin accumulation is expected to flow back into the FM layer by generating a spin backflow current (I_s^{back}). I_s^{back} is controlled by the spin accumulation at the NM/FM interface and dependent on the spin backflow factor (β) of the NM layer. The largest enhancement of damping is noticed when there is no backscattered spin current, which means, that β → 0. When I_s^{back} becomes significant, damping enhancement reduces from the highest value. On the contrary, when $\beta >> 1/g_r^{\uparrow\downarrow}$, the damping enhancement is negligible. The pumped spin current to the NM layer is almost entirely returned to the FM layer.

For becoming an efficient spin sink, the NM layer thickness should be a few times higher than its spin diffusion length. The enhancement of the Gilbert damping parameter is higher for NM layers with a higher spin-flip relaxation rate (r). These NM layers with high r values could overcome the spin accumulation at the NM/FM interface. This r can be roughly expressed as:

$$r \propto Z^4 \qquad (2.29)$$

Here, Z is the atomic number. The heavier elements with $Z \geq 50$ have a very high r value, which make them ideal for being used as spin sink material. Therefore, large damping enhancement is expected for NM/FM heterostructures in which the NM layer is a heavy metal like W, Ta, Pt or Pd. However, for light materials with $Z \leq 50$, such as Cu, Ru or Al the r is considerably smaller, making them less effective as spin sink material.

2.2.5 Interfacial spin transparency

The spin transparency (T) of an interface between the NM and FM layer takes into account all possible effects that lead to the electrons being reflected instead of being transmitted from the NM/FM interface and controls the flow of spin angular momentum across the interface. T depends on both intrinsic and extrinsic interfacial factors, such as the thickness of NM and FM layer, resistivity of NM layer, spin-mixing conductances, band-structure mismatch, Fermi velocity, interface imperfections, etc. For pure spin current-based device applications, an interface is desired to have high and tunable T-value which makes the investigation of T in NM/FM heterostructures an important research topic of modern spintronics. To find the T-value of an NM/FM interface, two models can be followed, namely: i) spin Hall magnetoresistance model [66, 67] and ii) spin transfer torque-based model [68]. The spin Hall magnetoresistance model takes into consideration the effect of spin backflow where the spin current density that diffuses into the NM layer is smaller than the actual spin current density generated via the spin pumping in the FM layer. In the spin transfer torque-based model, T-value is calculated in the light of damping and field-like torques utilizing the drift-diffusion approximation. Here, the effects of spin backflow are neglected (by assuming the thickness of the NM layer to be much greater than the spin diffusion length) as it causes a reduction in the spin-torque efficiencies.

2.2.6 Relationship between Gilbert damping parameter and ultrafast demagnetization time

The unification of magnetization dynamics occurring over a femtosecond to nanosecond timescale is an enduring problem for the magnetism community. In 2005, Koopmans *et al*. proposed a microscopic model to draw a correlation between a femtosecond phenomenon like ultrafast demagnetization with a nanosecond phenomenon like magnetic damping [69]. This model was based on the assumption that both ultrafast demagnetization and magnetic damping require spin-flip scattering to dissipate the energy to the lattice while the dominant angular momentum transfer channels in both situations are the same. According to this model, at a temperature much below the Curie temperature (T_c), the correlation between ultrafast demagnetization time (τ_m) and α can be given as:

$$\tau_m = \frac{\hbar}{4k_B T_c \alpha} \tag{2.30}$$

However, this model could not explain these phenomena at higher temperatures where ordinary scattering becomes dominant. Also, it has a few drawbacks, like i) an oversimplified treatment of the electronic spin-flip scattering by just one effective parameter and ii) the effect of band structure variation is neglected. A micromagnetic model was further developed by Djordjevic *et al*. in 2007, where an additional magnetic relaxation path was suggested [70]. They proposed an instantaneous ultrafast demagnetization due to the spin-flip scattering events and followed by an energy transfer between excited magnetic states and spin wave relaxation chains through different spin wave relaxation channels.

In 2008, Walowski *et al*. challenged the Koopmans model and showed a discrepancy in the inverse relationship between τ_m and α for rare earth (Dy) doped ferromagnetic Py films [71]. This discrepancy is due to missing electron relaxation channels that appear in the presence of rare earth metals. Only one spin relaxation channel was considered for both femtosecond and nanosecond time scales, which is not true in the presence of f-band electrons. This f-band has a very small contribution much above and below the Fermi level due to slight hybridization. Therefore, its contribution to the femtosecond relaxation process is negligible, while it plays a significant role in the nanosecond spin relaxation process. In 2009, Radu *et al.* also observed similar discrepancies against Koopman's model by investigating τ_m and α in presence of Dy, Ho, Gd and Tb impurities in Py films [72].

To solve these discrepancies, M. Fähnle *et al.* proposed another model to correlate between τ_m and α [73]. They considered the electronic band structure details and different possible electronic transitions between states to make this model a universal one. Depending upon the dominant contribution to magnetic damping, the relation between τ_m and α can either be proportional or inversely proportional. There will be a proportional relation between τ_m and α if the damping has a dominant conductivity-like contribution. This conductivity-like contribution to damping is due to the intra-band relaxation of electrons and holes and can be modelled by the "breathing Fermi surface" model of damping. In this case, the relation between τ_m and α can be expressed as:

$$\tau_m = \frac{M}{\gamma F_{el} p b^2}\alpha \qquad (2.31)$$

Here, p is a material-specific parameter, b^2 is the spin-mixing parameter and F_{el} is a quantity determined by the properties of the electronic states. An inverse relationship between τ_m and α is expected when resistivity-like contribution dominates the damping mechanism. This resistivity-like contribution is due to the inter-band relaxation of electrons and holes and can be modelled by the "bubbling Fermi surface" model of the damping. In this case, the relation between τ_m and α can be given by:

$$\tau_m = \frac{F'_{el}}{p b^2 \alpha} \qquad (2.32)$$

Here, F'_{el} is a quantity determined by the properties of the electronic states but it is different from F_{el}. However, this model from Fähnle *et al.* ignored the contributions from any spin transport effects. So, this model is only valid for standard FMs with only spin-flip scattering contribution to both ultrafast demagnetization and damping. Later, Zhang *et al.* [74], Pan *et al.* [75] and Guillemard *et al.* [76] showed a strong correlation between τ_m and α in ferromagnetic Heusler alloy thin films. Recently, Tveten *et al.* theoretically predicted the possibility of explaining τ_m in terms of spin current-induced damping in NM/FM heterostructures based on electron-magnon scattering theory [77]. This was later experimentally demonstrated in different systems. It was argued that ultrafast demagnetization mechanisms are generally divided into two categories: i) spin-flip scattering (including electron-phonon, electron-electron, electron-magnon etc.) and ii) spin current transport. A direct relationship between τ_m and α would validate spin-flip scattering as the major contribution to the ultrafast demagnetization [78], while an inverse dependency would point towards the spin current transport as the dominant microscopic mechanism behind the ultrafast demagnetization process [79]. From this inverse dependence, one can also extract the spin chemical potential (μ_s) for different NM/FM interfaces using the equation:

$$\frac{1}{\tau_m} = \frac{\mu_s}{\hbar}(\alpha - \alpha_0) \qquad (2.33)$$

Here, α_0 is the intrinsic Gilbert damping parameter in the absence of any NM underlayers. The femtosecond laser-induced spin current is very short-lived (sub-picosecond), while spin pumping-induced spin current can live for nanoseconds. However, despite occurring at two different time scales the physical nature of both the spin currents are similar. The femtosecond spin current causes a lowering of the τ_m, while the spin pumping-induced spin current leads to a lowering of the precessional relaxation time (i.e., increased α). Therefore, τ_m and α becomes inversely proportional and therefore connecting the effects of the two is justified.

2.3 Magneto-optical Kerr effect (MOKE)

The interaction of the light beam with magnetic material leads to a change in polarization, intensity, phase and spectrum of the output beam. This effect is known as the magneto-optical effect which was first proposed in 1845 by Michael Faraday when he observed that a linearly polarized light is converted to an elliptically polarized light after transmitting through a glass plate placed under a magnetic field [80]. This effect is recognized as the Faraday effect. Later in 1877, John Kerr observed a similar change in polarization of light after being reflected from the surface of a magnetic material [81]. This effect is known after his name and called as magneto-optical Kerr effect (or simply MOKE). Subsequently, MOKE is proved to be an efficient method to detect the magnetization of a magnetic material. Nowadays, it is very widely used to investigate the static and dynamic magnetic properties of different magnetic materials at a broad range of length and time scales. The angle of rotation in the plane of polarization due to the Kerr effect is known as Kerr rotation (θ_k) and the ellipticity introduced is called Kerr ellipticity (ϵ_k). Both θ_k and ϵ_k are proportional to the magnetization of the system and related to each other via the relation:

$$\theta_k + i\epsilon_k = \frac{k}{r}, \text{ where } k \ll r \qquad (2.34)$$

Here, k and r are the components of the electric field vector (E) of the reflected beam along with the perpendicular and parallel directions. To understand the origin of MOKE, several theories are proposed based on semiclassical and quantum mechanical principles which are discussed briefly below.

2.3.1 Origin of MOKE

There are two theories to explain the origin of MOKE one is macroscopic and the other one is microscopic [82]. According to the macroscopic point of view, when light propagates through a magnetic medium, electrons inside the magnetic medium follow the electric field vector of the light beam. These electrons will go through the left circular motion for left circular polarized (LCP) light and right circular motion for right circular polarized (RCP) light. The radius of this circular motion will depend upon the force exerted on these electrons. A linearly polarized light can be considered to be a combination of LCP and RCP of equal amplitude. When a linearly polarized light is incident on a magnetic material without any magnetic field, the radius of left circular motion and right circular motion of electrons are equal. In this case, the dielectric tensor will be equal in both left and right polarized modes. However, in the presence of a magnetic field, a Lorentz force is felt by the electrons. This additional force affects the radius of left circular motion and right circular motion and results in a finite difference in the dielectric tensor between both modes. Hence, the reflected light will not remain in the same linearly polarized state but convert into an elliptically polarized state. This conversion of linearly polarized incident light to elliptically polarized light upon reflection is popularly called as MOKE.

Microscopically, MOKE can be assumed to be originated from the spin-orbit interaction. As per this theory, the movement of the electrons under the influence of the electric field of light affects the spin-orbit interaction of the system. This change in spin-orbit interaction can be given by: $S \times \nabla V$, S and ∇V are the spin angular momentum of an electron and the electric field acting on the electron respectively. Although this effect is present in both FM and NM materials but it is more prominent in FM materials, because of the imbalance between up-spin and down-spin in them.

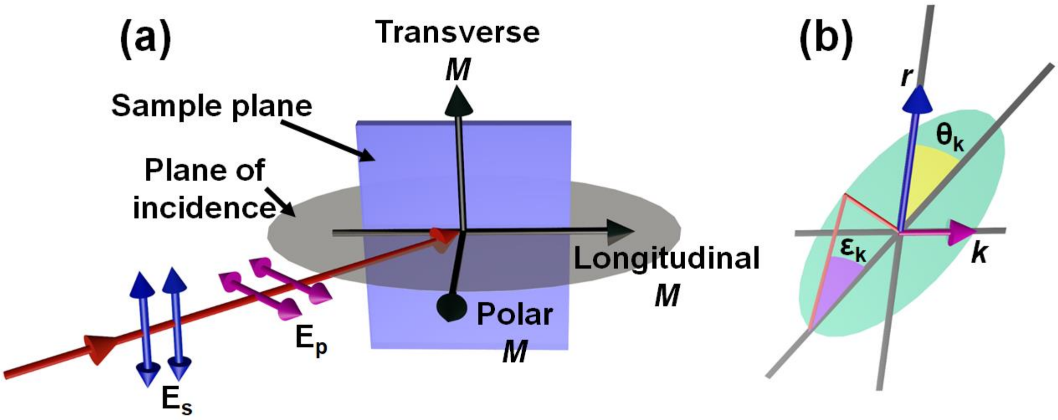

Figure 2.4: (a) Schematics of polar, longitudinal and transverse MOKE geometries are shown. (b) The geometry of the Kerr rotation (θ_k) and Kerr ellipticity (ε_k).

2.3.2 MOKE Geometries

Depending upon the orientation of the magnetization of the sample *w.r.t.* the plane of incidence of light and sample surface, MOKE can be divided into three configurations, namely, polar, longitudinal and transverse Kerr geometries as represented in Figure 2.4(a). Figure 2.4(b) schematically shows the θ_k, ϵ_k and respective orthogonal components of the electric field vector (k and r). In the polar geometry, the magnetization of the sample is parallel to the incident plane but perpendicular to the sample surface. In the longitudinal geometry, sample magnetization lies parallel to both the incident plane and sample surface. Both polar and longitudinal MOKE occur for s- and p-polarized light. On the contrary, in the transverse MOKE geometry magnetization of the sample lies perpendicular to the incident place but parallel to the sample surface and Kerr rotation in this geometry is only observed for p-polarized light. In this transverse MOKE geometry, electrons move in the perpendicular direction *w.r.t.* the incident plane. Hence, s-polarized light in this geometry has magnetization of the sample parallel to the electron's velocity but perpendicular to the incident plane (hence, $v \times B = 0$). Therefore, there is no additional Lorentz force (which is proportional to $v \times B$) on the electron and hence, there is no Kerr rotation. However, reflectivity changes slightly in this case when magnetization reverses.

References

1. P. Langevin, J. Phys. Theor. Appl. **4**, 678-693 (1905).
2. L. Landau, Z. Phys. **64**, 629-637 (1930).
3. A. Abragam, B. Bleaney, Electron Paramagnetic Resonance of Transition Ions (OUP Oxford, 2012).
4. X. Oudet, J. Magn. Magn. Mater. **98**, 307-332 (1991).
5. P. Weiss, J. Phys. Theor. Appl. **6**, 661 (1907).
6. A. Aharoni, Introduction to the Theory of Ferromagnetism 2000).
7. W. Heisenberg, Zeitschrift für Physik **38**, 411-426 (1926).
8. A. Barman and A. Haldar, Time-domain study of magnetization dynamics in magnetic thin films and micro-and nanostructures. Solid State Phys, vol 65. (Elsevier Inc., Burlington, 2014).
9. E. Beaurepaire, J. C. Merle, A. Daunois and J. Y. Bigot, Phys. Rev. Lett. **76**, 4250-4253 (1996).
10. L. Mayer, J. Appl. Phys. **29**, 1003-1003 (1958).
11. B. Koopmans, G. Malinowski, F. Dalla Longa, D. Steiauf, M. Fähnle, T. Roth, M. Cinchetti and M. Aeschlimann, Nat. Mater. **9**, 259-265 (2010).
12. A. Mekonnen, A. R. Khorsand, M. Cormier, A. V. Kimel, A. Kirilyuk, A. Hrabec, L. Ranno, A. Tsukamoto, A. Itoh and T. Rasing, Phys. Rev. B **87**, 180406 (2013).
13. J. W. Kim, K. D. Lee, J. W. Jeong and S. C. Shin, Appl. Phys. Lett. **94**, 192506 (2009).
14. M. Battiato, K. Carva and P. M. Oppeneer, Phys. Rev. Lett. **105**, 027203 (2010).
15. B. L. K. S. I. Anisimov and T. L. Perel'man, Sov. Phys. JETP **39**, 375 (1974).
16. F. Dalla Longa, J. T. Kohlhepp, W. J. M. D. Jonge and B. Koopmans, Phys. Rev. B **75**, 224431 (2007).

17. G. P. Zhang and W. Hübner, Phys. Rev. Lett. **85**, 3025-3028 (2000).
18. M. Krauß, T. Roth, S. Alebrand, D. Steil, M. Cinchetti, M. Aeschlimann and H. C. Schneider, Phys. Rev. B **80**, 180407 (2009).
19. E. Carpene, E. Mancini, C. Dallera, M. Brenna, E. Puppin and S. D. Silvestri, Phys. Rev. B **78**, 174422 (2008).
20. J. Y. Bigot, M. Vomir and E. Beaurepaire, Nat. Phys. **5**, 515-520 (2009).
21. C. Dornes, Y. Acremann, M. Savoini, M. Kubli, M. J. Neugebauer, E. Abreu, L. Huber, G. Lantz, C. A. F. Vaz, H. Lemke, E. M. Bothschafter, M. Porer, V. Esposito, L. Rettig, M. Buzzi, A. Alberca, Y. W. Windsor, P. Beaud, U. Staub, D. Zhu, S. Song, J. M. Glownia and S. L. Johnson, Nature **565**, 209-212 (2019).
22. E. Beaurepaire, G. M. Turner, S. M. Harrel, M. C. Beard, J. Y. Bigot and C. A. Schmuttenmaer, Appl. Phys. Lett. **84**, 3465-3467 (2004).
23. P. Tengdin, C. Gentry, A. Blonsky, D. Zusin, M. Gerrity, L. Hellbrück, M. Hofherr, J. Shaw, Y. Kvashnin, K. Delczeg-Czirjak Erna, M. Arora, H. Nembach, J. Silva Tom, S. Mathias, M. Aeschlimann, C. Kapteyn Henry, D. Thonig, K. Koumpouras, O. Eriksson and M. Murnane Margaret, Sci. Adv. **6**, eaaz1100 (2020)
24. M. Hofherr, S. Häuser, J. K. Dewhurst, P. Tengdin, S. Sakshath, H. T. Nembach, S. T. Weber, J. M. Shaw, T. J. Silva, H. C. Kapteyn, M. Cinchetti, B. Rethfeld, M. M. Murnane, D. Steil, B. Stadtmüller, S. Sharma, M. Aeschlimann and S. Mathias, Sci. Adv. **6**, eaay8717 (2020)
25. J. Stöhr, H. C. Siegmann, From Fundamentals to Nanoscale Dynamics (Springer: Berlin, 2006).
26. G. Malinowski, F. Dalla Longa, J. H. H. Rietjens, P. V. Paluskar, R. Huijink, H. J. M. Swagten and B. Koopmans, Nat. Phys. **4**, 855-858 (2008).
27. T. L. J. I. T. O. M. Gilbert, **40**, 3443-3449 (2004).
28. E. M. L. L. D. Landau, Phys. Z. Sowjet. **8**, (1935).
29. T. L. Gilbert, Phys. Rev. **100**, (1955).
30. C. Kittel, Phys. Rev. **73**, (1948).
31. F. Bloch, Z. Physik **61**, (1930).
32. B. Hillebrands and K. Ounadjela, Spin Dynamics in Confined Magnetic Structures II (Springer: New York, 2003).
33. C. Herring and C. Kittel, Phys. Rev. **81**, (1951).
34. B. Heinrich and J. A. C. Bland, Spin relaxation in magnetic metallic layers and multilayers (Springer: New York, 2005).
35. A. Barman and J. Sinha, Spin Dynamics and Damping in Ferromagnetic Thin Films and Nanostructures (Springer: Switzerland, 2018).
36. Y. Tserkovnyak, A. Brataas and G. E. W. Bauer, Phys. Rev. Lett. **88**, 117601 (2002).
37. J. F. C. B. Heinrich and K. Myrtle, J. Appl. Phys. **53**, (1982).
38. N. M. P. Krivosik, S. Kalarickal and C. E. Patton,, J. Appl. Phys. **101**, (2007).
39. J. O. Rantschler, R. D. McMichael, A. Castillo, A. J. Shapiro, W. F. Egelhoff, B. B. Maranville, D. Pulugurtha, A. P. Chen and L. M. Connors, J. Appl. Phys. **101**, 033911 (2007).
40. B. Sahoo, K. Roy, P. Gupta, A. Mishra, B. Satpati, B. B. Singh and S. Bedanta, Adv. Quantum Technol. **4**, 2000146 (2021).
41. A. Krysztofik, S. Özoğlu, R. D. McMichael and E. Coy, Sci. Rep. **11**, 14011 (2021).
42. A. K. Chaurasiya, A. Kumar, R. Gupta, S. Chaudhary, P. K. Muduli and A. Barman, Phys. Rev. B **99**, 035402 (2019).

43. V. Kamberský, Czechoslov. J. Phys. B **26**, (1976).
44. R. J. Elliott, Phys. Rev. **96**, (1954).
45. F. S. Y. Yafet and D.Turnbull Solid State Phys. **14**, 1-98 (1963).
46. C. Kittel and A. H. Mitchell, Phys. Rev. **101**, (1956).
47. J. Kuneš and V. Kamberský, Phys. Rev. B **65**, 212411 (2002).
48. V. Kamberský, Phys. Rev. B **76**, 134416 (2007).
49. K. Gilmore, Y. U. Idzerda and M. D. Stiles, Phys. Rev. Lett. **99**, 027204 (2007).
50. H. Suhl, IEEE Trans. Magn. **34**, 1834-1838 (1998).
51. B. Heinrich, R. Urban and G. Woltersdorf, IEEE Trans. Magn. **38**, 2496-2501 (2002).
52. S. Qiao, W. Yan, S. Nie, J. Zhao and X. Zhang, AIP Adv. **5**, 087170 (2015).
53. B. Heinrich, J. F. Cochran and R. Hasegawa, J. Appl. Phys. **57**, 3690-3692 (1985).
54. J. Lindner, K. Lenz, E. Kosubek, K. Baberschke, D. Spoddig, R. Meckenstock, J. Pelzl, Z. Frait and D. L. Mills, Phys. Rev. B **68**, 060102 (2003).
55. T. Valet and A. Fert, Phys. Rev. B **48**, 7099-7113 (1993).
56. J. C. Rojas-Sánchez, N. Reyren, P. Laczkowski, W. Savero, J. P. Attané, C. Deranlot, M. Jamet, J. M. George, L. Vila and H. Jaffrès, Phys. Rev. Lett. **112**, 106602 (2014).
57. K. Gupta, R. J. H. Wesselink, R. Liu, Z. Yuan and P. J. Kelly, Phys. Rev. Lett. **124**, 087702 (2020).
58. K. Dolui and B. K. Nikolić, Phys. Rev. B **96**, 220403 (2017).
59. M. I. Dyakonov and V. I. Perel, Phys. Lett. A **35**, 459-460 (1971).
60. V. M. Edelstein, Solid State Commun. **73**, 233-235 (1990).
61. O. Gomonay, K. Yamamoto and J. Sinova, J. Phys. D: Appl. Phys. **51**, 264004 (2018).
62. G. D. H. Hurdequint, J. Phys. Paris, Colloq. **49**, (1988).
63. L. Berger, Phys. Rev. B **54**, 9353-9358 (1996).
64. Y. Tserkovnyak, A. Brataas, G. E. W. Bauer and B. I. Halperin, Rev. Mod. Phys. **77**, 1375-1421 (2005).
65. Y. Tserkovnyak, A. Brataas and G. E. W. Bauer, Phys. Rev. B **66**, 224403 (2002).
66. Y. T. Chen, S. Takahashi, H. Nakayama, M. Althammer, S. T. B. Goennenwein, E. Saitoh and G. E. W. Bauer, Phys. Rev. B **87**, 144411 (2013).
67. W. Zhang, W. Han, X. Jiang, S. H. Yang and S. S. P. Parkin, Nat. Phys. **11**, 496-502 (2015).
68. C. F. Pai, Y. Ou, L. H. V. Leao, D. C. Ralph and R. A. Buhrman, Phys. Rev. B **92**, 064426 (2015).
69. B. Koopmans, J. J. M. Ruigrok, F. D. Longa and W. J. M. de Jonge, Phys. Rev. Lett. **95**, 267207 (2005).
70. M. Djordjevic and M. Münzenberg, Phys. Rev. B **75**, 012404 (2007).
71. J. Walowski, G. Müller, M. Djordjevic, M. Münzenberg, M. Kläui, C. A. F. Vaz and J. A. C. Bland, Phys. Rev. Lett. **101**, 237401 (2008).
72. I. Radu, G. Woltersdorf, M. Kiessling, A. Melnikov, U. Bovensiepen, J. U. Thiele and C. H. Back, Phys. Rev. Lett. **102**, 117201 (2009).
73. M. Fähnle, J. Seib and C. Illg, Phys. Rev. B **82**, 144405 (2010).
74. W. Zhang, W. He, X. Q. Zhang, Z. H. Cheng, J. Teng and M. Fähnle, Phys. Rev. B **96**, 220415 (2017).
75. S. Pan, T. Seki, K. Takanashi and A. Barman, Phys. Rev. B **101**, 224412 (2020).
76. C. Guillemard, W. Zhang, G. Malinowski, C. de Melo, J. Gorchon, S. Petit-Watelot, J. Ghanbaja, S. Mangin, P. Le Fèvre, F. Bertran and S. Andrieu, Adv. Mater. **32**, 1908357 (2020).

77. E. G. Tveten, A. Brataas and Y. Tserkovnyak, Phys. Rev. B **92**, 180412 (2015).
78. M. R. Karim, A. Adhikari, S. N. Panda, P. Sharangi, S. Kayal, G. Manna, P. S. A. Kumar, S. Bedanta, A. Barman and I. Sarkar, J. Phys. Chem. C **125**, 10483-10492 (2021).
79. W. Zhang, Q. Liu, Z. Yuan, K. Xia, W. He, Q. F. Zhan, X. Q. Zhang and Z. H. Cheng, Phys. Rev. B **100**, 104412 (2019).
80. M. Faraday, Trans. R. Soc. (London) **5**, (1846).
81. J. Kerr, Philos. Mag. **3**, (1877).
82. Z. Q. Qiu and S. D. Bader, Rev. Sci. Instrum. **71**, 1243-1255 (2000).

Chapter-3

Experimental methods

3.1 Introduction

In this chapter, we will give an overview of the sample preparation, static characterization and dynamic magnetic properties measurement tools that have been used to investigate different systems in this doctoral thesis work. Fabrication of high-quality samples with dimensions down to the sub-nanometre range is of paramount importance for future technological innovations. This miniaturization depends solely on advanced engineering with high precision on-chip device growth and the choice of ideal materials. To achieve these demands, scientists have developed several sophisticated fabrication techniques to grow different thin film heterostructures and confined nanostructures with high perfection and minimal unwanted defects. Two different methods have been mostly followed to fabricate these desired samples. One is the bottom-up approach or chemical method, while the other one is the top-down approach or physical method. The bottom-up approach relies upon chemical reactions to synthesize different nanowires, nanoparticles etc. Although this method is cost-effective and easier to handle, it is very difficult to control this deposition process. Also, the deposition of ordered crystalline structures and monodispersed samples using this process is very tough. On the other hand, by using the top-down approach, one can efficiently deposit high-quality nanostructures, ultrathin films and multilayers with desired structure and composition. In recent times, a combined process using both bottom-up and top-down approaches is used to fabricate high-quality samples as per the convenience of the user. The works presented in this thesis have used different thin films and heterostructures deposited by the RF/DC magnetron sputtering technique. By using this sputtering technique, one can achieve ultrahigh quality films on a substrate with a sharp interface and minimum structural disorders. After deposition of these thin films, different static structural characterizations are performed using atomic force microscopy (AFM), X-ray reflectivity (XRR), X-ray diffraction (XRD) and micro-Raman spectroscopy analysis techniques. The static magnetic properties are measured by the static MOKE (S-MOKE) magnetometer and vibrating sample magnetometer (VSM). Finally, we have employed a custom-built non-collinear TR-MOKE magnetometer for studying the magnetization dynamics. In the following, we will briefly discuss the working principles of these fabrication and characterization techniques.

3.2 Sample fabrication technique

There are various techniques such as molecular beam epitaxy, thermal evaporation, chemical vapour deposition, electron beam evaporation, magnetron sputtering, pulsed laser deposition etc., to deposit thin films on a substrate. One can control the quality of the samples by choosing the suitable technique for its desired material deposition and controlling various deposition conditions to optimize this technique. We have deposited our thin films and heterostructures using the magnetron sputtering technique as it has some distinct advantages over other techniques, such as:

i) In sputtering entire target surface act as the source.

ii) Better adhesion with the substrate is achieved due to the high velocity of sputtered particles.

iii) Deposited materials have higher melting temperatures due to several cooling procedures.

3.2.1 Magnetron sputtering

Magnetron sputtering [1] is the most versatile and efficient physical vapour deposition technique to grow good quality thin films and heterostructures. Primarily, there are four major parts inside the sputtering chamber. They are the target (made of the material that we want to deposit), substrate (on which we want to deposit), sputter gun and plasma. The working principle of sputtering is to have momentum transfer between particles through elastic collisions which eventually leads to the transfer of molecules from the target to the substrate. The target is negatively charged and placed at the bottom portion of the sputtering chamber, while the substrate is used as ground potential and placed at the top part of the sputtering chamber (shown in Figure 3.1). A high voltage power supply is used to ionize the inert gas and create plasma that contains the electrons, ions and neutral atoms inside the chamber. The electrons in this plasma are repulsed from the negatively charged target and collide with neutral atoms. This collision produces secondary electrons and helps to maintain the electron density inside the plasma. The positively charged ions are accelerated at a very high velocity towards the target and dislodge some of the target atoms. Subsequently, these dislodged atoms are directed towards the anode (the substrate) and get deposited over it. All these processes inside the sputtering chamber occur under a vacuum of about 10^{-7} Torr or better. Among the inert gases, argon is widely used inside the sputtering chamber due to two reasons: i) argon atoms are heavier than helium and neon atoms and ii) argon is much cheaper than krypton and xenon. The efficiency of a sputtering system can be given by a parameter called sputtering yield (S) which can be written as:

$$S \propto \frac{m_1 m_2}{(m_1+m_2)^2} \tag{3.1}$$

where m_1 and m_2 represent the mass of the target and inert gas atom. A very strong magnetic field is applied during deposition to direct the secondary electrons on a helical track around the target. This increases the ionization probability of inert gas inside the chamber which causes an enhancement in the sputter yield, reduces the concentration of the impurities and allows to lower the substrate temperature during the deposition.

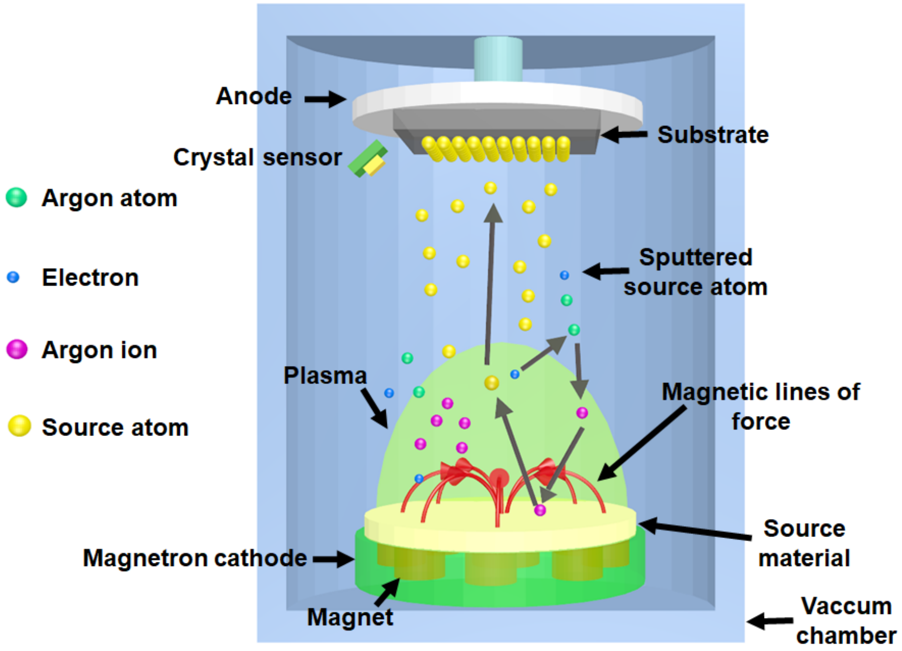

Figure 3.1: Schematic diagram of RF/DC magnetron sputtering.

Depending upon the power supply used during the deposition, sputtering can be divided into two categories: i) direct current (DC) sputtering and ii) radio frequency (RF) sputtering. In the DC sputtering, a DC voltage is applied between the electrodes during the deposition. Although DC sputtering is an efficient and cost-effective method to deposit conductive materials, it is not suitable for the deposition of dielectric or nonconducting materials such as insulators and oxides. Deposition of dielectric or nonconducting materials using this sputtering technique generate a polarized charge near the target that can cause problems, such as arcing (intensely focused discharge comes out from the target which can cause non-uniform deposition) and the target poisoning with some unwanted charged particles that can completely damage the sputtering chamber. To avoid this polarized charge building problem, RF sputtering technique is employed where the target material is continuously bombarded with positive and negative ions by changing the electrical potential of the target at radio frequencies. All in all, high-quality ultrathin films and multilayers can be grown by using the sputtering technique by suitably selecting the electrode voltage (DC or RF), controlling the deposition rate through a quartz crystal monitor and optimizing pressure inside the sputtering chamber.

3.3 Static characterization techniques

3.3.1 X-ray diffraction

The crystalline properties of a material are investigated by using the X-ray diffraction (XRD) technique [2]. This widely used technique was proposed in 1912 by Max von Laue. As per his proposal, X-rays have a wavelength comparable to the lattice spacing of crystalline materials. Hence, the internal crystalline structure of that material can be probed from the diffraction pattern. According to Bragg's law [3], if the X-rays of wavelength λ are diffracted from the lattice planes that are separated by distance d then it satisfies Bragg's condition: $2dsin(\theta) = n\lambda$, where n is the order of diffraction and θ is the incident angle. During the XRD experiment, θ is varied in very small steps and the intensity of the diffracted X-ray beam at 2θ angle *w.r.t.* the direction of the incident beam is recorded (see Figure 3.2). The position of diffraction peaks gives information about the atomic planes from which X-ray beams are reflected and the spacing between these planes that helps to identify different elements present in the sample and their crystal structure. During the measurements that were performed for this thesis work, we used a Cu-Kα X-ray source of wavelength 1.54Å.

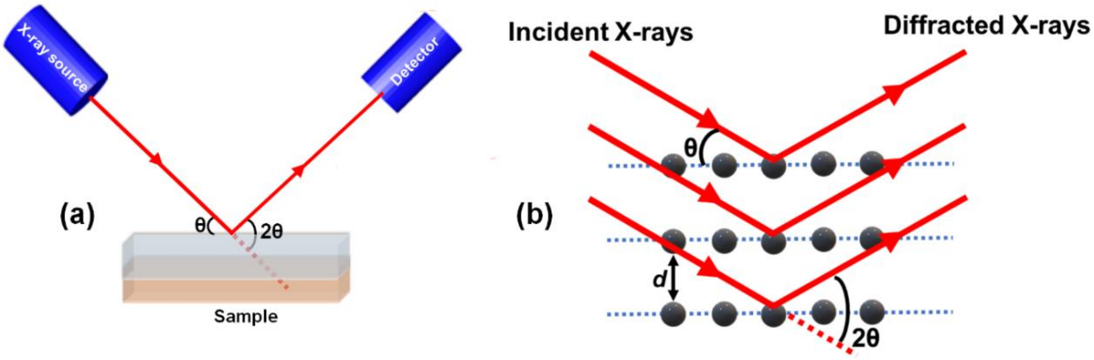

Figure 3.2: (a) Schematic diagram of X-ray diffractometer. (b) X-ray diffraction from the lattice planes.

3.3.2 X-ray reflectivity

Any thin film-based technological application needs precise determination of the thickness of these films. This is because most of the properties of a thin film are thickness-dependent. Therefore, the determination of the thickness of thin films with high precision is very important for these technological applications. X-ray reflectivity (XRR) is a non-contact and non-destructive technique for probing the quality of the surfaces and interfaces which was first applied in 1954 by Lyman G. Parratt to explore the surface of a copper-coated glass [4]. This measurement technique provides information about the thickness, interfacial roughness and average electron densities of different sub-layers of a thin film. The operational principle of XRR is to monitor the intensity of the reflected X-ray beam from the sample placed at a grazing angle. A monochromatic X-ray beam of wavelength λ is incident on a sample placed at a grazing angle θ and the reflected intensity at a 2θ angle is recorded. The X-ray beams are reflected from different surfaces and interfaces which act as classical optics due to different refractive indices and electron densities. When θ is below the critical angle ($\theta_c \leq 0.3^o$ for most materials), the total external reflection occurs. The value of θ_c for a material is determined by its electron density. Above θ_c, the reflected beams will interfere and produce interference fringes. The period and decay profile of these fringes decide the thickness and roughness of different layers. In this thesis, we have analysed the reflectivity data by using the Parratt Formalism. If the sample surface and different interfaces are not smooth then the intensity of the reflected X-ray beam will deviate from Fresnel's law of reflectivity. This deviation is analysed by the classical treatment of the changing electric and magnetic field vectors. In this formalism, only a single reflection from each layer is considered which significantly reduces the contribution of the higher order reflected terms in the overall reflectivity of the multilayers (see Figure 3.3). If the surface is not smooth, then the reflectivity (R) can be expressed as:

$$R = \left| \frac{1}{\rho_\infty} \int_{-\infty}^{\infty} \frac{d\rho_e}{dz} e^{iQz} dz \right|^2 \tag{3.2}$$

Here, ρ_e is the electron density profile. $Q = 4\pi\sin\theta/\lambda$, where λ is the wavelength of the X-ray. ρ_∞ is the density of the material at the bottom-most position. There are two different regions in the XRR data.

i) When $\theta < \theta_c$, then $R = 1$, which means 100% of the incident radiation is reflected.

ii) when $\theta \geq \underline{\theta_c}$, then $R \propto Q^4$ and XRR-traces show oscillations with an angle, which are called Kiessig fringes.

According to the Parratt's formalism the ratio of reflected and transmitted amplitudes between j^{th} and $j+1^{\text{th}}$ layers (X_j) can be given as:

$$X_j = \frac{r_{j,j+1} + X_{j+1} e^{2ik_{j+1,z}d_j}}{1 + r_{j,j+1} X_{j+1} e^{2ik_{j+1,z}d_j}} e^{-2ik_{j,z}d_j} \tag{3.3}$$

Here, d_j represents the thickness of the j^{th} layer, $k_{j,z}$ is the z-component of the wavenumber and $r_{j,j+1}$ is the Fresnel's coefficient which can be represented by:

$$r_{j,j+1} = \frac{k_{j,z} - k_{j+1,z}}{k_{j,z} + k_{j+1,z}} \tag{3.4}$$

In the convention of this module $j = 0$ is the air and $j = n + 1$ is the substrate. The assumption that no reflection was from the substrate makes $X_{n+1} = 0$. Reflection from random rough surfaces poses a lot of analytical problems as the inclusion of the boundary conditions for the electromagnetic wave is nontrivial. A simplifying assumption proposed by N´evot and Croce [5] has been included in our Parratt's analysis module, where the roughness profile σ is considered to have a nature similar to the error function having the functional form:

$$Erfc(x) = \frac{2}{\sqrt{\pi}}\int_x^{\infty} e^{-t^2} dt \tag{3.5}$$

Also, in our Parratt's analysis module, the θ_c and total film thickness d are approximated by the relation:

$$\theta^2 = \left(\frac{\lambda}{2d}\right)^2 N^2 + \theta_c^2 \tag{3.6}$$

Where N is the peak number and the angles are in radian.

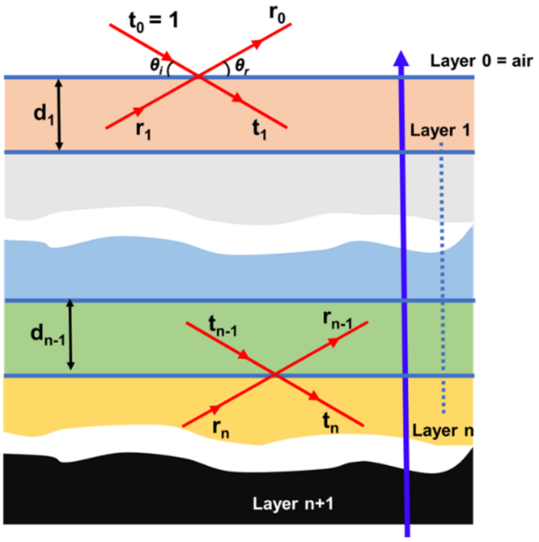

Figure 3.3: Schematic of multiple reflections from a multilayer film having n-layers on a substrate with n+1 interfaces.

3.3.3 Atomic force microscopy

The atomic force microscopy (AFM) technique was first developed in 1986 by IBM to study the morphology and topography of a sample surface [6]. This scanning microscopy technique can have a vertical resolution of 0.1 nm and lateral resolution of about 20 nm under ambient condition. In this technique, the atomic force between a cantilever tip and sample surface is probed and later imaged. This method can easily characterize a wide range of materials such as polymer, ceramic, glass, composite materials, thin films, biological membranes etc. A multimodal AFM set-up has mainly four parts: i) optical head, ii) piezoelectric scanning stage, iii) mechanical cantilever with a sharp tip and iv) controller which is connected to the computer (shown in Figure 3.4). The optical head contains a laser and a few photodetectors. The sample is placed on a piezoelectric x-y-z scanning stage that enables very precise and accurate scanning with a resolution better than the optical diffraction limit. A sharp tip (coated with metals or doped diamond etc.) attached to a cantilever (coated with Pt-Ir, Co-Cr etc.) is utilized to scan the sample surface. When the cantilever tip is brought closer to the sample surface, it starts to experience different atomic forces such as capillary force, electrostatic force, the force due to chemical bonding, magnetic force, van der Waals force etc. These forces cause the deflections from the usual cantilever motion. This deflection is mapped by the laser that is reflected from the upper surface of the cantilever and this laser deflection is detected by sensitive photodetectors attached to the optical head. The signal from the photodetector is collected via the controller in terms of voltage and a three-dimensional image of the sample surface is formed in the computer.

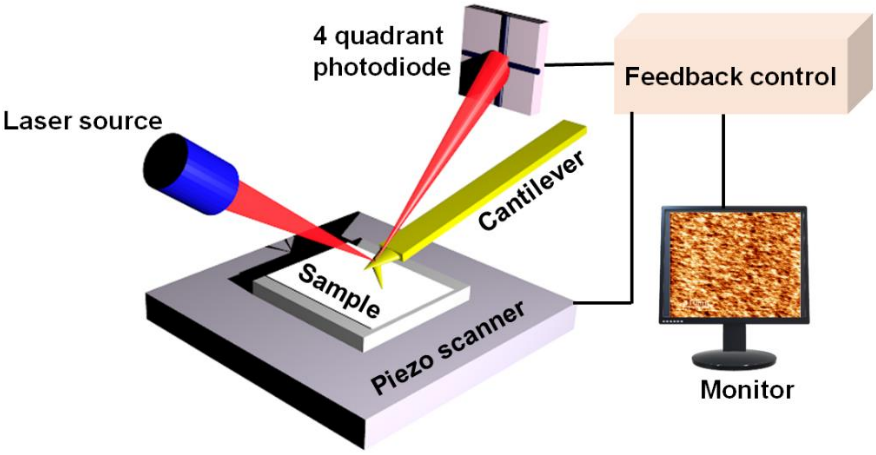

Figure 3.4: Schematic of atomic force microscopy.

Any change in surface topography leads to a deflection of the cantilever tip and this deflection can be imprinted on a three-dimensional image collected through the controller. An AFM set-up can operate in three different modes: i) contact mode, ii) non-contact mode, and iii) tapping mode. In the contact mode of operation, the tip of the cantilever is kept very close to the sample surface (within a few Å distances) which experiences a repulsive van der Waals force. To avoid any damage to the cantilever tip and the sample surface during the scanning process, these cantilevers are made of highly flexible substances. In the non-contact mode of operation, the cantilever tip remains at a distance from the sample surface so that it could experience an attractive van der Waals force. Tapping mode is the most preferred mode of operation for AFM set-up. In this case, the cantilever tip vibrates at the resonance frequency and the distance between tip to sample surface oscillates between contact to non-contact mode. Here, close to the sample surface, the tip experiences a repulsive force which results in a decrease in the oscillation amplitude. With increasing distance between the tip and the sample surface, the strength of this repulsive force decreases and eventually turns into an attractive force at a certain distance. The final AFM image is an imprint of the changing amplitude of the cantilever tip.

3.3.4 Micro-Raman spectroscopy

Micro-Raman spectroscopy [7] is one of the most informative spectroscopic technique to characterize carbon-based materials. Raman scattering [8] was first proposed in 1930 by C. V. Raman where photons are inelastically scattered from the molecules and modified their energy. The difference in the energy between the incident photon and the scattered photon is called the Raman shift. This energy difference gives information about the amount of phonon excitation and change in the electronic state of a material due to the scattering process. Raman scattering can be of two types, namely Stokes and anti-Stokes. In the Stokes scattering, the energy of the photons after scattering decreases while after the scattering, molecules are in a higher vibrational energy state. In contrast, photon energy increases by lowering the vibrational energy states in the anti-Stokes Raman scattering process. Different wavelengths from various types of lasers can be used for Raman spectroscopy. Optical fibre cables are used to acquire the transmitted laser beams from the samples and a charge-coupled device displays it as the Raman spectrum. In this thesis work, we have used this micro-Raman spectroscopy to determine the defect density, quality and number of graphene layers. For this measurement, we have used a 532 nm wavelength argon-ion laser, a thermoelectrically-cooled charge-coupled device detector with 1024×256-pixels, a 100X objective and 600 gr/mm grating with a numerical aperture of 0.9 (laser spot diameter of ~ 0.7 μm) (Schematic of the set-up is shown in Figure 3.5).

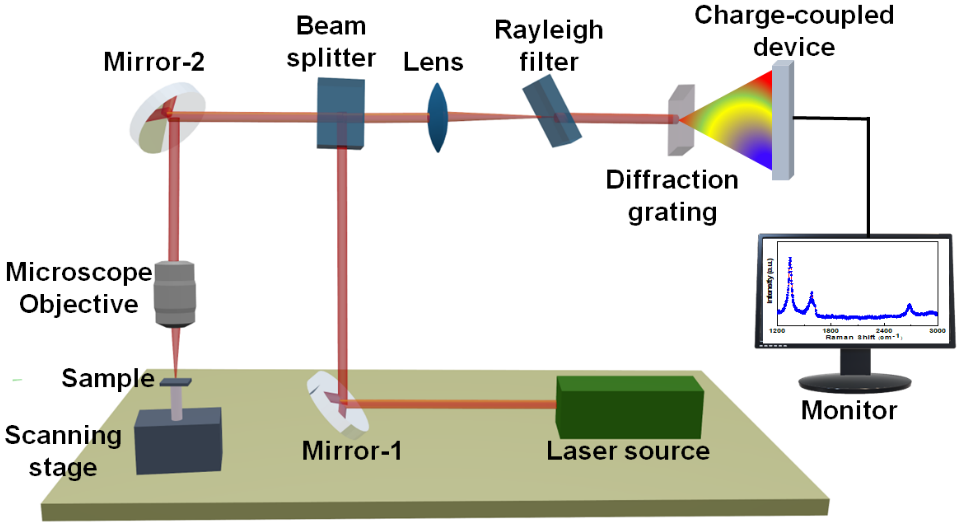

Figure 3.5: Schematic diagram of micro-Raman spectroscopy.

3.3.5 Vibrating sample magnetometry

The magnetic moment of a material can be quantified by several methods such as the inductive method, magneto-optical method, force method and electrical method. Vibrating sample magnetometry (VSM) [9] is an efficient and widely-used inductive method to investigate the magnetic moments of a material as a function of the applied magnetic field and temperature. This measurement technique was first developed in 1956 by Simon Foner. Over the years, its versatility and sensitivity have improved. The basic working principle behind VSM measurement is based on Faraday's law of magnetic induction. According to this law, a change in the magnetic flux passing through a coil can generate an induced electromotive force (E) in that coil. This E can be given as:

$$E = -NA\frac{dB}{dt} \tag{3.7}$$

Here, A is the area of each coil, N is the number of turns in the coil and B is the magnetic induction. B is connected to the system magnetization (M) through the relation: $B = H + 4\pi M$, where H can be assumed to be a constant parameter. Utilizing the value of B in equation 3.7, we will obtain:

$$E = -4\pi NA\frac{dM}{dt} \tag{3.8}$$

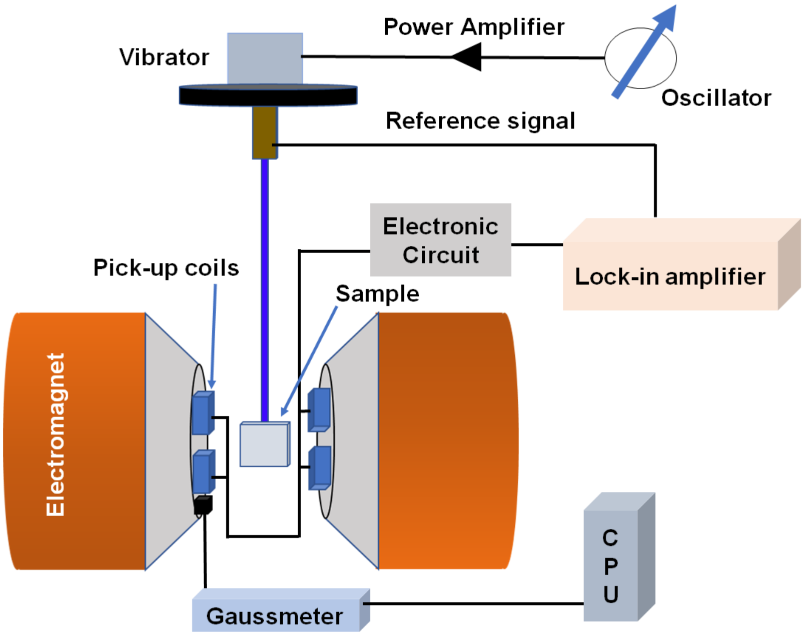

Figure 3.6: Schematic of a vibrating sample magnetometer.

During the VSM measurement, the sample is mounted on a nonmagnetic plastic or quartz rod and placed vertically hanging in between two magnetic pole pieces of an electromagnet (see Figure 3.6). This electromagnet will provide the sample with a uniform magnetic field and will try to align its spins along the field direction. A piezoelectric transducer is attached to the sample rod which helps to oscillate the rod sinusoidally along the vertical direction. This vertical oscillation of the sample will provide a perturbation to the external magnetic field which will eventually be picked up by the coils.

This perturbation will change the magnetic flux linking through the coil and induce an electromotive force that can be given by:

$$E = -2\pi f m y_0 z N G N_c \cos(2\pi f t) \tag{3.9}$$

Where, N_c and y_0 are the number of pick-up coils and the distance between the coils. f and z are the frequency and amplitude of the vibration and m is the sample's DC magnetic moment. This induced electromotive force is detected by a lock-in amplifier. The reference signal for the lock-in amplifier is given from the piezoelectric transducer. To obtain the magnetic hysteresis loops, one can vary the external magnetic field, while the temperature-dependent magnetic measurement will give the Curie and Neel temperature of the sample.

3.3.6 Static magneto-optical Kerr effect magnetometry

The S-MOKE is a magneto-optical method that is used to measure the magnetization of thin films and nanostructures in terms of Kerr rotation or ellipticity [10, 11]. It is a local and non-invasive technique for magnetization measurement. Although S-MOKE can measure Kerr signal in all three MOKE geometries, but in our thesis, we have primarily used the longitudinal Kerr geometry where the sample magnetization is parallel to both the incident plane and sample surface. A continuous-wave He-Ne laser (wavelength = 632.8 nm) is used for the detection of the Kerr rotation. Before exciting the sample, the laser beam passes through a polarizer to make the incident beam fully linearly polarized. An in-plane magnetic field is applied via an electromagnet. The reflected beam from the sample is directed towards an optical bridge detector (OBD) which can detect the rotation in the plane of the polarization. The output signal from the OBD is measured in a phase-sensitive manner using a lock-in amplifier (see Figure 3.7). The laser beam is modulated at a 1 kHz frequency by a photo elastic modulator (PEM). The optical head of PEM is connected to a controller unit via an electrical head. The frequency of the PEM provides the reference signal to the lock-in amplifier. For the magnetic hysteresis loop measurement, the external in-plane magnetic field is varied from the positive direction to the negative direction and the change in the Kerr signal is monitored at each field value with the help of LabView software.

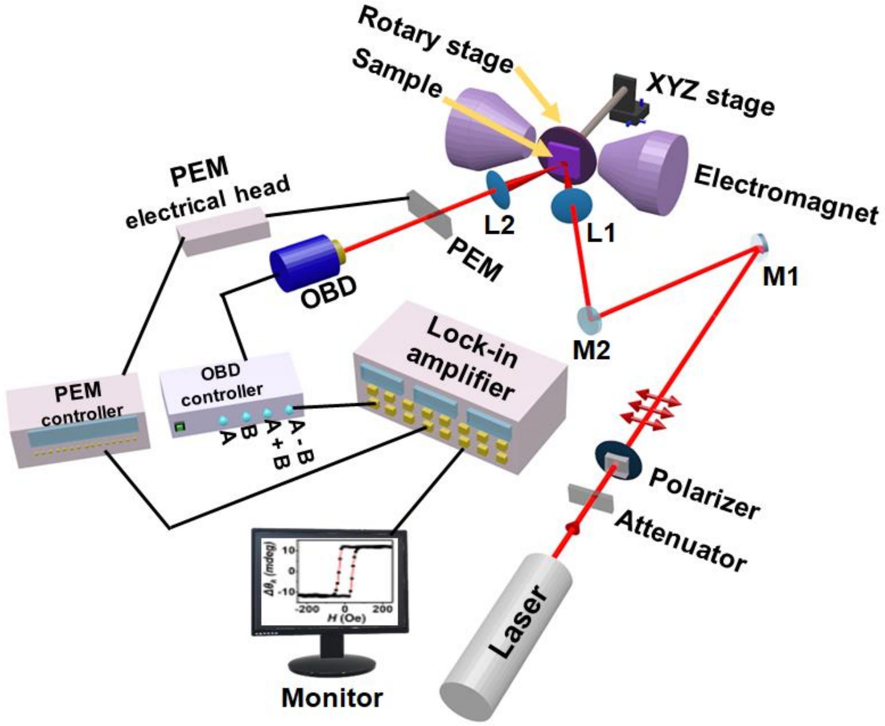

Figure 3.7: Schematic of a static magneto-optical Kerr effect set-up.

3.4 Dynamic measurement technique

To investigate the ultrafast spin dynamics of the magnetic systems, we have used a non-collinear TR-MOKE magnetometry based on the amplified femtosecond laser system. TR-MOKE is a dual-beam pump-probe experiment, where a pump pulse first excites the system under the investigation, after which a probe pulse, detects the pump-induced changes in the system at different delay times [10-13]. By scanning over a broad timescale, the temporal evolution of the system after the initial perturbation can be obtained. It can detect a series of phenomena such as ultrafast demagnetization (occurs in a few hundreds of femtosecond timescale), fast remagnetization (occurs in a few picoseconds timescale) and slow remagnetization superimposed with damped precessional oscillation (occurs in a few nanoseconds timescale). This amplifier laser-based TR-MOKE magnetometry has also many advantages like:

1. This technique has a very high temporal resolution of ~ 35 fs.
2. No complicated microfabrication is required for measuring a sample using this technique.
3. It is a local technique with a spatial resolution of ~ 100 μm and hence have minimal effects arising from large area averaging.

4. The amplifier laser is used for this TR-MOKE operation which has a very high average pulse energy of ~ 4.2 mJ/pulse where we can easily deliver very high fluence values of ~ 100 mJ/cm^2. Also, we can vary the wavelength of the laser beam from 250 nm to 2200 nm by using an optical parametric amplifier system.
5. This is an all-optical and non–invasive measurement technique that is also free from any effects arising from electrical leakages.

In the following section, we will discuss the experimental arrangements of this set-up in detail.

3.4.1 TR-MOKE magnetometry

In the TR-MOKE magnetometer set-up, a fundamental laser pulse of 800 nm wavelength and 35 fs pulse width is generated by the regenerative amplification (RA) method. The amplifier laser system (Libra, Coherent, Inc.) consists of [14]:

I. A seed laser (named Vitesse)
II. A pump laser (called Evolution)
III. Regenerative cavity
IV. Stretcher and compressor gratings
V. Synchronization and delay generator

In this pump-probe set-up, the fundamental laser beam is split into two parts. One part is frequency-doubled (wavelength = 400 nm) by using a second-harmonic generator, which is used as the pump beam to excite the sample. The other part (wavelength = 800 nm) is used as the probe beam to detect the subsequent dynamics. The pump beam is incident on the sample obliquely while the probe beam is incident normal to the plane of the sample. The back-reflected probe beam is used to measure the time-dependent polar Kerr rotation and reflectivity signals simultaneously. Below, we will elaborately discuss different components of this set-up and their working principles.

3.4.1.1 Vitesse

The Vitesse laser module acts as the seed laser in the regenerative amplification process [15]. This module generates an 800 nm mode-locked laser beam with a repetition rate ~ 80 MHz, pulse width ~ sub-100 fs and an average output power > 200 mW. There are two main components of this unit. The first one is the laser head unit and the other one is its power supply that also contains a diode laser assembly called a fibre array package. These two components are interconnected via an umbilical that carries a bundle of fibre cables for transmitting the laser beam from the fibre array package to the laser head. This umbilical also carries electrical cables to control and monitor the signals between the power supply and the laser head. The laser head unit has three sub-systems (See Figure 3.8): i) a diode-pumped solid-state laser called Verdi attached with a Ti: Sapphire oscillator, ii) an assembly mirrors along with a power-track mirror and iii) a Verdi-pumped ultrafast (VPUF) laser.

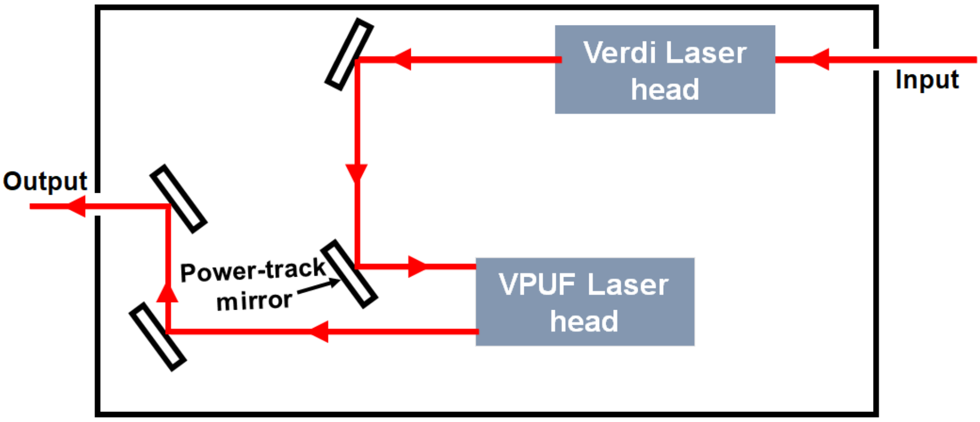

Figure 3.8: Schematic diagram of the Vitesse laser head.

A. Verdi laser head

Verdi laser head is designed to produce multi-watt-level single frequency continuous-wave green (532 nm) laser by employing intra-cavity second-harmonic generation. The optical elements of Verdi consist of a gain medium of Nd-doped yttrium ortho-vanadate (Nd: YVO_4), a frequency doubling crystal of lithium tri-borate (LiB_3O_5, commonly called LBO), an intra-cavity etalon for the single frequency selection, astigmatic compensator, an optical diode, two end mirrors and two pump mirrors. All these optical elements are mounted upon an immovable base plate attached with a strong Invar slab with zero thermal expansion coefficient, high specific heat capacity and good passive thermal stability. The permanently aligned resonator assembly is kept in a clean-room environment inside a sealed enclosure. The Nd: YVO_4 gain medium of Verdi is pumped by an 808 nm laser beam obtained from the fibre array package and emits a strong single frequency beam of 1064 nm. This output beam is passed through the LBO crystal which generates a 532 nm beam by second-harmonic generation. The laser resonator goes through a unidirectional single-frequency oscillation by using an intra-cavity etalon along with the optical diode. The single-frequency selectivity is enhanced by the temperature-stabilized Fabry-Perot etalon, while the optical diode uses the “spatial hole burning” mechanism to achieve a unidirectional lasing. Any thermal gradient inside the laser resonator can cause astigmatism due to thermal focusing, which can be minimized by temperature optimization. Astigmatism may also appear due to the use of spherically curved mirrors inside the resonator cavity which is eliminated by using the Brewster plate compensator. For maximum efficiency of the Verdi laser head, the LBO crystal needs to satisfy a band matching condition where the fundamental beam and its second-harmonic travel inside the crystal at the same velocity. This phase matching can be achieved by tuning the temperature of the LBO crystal which is approximately 149°C for the fundamental laser beam of 1064 nm wavelength. To avoid sudden temperature fluctuation, which can damage the optical coating on the LBO crystal, there is a central processing unit to continuously monitor this temperature. A slow heater ramp-up cycle is used to heat the LBO crystal while a slow cool-down cycle is utilized to cool it down. There is a battery backup circuit in the power supply for the controlled cooling of the LBO crystal in case of a sudden power cut. The 532 nm wavelength output beam from the Verdi laser head is guided towards the VPUF laser head through the power-track mirror.

B. Power-track function

The power-track function is used to maintain the alignment of the Verdi pump beam into the VPUF laser cavity. This helps to minimize the fluctuations inside the cavity which eventually leads to stable output power. These power-track mirrors are connected to some levers which help them to scan (via changing the tilt and altering the pointing direction) in the XY-plane. These levers are controlled by a piezoelectric transducer (PZT). When the Vitesse system is turned on, then the PZT controller supplies some voltage to the levers and starts raster scanning by changing the pump beam position on the mirror. After a set of course adjustments, the raster scan is transformed into a smaller amplitude dither scan (the change in the PZT voltage is much smaller) for fine adjustment. System electronics can distinguish the change in PZT voltage between raster scan and dither scan through an increase in the output power which allows for optimization of the pump beam alignment by fine-tuning this PZT voltage.

C. Verdi-pumped ultrafast (VPUF) laser

The Ti: Sapphire is the active medium of the VPUF laser system. The 532 nm continuous-wave output laser of the Verdi laser head is used to pump this gain medium which gives a pulsed sub-100 fs output beam of 800 nm wavelength. In this laser head, Kerr-lens mode-locking technique is used to achieve mode-locking. Interaction of a material with a laser pulse can change the refractive index of that material by creating atomic distortion. This effect is called as optical Kerr effect. In the case of a pulsed laser beam, the central portion of the beam has a higher intensity than that at the edges. Due to the optical Kerr effect, the refractive index at the edges and the centre of the pulsed laser beam will also be different forming a Kerr lens. This laser beam will narrow down and only the intense potion will only allow it to pass through. This output narrow beam is passed through a slit that allows only that narrow portion of the beam to pass through unattenuated which provides the driving force for the mode-locking. The laser beam also passes through different optical components with different refractive indices. This causes a change in the shape of the laser pulse and introduces spectral chirping (negative or positive) in it. This effect is known as group velocity dispersion (GVD). Also, Kerr lensing leads to different phase shifts for different frequency components which can further increase the chirping and cause pulse broadening. This effect is known as self-phase modulation (SPM). A few negative dispersion mirrors, which are mainly Febry-Perot etalons, are employed inside the cavity to minimize the effect of GVD and SPM. Finally, a sub-100 fs pulsed laser output of 800 nm is obtained from the VPUF laser head which is further used for the amplification.

3.4.1.2 Evolution

The Evolution-30 is a Q-switched laser made of Neodymium-doped yttrium lithium fluoride (Nd: YLF) gain medium [16]. This gain medium is pumped by an AlGaAs diode laser. It delivers a 527 nm output laser with a repetition rate of 1 kHz and average pulse energy greater than 20 mJ. An LBO crystal is employed for the maximum possible second-harmonic generation with a non-critical phase matching procedure. The entire evolution system consists of four units: (1) optical laser bench assembly, (2) power supply, (3) controlling computer, and (4) closed-loop chiller. These units are described below in detail.

A. The optical laser bench assembly

A sealed monolithic aluminium chassis that contains the parts like (i) four high-power laser diodes, (ii) a diode-pumped Nd: YLF laser, (iii) an optical resonator, (iv) a LBO crystal, (v) an acousto-optical switch, and (vi) a safety shutter constitute the entire optical laser bench assembly for the evolution laser system. Brief discussions about these components are given below.

i. Diode lasers: The Evolution-30 laser system employs four AlGaAs diode laser bars in a three-block arrangement to pump the laser gain medium. A water-cooled heat sink is connected with the diode laser bars for continuous temperature maintenance. These diode lasers are used to pump the Nd: YLF gain medium.

ii. Nd: YLF laser: The Nd: YLF gain medium is very efficient for the generation of high-energy pulses with a low repetition rate. This is due to its long upper-state lifetime (approximately 470 μs) which is very efficient in storing energy. Its natural birefringence and low thermal lensing help to avoid beam quality loss. An intra-cavity polarizer allows one to choose either 1047 nm or 1053 nm as the emission wavelength. However, Evolution-30 normally operates at 1053 nm wavelength due to lower thermal lensing at this wavelength.

iii. Acousto-optic Q-switching: Interaction of an optically transparent material with the ultrasonic vibration leads to a coupling between the refractive index of the material and the strain field of ultrasonic vibration. This effect is known as the photo-elastic effect and it converts the optically transparent material into a grating. If a laser pulse is incident on this grating, then it diffracts the laser beam with different refractive indices in different directions. This results in a loss of energy within the cavity and decreases the Q factor of the cavity. A PZT is used to produce ultrasonic waves from an electrical signal. By switching off the PZT voltage one can stop the ultrasonic vibration in the optically transparent material (in our case fused silica) and tune the laser cavity into a high Q factor state. So, by tuning the voltage of this transducer a Q-switched laser pulse is emitted.

iv. Frequency doubling component: A nonlinear LBO crystal, which provides high-efficiency frequency conversion and a large acceptance angle, is employed as an output coupler to generate a frequency-doubled Q-switched beam. A heater is used to maintain the temperature of the LBO crystal at 327.4°F (164.1°C) for its maximum efficiency. This LBO crystal can also work efficiently in between the 157°C and 171°C temperature range. It converts a 1053 nm input laser beam into a 527 nm beam. The crystal is coated with an anti-reflection coating for reducing the reflection for 1053 nm and 527 nm laser beams.

B. The power supply assembly

The main function of the power supply assembly is to apply DC voltage to all the electronics. It is connected to the optical bench assembly through an umbilical cable. The major components of the power supply assembly are master control electronics, diode power supply, LBO temperature controller, Q-Switch driver and few accessory electronics.

C. Control computer

All the operations inside Evolution-30 are controlled through the “Evolution” LabView software installed on an external computer. The laser system is connected to this pre-configured computer through a USB interface.

D. Closed-loop chiller

A closed-loop chiller unit is provided for the waste heat dissipation inside the Evolution-30 system. Also, it maintains the wavelength of the diode lasers and ensures its maximum absorption in the Nd: YLF gain medium. The temperature and pressure of this chiller unit are kept at 18.5°C and 60 PSI.

3.4.1.3 Working principle of Libra

Different phenomena are involved in the regenerative amplification process inside Libra. All the phenomena are described in the following section.

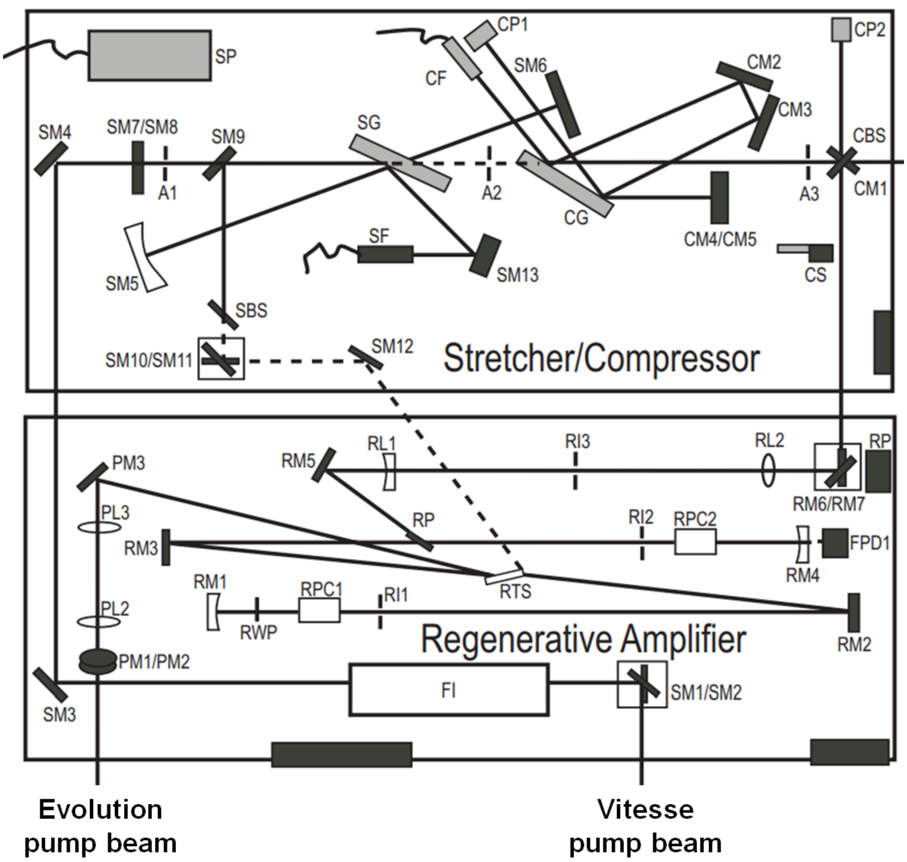

Figure 3.9: Schematic diagram of the stretcher, regenerative amplifier and compressor optical components.

A. Chirped pulse amplification (CPA)

CPA is a technique for obtaining a high energy pulse from an ultrashort low energy pulse. Before this amplification, the laser pulse is temporally stretched by approximately 10,000 times. This stretching help to avoid energy loss due to self-focusing where a highly intense beam loses some energy due to a very short path length. After stretching, the peak power of the laser pulse is significantly reduced. This low-power pulse is then amplified by about a factor of 10^6 by using the regenerative amplifier. After amplification, this amplified laser pulse is compressed back to its original temporal duration.

B. Pulse stretching and compressing

Pulse stretchers and compressors are devices that can delay certain frequencies relative to others by sending different frequencies in different directions. These devices are mainly diffraction gratings which can stretch a short laser pulse into a longer one and compress a long laser pulse into a shorter one. Inside the stretcher optical components, the bluer (higher) frequency travels a longer optical path than the redder (lower) frequencies. Thus, the redder frequencies exit from the stretcher first and the optical pulse get stretched due to positive group velocity dispersion (GVD). The output laser pulse is also called a positively chirped pulse. Pulse compression is the reverse mechanism of pulse stretching.

Here, the bluer frequencies tend to travel a shorter optical path in comparison to the redder frequencies resulting in a negative GVD. In this case, the output pulse is called a negatively chirped pulse. Although after passing through the stretcher the laser pulse gets stretched temporally, after compression, it returns to its initial temporal width again.

C. Regenerative amplification

Regenerative amplification is a process to convert a low peak power laser pulse into a high peak power laser pulse. A Ti: Sapphire crystal is used in this amplification process. This Ti: Sapphire crystal is highly thermal-strain-resistive which makes it durable for high-power optical pumping. The operation principle of regenerative amplifier (RA) is to amplify a confined single laser pulse by using its polarization state followed by dumping the cavity output. A nano-Joule order laser pulse is amplified into a milli-Joule order pulse that indicates its amplification by a factor of 10^6. The amplification factor in each pass through the Ti: Sapphire crystal is only 2-3 times, but this huge 10^6 times amplification is achieved by multi-passing the seed laser through the pumped Ti: Sapphire crystal.

The optical components (shown in Figure 3.9) that are involved in the amplification process are described below:

(1) Stretching operation: The path traversed by a laser beam during the stretching operation is as follows: SM1-SM2-FI-SM3-SM4-SM3-SG-SM5-SM6-SG-SM3-SM4-SM3-SG-SM7-SM8-SM9-SM10-RA cavity

(2) Regenerative amplification operation: A “Z-fold configuration” is employed inside the regenerative amplifier cavity. The path of the laser beam during this regenerative amplification operation is as follows: RM1- RWP- RPC1-RI1-RM2-RTS-RM3-RP-RI2-RPC2-RM4.

Synchronization and delay generator and the Pockels cells: The Pockels effect mainly appears in materials like lithium niobate ($LiNbO_3$), which shows inversion symmetry breaking. These materials constitute Pockels cells (PCs) which produce birefringence through the linear electro-optic effect with the application of the electric field. PC is a major component of electro-optic modulators and mainly acts as a voltage-controlled waveplate. Two PCs are used in the regenerative amplification operation. With the application of voltage, these PCs act like quarter-wave plates and rotate the polarization by 90° by a double-pass mechanism. The first PC traps the beam inside the resonator cavity for the regenerative amplification while the second PC ejects the amplified beam out of the cavity. This trapping and ejection of beams need to happen in a synchronized way with a time gap of approximately 150 ns in between them. Also, the first PC must be synchronized with the pulse train of the Vitesse seed laser to allow only a single laser pulse into the resonator. These synchronization operations are controlled by the synchronization and delay generator (SDG) unit [17]. In addition, SDG introduces an optimum delay between two PCs to achieve maximum gain during the multi-pass operation. SDG is connected to the band-width detector (BWD) interlock system for the protection of the regenerative amplifier unit from any intense laser pulses that can damage the unit.

(3) Compressing operation: The path of the laser beam during the compressing operation is as follows: CM1-CG- CM2-CM3–CG-CM4-CM5-CG-CM3-CM2-CG-Output.

Finally, the Libra laser system emits the 800 nm fundamental pulsed laser beam with pulse width ~ 35 fs, average pulse energy ~ 4.2 mJ, repetition rate ~ 1 kHz and output power ~ 4 W. For day-to-day operation, this output pulse is optimized remotely by tuning a knob connected with the compressor grating and a few associated mirrors inside the Libra.

3.4.1.4 Verification of cavity build-up process inside Libra laser system

The efficiency of the regenerative amplification process depends upon the precise coordination between Vitesse seed pulse, Evolution pump pulse and amplifier PCs. The alignment procedures of the regenerative amplifier (RA) have three distinct steps:

i. Pre-alignment of optics using He-Ne laser (Done at the time of installation).

ii. Alignment of the Evolution pump beam.

iii. Alignment of Vitesse seed beam.

To optimize the RA cavity, the Ti: Sapphire crystal in the RA is pumped by the Evolution laser pulse. This pump beam is focused into the Ti: Sapphire crystal by maintaining a constant height (~ 5 inches). Furthermore, the stretched Vitesse seed laser pulse from the stretcher is used as an input to the RA. Some portion of the mode-locked seed laser beam is also directed towards a photo diode which is connected to an output line (called regen build-up line) located at the backside of the Libra chassis. This output line and a trigger coming from the front panel of SDG (labelled as ‘sync out delay ns’) are connected to a 1 GHz digital oscilloscope to monitor the intra-cavity build-up during system operation. The time base of this oscilloscope is set to 100-200 ns per division. This oscilloscope produces an output of a megahertz pulse train. Here, each pulse is the same laser pulse on its multiple passes through the RA cavity. The photodiode signal without and with a well-aligned seed beam is shown in Figures 3.10(a) and 3.10(b), respectively. In the well-aligned condition, the delay time between two PCs is optimized through SDG to cavity-dump the amplified output pulse(as shown in Figure 3.10(c)) and achieve maximum output power. After efficient generation of amplified pulse, the pulse width of the beam can be optimized by the user externally by fine-tuning the compressor delay stage. The RA cavity remains stable if the temperature, humidity and dust level in the air is maintained carefully.

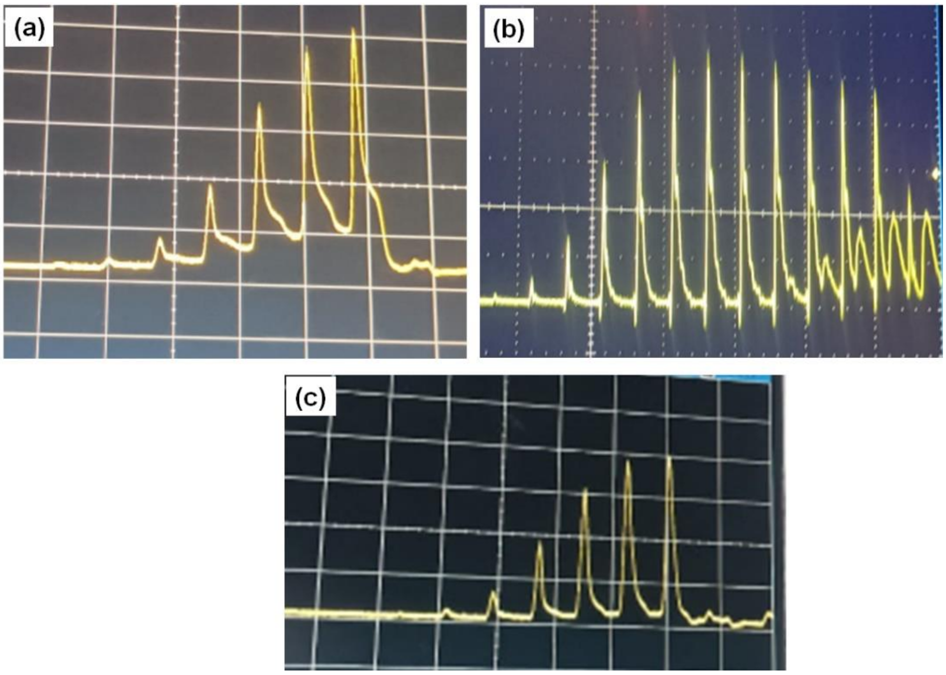

Figure 3.10: Photodiode signal at (a) unseeded, (b) seeded and (c) perfectly optimized condition of RA cavity.

3.4.1.5 Second-harmonic generator

In our pump-probe experiment, the 800 nm fundamental output beam from the Libra is used as the probe while its second-harmonic, i.e., 400 nm wavelength is used as the pump. A second-harmonic generator (SHG) (Model number: Harmonic, HGS-T) is used to generate this 400 nm second-harmonic beam for our pump-probe experiment. This model also can generate a third harmonic beam of deep ultraviolet wavelength. The basic operational principle of SHG depends on the nonlinearity in the optical properties of a dielectric material. The polarization and refractive index of dielectric materials can have both linear and higher-order nonlinear electric field terms. In the non-linear crystals, the generation of the second-harmonic beam is the result of coherent dipole radiation which is connected to the second-order polarization term. If dipoles of a non-centrosymmetric crystal are placed under an oscillating electric field of frequency ω, then its output radiation contains both fundamental frequency ω and its second-harmonic frequency 2ω. The second-harmonic output power can be expressed as:

$$P \propto \frac{l^2 P_\omega^2 \eta^2 \phi}{A} \qquad (3.10)$$

Where, l is the length of the non-linear crystal, P_ω is the input power, η is the non-linear coefficient, ϕ is the phase-matching coefficient and A is the beam spot-size. To increase the output power of the second-harmonic beam, the beam spot size is decreased and collimated by using pair of lenses. The collimated beam is then tightly focused on the non-linear SHG crystal (which is Barium Beta-borate (BBO) for our case) which generates a horizontally-polarised frequency-doubled beam and a vertically-polarized residual of the fundamental beam. These two beams are isolated by a prism which diffracts the second-harmonic beam onto another pair of prisms. This type of optical arrangement has three purposes: (i) the second-harmonic beam becomes parallel to the fundamental beam, (ii) the output beam maintains a fixed direction independent of the crystal orientation, and (iii) the ellipticity induced in the second-harmonic beam is compensated. In the end, both the fundamental and second-harmonic beams exit parallelly through two different output ports. To minimize the temporal broadening due to GVD, a very thin BBO crystal is used. In addition, for avoiding moisture accumulation in the crystal, it is kept within a sealed cylinder with antireflection coating and filled with index-matching fluid.

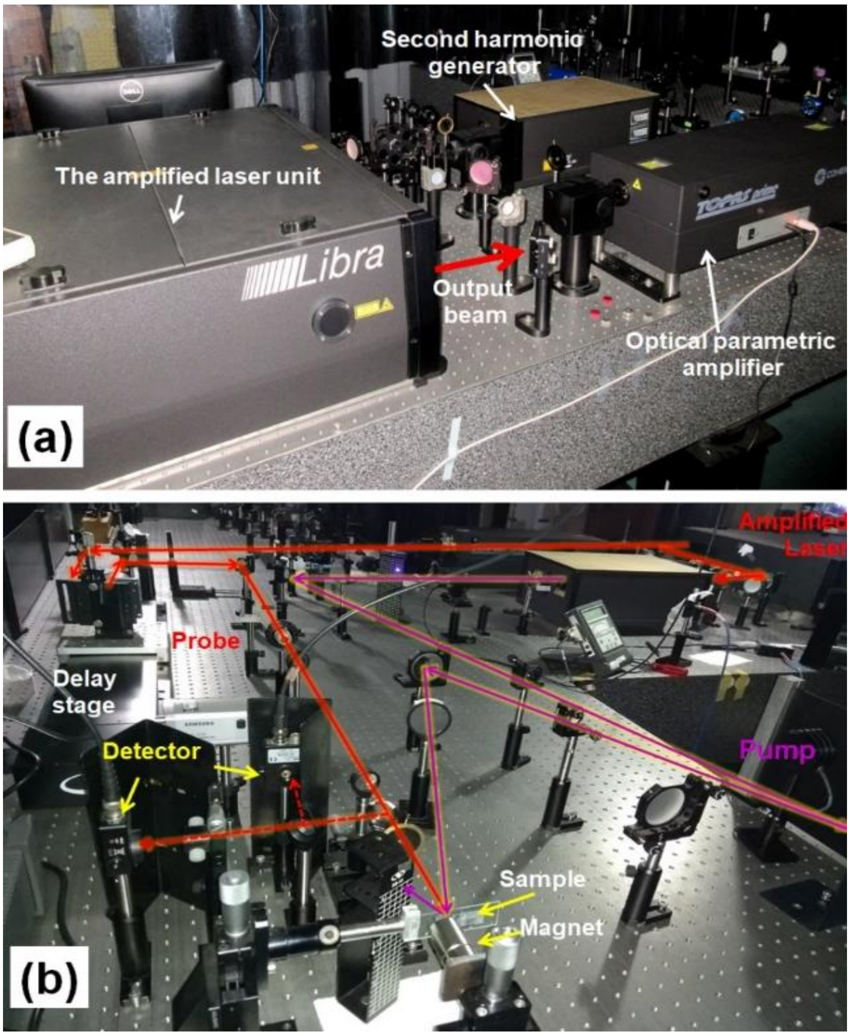

Figure 3.11: Photograph of the non-colinear TR-MOKE set-up in our laboratory.

3.4.1.6 Description of the non-collinear TR-MOKE set-up

The vertically-polarized output beam of the Libra amplifier laser is split into two parts using a beam splitter. One part of this fundamental beam is passed into the SHG for frequency doubling. The frequency-doubled output beam of SHG is used as the pump beam. The other fundamental part is attenuated into a very low power beam which is eventually used as the probe beam. Before probing the sample, this beam is collimated by using a pair of plano-convex lenses of 10 and 15 cm focal length. This collimated beam is steered into a motorized delay stage (from Newport, Model: ESP301-1N) with a retro-reflector (Model: M-IMS500PP) for the introduction of a variable time delay. The output beam from the retro-reflector is guided towards the sample and falls onto the sample surface after passing through a plano-convex lens. A Glan-Thompson polarizer (Thorlabs, Model: GTH5M) with a 100000:1 extinction ratio, is used in the probe beam path for the high degree of polarization. Few variable attenuators are placed in the pump and probe paths for power adjustment. The sample is placed on a holder which is connected to an x-y-z translational stage. The pump beam excites the sample obliquely while the probe beam is incident normally on the sample. Both pump and probe beam are kept slightly defocused on the sample to avoid any damage to the metallic thin film samples. The spot size of the pump and probe beam is about 200 and 100 μm, respectively. The probe beam is placed at the centre of the pump beam to avoid probing any non-uniform exciting part of the sample. The reflected pump beam from the sample is blocked while the reflected probe beam is split into two parts by using a beam splitter. One part directly falls on a silicon photodetector to measure the total reflectivity of the sample. The other part passes through a Glan-Thompson polarizer (which works as an analyzer) and falls on a silicon photodetector to measure the Kerr rotation. The analyser is kept at the extinction angle so that it only passes the Kerr rotated probe beam with a minimal reflectivity background. The output of both silicon photodetectors is measured by two different lock-in amplifiers (Stanford research system, Model: SR830). An external magnetic field in the desired configuration is applied by using a permanent bar magnet. The pump beam is periodically chopped (chopper frequency ~ 373 Hz) by an optical chopper (Thorlabs, Model: MC2000B with 10 slots chopper blade). This chopper also provides the reference to the lock-in amplifiers for a phase-sensitive measurement of both time-resolved reflectivity and Kerr rotation. The time-dependent dynamic data is collected by using a home-built LabView software. The humidity and temperature of the laboratory are maintained below 30% and 22°C respectively. A photograph and schematic diagram of the TR-MOKE set-up is shown in Figure 3.11 and Figure 3.12.

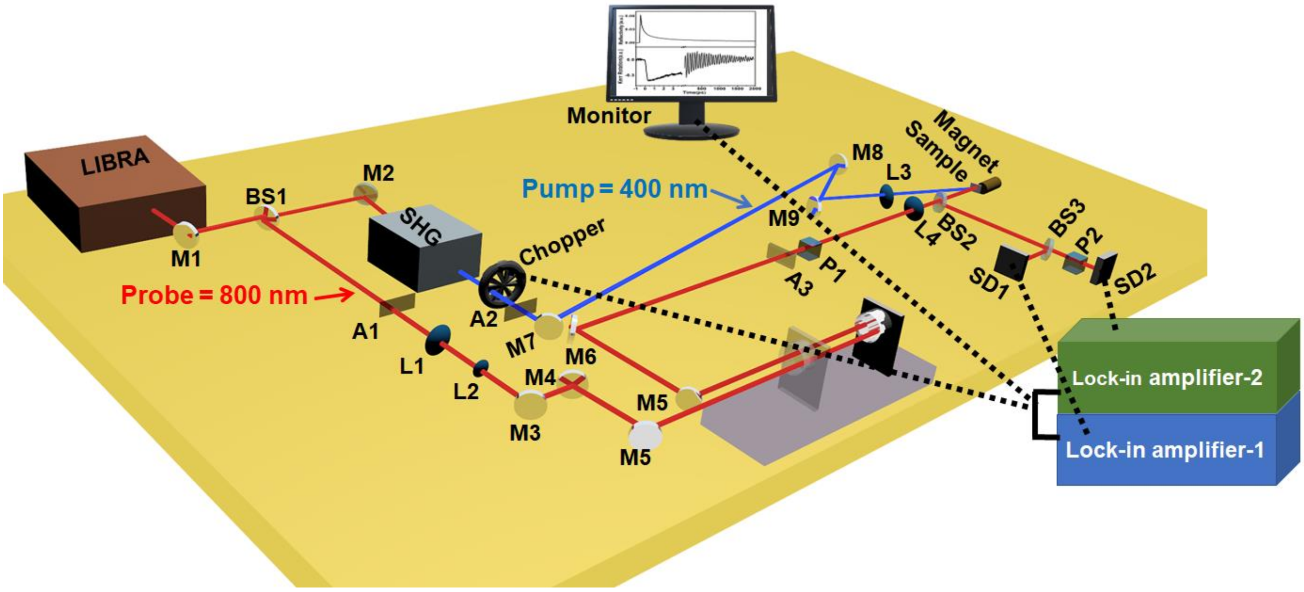

Figure 3.12: Schematic diagram of the non-collinear TR-MOKE system.

3.4.1.7 Standard measurement protocols of time-resolved dynamics

After maximizing the output power from the Libra amplified laser and the SHG, the probe and pump beam are kept at a suitable fluence for the further fine-tuning of the TR-MOKE system. Usually, the total reflectivity signal of a reference silicon substrate is monitored at different delay times by moving the motorized delay stage. The reflectivity data shows a sharp rise followed by an exponential decay. The onset of this sudden rise of reflectivity can be identified as the position of zero-delay position when there is perfect temporal overlapping with no time delay between probe and pump beam. The profile and decay time of exponential decay in the positive delay provide information about the quality of pump-probe alignment. This alignment can be improved by adjusting the mirrors placed in the path of the pump beam. After optimization of the transient reflectivity signal, the magnetic samples are placed in the place of a silicon substrate and a magnetic field is applied along the desired direction by using a bar magnet. The reflectivity and Kerr rotation signal are captured in the computer at different time delays through an automated way by using a home-built LabView program. The total delay time depends upon the length of the delay stage which is about 2 ns for our case.

References

1. Sputtering by Particle Bombardment (Springer: Berlin, 2007)
2. H. P. Klug and L. E. Alexander, X-Ray Diffraction Procedures: For Polycrystalline and Amorphous Materials (Wiley, 1974).
3. W. H. Bragg and W. L. Bragg, Proc. R. Soc. Lond. A **88**, 428-438 (1913).
4. L. G. Parratt, Phys. Rev. **95**, 359–369 (1954).
5. L. Nevot and P. Croce, Rev. Phys. Appl. **15**, 761–779 (1980).

6. E. Meyer, Progress in Surface Science **41**, 3-49 (1992).
7. A. C. Ferrari and D. M. Basko, Nat. Nanotechnol. **8**, 235-246 (2013).
8. C. V. Raman, Indian J. Phys. **2**, 387-398 (1928).
9. S. Foner, Rev. Sci. Instrum. **30**, 548-557 (1959).
10. A. Barman and A. Haldar, Time-domain study of magnetization dynamics in magnetic thin films and micro-and nanostructures. Solid State Phys, vol 65. (Elsevier Inc., Burlington, 2014).
11. A. Barman and J. Sinha, Spin Dynamics and Damping in Ferromagnetic Thin Films and Nanostructures (Springer: Switzerland, 2018).
12. B. Rana and A. Barman, Spin **3**, 1330001 (2013).
13. B. Rana, D. Kumar, S. Barman, S. Pal, Y. Fukuma, Y. Otani and A. Barman, ACS Nano **5**, 9559-9565 (2011).
14. Operator's Manual, Libra Ultrafast Amplifier Laser System, Coherent, California.
15. Operator's Manual: Vitesse Diode Pumped Mode-Locked Ti: Sapphire Laser, Coherent, California.
16. Operator's Manual, Evolution-15/30 High Energy High Average Power Q Switched Laser System, Coherent, California.
17. Operator’s Manual, SDG Elite-Synchronization and Delay Generator, Coherent, California.

Chapter-4

All-optical detection of interfacial spin transparency from spin pumping in β-Ta/CoFeB thin films

4.1 Introduction

Development of advanced spintronic [1-4] devices with minimal power dissipation has attracted great interest in recent times. The major goal of modern spintronics is to harness pure spin current [5, 6] to enable more efficient information processing through non-volatility, rapid switching and energy-efficient on-chip integration of magnetic bits in memory devices. Since pure spin current does not involve net flow of charge, Joule heating and stray Oersted field effects can be avoided in spin current-based devices [7]. Pure spin current or flow of spin angular momentum can be originated from the spin-dependent scattering in heavy metals such as the spin Hall effect [8, 9], Rashba-Edelstein effect [10, 11], spin pumping [12, 13], electrical injection from ferromagnet in a non-local geometry [14, 15] and spin caloritronic effect [16, 17]. The fundamental concept of spin pumping is depicted as follows: precessing spins in a FM transfer angular momentum to the conduction electrons of an adjacent NM layer. This can act as a sensitive probe for many bulk and interface spin-orbit effects. The extent of spin pumping is calculated from the modulation of the Gilbert damping parameter; the latter plays an important role in determining the switching efficiency of spin transfer torque-based spintronic devices. The plethora of works in the emerging field of spin-orbitronics [18] have revealed that interfacial transport observed in spin Hall effect [8, 9], Rashba- Edelstein effect [10,11], spin-Seebeck effect [19], spin-Nernst effect [20] etc. is highly influenced by spin conductance at the interface. Interfacial spin transparency [21] as a function of spin-mixing conductance [22] effectively determines the extent of spin current diffused through the NM/FM interface. The role of transparency in a Pt-based interface while determining the amount of spin Hall effect has been reported in recent studies [21]. Later, the influence of spin transparency on the spin pumping effect has been studied in a Co_2FeAl/β-Ta interface using an electrical detection technique [23]. However, to the best of our knowledge, investigation with a perspective of determining spin-mixing conductance and interfacial spin transparency by using all-optical excitation and detection technique is missing in the literature. In addition, the determination of interfacial spin transparency of technologically important β-Ta/CoFeB is also absent in the literature. It is worth mentioning that β-Ta possesses a large spin Hall angle, in addition to being a good spin sink material and cost-effective in comparison to Pt. On the other hand, CoFeB is technologically important because of high spin polarization, exhibition of large tunnel magnetoresistance when used as FM electrode in magnetic tunnel junction and low intrinsic Gilbert damping. The presence of Boron at the interface between β-Ta/CoFeB makes this system intriguing as some of the earlier studies suggest that small amounts of Boron help in achieving a sharp interface, although excess Boron leads to contamination at the interface.

In an NM/FM bilayer, there are other mechanisms of dissipation of spin angular momentum at the interface than interfacial spin transparency, which may affect the magnitude of spin pumping, *i.e.* spin memory loss [24], Rashba effect [11], two-magnon scattering [25], interfacial band hybridization [26], etc. However, for the sake of energy-efficient device fabrication, the interface in the engineered structure should have a high spin transmission probability. So, it is imperative to get a deep insight into the mechanisms involved to optimize the efficiency of generation and transfer of pure spin current.

In this chapter, we have performed TR-MOKE measurements [27] to explore the effect of spin pumping phenomena in the β-Ta/CoFeB bilayer system. Measurements of the spin pumping effect performed so far by using electrical excitation and detection techniques, such as spin-torque ferromagnetic detection technique (ST-FMR) and spin Hall magnetoresistance methods that require extremely delicate micro-fabrication. Extraction of magnetic damping from FMR linewidth measurement, where excitation of multiple modes and effect of impurity scattering centres may lead to inhomogeneous line broadening, resulting in an overestimation of damping values. Here, we have reliably probed spin pumping and interfacial spin transparency using a non-invasive all-optical method without the requirement of a complicated micro-fabrication procedure. Magnetic damping can be directly extracted from the decaying amplitude of time-resolved Kerr rotation data, free from any experimental artefacts. In the case of multi-modal oscillation, the time-resolved data can be appropriately analyzed to extract the damping of individual modes precisely. From modulation of damping with Ta thickness, we have determined the intrinsic spin-mixing conductance of β-Ta/CoFeB interface (which does not involve the backflow of spin angular momentum) and spin diffusion length [28] of β-Ta. Later, effective spin-mixing conductance (which involves backflow of spin angular momentum) is estimated from the dependence of damping on FM layer thickness. By using a spin Hall magnetoresistance model [29], we have calculated the interfacial spin transparency of β-Ta/CoFeB. We further investigate the possible effects of other interface phenomena, including spin memory loss, by incorporating a thin Cu spacer layer between the β-Ta and CoFeB layers. Negligible modulation of damping with Cu spacer layer thickness confirms the dominance of spin pumping generated pure spin current and its efficient transport in this system.

4.2 Experimental details

The heterostructured thin films of Sub/Ta (*t*)/CoFeB (*d*)/SiO_2 (2 nm), where nonmagnetic layer thickness, t = 0, 1, 2, 3, 4, 5, 6, 7, 10, 15, 20 nm and ferromagnetic layer thickness, d = 1, 2, 3, 4, 6, 10, 13 nm, were deposited with RF/DC magnetron sputtering system on Si (100) wafers coated with 100 nm-thick SiO_2. The depositions were done at an average base pressure of 4.0×10^{-7} Torr and argon pressure of about 1.0 mTorr at a deposition rate of 0.2 Å/s. Very slow deposition rates were chosen to have films with uniform thickness even at a very thin regime down to 1 nm. The Ta and SiO_2 were deposited using RF power of 40 and 60 W, respectively, while CoFeB was deposited using DC voltage of 380 V. All other deposition conditions were carefully optimized and kept almost identical for all samples. In another set of samples, we introduced a thin Cu spacer layer in between the FM and NM layers and varied its thickness from 0.4 to 1 nm. The Cu layer was deposited at a DC voltage of 345 V, argon pressure of 1.0 mTorr and deposition rate of 0.2 Å/s.

TR-MOKE technique is exploited to study the precessional magnetization dynamics of the samples in polar Kerr geometry. The fundamental beam (pulse width ~ 40 fs, wavelength ~ 800 nm and repetition rate ~ 1 kHz) of an amplified laser system (Libra, Coherent) is used as a probe while a part of this beam is frequency doubled (wavelength ~ 400 nm and pulse width ~ 50 fs) to be used as the pump pulse. The probe and pump beams (spot size of 100 and 200 μm, respectively) fall non-collinearly on the sample to detect the polar Kerr rotation as a function of the time delay between pump and probe beams introduced through a variable delay generator. The sample is subjected to a magnetic field with 10^o to 15^o out-of-plane tilt from the sample plane and the in-plane component of this field is referred to as the bias magnetic field (H). This introduces a significant demagnetizing field which is modulated by the pump pulse to launch the precession in the sample. The probe was placed carefully at the centre of the pump spot so that there is no additional effect on the Gilbert damping due to the dissipation of energy of uniform precessional mode flowing out of the probed area. All the measurements are performed in ambient conditions.

4.3 Results and discussions

Static characterizations: Figure 4.1(a) shows the X-ray diffraction patterns of Sub/Ta (*t*)/CoFeB (3 nm)/SiO_2 (2 nm) heterostructures at the glancing angle of 1^o. The formation of a highly textured β-Ta phase is established from the presence of very intense (002) peaks of the β-Ta phase at a 2θ value of ~ 33.5^o. We have not observed any signs of the α-Ta phase, which generally appears at the 2θ value of ~ 38.5^o, in our experimental thickness regime. The d-value obtained from the β-Ta peak at 33.5^o

corresponds to ~ 2.6 Å, which ensures the growth of the Ta-thin films in the desired tetragonal β-phase having a preferential orientation of (002) planes [30].

Further, we measured the thickness-dependent resistivity of the Ta layer from the heterostructures. Charge current was applied along the length of the sample and the experiment was performed in constant current mode. The sheet resistance (R_s) of the film stack as a function of Ta thickness is plotted in Figure 4.1 (b). The result has been fitted using the parallel resistors model. We have obtained a stable phase of β-Ta over the whole experimental thickness regime with constant resistivity (ρ_{Ta}) of 248 ± 24 μΩ.cm and for CoFeB this (ρ_{CoFeB}) is found to be 139 ± 13 μΩ.cm which are very close to the values reported in the literature [31].

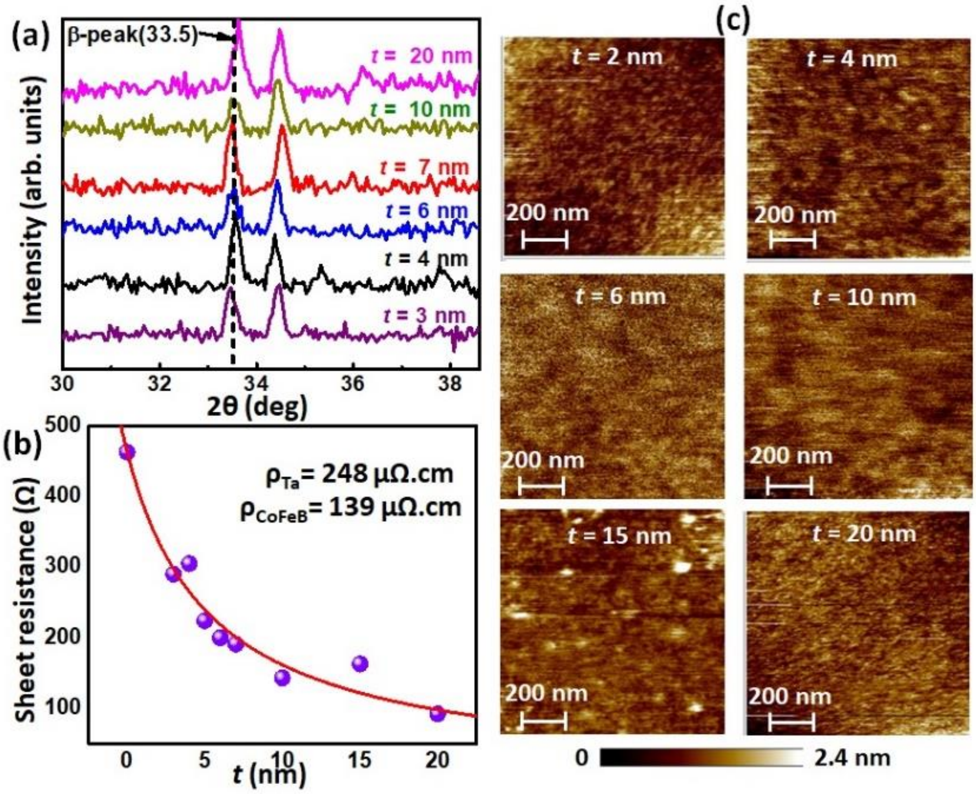

Figure 4.1: (a) X-ray diffraction patterns measured at 1° grazing angle incidence for different Ta thicknesses. Peaks corresponding to the β phase of Ta are shown with a dashed line. (b) Variation of sheet resistance with Ta thickness. The solid line is fit. (c) Measurement of topographical properties of samples using AFM.

Table 4.1: The average topographical roughness values obtained using atomic force microscopy for Sub/Ta (*t*)/ CoFeB (3 nm)/SiO_2 (2 nm) samples with different Ta thicknesses.

t (nm)	0	2	4	6	10	15	20
Roughness (nm)	0.16	0.15	0.19	0.13	0.16	0.25	0.17

The AFM images for Sub/Ta (t)/CoFeB (3 nm)/SiO$_2$ (2 nm) samples are investigated to study surface topography as shown in Figure 4.1(c). From these images, we obtained the average topographical roughness for the samples with t = 0, 2, 4, 6, 10, 15 and 20 nm as listed in Table 4.1. The roughness values vary a little when measured at various regions of space of the same sample. Overall, the topographical roughness is found to be significantly small for all the samples. Due to the small thicknesses of the thin film heterostructures, presumably, the interfacial roughness will clearly show its imprint on the topographical roughness. We thus conclude that the average interfacial roughness, if any, present in these heterostructures is very small and is similar in all samples.

The principle behind the determination of spin pumping: Along with the local damping which arises due to energy dissipation within the electron and phonon of ferromagnet itself, nonlocal damping in the NM/FM system when magnetic energy is dissipated from FM to the adjacent NM layer can be present. The optically-induced magnetization precession in the FM layer causes the generation of spin current at the NM/FM interface. These spins carry angular momentum to the adjacent NM layer which acts as a spin sink by absorbing the spin current after traversing the spin diffusion length and leads to an enhancement of the Gilbert damping parameter. This phenomenon is known as spin pumping and can be described by the modified Landau-Lifshitz-Gilbert (LLG) equation as given below:

$$\frac{dM}{dt} = -\gamma\,(M \times H_{\mathrm{eff}}) + \alpha_0\,\left(M \times \frac{dM}{dt}\right) + \frac{\gamma}{\mathrm{V}M_s} I_s \tag{4.1}$$

where γ is the gyromagnetic ratio, H_{eff} is the effective magnetic field, α_0 is the intrinsic Gilbert damping parameter, V is volume and M_s is saturation magnetization of the ferromagnet. The total spin current I_s consists of the DC current I_s^0 which does not exist in our case, current due to pumped spins from the ferromagnet I_s^{pump} and current returned to the FM (backflow current) I_s^{back}.

$$I_s = I_s^0 + I_s^{\mathrm{pump}} + I_s^{\mathrm{back}} \tag{4.2}$$

Spins that are pumped out can either accumulate at the interface or relax through spin-flip scattering causing a flow of angular momentum from the FM to the NM layer through the NM/FM interface. The NM layer does not always act as a perfect spin reservoir due to the spin accumulation effect which mainly causes I_s^{back}. This backflow of spin current towards FM solely depends on the spin diffusion length of the adjacent NM layer. On the other hand, the flow of spin angular momentum through the NM/FM interface is quantified by spin-mixing conductance.

The theoretical framework described by Y. Tserkovnyak *et al.* [12,13] includes a backflow factor of spin angular momentum during relaxation of injected spins into the NM layers, which is given as:

$$\beta = \left(2\pi G_{\uparrow\downarrow}\sqrt{\frac{\varepsilon}{3}}\tanh\left(\frac{t}{\lambda}\right)\right)^{-1} \tag{4.3}$$

where ε is the ratio of the spin-conserved to spin-flip scattering times (spin-flip probability), which is material dependent and can be given as:

$$\varepsilon = (\lambda_{\mathrm{el}}/\lambda)^2/3 \tag{4.4}$$

where λ_{el} and λ are the mean free path and spin diffusion length, respectively.

Nonlocal damping at NM/FM interface directly depends on spin-mixing conductance. It can be of two types: (a) intrinsic spin-mixing conductance ($G_{\uparrow\downarrow}$), which does not consider the backflow factor and (b) effective spin-mixing conductance (G_{eff}), which considers the backflow of spin angular momentum [32]. $G_{\uparrow\downarrow}$ describes the electronic conductance property of channels in the interface between NM and FM, where NM thickness is kept much longer than its spin diffusion length so that no backflow can occur. Its dependence on the Gilbert damping parameter and NM thickness is given by [33,34],

$$G_{\mathrm{eff}} = G_{\uparrow\downarrow}\left(1 - e^{-\frac{2t}{\lambda}}\right) = \frac{4\pi d M_{eff}}{g\mu_B}\,(\alpha_{\mathrm{eff}} - \alpha_0) \tag{4.5}$$

$$\Delta\alpha = \alpha_{\mathrm{eff}} - \alpha_0 = \frac{G_{\uparrow\downarrow}\left(1-e^{-\frac{2t}{\lambda}}\right)g\mu_B}{4\pi d M_{eff}} \tag{4.6}$$

Here, the factor of 2 in the exponential term signifies the distance traversed by the spins inside the NM layer due to reflection from the NM/air interface, which is assumed to be the perfect reflector.

The spin transmission probability of the NM/FM interface may be determined from the spin backflow, which is linked to G_{eff}. Therefore, the reduction of spin transmission probability can be explained by intermixing and disorder at the interface. The interfacial spin transparency (T) between two layers takes into account all such effects that lead to the electrons being reflected instead of being transmitted at the NM/FM interface and controls the flow of spin angular momentum across the interface. Furthermore, it is known that T depends on both intrinsic and extrinsic interfacial factors, such as band-structure mismatch, Fermi velocity, interface imperfections, etc. [21,35]. To find the transparency of channels we followed a spin Hall magnetoresistance model [29] where the spin current density that diffuses into the NM layer is smaller than the actual spin current density generated via the spin pumping in the FM layer. This can be linked to the effective spin-mixing conductance (G_{eff}) by the following relation [21]:

$$T = \frac{G_{\mathrm{eff}}\tanh\left(\frac{t}{2\lambda}\right)}{G_{\mathrm{eff}}\coth\left(\frac{t}{\lambda}\right) + \frac{h}{2\lambda e^2 \rho}} \tag{4.7}$$

where ρ is the resistivity and λ is the spin diffusion length of the NM layer.

All-optical investigation of magnetization dynamics: Figure 4.2(a) shows a schematic of the spin pumping mechanism along with the experimental geometry. Figure 4.2 (b) shows the time-resolved Kerr rotation data for the Sub/CoFeB (3 nm)/SiO$_2$ (2 nm) sample at H = 1.73 kOe which consists of three different temporal regimes.

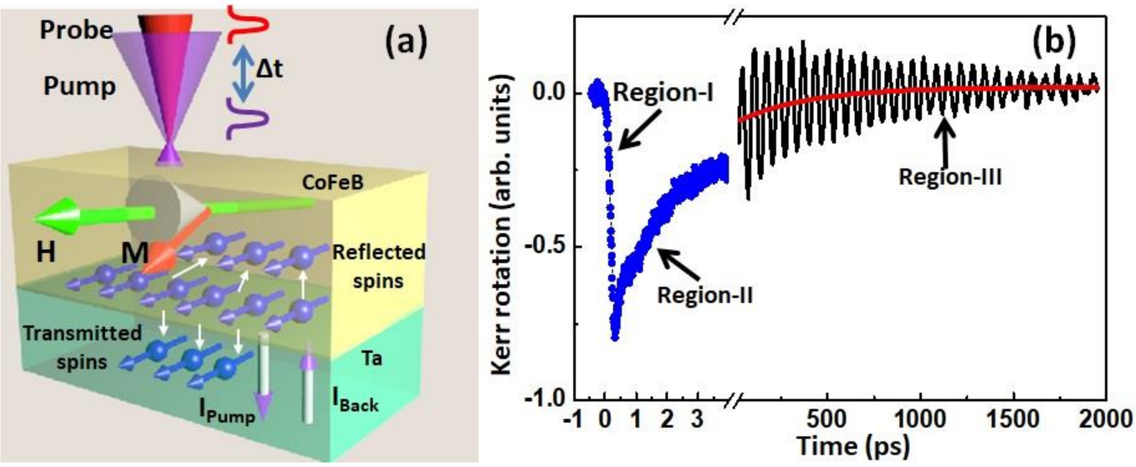

Figure 4.2: (a) Experimental geometry, (b) Time-resolved Kerr rotation data for Sub/CoFeB (3 nm)/SiO$_2$ (2 nm) sample at applied field, H = 1.73 kOe is shown. The three different temporal regimes are indicated in the graph.

When a femtosecond laser excites the sample, a sharp drop in the magnetization is observed immediately after zero delay which corresponds to ultrafast demagnetization (regime I). Regime II corresponds to the fast remagnetization due to the spin-lattice relaxation and regime III consists of slower relaxation along with magnetization precession. The slower relaxation is due to heat diffusion from the lattice to the surrounding. We are mainly interested in the extraction of decay time from the damped sinusoidal oscillation about a bias magnetic field and its modulation due to the spin pumping effect. The red line in Figure 4.2(b) corresponds to the biexponential background present in the precessional data in regime III. We subtract this background from the raw data and fit the resulting data using the damped harmonic function:

$$M(t) = M(0)e^{-\left(\frac{t}{\tau}\right)}\sin(\omega t + \varphi) \tag{4.8}$$

where τ is the decay time, φ is the initial phase and $\omega = 2\pi f$, f being the precessional frequency. From the fit, we estimate the effective damping, α_{eff}, using the expression:

$$\alpha_{eff} = \frac{1}{\gamma\tau(H+2\pi M_{\mathrm{eff}})} \tag{4.9}$$

where H is the applied bias magnetic field and M_{eff} is the effective magnetization. The bias field dependence of precessional frequency can be fitted using the Kittel formula mentioned below:

$$f = \frac{\gamma}{2\pi}\left(H(H + 4\pi M_{\mathrm{eff}})\right)^{1/2} \tag{4.10}$$

where $\gamma = g\mu_B/\hbar$ is the gyromagnetic ratio and g is the Lande g-factor. From the fit, M_{eff} and g are determined as fitting parameters. For these film stacks, we obtained effective magnetization, M_{eff} ~ 1200 ± 100 emu/cc and g = 2.0 ± 0.1. The comparison between M_{eff} obtained from the dynamic measurement and M_s from the VSM measurement proved that for almost all the film stacks investigated here, M_{eff} is close to the saturation magnetization M_s, which indicates that the interface anisotropy is small in these heterostructures.

Modulation of Gilbert damping parameter due to spin pumping: In Figure 4.3(a) we have shown background subtracted time-resolved data for Sub/Ta (t)/CoFeB (3 nm)/SiO_2 (2 nm), where we have varied t from 0 to 20 nm. The intrinsic Gilbert damping (α_0) of 3 nm thick CoFeB layer is found to be 0.006 ± 0.0005 for the high field regime, where the magnetization remains saturated. In presence of Ta underlayer, effective damping (α_{eff}) is found to be increased nonmonotonically in the lower thickness regime whereas it gets saturated at the higher thickness of Ta.

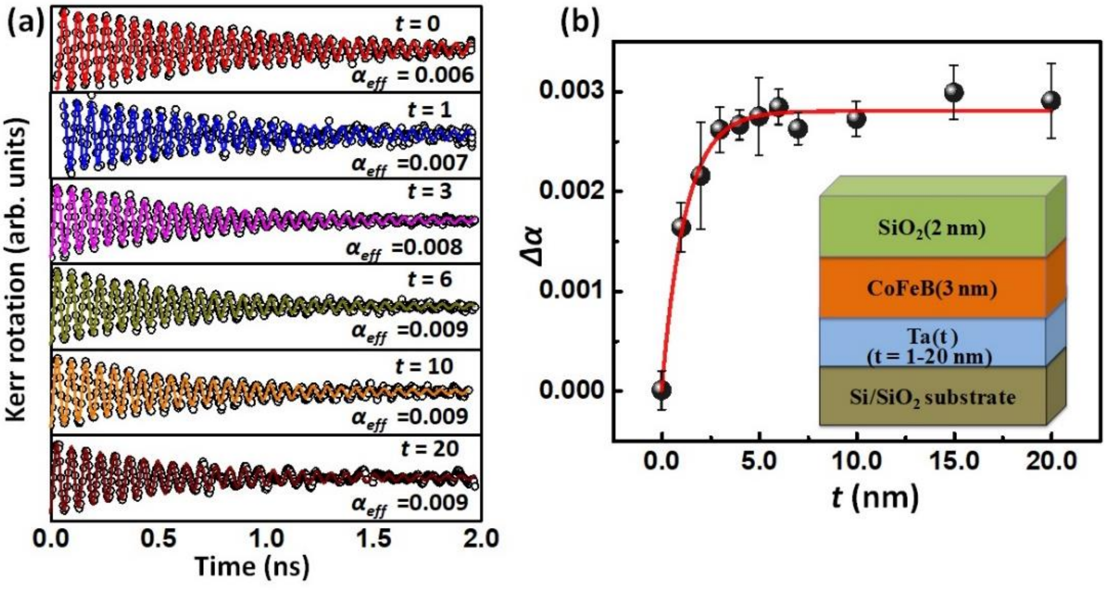

Figure 4.3: (a) Time-resolved Kerr rotation data for t = 0, 1, 3, 6, 10 and 20 nm at 1.73 kOe field. (b) Modulation of damping with Ta thickness, fitted with a spin pumping model to extract spin diffusion length and intrinsic spin-mixing conductance.

As shown in Figure 4.3(b), the modulation of damping in the FM layer is found to be more than 40% due to the spin pumping in these heterostructures. The α_{eff} shows exponential dependence with Ta thickness with an asymptotic value of 0.009 ± 0.0005 for $t \to \infty$. Thus, we have fitted our results with equation (4.6), where we determined the intrinsic spin-mixing conductance ($G_{\uparrow\downarrow}$) = (7.22 ± 0.05) × 10^{14} cm^{-2} [36,37]. Subsequently, we obtained the spin diffusion length (λ) of Ta to be 2.44 ± 0.16 nm as a fitting parameter, which is very close to the literature value [23]. Using values for λ_{el} (about 0.5 nm for Ta) [38] and λ derived for these heterostructures we have determined the spin-flip probability, $\varepsilon = 1.4 \times 10^{-2}$ from equation (4.4). For a nonmagnetic metal to be an efficient spin sink, the requirement is $\varepsilon \geq 1.0 \times 10^{-2}$ [15]. So we can infer that the model describing the spin pumping effect is applicable for our experimental film stacks and the β-Ta layer acts as an efficient spin sink here. The backflow factor β is mainly element-dependent and can be extracted from equation (4.3). We have quantified the modulation of backflow factor ($\Delta\beta$) to be 61% within our experimental thickness regime of $1 \text{ nm} \leq t \leq 20 \text{ nm}$. The spin transmission probability of the NM/FM interface can be determined from the spin backflow, which is linked to G_{eff}.

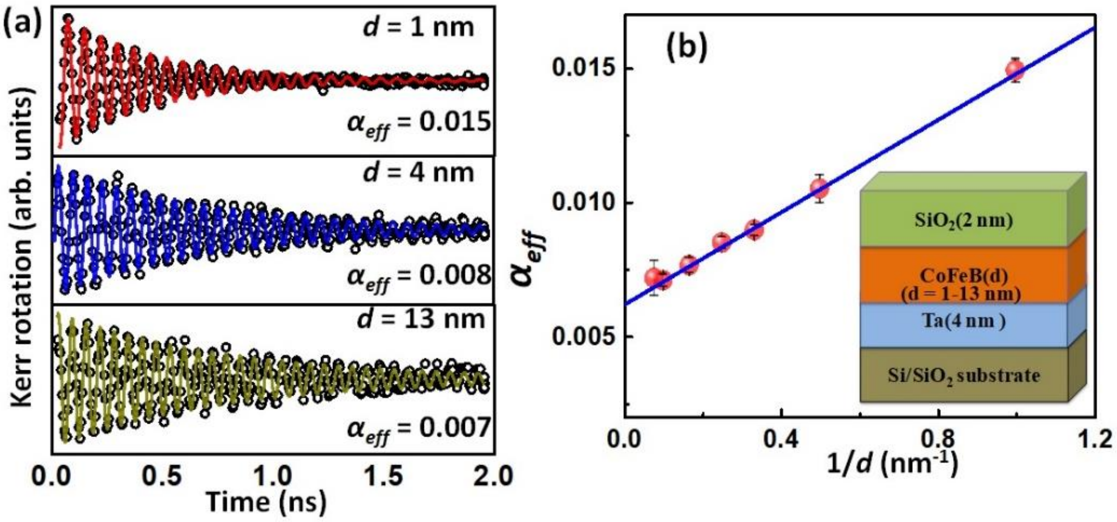

Figure 4.4: (a) Time-resolved Kerr rotation data for d = 1, 4 and 13 nm. (b) Variation of damping with FM layer thickness linearly fitted by using a spin pumping formalism to extract intrinsic Gilbert damping parameter and effective spin-mixing conductance.

To experimentally determine the value of G_{eff}, we have investigated precessional dynamics for Sub/Ta (4 nm)/CoFeB (d)/SiO_2 (2 nm) samples by varying FM layer thickness as, $1 \text{ nm} \leq d \leq 13 \text{ nm}$ at H = 1.73 kOe (Figure 4.4(a)). The α_{eff} is observed to vary linearly with the inverse of ferromagnetic layer thickness and saturates for $d > 10$ nm, while the thickness of the NM layer is fixed at 4 nm (Figure 4.4(b)). This is another confirmation that β-Ta is a good spin sink material resulting in a strong spin pumping effect [15]. After fitting those data with equation (4.5), the effective spin-mixing conductance of the Ta/CoFeB interface is found to be (6.92 ± 0.04) × 10^{14} cm^{-2}. For energy-efficient applications of spin current in multilayered devices, large interface transparency (T) is required and this primarily becomes associated with G_{eff} (t) [37]. After determining the resistivity of these heterostructures and

G_{eff} experimentally, we have found the value of T as 0.50 ± 0.03 by using equation (4.7), which is comparable with Pt/FM interfaces [38]. To the best of our knowledge, this is the first measurement of interfacial spin transparency for β-Ta/CoFeB bilayer and this shows the formation of a moderately transparent interface.

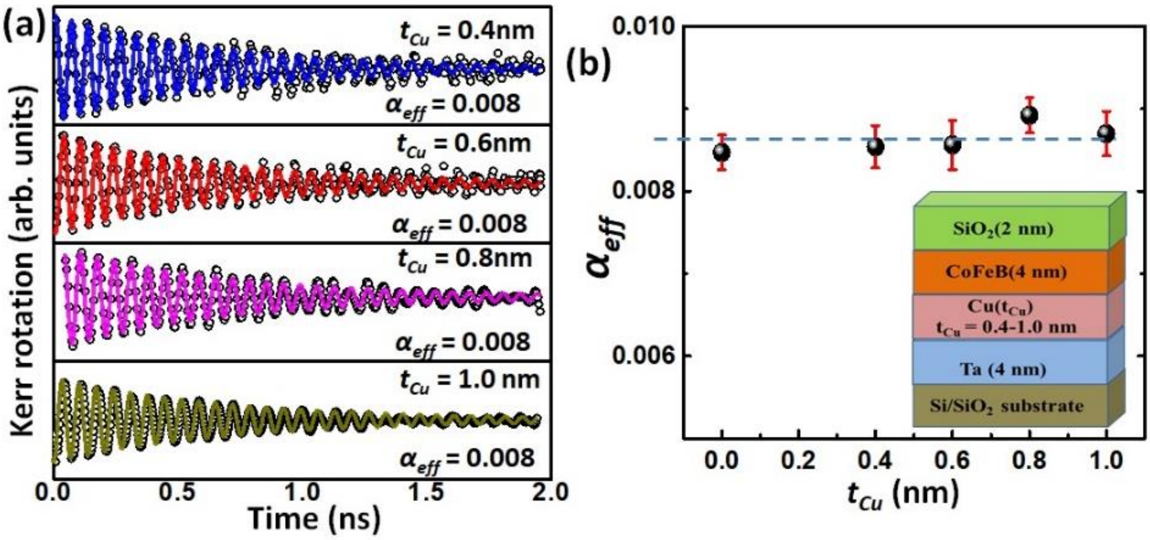

Figure 4.5: (a) Time-resolved Kerr rotation data for t_{Cu} = 0.4, 0.6 0.8 and 1.0 nm. (b) Variation of damping parameter with spacer layer thickness is shown. The dotted line is a guide to the eye.

There is a probability in these heterostructures to have some loss of spin angular momentum due to interfacial depolarization, known as spin memory loss, where spin angular momentum carried by the spin current is not transferred to NM, but instead transferred to the lattice through interfacial spin-orbit scattering [22]. So, the total transfer of spin current to the NM will be determined by a combined effect of interfacial spin transparency and spin memory loss. It is the loss of spin information at the interface due to spin-flip scattering. In this case loss of spin polarization occurs due to interfacial spin-orbit scattering. Whereas, interfacial spin transparency is an electronic property of a material interface and transmission of conduction electrons depends upon the electronic band matching of two materials on either side of the interface. There can also be other interfacial effects, such as Rashba effect, two-magnon scattering, interfacial band hybridization and defects, which may affect the net transfer of spin current to the NM. To understand the contributions of the above effects in addition to the spin pumping effect, we have introduced a copper spacer layer of different thicknesses between the Ta and CoFeB layers. Copper (Cu) has a very small spin-orbit coupling and spin-flip scattering parameter, so it shows a very high spin diffusion length [28]. Thus, a thin copper spacer layer is not expected to affect the damping of the FM layer due to the spin pumping effect but can change or eliminate other interface effects. Consequently, if other interface effects are significantly present in our samples, the introduction of the copper spacer layer would significantly vary the damping with the variation of copper spacer layer thickness (t_{Cu}). The time-resolved Kerr rotation data for the Sub/Ta (4 nm)/Cu (t_{Cu})/CoFeB (4 nm)/SiO_2 (2 nm) heterostructures with 0.4, 0.6, 0.8, 1.0 nm-thick copper layers are presented in Figure 4.5(a) at H = 1.73 kOe and Figure 4.5(b) shows the plot of damping as a function of copper layer thickness. Almost no modulation of damping with the thickness of the copper spacer layer is observed, which confirms that Cu/CoFeB interface is nearly transparent [39] and other possible interface effects are negligible. Thus, the transparency of Ta/CoFeB is similar to that of Ta/Cu/CoFeB due to similar electronic structures. Thus, we have been able to measure the spin pumping effect and interfacial spin transparency by the all-optical TR-MOKE technique in a new thin film heterostructure, which is very important for future spintronic applications.

4.4 Conclusions

We have investigated spin pumping phenomena in β-Ta/CoFeB thin films from the modulation of Gilbert damping by using an all-optical TR-MOKE magnetometer. For a stable phase of β-Ta over the thickness range between 0 and 20 nm, we have extracted the spin diffusion length as 2.44 ± 0.16 nm and intrinsic spin-mixing conductance as $(7.22 \pm 0.05) \times 10^{14}$ cm^{-2} from the variation of damping as a function of Ta thickness. By considering the backflow factor in our theoretical model, we have extracted the effective spin-mixing conductance at the Ta/CoFeB interface as $(6.92 \pm 0.04) \times 10^{14}$ cm^{-2} from the variation of damping as a function of CoFeB thickness. By fitting our data with the spin Hall magnetoresistance model, we have obtained the interfacial spin transparency of Ta/CoFeB as 0.50 ± 0.03 for Ta thickness of 4 nm which shows the Ta/CoFeB interface is comparable with various studied heavy metal/ferromagnet interface such as Pt/FM. To understand the effects of other possible interface effects, which may affect the Gilbert damping apart from the spin pumping effect, we have introduced a thin copper spacer layer of varying thickness and found negligible modulation of damping. This is due to the similar spin conductivity of copper and Ta and confirms the absence of other interface effects in these structures. The low intrinsic Gilbert damping parameter, high effective spin-mixing conductance with moderately high transparency of the β-Ta/CoFeB bilayer system make it a key material for spin transfer torque magnetization switching and spin logic devices.

References

1. I. Zutic, J. Fabian and S. D. Sharma, Rev. Mod. Phys. **76**, 323-401 (2004).
2. S. A.Wolf , D. D. Awschalom, R. A. Buhrman, J. M. Daughton, S. von Molnar, M. L. Roukes, A. Y. Chtchelkanova and D. M. Treger, Science **294**, 1488-1495 (2001).
3. A. Hoffmann and S. D. Bader, Phys. Rev. Appl. **4**, 047001 (2015).

4. S. D. Bader and S. S. P. Parkin, Annu. Rev. Cond. Matter Phys. **1**, 71 (2010).
5. A. Hoffmann, Phys. Status Sol. C **4**, 4236 (2007).
6. P. Sharma, Science **307**, 531-533 (2005).
7. C. Chappert and J. V. Kim, Nat. Phys. **4**, 837-838 (2008).
8. L. Liu, C.-F. Pai, Y. Li, H. W. Tseng, D. C. Ralph and R. A. Buhrman, Science **336**, 555-558 (2012).
9. J. Sinova, S. O. Valenzuela, J. Wunderlich, C. H. Back and T. Jungwirth, Rev. Mod. Phys. **87,** 1213-1259 (2015).
10. J. C. Rojas Sanchez, L. Vila1, G. Desfonds, S. Gambarelli, J. P. Attane, J. M. De Teresa, C. Magen and A. Fert, Nat. Commun. **4**, 2944 (2013).
11. Y. A. Bychkov and E. I. Rashba, JETP Lett. **39**, 78–81 (1984).
12. Y. Tserkovnyak, A. Brataas and G. E. W. Bauer, Phys. Rev. Lett. **88**, 117601 (2002).
13. Y. Tserkovnyak, A. Brataas and G. E. W. Bauer, Phys. Rev. B **66**, 224403 (2002).
14. Y. Fukuma, L. Wang, H. Idzuchi, S. Takahashi, S. Maekawa and Y. Otani, Nat. Mater. **10,** 527-531 (2011).
15. V. E. Demidov, S. Urazhdin, R. Liu, B. Divinskiy, A. Telegin and S. O. Demokritov, Nat. Commun. **7,** 10446 (2016).
16. G. E. W. Bauer, E. Saitoh and B. J. van Wees, Nat. Mater. **11**, 391–399 (2012).
17. W. Lin, M. Hehn, L. Chaput, B. Negulescu, S. Andrieu, F. Montaigne and S. Mangin, Nat. Commun. **3,** 744 (2012).
18. A. Soumyanarayanan, N. Reyren, A. Fert and C. Panagopoulos, Nature **539**, 509–517 (2016).
19. K. Uchida, S. Takahashi, K. Harii, J. Ieda, W. Koshibae, K. Ando, S. Maekawa and E. Saitoh, Nature **455**, 778-781 (2008).
20. P. Sheng, Y. Sakuraba, Y. Lau, S. Takahashi, S. Mitani and M. Hayashi, Sci. Adv. **3**, e1701503 (2017).
21. W. F. Zhang, W. Han, X. Jiang, S. H. Yang and S. S. P. Parkin, Nat. Phys. **11**, 496-502 (2015).
22. A. Brataas, Y. V. Nazarov and G. E. W. Bauer, Phys. Rev. Lett. **84**, 2481-2484 (2000).
23. S. Akansel, A. Kumar, N. Behera, S. Husain, R. Brucas, S. Chaudhary and P. Svedlindh, Phys. Rev. B **97**, 134421 (2018).
24. J.C. Rojas-Sánchez, N. Reyren, P. Laczkowski, W. Savero, J.-P. Attané, C. ranlot, M. Jamet, J.-M. George, L. Vila and H. Jaffrès, Phys. Rev. Lett. **112**, 106602 (2014).
25. M. J. Hurben and C E Patton, J. Appl. Phys. **83**, 4344 (1998).
26. N. Nakajima, T. Koide, T. Shidara, H. Miyauchi, H. Fukutani, A. Fujimori, K. Iio, T. Katayama, M. Nývlt and Y. Suzuki, Phys. Rev. Lett. **81**, 5229 (1998).
27. A. Barman and J. Sinha, Spin dynamics and damping in ferromagnetic thin films and nanostructures. (Springer: Switzerland, 2018)
28. J. Bass and W. P. Pratt Jr, J. Phys. Condens. Matter. **19**, 183201 (2007).
29. Y. Chen, S. Takahashi, H. Nakayama, M. Althammer, S. Goennenwein, E. Saitoh and G. Bauer, Phys. Rev. B **87**, 144411 (2013).
30. J. J. Colin, G. Abadias, A. Michel and C. Jaouen, Acta Mater. **126**, 481-493 (2017).
31. S. Mondal, S. Choudhury, N. Jha, A. Ganguly, J. Sinha and A. Barman, Phys. Rev. B **96**, 054414 (2017).
32. J. Shaw, H. Nembach and T. J. Silva, Phys. Rev. B **85**, 054412 (2012).
33. H. Jiao and G. E. W. Bauer, Phys. Rev. Lett. **110**, 217602 (2013).

34. O. Mosendz, V. Vlaminck, J. E. Pearson, F. Y. Fradin, G. E. W. Bauer, S. D. Bader and A. Hoffmann, Phys. Rev. B **82**, 214403 (2010).
35. J. Aarts, J. M. E. Geers, E. Bruck, A. A. Golubov and R. Coehoorn, Phys. Rev. B **56**, 2779 (1997).
36. G. Allen, S. Manipatruni, D. E. Nikonov, M. Doczy and I. A. Young, Phys. Rev. B **91**, 144412 (2015).
37. A. Kumar, S. Akansel, H. Stopfel, M. Fazlali, J. Akerman, R. Brucas and P. Svedlindh, Phys. Rev. B **95**, 064406 (2017).
38. C.F Pai, Y. Ou, L. H. V. Leao, D. Ralph and R. A. Buhrman, Phys. Rev. B **92**, 064426 (2015).
39. P. M. Levy and I. Mertig, Spin Dependent Transport in Magnetic Nanostructures (Taylor & Francis, 2002).

Chapter-5

Structural phase-dependent giant interfacial spin transparency in W/CoFeB thin film heterostructure

5.1 Introduction

The rapid emergence of spintronics has promised a new paradigm of spin-based electronics either associated with the charge or by itself [1-3]. This has potential advantages of non-volatility, decreased electrical power consumption, enhanced data processing speed and increased integration densities as opposed to its semiconductor counterpart [4]. A major objective of modern spintronics is to exploit pure spin current, comprising the flow of spins without any net flow of charge current [5, 6]. This has the inherent benefit of reduced Joule heating and Oersted fields together with the ability to manipulate magnetization. Three major aspects of spin current are its generation, transport and functionalization. Some popular mechanisms for the generation of pure spin current are the spin Hall effect [7, 8], Rashba-Edelstein effect [9, 10], spin pumping [11-13], current injection in a lateral spin valve using a non-local geometry [14, 15] and spin caloric effects [16, 17]. Among these, spin pumping is an efficient and extensively used method of spin current injection from FM to NM. Here, the precessing spins in FM cause spin angular momentum transfer to the conduction electrons of the neighbouring NM layer in an NM/FM heterostructure, which eventually gets dissipated by spin-flip scattering. The spin pumping efficiency is parametrized by spin-mixing conductance of the NM/FM interface and spin diffusion length of the NM layer. The spin current dissipation into the NM layer results in a reduction of spin angular momentum in the FM layer leading to an enhanced effective Gilbert damping parameter (α_{eff}). Thus, spin pumping controls the magnetization dynamics in NM/FM heterostructures, which is crucial for deciding the efficiency of switching in spin-torque-based spintronic devices. The enhancement in α_{eff} is greater in heavy metals having large SOC due to stronger spin-lattice interaction. Intense research in the field of spin-orbitronics has unfolded that interface-dependent spin transport is highly influenced by spin transparency, which essentially decides the amount of spin current passed through an interface [18, 19].

The highly resistive β-W, which shows a distorted tetragonal phase generally known as the A15 structure, is well known for exhibiting a large spin Hall angle (SHA) (up to ~ 0.50) [20, 21] in comparison with other heavy metals like Pt (~ 0.08) [22] and β-Ta (~ 0.12) [7]. Besides, in W/FM heterostructures, highly stable perpendicular magnetic anisotropy [23], large spin Hall magnetoresistance [24] and interfacial Dzyaloshinskii-Moriya interaction [25] have been observed.

Another important feature related to W is its thickness-dependent phase transition in the sub-10 nm-thickness regime [26, 27]. Generally, sputter-deposited W thin films having thicknesses well below 10 nm are found in the β phase with high resistivity, while the films having thicknesses above 10 nm are predominantly in the low resistive α phase (bcc structure). A small to moderate SHA has been reported for the α-W and mixed (α+β)-W (<0.2) [26]. As SHA is correlated with effective spin-mixing conductance (G_{eff}), one would expect that interfacial spin transparency (T), which is also a function of G_{eff}, should depend on the phase of W thin films. Furthermore, the magnitude of spin-orbit torque (SOT) depends on spin current transmission efficiency (i.e., T) across the interface of NM/FM heterostructures. It is worth mentioning that due to its high SOC strength, W is an acceptable spin-sink material and also cost-effective as compared to the widely used NM like Pt. Whereas, CoFeB due to its notable properties like large tunnel magnetoresistance, high spin polarization and low intrinsic Gilbert damping, is used as FM electrode in magnetic tunnel junctions. The occurrence of boron at the NM/CoFeB interface makes this system interesting as some recent reports indicate that a small amount of boron helps in obtaining a sharp interface and increases the spin polarization, although an excess of it causes contamination of the interface [28]. To this end, the determination of T of the technologically important W/CoFeB interface and its dependence on the W-crystal phase is extremely important but still absent in the literature.

Besides spin pumping, there are different mechanisms like spin memory loss (SML) [29], Rashba effect [10], two-magnon scattering (TMS) [30] and interfacial band hybridization [31] which may also cause decay of spin angular momentum at NM/FM interface, resulting in an increase of α_{eff} and decrease of the spin transmission probability. However, for improved energy efficiency, the NM/FM interface in such engineered heterostructures must possess a high probability of spin transmission. Consequently, it is imperative to get a deeper insight into all the processes involved to generate and transfer pure spin current for optimizing its efficiency. In this thesis chapter, we have investigated the effects of spin pumping on the damping constant in W/CoFeB bilayer thin films as a function of W thickness using a recently developed all-optical technique, which is free from delicate micro-fabrication and electrical excitation and detection [32]. This is a local and non-invasive method based on TR-MOKE magnetometry. Here, the damping is extracted directly from the time-dependent decaying magnetization precession amplitude, which is free from experimental artefacts stemming from multimodal oscillation, sample inhomogeneity and defects. From the W-thickness dependent damping modulation, we have extracted the intrinsic spin-mixing conductance ($G_{\uparrow\downarrow}$) of the W/CoFeB interface which excludes the spin angular momentum backflow and spin-diffusion length (λ_{sd}) of W. Furthermore, we have modelled the spin transport using both the ballistic transport model [33, 34] and the model based on spin diffusion theory [35, 36]. Subsequently, G_{eff}, which includes the spin angular momentum backflow, is extracted from the CoFeB-thickness dependent damping modulation. By using both the spin Hall magnetoresistance model [37] and a spin transfer torque-based model utilizing the drift-diffusion approximation [38], we have calculated the T of the W/CoFeB interface. The spin Hall magnetoresistance model gives a lower value of T than the drift-diffusion model, but the former is considered more reliable as the latter ignores the spin current backflow. We found a giant value of T exceeding 0.8 in the β phase of W, which exhibits a sharp decrease to about 0.6 in the mixed (α+β) phase using the spin Hall magnetoresistance model. Furthermore, we have investigated the other possible interface-related effects in our W/CoFeB system, by inserting a copper (Cu) spacer layer of varying thickness between the W and CoFeB layers. Insignificant damping modulation with Cu spacer layer thickness affirms the domination of pure spin current stemmed from spin pumping and its subsequent transport in the modulation of damping in our system.

5.2 Experimental details

Thin films of Substrate/W (t)/CoFeB (d)/SiO_2 (2 nm) were grown using RF/DC magnetron sputtering system on Silicon (100) wafers having 285-nm-thick SiO_2 coating. We varied the W layer thickness as t = 0, 0.5, 1, 1.5, 2, 3, 4, 5, 8, 10 and 15 nm and CoFeB layer thickness as d = 1, 2, 3, 5 and 10 nm. We deposited the films at 1.8×10^{-7} Torr average base pressure and about 0.5 mTorr argon pressure at a rate of deposition of about 0.2 Å/s. A slow deposition rate was adopted for achieving a uniform thickness of the films even at a very thin regime down to sub-nm. The W and CoFeB layers were deposited using average DC voltages of 320 and 370 V, respectively, while SiO_2 was deposited using average RF power of 55 watts. All the other deposition parameters were thoroughly optimized and maintained at the same level for all the samples. In another sample set, we inserted a thin Cu layer in between the CoFeB and W layers and varied its thickness from 0 nm to 1 nm. The Cu layer was deposited at an argon pressure of 0.5 mTorr and DC voltage of 350 V and a rate of deposition of about 0.2 Å/s.

AFM was exploited to study the surface topography and VSM was utilized to measure the static magnetic characteristics of the samples. By utilizing a conventional four-probe method the resistivity of the W films was extracted and grazing incidence XRD (GI-XRD) was employed to investigate the structural phase of W. The thickness, electron density and interface roughness of different layers in W/CoFeB heterostructures are determined by XRR measurement. To investigate the magnetization dynamics, we used a customized TR-MOKE magnetometer based on a two-colour, collinear optical pump-probe technique. Here, the frequency-doubled 400 nm laser pulse (pulse width >40 fs, repetition rate = 1 kHz) of a femtosecond amplified laser, obtained using a regenerative laser amplifier system (Libra, Coherent) was employed to excite the magnetization dynamics, whereas a small fraction of the fundamental 800 nm laser output (pulse width ~ 40 fs, repetition rate = 1 kHz) was employed to detect the time-varying polar Kerr rotation in the samples. The pump laser beam was slightly defocused to a spot diameter of ~ 300 μm and was obliquely (making ~ 30° angle with the sample normal) incident on the sample. The probe beam having a spot size of ~ 100 μm was normally incident on the sample, keeping a perfect spatial overlap with the pump spot to avoid any spurious effects contributing to Gilbert damping due to the loss of uniform precessional mode energy flowing out of the probed volume. We applied a sufficiently large magnetic field making an angle of ~ 25° with the plane of the sample to saturate its magnetization. Subsequently, we reduced the magnetic field to the desired bias field value (H is the in-plane component of the bias field) to ensure that the magnetization remained saturated along the bias field direction. The magnetization tilt from the sample plane ensured a non-zero demagnetizing field along the pump beam direction, which was further altered by the pump beam to generate precessional dynamics in the sample. The pump was modulated at a frequency of 373 Hz using an optical chopper and the dynamic Kerr rotation angle in the probe beam was picked up in a phase-sensitive manner using a lock-in amplifier. The probe and pump fluences were kept constant at 2 mJ/cm^2 and 10 mJ/cm^2, respectively, during the measurement. All the measurements were conducted under ambient conditions at room temperature. These ensure that no unwanted effects like inter-diffusion of B atoms at the W/CoFeB interface or the variation of the crystal structure of the W layer occur due to a large rise in temperature during the onset of precessional dynamics in the studied samples.

5.3 Results and discussions

Static characterizations: Figure 5.1(a) displays the GI-XRD data from Substrate/W (t)/CoFeB (3 nm)/SiO$_2$ (2 nm) at a glancing angle of 2°. In this plot, the peaks corresponding to α-W and β-W are noted. The highly intense GI-XRD peak at ~44.5° and low-intensity peak at ~64.0° primarily correspond to the β phase (A15 crystal structure) of W (211) and W (222) orientation, respectively. Interestingly, we find these peaks to appear at all thicknesses of W, but when $t > 5$ nm, an additional peak at ~40.1° corresponding to α-W with (110) crystal orientation appears. Consequently, we understand that for $t \leq 5$ nm, W is primarily in the β-phase, while for $t > 5$ nm a fraction of the α phase appears, which we refer to as the mixed (α+β) phase of W. These results are in consonance with existing literature [26,27]. Some reports claimed that this phase-transition thickness can be varied by controlling the conditions of the W thin film deposition [39]. The average lattice constants obtained from the β-W peak at 44.5° and α-W peak at 40.1° correspond to about 4.93 and 3.15 Å, respectively. By using the Debye-Scherrer formula, we find the average crystallite size in the β and the α phases of W to be about 14 and 7 nm, respectively.

The formation of the β-W phase can also be characterized by its high resistivity due to the A15 crystal structure which is related to the strong electron-phonon scattering, whereas the α-W exhibits comparatively lower resistivity due to weak electron-phonon scattering. We measured the change in resistivity of W with its thickness across two different phases, using the four-probe method. The inversed sheet resistance (1/R_s) as a function of W thickness is plotted in Figure 5.1(b). A variation in the slope is observed beyond 5 nm, which indicates a modification in the W resistivity. The data have been fitted using the parallel resistors model [26]. We extracted the resistivity of W (ρ_W) in β and mixed (α+β) phase as about 287 ± 19 and 112 ± 14 μΩ.cm, respectively, while the CoFeB layer resistivity (ρ_{CoFeB}) is found to be 139 ± 16 μΩ.cm. Thus, the resistivity data is consistent with those of the XRD results.

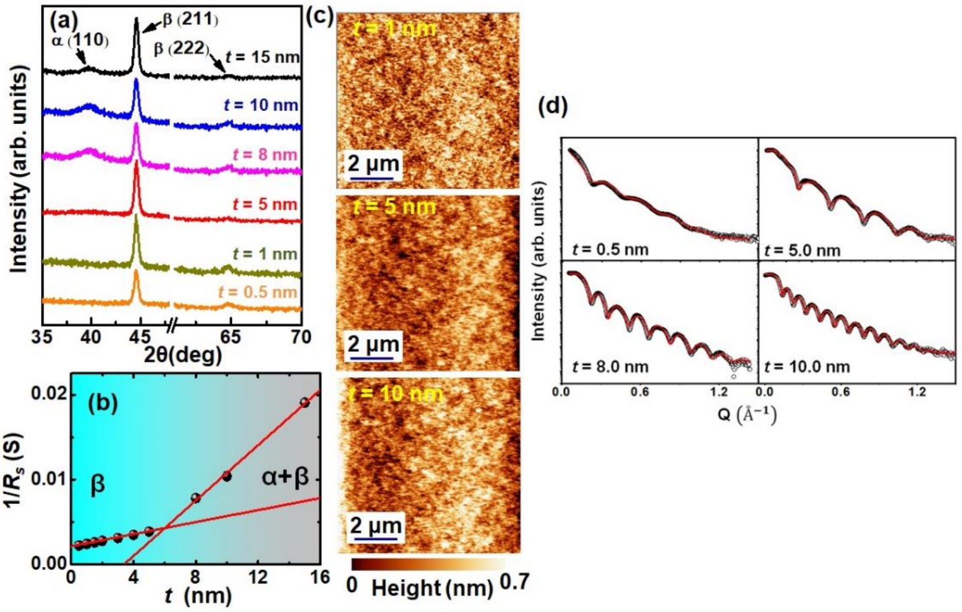

Figure 5.1: (a) X-ray diffraction plots of Sub/W (*t*)/CoFeB/SiO_2 (2 nm) samples measured at 2° grazing incidence angle for different W thickness. (b) Variation of inverse sheet resistance of Sub/W (*t*)/CoFeB/SiO_2 (2 nm) samples with W thickness. (c) AFM images of the Sub/W (*t*)/CoFeB/SiO_2 (2 nm) samples showing the surface topography. (d) XRR spectra (symbols) for Sub/W (*t*)/CoFeB/SiO_2 (2 nm) samples fitted using Parratt's formalism (solid red lines).

The AFM image of Substrate/W (*t*)/CoFeB (3 nm)/SiO_2 (2 nm) (*t* = 1, 5 and 10 nm) samples in Figure 5.1(c) revealed the surface topography. We have applied the WSxM software to analyze the images [40]. The variation in the average surface roughness of the films with W thickness is tabulated in Table

5.1. The variation in topographical roughness is very small when probed at different locations of the same sample. The surface roughness of the samples is found to be small independent of the crystal phase of W. Due to the low thickness values of various layers in the samples, the interface roughness is expected to reflect its nature on the measured surface roughness. We thus understand that the interface roughness is reasonably small and similar in all studied samples. The interfacial roughness values of Substrate/W (t)/CoFeB (3 nm)/SiO_2 (2 nm) thin films have also been extracted from X-ray reflectivity (XRR) measurements (As shown in Figure 5.1(d)). The variation in the W/CoFeB interface roughness of the films with W thickness is tabulated in Table 5.2. The interfacial roughness values obtained from XRR measurements are also small and close to those obtained from AFM measurements.

Table 5.1: The average surface roughness values of Substrate/W (*t*)/CoFeB (3 nm)/SiO_2 (2 nm) samples obtained using AFM.

t (nm)	0	0.5	1.0	1.5	2	3	5	8	10	15
Average Roughness (nm)	0.23	0.21	0.32	0.28	0.25	0.21	0.19	0.29	0.28	0.22

Table 5.2: The parameter values obtained from fitting XRR spectra for Sub/W (*t*)/CoFeB (3 nm)/SiO_2 (2 nm) using Parratt's formalism.

t (nm)	0.5	1	1.5	5	8	10	15
Interface roughness (nm)	0.30	0.22	0.32	0.28	0.2	0.2	0.3

Principles behind the modulation of damping with layer thickness: In an NM/FM bilayer magnetic damping can have various additional contributions, namely two-magnon scattering, eddy current and spin pumping in addition to the intrinsic Gilbert damping. Among these, the spin pumping effect is a non-local effect, in which an external excitation induces magnetization precession in the FM layer. This precession of magnetization causes an accumulation of spins at the NM/FM interface. An adjacent NM layer, which acts as a perfect spin sink, absorbs these accumulated spins by spin-flip scattering, leading to an enhancement of the Gilbert damping parameter of FM. In 2002, Tserkovnyak and Brataas theoretically demonstrated the spin pumping-induced enhancement in Gilbert damping in NM/FM heterostructures using time-dependent adiabatic scattering theory where the time-varying magnetization combined with spin pumping can be expressed by a modified Landau-Lifshitz-Gilbert (LLG) equation as [11-13]:

$$\frac{dm}{dt} = -\gamma\ (m \times H_{eff}) + \alpha_0\ (m \times \frac{dm}{dt}) + \frac{\gamma}{VM_s} I_s \tag{5.1}$$

where γ is the gyromagnetic ratio, I_s is the total spin current, H_{eff} is the effective magnetic field, α_0 is the intrinsic Gilbert damping parameter, V is the volume of ferromagnet and M_s is the saturation magnetization of the ferromagnet. As shown in equation (5.2), I_s generally consists of a direct current contribution I_s^0 which is nonexistent in our case as we do not apply any charge current, I_s^{pump}, i.e. pumped spin current from the FM to NM and I_s^{back}, i.e. a spin current backflow to the FM reflecting from the NM/substrate interface assuming it to be a perfect reflector.

$$I_s = I_s^0 + I_s^{\text{pump}} + I_s^{\text{back}} \tag{5.2}$$

Here, I_s^{back} is controlled by the spin diffusion length of the NM. Its contribution to Gilbert damping for a heavy metals with a small impurity concentration is parametrized by a backflow factor β which can be expressed as [41]:

$$\beta = \left(2\pi G_{\uparrow\downarrow}\sqrt{\frac{\varepsilon}{3}}\tanh\left(\frac{t}{\lambda_{sd}}\right)\right)^{-1} \tag{5.3}$$

where ε is the material-dependent spin-flip probability, whose value is also equal to the ratio between spin-conserved to spin-flip scattering time. It can be expressed as [13, 42]:

$$\varepsilon = (\lambda_{el}/\lambda)^2/3 \tag{5.4}$$

where λ and λ_{el} are the spin diffusion length and electronic mean free path of NM, respectively.

The spin transport through the interface of NM/FM depends directly on the spin-mixing conductance, which has two different types: (a) $G_{\uparrow\downarrow}$, which ignores the contribution of spin angular momentum backflow and (b) G_{eff}, which includes the backflow contribution. Spin-mixing conductance represents the conductance property of spin channels at the NM/FM interface. Also, spin transport across the interface affects the damping parameter giving rise to α_{eff} of the system that can be modelled by both ballistic and diffusive spin transport theory. In the ballistic spin transport model, the α_{eff} is expressed by the following exponential function [33, 34, 41]:

$$G_{eff} = G_{\uparrow\downarrow}\left(1 - e^{-\frac{2t}{\lambda_{sd}}}\right) = \frac{4\pi d M_{eff}}{g\mu_B}\ (\alpha_{eff} - \alpha_0) \tag{5.5}$$

$$\Delta\alpha = \alpha_{eff} - \alpha_0 = \frac{g\mu_B G_{\uparrow\downarrow}\left(1-e^{-\frac{2t}{\lambda_{sd}}}\right)}{4\pi d M_{eff}} \tag{5.6}$$

Here, the exponential term signifies the backflow spin current contribution and a factor of two in the exponent implies the distance travelled by the spins in the NM layer owing to reflection at the interface of NM/substrate.

The ballistic approach does not consider the resistivity of the NM, whereas the NM thickness is considered to be smaller than its mean free path. To account for the charge properties of NM on spin transport, the spin diffusion theory-based model is used to represent α_{eff} (t). According to this model, the damping modulation due to spin pumping can be expressed as [35, 36, 39]:

$$G_{eff} = \frac{G_{\uparrow\downarrow}}{\left(1+\frac{e^2\rho\lambda G_{\uparrow\downarrow}}{h}\coth\left({}^{t}/_{\lambda}\right)\right)} = \frac{4\pi d M_{eff}}{g\mu_B}\ (\alpha_{\mathrm{eff}} - \alpha_0\ ) \tag{5.7}$$

$$\Delta\alpha = \alpha_{\mathrm{eff}} - \alpha_0 = \frac{g\mu_B G_{\uparrow\downarrow}}{4\pi d M_{eff}\left(1+\frac{e^2\rho\lambda G_{\uparrow\downarrow}}{h}\coth\left({}^{t}/_{\lambda}\right)\right)} \tag{5.8}$$

where ρ is the resistivity of the NM layer. Here the term $\frac{e^2\rho\lambda G_{\uparrow\downarrow}}{h}\coth\left({}^{t}/_{\lambda}\right)$ denotes the spin current backflow into the FM layer.

A reduced spin transmission probability in an interface implies a lack of electronic band matching, disorder and intermixing at that interface. The spin transparency, T of an NM/FM interface includes all such effects that hinder the transmission of the electrons. Furthermore, T relies on both the extrinsic as well as the intrinsic properties of the interface, e.g. interface imperfections, mismatch of band-structure, Fermi velocity, etc. [19, 41] According to the spin Hall magnetoresistance model, the spin current that is detected in the NM layer is lower than the actual spin current generated in the FM layer. This model connected T with G_{eff} by the following relation [37, 41]:

$$T = \frac{G_{eff}\ \tanh\left(\frac{t}{2\lambda}\right)}{G_{eff}\ \coth\left(\frac{t}{\lambda}\right)+\frac{h}{2\lambda e^2\rho}} \tag{5.9}$$

The interfacial spin transparency was also calculated by Pai *et al.* in the light of field-like torque and damping-like torque utilizing a drift-diffusion approximation. Here, the effects of spin backflow are neglected as it causes a reduction in the spin-torque efficiencies. Assuming $t \gg \lambda$ and a very high value of d, T can be expressed as [38]:

$$T = \frac{2G_{\uparrow\downarrow}/G_{NM}}{1+2G_{\uparrow\downarrow}/G_{NM}} \tag{5.10}$$

where, $G_{NM} = \frac{h}{\rho\lambda_{sd}e^2}$ represents the spin conductance of the NM layer.

In an NM/FM heterostructure, other than spin pumping, there is a finite probability of having a loss of spin angular momentum due to interface depolarization and surface inhomogeneities, termed as SML and TMS, respectively. In SML, loss of spin angular momentum occurs when the atomic arrangement at the interface acts as an ideal spin sink due to the interfacial spin-orbit scattering or proximity effect causing a loss of spin angular momentum [29]. The TMS arises when a uniform FMR mode is destroyed and degenerate magnons of different wave vectors are created [30]. The momentum non-conservation is accounted for by considering a pseudo-momentum derived from the internal field inhomogeneities or secondary scattering. SML and TMS may result in increment in the Gilbert damping parameter considerably. Recently TMS is found to be the dominant contribution to the Gilbert damping of Pt/FM heterostructures [43]. In the presence of TMS and SML effective Gilbert damping can be approximated as [43]:

$$\alpha_{eff} = \alpha_0 + \alpha_{SP} + \alpha_{SML} + \alpha_{TMS}$$

$$\Delta\alpha = \alpha_{eff} - \alpha_0 = g\mu_B \frac{G_{eff} + G_{SML}}{4\pi d M_{eff}} + \beta_{TMS} d^{-2} \tag{5.11}$$

where G_{SML} is the "effective SML conductance" and β_{TMS} is a "coefficient of TMS" that depends on both interfacial perpendicular magnetic anisotropy field and the magnetic defect density at the FM surfaces.

TR-MOKE measurement of magnetization dynamics: A schematic showing the spin pumping mechanism and the measurement geometry is presented in Figure 5.2(a). A representative time-resolved Kerr rotation data for the Substrate/CoFeB (3 nm)/SiO_2 (2 nm) sample at a bias magnetic field, H = 2.30 kOe is shown in Figure 5.2(b) which comprises of three distinct temporal regimes. The first regime is called ultrafast demagnetization, where a sharp fall in the Kerr rotation (magnetization) of the sample is observed instantly after femtosecond laser excitation. The second regime represents the fast remagnetization where magnetization recovers to equilibrium by spin-lattice interaction. The last regime consists of slower relaxation due to diffusion of heat to the surrounding (substrate) superposed with damped magnetization precession. The red line in Figure 5.2(b) denotes the bi-exponential background that exists in the precessional data. We focus here on the extraction of precessional decay time (τ) from the decaying sinusoidal oscillation around an effective magnetic field direction and its variation with the thickness of FM and NM layers.

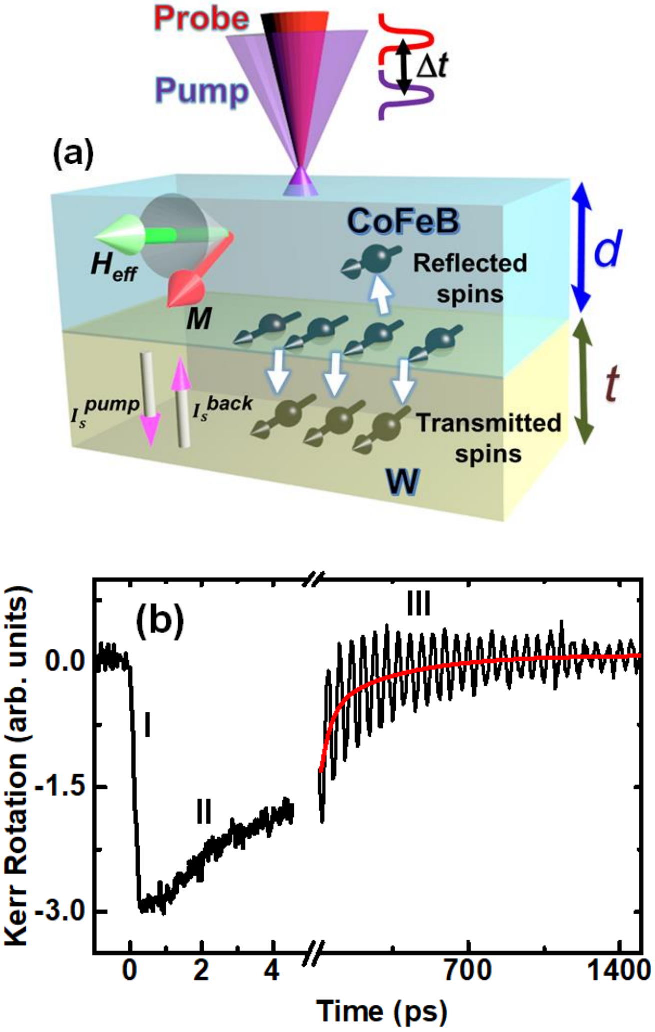

Figure 5.2: (a) An illustration of the experimental geometry and (b) a typical TR-MOKE data from CoFeB (3 nm)/SiO$_2$ (2 nm) heterostructure at an applied bias magnetic field of 2.30 kOe. The three important temporal regions are specified in the figure. The red solid line signifies a biexponential fit to the decaying background of the time-dependent Kerr rotation signal.

We fit the time-resolved precessional data using a damped sinusoidal function given by [44]:

$$\theta_k(t) = Ae^{-\left(\frac{t}{\tau}\right)}\sin(2\pi ft + \varphi) \tag{5.12}$$

where A is the precessional amplitude, τ is the precessional decay time, φ is the initial oscillation phase and f is the frequency of precession. For all these samples we have investigated the precessional dynamics at varying bias magnetic field magnitude (H) using TR-MOKE. Fast Fourier transformation (FFT) of the exponential background subtracted precessional oscillation provides the value of precessional frequency f for different values of H. This f vs. H data is fitted using the Kittel formula given below to find the effective saturation magnetization (M_{eff}):

$$f = \frac{\gamma}{2\pi}\left(H(H + 4\pi M_{\mathrm{eff}})\right)^{1/2} \qquad (5.13)$$

where $\gamma = g\mu_B/\hbar$, g and $\hbar$ are the Landé g-factor and reduced Planck's constant, respectively. M_{eff} and g are determined as the fitting parameters here. We obtained $M_{eff} \approx 1200 \pm 100$ emu/cc and $g = 2.0 \pm 0.1$ for our film stacks from the fit. The values of M_{eff} obtained as above and M_s extracted from VSM measurements are found to be close to each other, which signifies that the interfacial anisotropy is negligible in these thin films [45, 46]. This avoids any significant increase in the Gilbert damping through spin-lattice relaxation. We have observed a smaller value of M_s of the CoFeB films with or without W underlayer than the nominal CoFeB saturation magnetization of 1500 emu/cc [47]. This may indicate the dead layer formation at the interface as reported before [24, 48]. We estimate α_{eff} using the expression [49]:

$$\alpha_{eff} = \frac{1}{\gamma\tau\left(H+2\pi M_{eff}\right)} \qquad (5.14)$$

where $\gamma = 1.76 \times 10^7$ Hz/Oe, τ is the decay time obtained from the fit of the precessional oscillation with equation (5.12) and M_{eff} is the effective saturation magnetization as obtained by fitting the bias field dependent precessional frequency with the Kittel formula of equation (5.13).

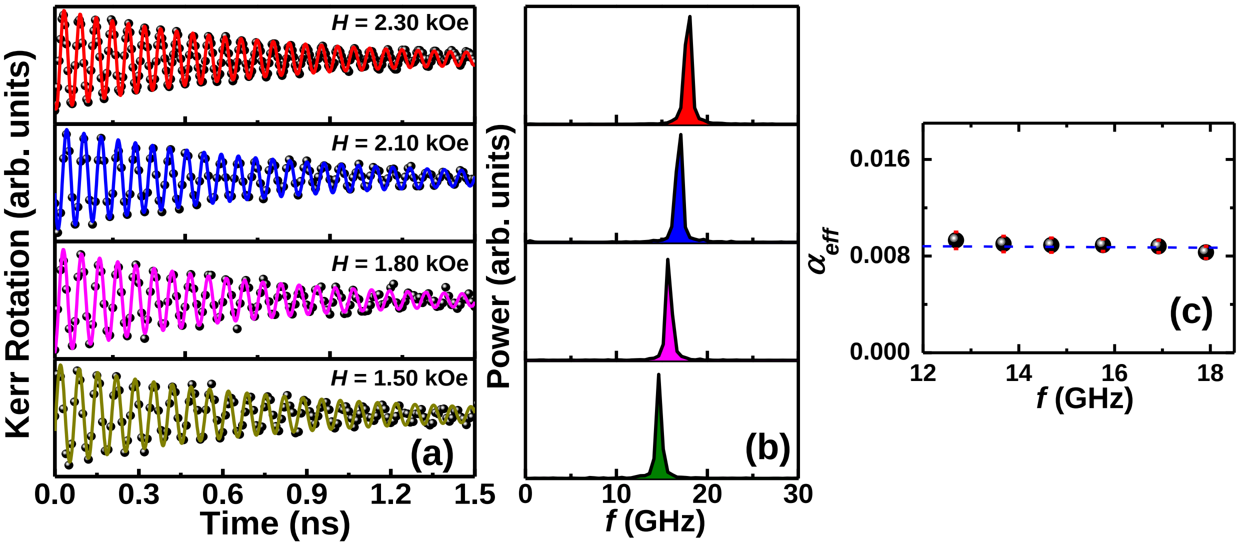

Figure 5.3: (a) Background subtracted time-resolved precessional oscillations at different bias magnetic fields for Sub/W (0.5 nm)/CoFeB (3 nm)/SiO$_2$ (2 nm) sample, where symbols represent the experimental data points and solid lines represent fits using equation (5.12). (b) The FFT power spectra of the time-resolved precessional oscillations showing the precessional frequency. (c) Variation of effective damping with precessional frequency is shown by symbol and the dotted line is a guide to the eye.

We have shown the variation of time-resolved precessional oscillation with the bias magnetic field and the corresponding power spectra obtained from FFT in Figure 5.3(a) and Figure 5.3(b) respectively. The extracted values of α_{eff} are found to be independent of the precession frequency *f* (Shown in Figure 5.3(c)). Recent studies show that in presence of extrinsic damping contributions like TMS, α_{eff} should increase with *f*, while in presence of inhomogeneous anisotropy in the system α_{eff} should decrease with *f* [50]. Thus, frequency-independent α_{eff} rules out any such extrinsic contributions to damping in our system.

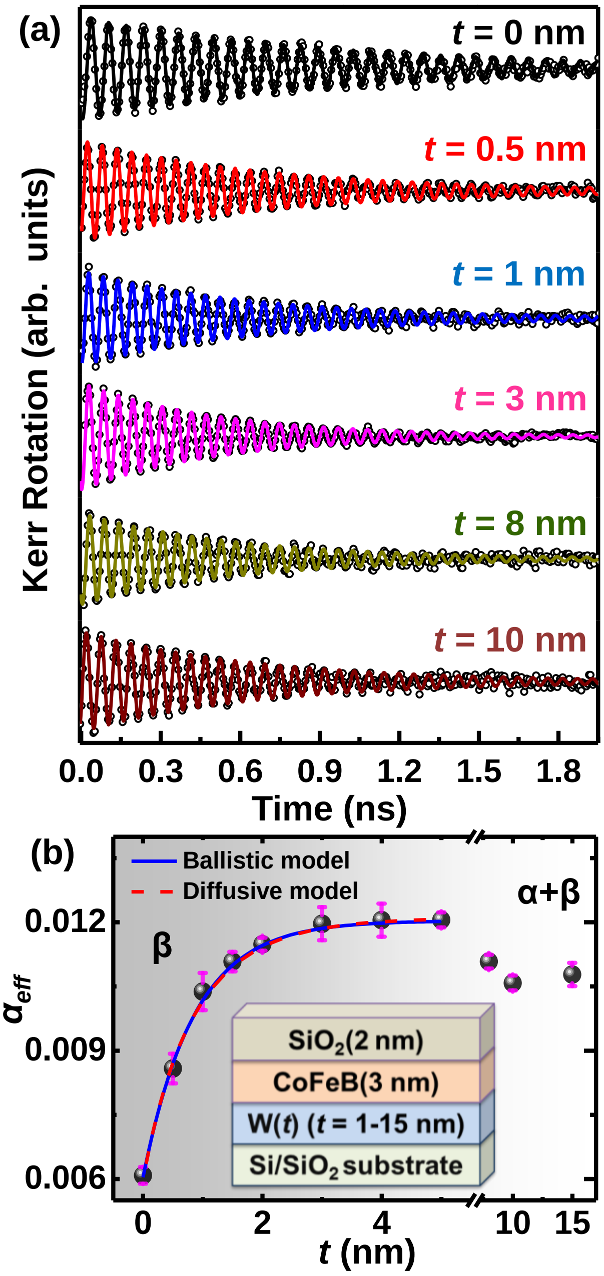

Figure 5.4: (a) Background deducted time-resolved Kerr rotation signal showing precessional oscillation for Substrate/W (*t*)/CoFeB (3 nm)/SiO_2 (2 nm) as a function of W thickness at an applied bias magnetic field of 2.30 kOe. (b) Experimental result of variation damping with *t* (symbol) fitted

with theoretical models (solid and dashed lines) of spin pumping. Two different regions corresponding to the W crystal phase, namely β and (α+β) are shown.

Modulation of the damping parameter: In Figure 5.4(a) we have presented time-resolved precessional dynamics for Substrate/W (t)/CoFeB (3 nm)/SiO_2 (2 nm) samples with $0 \leq t \leq 15$ nm at $H = 2.30$ kOe. The value of α_0 for the 3-nm-thick CoFeB layer without the W underlayer is found to be 0.006 ± 0.0005. The presence of the W underlayer causes α_{eff} to vary non-monotonically over the whole thickness regime as shown by the α_{eff} vs. t plot in Figure 5.4(b). In the lower thickness regime, i.e. $0 \leq t \leq 3$ nm, $\Delta\alpha$ increases sharply by about 90% due to spin pumping but it saturates for $t \geq 3$ nm. However, for $t > 5$ nm, $\Delta\alpha$ drops by about 30% which is most likely related to the thickness-dependent phase transition of W. At first, we have fitted our result for $t \leq 5$ nm with equation (5.6) of the ballistic transport model and determined $G_{\uparrow\downarrow} = (1.46 \pm 0.01) \times 10^{15}$ cm^{-2} and $\lambda_{sd} = 1.71 \pm 0.10$ nm as fitting parameters. Next, we have also fitted our results with equation (5.8) based on spin diffusion theory, where we have obtained $G_{\uparrow\downarrow} = (2.19 \pm 0.02) \times 10^{15}$ cm^{-2} and $\lambda_{sd} = 1.78 \pm 0.10$ nm. In the calculation of α_{eff} using the ballistic transport model, the W resistivity is ignored while the W thickness is considered to be smaller than its mean free path which causes the value of $G_{\uparrow\downarrow}$ using the ballistic model (where the contribution of spin backflow is given by an exponential term $e^{-\frac{2t}{\lambda}}$) to be about 28% lower than that of spin diffusion theory (contribution of spin backflow is given by the term $\frac{e^2\rho\lambda G_{\uparrow\downarrow}}{h}\coth\left({t}/{\lambda}\right)$) while the value of λ is nearly the same in both models which is very close to the reported values in the literature [51]. Using values for λ_{el} (about 0.45 nm for β-W) from the literature [52] and λ_{sd} derived from our experimental data, we have extracted the spin-flip probability parameter, $\varepsilon = 2.30 \times 10^{-2}$ from equation (5.4). To be considered as an efficient spin sink, a nonmagnetic metal must have $\varepsilon \geq 1.0 \times 10^{-2}$ and hence, we can infer that the W acts as an effective spin sink here [13]. The backflow factor β is determined from equation (5.3). We have obtained the backflow factor modulation ($\Delta\beta$) as about 68% in our experimental thickness range.

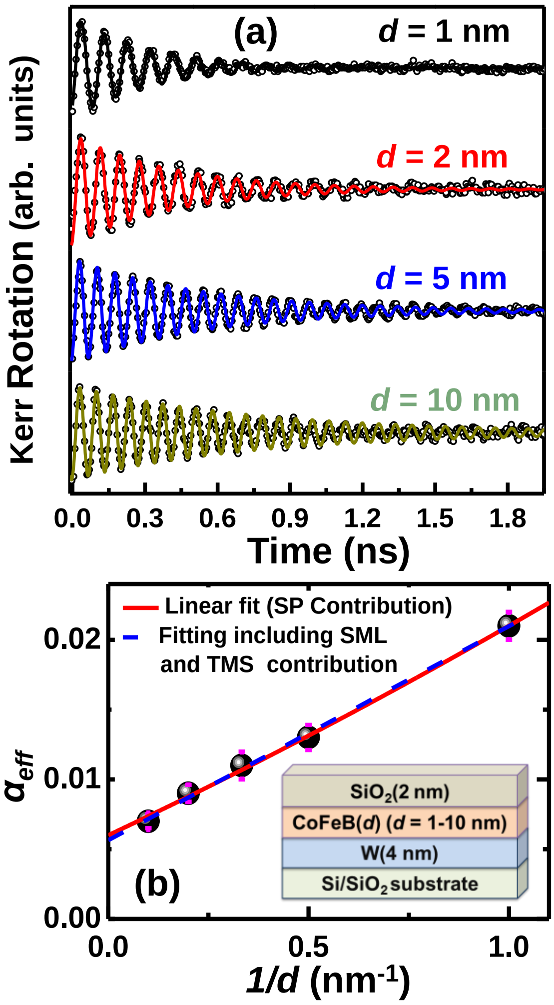

Figure 5.5: (a) Background deducted time-resolved Kerr rotation signal displaying precessional oscillation for Substrate/W (4 nm)/CoFeB (*d*)/SiO_2 (2 nm) as a function of CoFeB thickness *d* at a bias magnetic field of 2.30 kOe. (b) Experimental result of variation of damping vs 1/*d* (symbol) fitted with theoretical models (solid and dashed lines).

To determine the value of G_{eff} directly from the experiment, we have measured the temporal-evolution of precessional dynamics for Substrate/W (4 nm)/CoFeB (*d*)/SiO_2 (2 nm) samples with 1 nm $\leq d \leq$ 10 nm at H = 2.30 kOe as shown in Figure 5.5(a). The α_{eff} is found to increase with the inverse of FM layer thickness (Figure 5.5(b)). We have fitted our results first with the latter half of the equation (5.5) and equation (5.7) (given as: $G_{eff} = \frac{4\pi d M_{eff}}{g\mu_B}(\alpha_{eff} - \alpha_0)$), from which we have obtained G_{eff} and α_0 to be $(1.44 \pm 0.01) \times 10^{15}$ cm^{-2} and 0.006 ± 0.0005, respectively.

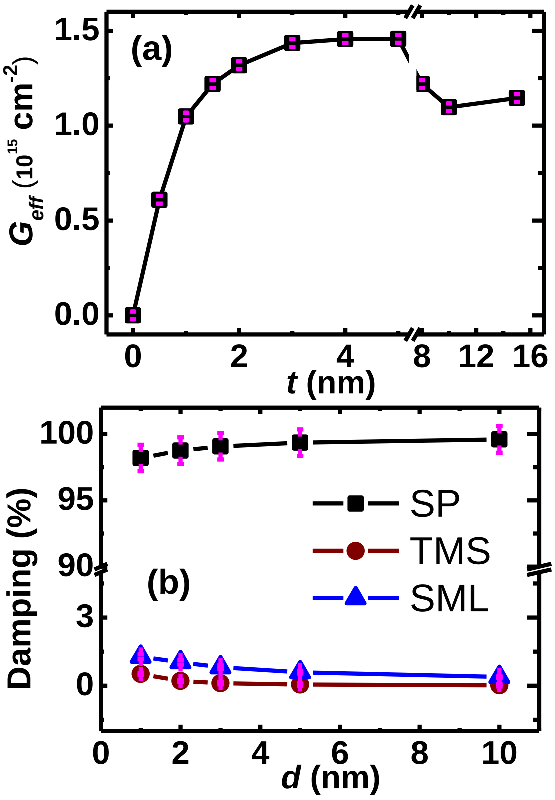

Figure 5.6: (a) Effective spin-mixing conductance (G_{eff}) variation with W layer thickness *t* (symbol). The solid line represents a guide to the eye. (b) Contributions of SP, SML and TMS to the modulation of damping for different CoFeB layer thickness *d* (symbol). The solid line represents a guide to the eye.

By modelling the W-thickness dependent modulation of damping of Figure 5.4(b) using equation (5.5), we have obtained G_{eff} of W/CoFeB in β-phase (where $\Delta\alpha \approx 0.006$) and (α+β) mixed phase (where $\Delta\alpha \approx 0.004$) of W to be (1.44 ± 0.01) × 10^{15} cm^{-2} and (1.07 ± 0.01) × 10^{15} cm^{-2}, respectively. From these, we conclude that the β-phase of W has higher conductance of spin channels in comparison to the (α+β) mixed phase. The modulation of G_{eff} with W layer thickness is presented in Figure 5.6(a), which shows that G_{eff} increases non-monotonically and nearly saturates for $t \geq 3$ nm. For t > 5 nm, G_{eff} shows a sharp decrease in consonance with the variation of α_{eff}.

We have further fitted the variation of α_{eff} with the inverse of FM layer thickness (Figure 5.5(b)) using equation (5.11) to isolate the contributions from SML, TMS and spin pumping (SP). The values of G_{SML} and β_{TMS} are found to be (2.45 ± 0.05) × 10^{13} cm^{-2} and (1.09 ± 0.02) × 10^{-18} cm^{2}, respectively. G_{SML} is negligible in comparison with G_{eff} which confirms the absence of SML contribution in damping. Contribution of TMS to damping modulation ($\beta_{TMS}d^{-2}$) is also below 2% for all the FM thicknesses. The relative contributions are plotted in Figure 5.6(b). It is clear that spin pumping contribution is highly dominant over the SML and TMS for our studied samples. The value of our G_{eff} in β-W/CoFeB is found to be much higher than that obtained for β-Ta/CoFeB [41] measured by the all-optical TRMOKE technique as well as various other NM/FM heterostructures measured by conventional techniques as listed in Table 5.3. This provides another confirmation of W being a good spin sink material giving rise to strong spin pumping effect.

We subsequently investigate the value of T for the W/CoFeB interface, which is associated with the spin-mixing conductances of an interface, spin diffusion length and resistivity of NM as denoted in equations (5.9) and (5.10). T is a material property that depends upon interfacial electronic band matching of the two materials. After experimentally determining the resistivity, spin diffusion length of W and spin-mixing conductances for the W/CoFeB interface, we have determined the value of T which depends strongly on the crystal structure of W. Using equation (5.9) based on the spin Hall magnetoresistance model, $T_{\beta\text{-W}}$ and $T_{(\alpha+\beta)\text{-W}}$ are found to be 0.81 ± 0.03 and 0.60 ± 0.02, respectively. However, the spin transfer torque-based model utilizing the drift-diffusion approximation (equation (5.10)) gives $T_{\beta\text{-W}}$ and $T_{(\alpha+\beta)\text{-W}}$ to be 0.85 ± 0.03 and 0.63 ± 0.02, respectively, which are slightly higher than the values obtained from spin Hall magnetoresistance model. However, we consider the values of T obtained from the spin Hall magnetoresistance model to be more accurate as it includes the mandatory contribution of spin current backflow from the W layer into the CoFeB layer. It is to be mentioned that the value of T does not change significantly if we consider M_s instead of M_{eff} during its calculation due to a very small variation of M_{eff} from M_s. Nevertheless, our study clearly demonstrates that the value of spin transparency of the β-W/CoFeB interface is the highest reported among the NM/FM heterostructures as listed in Table 5.3. This high value of T, combined with the high spin Hall angle of β-W makes it an extremely useful material for pure spin current-based spintronic and spin-orbitronic devices. The structural phase dependence of T for W also provides a particularly important guideline for choosing the correct thickness and phase of W for application in the above devices.

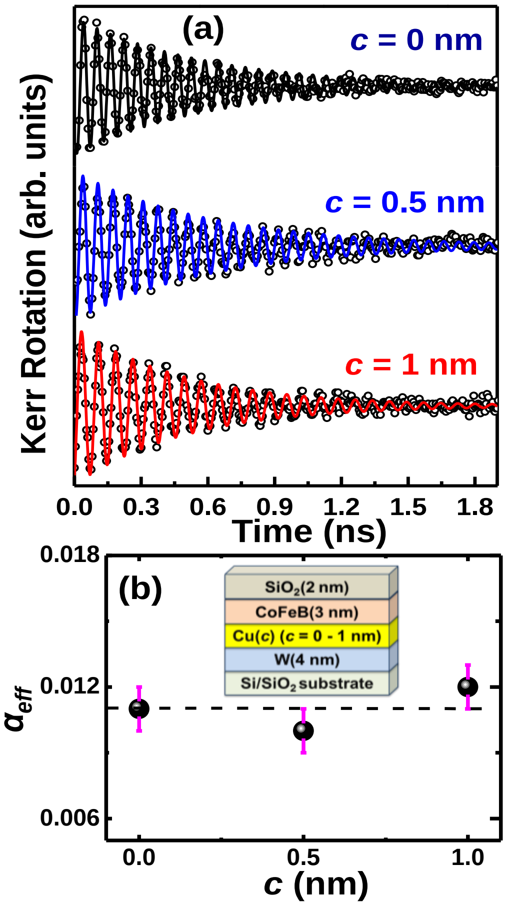

Figure 5.7: (a) Background deducted time-resolved Kerr rotation signal displaying precessional oscillation for Substrate/W (4 nm)/Cu (*c*)/CoFeB (3 nm)/SiO_2 (2 nm) as a function of Cu layer thickness (*c*) at a bias magnetic field of 2.30 kOe. (b) Experimental result of variation of damping vs *c*. The dotted line represents a guide to the eye, showing very little dependence of the effective damping constant on Cu spacer layer thickness.

Finally, to directly examine the additional possible interfacial effects present in the W/CoFeB system, we have inserted a thin Cu spacer in between the W and CoFeB layers. Cu possesses very small SOC strength and spin-flip scattering probability due to which it exhibits a very long spin diffusion length. Thus, the introduction of a thin Cu spacer layer must not influence the spin pumping-induced damping of the FM layer but can influence the other possible interfacial effects. Therefore, if other interfacial effects are substantial in our samples, the insertion of the Cu spacer would cause a notable modulation of damping with the increase of Cu spacer layer thickness (*c*) [19, 41]. The time-dependent Kerr rotation data for the Substrate/W (4 nm)/Cu (*c*)/CoFeB (3 nm)/SiO_2 (2 nm) thin films with $0 \leq c \leq 1$ nm are presented in Figure 5.7(a) at $H = 2.30$ kOe and Figure 5.7(b) shows α_{eff} as a function of *c*. The invariance of α_{eff} with *c* proves that the Cu/CoFeB interface is transparent for spin transport and possible additional interfacial contribution to damping is negligible, which is in agreement with our modelling as shown in Figure 5.6(b).

An important aspect of CoFeB-based thin film heterostructure is the variation of interface properties as a function of annealing temperature. The annealing temperature can play an important role in controlling the structural and magnetic properties like crystallite size, coercivity, saturation magnetization, Kerr rotation, exchange constant and Gilbert damping parameter in NM/FM heterostructures [53-55]. Annealing of amorphous CoFeB alloys at moderate temperature may lead to its crystallization to the bcc-CoFe phase with a subsequent B migration resulting in a decrease in the Gilbert damping parameter. On the other hand, high-temperature annealing may lead to higher Gilbert damping due to degradation by alloying, atomic intermixing, dead layer formation and interface shifting effects. It can therefore be conjectured that annealing temperature may also tune and optimize the interfacial spin transparency in an NM/FM heterostructure. A detailed study with the whole range of FM and NM thicknesses at different annealing temperatures would be necessary to underpin the effect of annealing temperature on *T*.

Table 5.3: Comparison of the effective spin-mixing conductance and interfacial spin transparency of the W/CoFeB samples studied here with the important NM/FM interfaces taken from the literature.

Material Interface	Effective Spin-Mixing Conductance ($\times 10^{15}$ cm^{-2})	Interfacial Spin Transparency
Pt/Py	1.52 [19]	0.25 [19]
Pt/Co	3.96 [19]	0.65 [19]
Pd/CoFe	1.07 [34]	N.A.
Pt/FM	0.6-1.2 [38]	0.34-0.67 [38]
β-Ta/CoFeB	0.69 [41]	0.50 [41]
β-Ta/ CFA	2.90 [42]	0.68 [42]
$Pd_{0.25}Pt_{0.75}$/Co	9.11 [43]	N.A.
$Au_{0.25}Pt_{0.75}$/Co	10.73 [43]	N.A.
Pd/Co	4.03 [43]	N.A.
$Pd_{0.25}Pt_{0.75}$/FeCoB	3.35 [43]	N.A.
$Au_{0.25}Pt_{0.75}$/ FeCoB	3.64 [43]	N.A.
Graphene/Py	5.26 [56]	N.A.
Ru/Py	0.24 [57]	N.A.
Pt/YIG	0.3-1.2 [58]	N.A.
MoS_2/CFA	1.49 [59]	0.46 [59]
Pd/Fe	0.49-1.17 [60]	0.04-0.33 [60]
Pd/Py	1.40 [61]	N.A.
Mo/CFA	1.56 [62]	N.A.
MoS_2/CoFeB	16.11 [63]	N.A.
Ta/YIG	0.54 [64]	N.A.
W/YIG	0.45 [64]	N.A.
Cu/YIG	0.16 [64]	N.A.

Ag/YIG	0.05 [64]	N.A.
Au/YIG	0.27 [64]	N.A.
β-W/CoFeB	1.44 (This work)	0.81 (This work)
Mixed (α+β)-W/CoFeB	1.07 (This work)	0.60 (This work)

((N.A. = Not available))

5.4 Conclusions

In summary, we have systematically investigated the effects of thickness-dependent structural phase transition of W in W (t)/CoFeB (d) thin film heterostructures and spin pumping-induced modulation of Gilbert damping by using an all-optical time-resolved magneto-optical Kerr effect magnetometer. The W film has exhibited a structural phase transition from a pure β phase to a mixed (α+β) phase for $t > 5$ nm. Subsequently, the β-W phase leads to larger modulation in effective damping (α_{eff}) than (α+β)-W. The spin diffusion length of W is found to be 1.71 ± 0.10 nm, while the spin pumping-induced effective spin-mixing conductance G_{eff} is found to be $(1.44 \pm 0.01) \times 10^{15}$ cm^{-2} and $(1.07 \pm 0.01) \times 10^{15}$ cm^{-2} for β and mixed (α+β) phase of W, respectively. This large difference in G_{eff} is attributed to different interface qualities leading towards different interfacial spin-orbit coupling. Furthermore, by analyzing the variation of α_{eff} with CoFeB thickness in W (4 nm)/CoFeB (d)/SiO_2 (2 nm), we have isolated the contributions of spin memory loss and two-magnon scattering from spin pumping, which divulges that spin pumping is the dominant contributor to damping. By modelling our results with the spin Hall magnetoresistance model, we have extracted the interfacial spin transparency (T) of β-W/CoFeB and (α+β)-W/CoFeB as 0.81 ± 0.03 and 0.60 ± 0.02, respectively. This structural phase-dependent T value will offer important guidelines for the selection of material phase for spintronic applications. By investigating the modulation of α_{eff} as a function of W layer thickness and modelling it by diffusive and ballistic spin transport formalisms, the spin-diffusion length (λ_{sd}) of W and spin-mixing conductances of the W/CoFeB interface are extracted. Irrespective of the used model, the value of T for the W/CoFeB interface is found to be highest among the NM/FM interfaces, including the popularly used Pt/FM heterostructures. The other possible interface effects on the modulation of Gilbert damping are found to be negligible as compared to the spin pumping effect. Thus, our study helps in developing a deep understanding of the role of W thin films in NM/FM heterostructures and the ensuing spin-orbit effects. The high effective spin-mixing conductance, low intrinsic Gilbert damping parameter combined with very high interfacial spin transparency and spin Hall angle can make the W/CoFeB system a vital material for spin-orbit torque-based spin logic, magnetization switching and spin wave devices.

References

1. C. Chappert, A. Fert and F. N. Van Dau, Nat. Mater. **6**, 813-823 (2007).
2. S. D. Bader and S. S. P. Parkin, Annu. Rev. Cond. Matter Phys. **1**, 71-88 (2010).
3. I. Žutić, J. Fabian and S. Das Sarma, Rev. Mod. Phys. **76**, 323-410 (2004).
4. S. A. Wolf, D. D. Awschalom, R. A. Buhrman, J. M. Daughton, S. von Molnár, M. L. Roukes, A. Y. Chtchelkanova and D. M. Treger, Science **294**, 1488-1495 (2001).
5. P.Sharma, Science **307**, 531-533 (2005).
6. A. Hoffmann, Phys. Status Sol. C, **4**, 4236-4241 (2007).
7. L. Liu, C. F. Pai, Y. Li, H. W. Tseng, D. C. Ralph and R. A. Buhrman. Science **336**, 555-558 (2012).
8. J. Sinova, S. O. Valenzuela, J. Wunderlich, C. H. Back and T. Jungwirth, Rev. Mod. Phys. **87**, 1213-1260 (2015).
9. Y. A. Bychkov and É. I. Rashba, JETP Lett. **39**, 78-81 (1984).
10. J. C. R. Sánchez, L. Vila, G. Desfonds, S. Gambarelli, J. P. Attané, J. M. De Teresa, C. Magén and A. Fert, Nat. Commun. **4**, 2944 (2013).
11. Y. Tserkovnyak, A. Brataas and G. E. W. Bauer, Phys. Rev. Lett. **88**, 117601 (2002).
12. Y. Tserkovnyak, A. Brataas, G. E. W. Bauer and B. I. Halperin, Rev. Mod. Phys. **77**, 1375-1421 (2005).
13. Y. Tserkovnyak, A. Brataas and G. E. W. Bauer, Phys. Rev. B **66**, 224403 (2002).
14. V. E. Demidov, S. Urazhdin, R. Liu, B. Divinskiy, A. Telegin and S. O. Demokritov, Nat. Commun. **7**, 10446 (2016).
15. Y. Fukuma, L. Wang, H. Idzuchi, S. Takahashi, S. Maekawa and Y. Otani, Nat. Mater. **10**, 527-531 (2011).
16. W. Lin, M. Hehn, L. Chaput, B. Negulescu, S. Andrieu, F. Montaigne and S. Mangin, Nat. Commun. **3**, 744 (2012).
17. G. E. W. Bauer, E. Saitoh and B. J. van Wees, Nat. Mater. **11**, 391-399 (2012).
18. A. Soumyanarayanan, N. Reyren, A. Fert and C. Panagopoulos, Nature **539**, 509-517 (2016).
19. W. Zhang, W. Han, X. Jiang, S. H. Yang and S. S. P. Parkin, Nat. Phys. **11**, 496-502 (2015).
20. K. U. Demasius, T. Phung, W. Zhang, B. P. Hughes, S. H. Yang, A. Kellock, W. Han, A. Pushp and S. S. P. Parkin, Nat. Commun. **7**, 10644 (2016).
21. C. F. Pai, L. Liu, Y. Li, H. W. Tseng, D. C. Ralph and R. A. Buhrman, Appl. Phys. Lett. **101**, 122404 (2012).
22. K. Ando, S. Takahashi, K. Harii, K. Sasage, J. Ieda, S. Maekawa and E. Saitoh, Phys. Rev. Lett. **101**, 036601 (2008).
23. G. G. An, J. B. Lee, S. M. Yang, J. H. Kim, W. S. Chung and J. P. Hong, Acta Materialia **87**, 259-265 (2015).
24. J. Kim, P. Sheng, S. Takahashi, S. Mitani and M. Hayashi, Phys. Rev. Lett. **116**, 097201 (2016).
25. A. K. Chaurasiya, C. Banerjee, S. Pan, S. Sahoo, S. Choudhury, J. Sinha and A. Barman, Sci. Rep. **6**, 32592 (2016).
26. S. Mondal, S. Choudhury, N. Jha, A. Ganguly, J. Sinha and A. Barman, Phys. Rev. B **96**, 054414 (2017).
27. J. Torrejon, J. Kim, J. Sinha, S. Mitani, M. Hayashi, M. Yamanouchi and H. Ohno, Nat. Commun. **5**, 4655 (2014).

28. S. X. Huang, T. Y. Chen and C. L. Chien, Appl. Phys. Lett. **92**, 242509 (2008).
29. J. C. Rojas-Sánchez, N. Reyren, P. Laczkowski, W. Savero, J.-P. Attané, C. ranlot, M. Jamet, J.-M. George, L. Vila and H. Jaffrès, Phys. Rev. Lett. **112**, 106602 (2014).
30. M. J. Hurben and C E Patton, J. Appl. Phys. **83**, 4344 (1998).
31. N. Nakajima, T. Koide, T. Shidara, H. Miyauchi, H. Fukutani, A. Fujimori, K. Iio, T. Katayama, M. Nývlt and Y. Suzuki, Phys. Rev. Lett. **81**, 5229 (1998).
32. A. Barman and J. Sinha, Spin dynamics and damping in ferromagnetic thin films and nanostructures (Springer: Switzerland, 2018).
33. J. Foros, G. Woltersdorf, B. Heinrich and A. Brataas, J. Appl. Phys. **97**, 10A714 (2005).
34. J. M. Shaw, H. T. Nembach and T. J. Silva, Phys. Rev. B **85**, 054412 (2012).
35. C. T. Boone, H. T. Nembach, J. M. Shaw and T. J. Silva, J. Appl. Phys. **113**, 153906 (2013).
36. C. T. Boone, J. M. Shaw, H. T. Nembach and T. J. Silva, J. Appl. Phys. **117**, 223910 (2015).
37. Y. T. Chen, S. Takahashi, H. Nakayama, M. Althammer, S. T. B. Goennenwein, E. Saitoh and G. E. W. Bauer, Phys. Rev. B **87**, 144411 (2013).
38. C. F. Pai, Y. Ou, L. H. Vilela-Leão, D. C. Ralph and R. A. Buhrman, Phys. Rev. B **92**, 064426 (2015).
39. D. Jhajhria, N. Behera, D. K. Pandya and S. Chaudhary, Phys. Rev. B **99**, 014430 (2019).
40. I. Horcas, R. Fernández, J. M. Gómez-Rodríguez, J. Colchero, J. Gómez-Herrero and A. M. Baro, Rev. Sci. Instrum. **78**, 013705 (2007).
41. S. N. Panda, S. Mondal, J. Sinha, S. Choudhury and A. Barman, Sci. Adv. **5**, eaav7200 (2019).
42. S. Akansel, A. Kumar, N. Behera, S. Husain, R. Brucas, S. Chaudhary and P. Svedlindh, Phys. Rev. B **97**, 134421 (2018).
43. L. Zhu, D. C. Ralph and R. A. Buhrman, Phys. Rev. Lett. **123**, 057203 (2019).
44. S. Mondal and A. Barman, Phys. Rev. Appl. **10**, 054037 (2018).
45. S. Mizukami, E. P. Sajitha, D. Watanabe, F. Wu, T. Miyazaki, H. Naganuma, M. Oogane and Y. Ando, Appl. Phys. Lett. **96**, 152502 (2010).
46. H. S. Song, K. D. Lee, J. W. Sohn, S. H. Yang, S. S. P. Parkin, C. Y. You and S. C. Shin, Appl. Phys. Lett. **103**, 022406 (2013).
47. R. M. Bozorth, Ferromagnetism. (Wiley-IEEE Press, Piscataway, New Jersey, 1993).
48. J. Sinha, M. Hayashi, A. J. Kellock, S. Fukami, M. Yamanouchi, H. Sato, S. Ikeda, S. Mitani, S. H. Yang, S. S. P. Parkin and H. Ohno, Appl. Phys. Lett. **102**, 242405 (2013).
49. J. Walowski, M. Djordjevic Kaufmann, B. Lenk, C. Hamann, J. McCord and M. Munzenberg, J. Phys. D: Appl. Phys. **41**, 164016 (2008).
50. G. Woltersdorf, M. Buess, B. Heinrich and C. H. Back, Phys. Rev. Lett. **95**, 037401 (2005).
51. S. Cho, S. H. C. Baek, K. D. Lee, Y. Jo and B. G. Park, Sci. Rep. **5**, 14668 (2015).
52. Q. Hao, W. Chen and G. Xiao, Appl. Phys. Lett. **106**, 182403 (2015).
53. Y. Kim, B. Kim, B. Bhoi, Y. H. Lee, Y. W. Kim and S. K. Kim, J. Appl. Phys. **128**, 223901 (2020).
54. D. M. Lattery, D. Zhang, J. Zhu, X. Hang, J. P. Wang and X. Wang, Sci. Rep. **8**, 13395 (2018).
55. A. Conca, E. T. Papaioannou, S. Klingler, J. Greser, T. Sebastian, B. Leven, J. Lösch and B. Hillebrands, Appl. Phys. Lett. **104**, 182407 (2014).
56. A. K. Patra, S. Singh, B. Barin, Y. Lee, J.-H. Ahn, E. d. Barco, E. R. Mucciolo and B. Özyilmaz, Appl. Phys. Lett. **101**, 162407 (2012).

57. N. Behera, M. S. Singh, S. Chaudhary, D. K. Pandya and P. K. Muduli, J. Appl. Phys. **117**, 17A714 (2015).

58. M. Haertinger, C. H. Back, J. Lotze, M. Weiler, S. Geprägs, H. Huebl, S. T. B. Goennenwein and G. Woltersdorf, Phys. Rev. B **92**, 054437 (2015).

59. S. Husain, A. Kumar, P. Kumar, A. Kumar, V. Barwal, N. Behera, S. Choudhary, P. Svedlindh and S. Chaudhary, Phys. Rev. B **98**, 180404 (2018).

60. A. Kumar, S. Akansel, H. Stopfel, M. Fazlali, J. Åkerman, R. Brucas and P. Svedlindh, Phys. Rev. B **95**, 064406 (2017).

61. M. Caminale, A. Ghosh, S. Auffret, U. Ebels, K. Ollefs, F. Wilhelm, A. Rogalev and W. E. Bailey, Phys. Rev. B **94**, 014414 (2016).

62. S. Husain, A. Kumar, V. Barwal, N. Behera, S. Akansel, P. Svedlindh and S. Chaudhary, Phys. Rev. B **97**, 064420 (2018).

63. G. Wu, Y. Ren, X. He, Y. Zhang, H. Xue, Z. Ji, Q. Y. Jin and Z. Zhang, Phys. Rev. Appl. **13**, 024027 (2020).

64. H. L. Wang, C. H. Du, Y. Pu, R. Adur, P. C. Hammel and F. Y. Yang, Phys. Rev. Lett. **112**, 197201 (2014).

Chapter-6

Femtosecond laser-induced spin dynamics in single layer graphene/CoFeB thin films

6.1 Introduction

Graphene [1], a monolayer of carbon atoms, is an extremely promising material for spintronics [2] because of the observation of long spin-diffusion length [3-5] and prolonged spin-relaxation time [6]. This is a consequence of weak SOC that causes electron spins to remain unaffected over unprecedented distances [7]. Besides this, graphene has many other interesting properties like high electron mobility [8], massless Dirac fermions in the linear dispersion of its electronic structure [9], well-defined monolayer formation [10], gate tunable spin transport in spin-valve devices [11], proximity-induced SOC [12], low resistivity [13], small nuclear spin [14] and weak hyperfine interaction [15], which project it as an attractive material for spintronics application.

The two-dimensional crystal structure of graphene is not stable at room temperature due to thermodynamic violation of the energy minimization which makes its formation only by out-of-plane deformations like wrinkles, ripples and crumples [16, 17]. Engineering of these deformations by adsorption, hybridization, fluorination and proximity with FM leads to a strong enhancement of the SOC strength and control over the properties of graphene by opening the band-gap and inducing localized states at the Fermi level [18]. When graphene is placed adjacent to FM, the strong hybridization of graphene $p\pi$ states with d_{z^2} states of FM and charge transfer from FM to graphene causes spin polarization in graphene which induces local magnetic moment in it while decreasing the net magnetic moment and spin polarization of the FM [19-22]. Recent observations of spin Hall effect [23], inverse spin Hall effect [24], spin pumping [25] and anomalous Hall effect [26] in graphene/FM at room temperature point towards enhanced SOC in graphene/FM system. So far, non-local spin injection is the most widely used technique for spin injection and transport in graphene, where the spin current is transferred to graphene by charge transport across the graphene/FM interface, but has small efficiency (< 30%) due to the impedance mismatch problem [27, 28]. Recently, spin pumping proved to be more efficient spin injection technique in graphene than non-local spin injection as it is devoid of impedance mismatch problem due to the non-involvement of charge current. Besides, it is a widely-used method to generate pure spin current where magnetization precession in FM directly transfers spin angular momentum to the adjacent nonmagnetic layer leading to an increase in α of the system [29, 30]. Also, deposition of FM on graphene causes enhanced magnetic disorder leading to a sizable contribution of two-magnon scattering (TMS) which is also responsible for the enhancement of α [31]. There are both theoretical and experimental debates over the precise contributions of spin pumping and TMS to α in graphene/FM hybrid systems, but a systematic study to quantify both contributions is still absent in the literature.

The magnetization of a ferromagnetic thin film can be modified or switched by a pulsed magnetic field [32,33] or spin-polarized current [34, 35]. However, the response time of these processes lies in the nanosecond to picosecond timescale. On the other hand, all-optical magnetization reversal and coherent control of magnetic order can be achieved in sub-picosecond timescale by single ultrashort circularly polarized laser pulses without the aid of an external magnetic field [36]. Femtosecond laser-induced ultrafast demagnetization was first introduced by Beaurepaire *et al.* in 1996 [37], which opened a new avenue for fast manipulation of magnetic order. More recently ultrafast demagnetization stemming from the optical inter-site spin transfer (OISTR) process has been probed by attosecond laser pulses [38]. Extensive theoretical modelling and subsequent experimental studies unravelled two more major microscopic mechanisms behind ultrafast demagnetization. The first contribution comes from the spin-flip scattering [39-42] while the second contribution comes from the spin current transport [43]. Recent experiments suggest the correlation between τ_m and α as an effective method to isolate the dominant contribution to ultrafast demagnetization in metallic heterostructures, where a proportional relation proves dominant local spin-flip scattering contribution, while an inverse dependence confirms a dominant spin current contribution [44, 45]. To the best of our knowledge, the correlation between τ_m and α in a graphene/FM system, which is important for graphene-based ultra-high speed spintronics applications, has not been reported to date.

In this thesis chapter, we have used an all-optical TR-MOKE magnetometry [46] to study the magnetization dynamics in SLG/CoFeB thin films. We have extracted τ_m using three-temperature modelling of time-resolved magnetization dynamics and found its monotonic variation with CoFeB thickness. The α is directly extracted from the decaying amplitude of precessional oscillation. We have modelled the thickness-dependent α to estimate spin-mixing conductance (G_{eff}) and coefficient of two-magnon scattering (β_{TMS}) for SLG/CoFeB interface which revealed spin pumping as the major contributor to modulation of α. Negligible damping modulation by the insertion of Copper (Cu) spacer between SLG and CoFeB confirms that additional interfacial effects including spin memory loss are absent in SLG/CoFeB system. Furthermore, we have observed an inverse relationship between τ_m and α for SLG/CoFeB heterostructures due to the dominance of spin pumping-induced nonlocal spin transport mechanism. On the contrary, τ_m and α show negligible modulation with CoFeB thickness in absence of SLG which signifies the role played by SLG in modulating the magnetization dynamics of CoFeB.

6.2 Experimental details

Large area SLG was procured from *Graphenea inc*. The SLG sample was prepared by chemical vapor deposition (CVD) method over Si/SiO_2 (300 nm) substrate. Briefly, the preparation process involved the CVD of methane on a Cu foil. Then polymethyl methacrylate (PMMA) coating was deposited atop via spin coating before the Cu foil was etched away. Finally, SLG was transferred onto a Si wafer with a 300 nm SiO_2 top layer by the wet transfer process. We deposited CoFeB (d) and SiO_2 (2 nm) layers over the SLG by using RF/DC magnetron sputtering. For the reference samples, CoFeB (d) and SiO_2 (2 nm) layers were deposited over Si/SiO_2 (300 nm) substrate also by RF/DC magnetron sputtering without SLG underlayer. We varied CoFeB layer thickness d as 1.5, 3, 4 and 6 nm. The depositions were done at an average base pressure of 3.0×10^{-7} Torr and argon pressure of about 1.2 mTorr at a deposition rate of 0.2 Å/s. A slow deposition rate was chosen for uniformity of samples even at a very small thickness. The CoFeB layer was deposited using a DC voltage of 375 V, while the SiO_2 layer was deposited using RF power of 60 W. All other deposition parameters were carefully optimized and kept almost identical for all the samples. In another sample, we have introduced a thin Cu spacer layer of 1 nm thickness in between the CoFeB and SLG layers. The Cu layer was deposited at a DC voltage of 343 V, argon pressure of 0.5 mTorr and the deposition rate of 0.2 Å/s.

AFM was used to investigate the surface topography and average topographical roughness of the samples. The electron density, thickness and interface roughness of individual layers in SLG/CoFeB heterostructures were determined by XRR measurement. The VSM was used to estimate the static magnetic properties like saturation magnetization (M_s) and coercivity (H_c) of the samples. Micro-Raman spectroscopy was used to determine the defect density, number and quality of the graphene layer. For investigating the magnetization dynamics, a custom-built TR-MOKE magnetometer based on the non-collinear optical pump-probe technique was used. The second-harmonic laser beam (wavelength = 400 nm, repetition rate = 1 kHz, pulse width >40 fs) of a regenerative amplifier system (Libra, Coherent) was used to excite the magnetization of the sample, while the time-delayed fundamental laser beam (wavelength = 800 nm, repetition rate = 1 kHz, pulse width ~ 40 fs) was used to probe the dynamics. The pump beam was focused to a spot size of 300 µm and obliquely incident on the sample (approximately 30° to the surface normal). The probe beam was focused to a spot size of about 100 µm and was normally incident on the sample, by maintaining an excellent spatial overlap with the pump spot for avoiding any additional contribution to Gilbert damping due to dissipation energy of uniform precessional mode out of the probed area. At first, a large magnetic field of 3.59 kOe was applied at a small angle of about 10° from the sample plane to saturate its magnetization, where the tilt ensured a finite demagnetizing field along the pump pulse direction to induce precessional dynamics in the sample. The pump beam was chopped at a frequency of 373 Hz and the dynamic signal was probed in a phase-sensitive manner using a lock-in amplifier. Throughout the measurement pump and probe fluences were kept constant at 5 mJ/cm^2 and 0.5 mJ/cm^2. All the experiments were conducted under ambient conditions and at room temperature.

6.3 Results and discussions

The micro-Raman scattering experiment was carried out to characterize the quality and number of graphene layers and underpin the effects of CoFeB deposition on it [47]. The Raman spectra of SLG in the absence and presence of CoFeB is shown in Figure 6.1(a). The main features in the Raman spectra of carbon-based materials are the G and 2D peaks which are observed at 1586.8 cm^{-1} and 2678.9 cm^{-1}, respectively. Deposition of CoFeB resulted in the appearance of defect peaks like D, D′ and (D + D′) at 1341, 1623 and 2939 cm^{-1}, respectively [47]. Furthermore, a perfect Lorentzian-shaped 2D peak shows the single layer nature of graphene. We notice that D-peak intensity (I_D) decreases by a factor of 14 when CoFeB thickness increases from 1.5 to 6.0 nm which signifies decrease in defect concentration and damages in the SLG with the increase in CoFeB thickness [48-50]. Although both I_D and I_G decrease with the increase in CoFeB thickness, the rate of decrease of I_G is much smaller in comparison to that of I_D which resulted in a decrease in the spectral weight ratio (I_D/I_G ratio; where I_G is the G-peak intensity) with the increase in CoFeB thickness. Average crystalline size (L_a), which is a measure of the average distance between two adjacent defects increases with the CoFeB thickness indicating a decrease in defect density at higher CoFeB thicknesses [51,52].

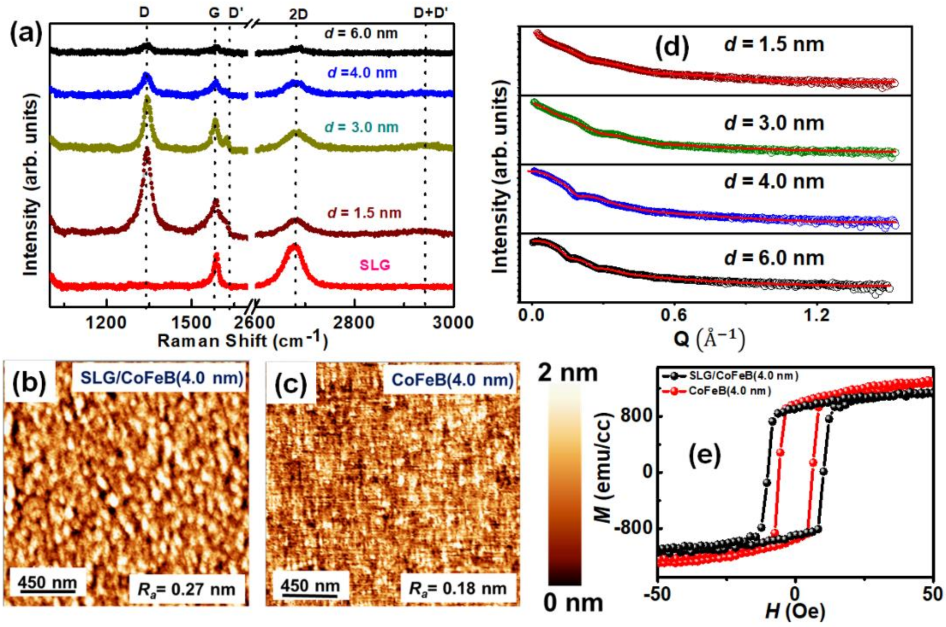

Figure 6.1: (a) Micro-Raman spectra for SLG and SLG/CoFeB (*d*). (b) AFM images of the SLG/CoFeB (4 nm). (c) AFM images of the CoFeB (4 nm). (d) XRR spectra (symbols) for SLG/CoFeB (*d*) samples fitted using Parratt's formalism (red solid lines). (e) Magnetic hysteresis loops for SLG/CoFeB (4 nm) and CoFeB (4 nm).

AFM images for Sub/SLG/CoFeB (4.0 nm)/SiO_2 (2.0 nm) and Sub/CoFeB (4.0 nm)/SiO_2 (2.0 nm) are shown in Figure 6.1(b) and Figure 6.1(c), respectively. The average surface roughness (R_a) for all the films is tabulated in Table 6.1. In presence of SLG, R_a value is found to be higher but it decreases with CoFeB layer thickness. This reduction is possibly due to the filling of the defect sites with an increase in CoFeB layer thickness [53]. In absence of SLG, R_a remains comparatively low and independent of CoFeB thickness, which reveals that the growth of CoFeB on SLG is different from that on Si/SiO_2. Due to the small thicknesses of the CoFeB films, the interfacial roughness will leave its imprint on the R_a. High R_a in SLG/CoFeB thin films is mainly due to the formation of low-density and large-sized clusters of CoFeB in the presence of SLG [31]. Although there is a possibility of enhancement of defect density with sputtering time but if this were to be the case the sample roughness should also have increased with CoFeB layer thickness [50,54]. However, we have observed that the roughness remains almost constant in the absence of SLG in agreement to that reported in the literature [46], while it decreases slightly with an increase in the CoFeB layer thickness in the presence of SLG. This indicates that sputtering time plays a minor role in the enhancement of the defect density and roughness in our case.

Table 6.1: The roughness values obtained from AFM.

Parameter	SLG/CoFeB (*d* nm)				CoFeB (*d* nm)			
	1.5	3.0	4.0	6.0	1.5	3.0	4.0	6.0
R_a (nm)	0.40	0.36	0.27	0.25	0.23	0.24	0.18	0.20

Figure 6.1(d) shows XRR spectra of SLG/CoFeB thin films of varying CoFeB thickness measured using 8 KeV X-ray source. Over the whole thickness regime, XRR spectra exhibit well-defined oscillations up to scattering vector of 1.0 Å^{-1} indicating uniform deposition thickness. The XRR spectra are fitted under Parratt's formalism where the electron density, thickness and roughness of SLG, CoFeB and SiO_2 are taken as fitting parameters. Fitted values of the layer thicknesses are close to the nominal values. The RMS surface roughness of the SLG/CoFeB interface decreases with increased CoFeB thickness similar to that observed from AFM measurement. In contrast, electron densities of CoFeB, SLG and SiO_2 are found to be 15.0×10^{-5}, 1.5×10^{-5} and 2.0×10^{-5} Ǻ$^{-2}$, respectively, independent of CoFeB layer thickness. These values of electron densities are close to the values reported in the literature [55].

Figure 6.1 (e) shows the VSM loops for CoFeB (4.0 nm) layer at room temperature in the presence and absence of the SLG underlayer. The variation of saturation magnetization (M_s) and coercive field (H_c) are tabulated in Table 6.2 for all samples. In presence of SLG, M_s is smaller than CoFeB without SLG underlayer. This is probably due to the lowering of the total energy of the system stemming from the strong interfacial hybridization between the graphene pπ states and d-band of Co/Fe in CoFeB, which may induce magnetic moments in the adjacent carbon atoms aligning it antiparallel to the Co/Fe moments [19, 21, 22, 43]. On the contrary, H_c is slightly higher in presence of SLG which indicates the somewhat different growth of CoFeB on SLG as opposed to Si/SiO_2. It can be argued that due to the low metal-carbon bond energy of carbon atoms in graphene, CoFeB layer tends to form large-sized clusters during the initial growth stages promoting multigrain films which lead to an increase in the domain wall pinning centres and subsequent increase in the coercivity [31].

Table 6.2: The saturation magnetization (M_s) and coercive field (H_c) obtained from VSM and effective saturation magnetization (M_{eff}) obtained from TR-MOKE.

Parameter	SLG/CoFeB (*d* nm)				CoFeB (*d* nm)			
	1.5	3.0	4.0	6.0	1.5	3.0	4.0	6.0
M_s (emu/cc)	1025	1075	1140	1158	1157	1220	1280	1300
H_c (Oe)	11.2	7.8	6.6	10	5.2	4.7	4.6	6
M_{eff} (emu/cc)	737	986	1057	1120	910	1146	1192	1253

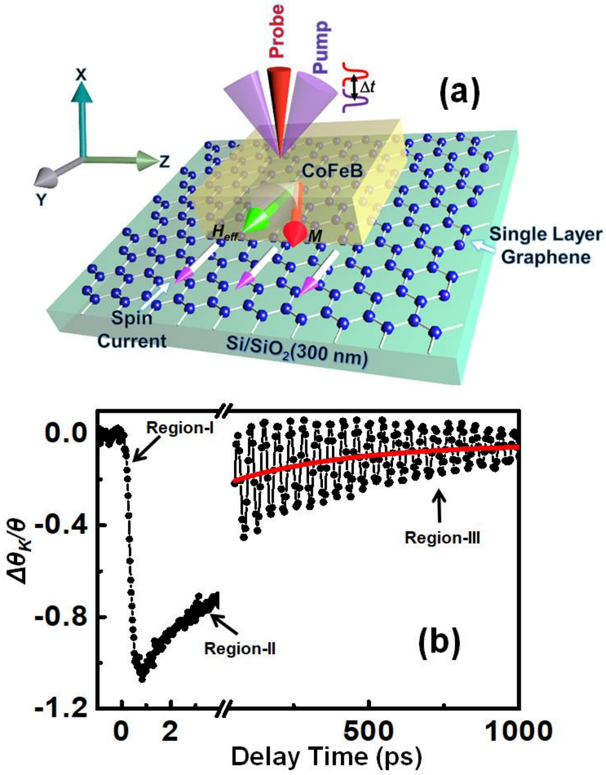

Figure 6.2: (a) Schematic of experimental geometry and (b) typical TR-MOKE trace from SLG/CoFeB (3 nm)/SiO_2 (2 nm) heterostructure at a bias magnetic field of 3.59 kOe. The three important temporal regimes are indicated in the graph. The solid red line shows a bi-exponential background of the time-resolved Kerr rotation data.

We used a TR-MOKE magnetometer based on the two-colour optical pump-probe technique to measure the magnetization dynamics. The experimental geometry of TR-MOKE measurement is shown in Figure 6.2(a) along with the direction of spin current flow. In our experiment, we have applied a sufficiently large magnetic field of 3.59 kOe at a small angle of about 10° from the sample plane to saturate the sample magnetization before the pump laser excitation. This tilt from the sample plane guarantees a finite demagnetizing field along the pump pulse direction, which is modified by the pump pulse. This results in a change of the equilibrium orientation and helps in triggering the initial precession of the magnetization in the sample around its new equilibrium orientation [56,57]. Figure 6.2(b) shows the time-resolved Kerr rotation data showing three different temporal regions, namely ultrafast demagnetization (Region-I), subsequent fast recovery (Region-II), followed by a slow relaxation superposed with precessional oscillation (Region-III). The time scale is broken into different temporal windows (few femtoseconds to a few hundred femtoseconds for Region-I, a few hundred femtoseconds to few picoseconds for Region-II and from a few picoseconds to a few nanoseconds for Region-III) to resolve and visualize different temporal phenomena with clarity. To interpret the ultrafast demagnetization data, a phenomenological thermodynamic model, namely the three-temperature model is very widely used where the dynamics of ultrafast demagnetization and fast relaxation can be expressed as [58, 59]:

$$-\frac{\Delta M_z}{M_z} = \left[\left\{\frac{A_1}{(t/\tau_0+1)^{\frac{1}{2}}} + \frac{A_1\tau_m - A_2\tau_e}{\tau_e-\tau_m}e^{-t/\tau_m} + \frac{A_2\tau_e - A_1\tau_e}{\tau_e-\tau_m}e^{-t/\tau_e}\right\}H(t) + A_3\delta(t)\right] \otimes G\,(t) \qquad (6.1)$$

This is an approximated form based on assumption that the FM system is divided into three subsystems, namely: electron, spin and lattice. Upon laser excitation, electron temperature increases instantaneously to create hot electrons above the Fermi-level which then excites the spin subsystem by electron-magnon interaction that results in quenching of magnetization. Subsequently, the energy rebalancing between the three subsystems causes the quenched magnetization to relax back to its original equilibrium position. In the above expression, A_1 represents the value of magnetization after equilibrium between electron, spin and lattice, A_2 is proportional to the maximum rise in the electron temperature and A_3 represents the magnitude of state filling effects during pump-probe temporal overlap well established by a Dirac-delta function ($\delta(t)$). The cooling time by heat diffusion is described by τ_0 representing the timescale of electron-phonon interactions. $H(t)$ and $G(t)$ are the Heaviside step function and Gaussian function, the latter corresponds to the laser pulse. The two exponential terms in the above equation mirror the timescale of magnetization loss by the ultrafast demagnetization time (τ_m) and the timescale of electron-phonon interaction by fast remagnetization time (τ_e). All the temporal changes of Kerr rotation ($\Delta\theta_k\,(t)$) are normalized by the saturation value of total Kerr rotation (θ_k) and then fitted with equation (6.1) to extract the value of τ_m and τ_e.

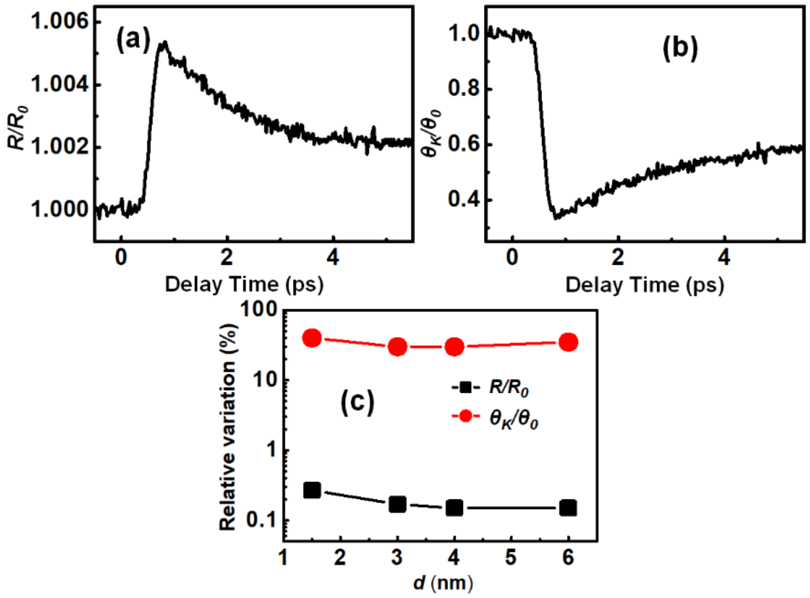

Figure 6.3: (a) Transient reflectivity for Sub/SLG/CoFeB (3 nm)/SiO$_2$ (2 nm) at pump fluence of 5 mJ/cm^2 normalized *w.r.t.* the corresponding negative delay value. (b) Transient Kerr rotation for Sub/SLG/CoFeB (3 nm)/SiO$_2$ (2 nm) normalized *w.r.t.* the corresponding negative delay value. (c)

Relative variation of the peak values of transient Kerr rotation and reflectivity for varying CoFeB thickness.

Before analyzing the demagnetization curves, we try to understand the possible contributions of the optical effects superposed with the true magnetic information. From the temporal variation of normalized reflectivity and Kerr rotation (as shown in Figures 6.3(a) and 6.3(b)), we found that the relative variation of reflectivity is negligibly small compared to that of the Kerr rotation (as shown in Figure 6.3(c)), implying negligible non-magnetic contributions in the Kerr rotation data for all samples.

Figure 6.4(a) shows the laser-induced ultrafast demagnetization curves obtained for Sub/SLG/CoFeB (*d* nm)/SiO_2 (2 nm). The variation in τ_m with CoFeB thicknesses in presence of SLG is plotted in Figure 6.4(b), where τ_m increases monotonically from 90 ± 5 fs to 230 ± 8 fs, when CoFeB thickness increases from 1.5 nm to 6.0 nm in presence of SLG. To understand the microscopic mechanisms responsible for this increase in τ_m, we have studied the precessional dynamics and its variation with CoFeB thickness.

In a graphene/FM heterostructure, graphene acts as a nonmagnetic layer to dissipate the spin angular momentum of FM by spin-flip scattering. Although graphene has low intrinsic SOC and small effective thickness (~0.3 - 0.4 nm), it shows a significant increase in extrinsic SOC and Rashba-SOC due to the deposition of FM above it, which makes it a good spin sink material [60,61]. When a graphene/FM heterostructure in an equilibrium saturated state is excited, the coherent magnetization precession in the FM layer causes spin accumulation at its interface due to SP. Accumulated spins gradually dissipate in the adjacent graphene layer which leads to an enhancement of α. In the presence of SP, the flow of spins through the graphene/FM interface is controlled by the conductivity of the spin channels at the interfaces parametrized as G_{eff}. The spin pumping contribution to the α can be expressed as a function of G_{eff} as [62]:

$$\Delta\alpha = \alpha - \alpha_0 = \frac{g\mu_B}{4\pi d M_s} G_{\mathrm{eff}} \qquad (6.2)$$

Here M_s is the saturation magnetization, d is FM layer thickness and α_0 denotes intrinsic Gilbert damping parameter.

In addition to SP, some extrinsic contributions due to surface defects and inhomogeneities can be present in the form of TMS in this system. The TMS contribution comes from the scatterings of the uniform precession mode into non-uniform modes. Using the first-order approximation, TMS contribution to the α is found to have an inverse square dependence on the FM thickness, whereas spin pumping contribution has an inverse dependence on FM thickness. In the presence of both TMS and SP, α can be approximated as [63]:

$$\alpha = \alpha_0 + g\mu_B \frac{G_{eff}}{4\pi d M_s} + \beta_{TMS} d^{-2} \tag{6.3}$$

Here β_{TMS} depends on both interfacial perpendicular magnetic anisotropy field and density of magnetic defects at the FM surface.

To extract α, we have fitted a bi-exponential background-subtracted damped precessional data using the following expression:

$$M(t) = M(0)e^{-\left(\frac{t}{\tau}\right)}\sin(2\pi f t + \phi) \tag{6.4}$$

where ϕ is the initial phase of the oscillation, τ is the precessional relaxation time and f is the precessional frequency. The variation of f with bias magnetic field (H) is fitted using the Kittel formula which is given as:

$$f = \frac{\gamma}{2\pi}\left(H\left(H + 4\pi M_{eff}\right)\right)^{1/2} \tag{6.5}$$

where $\gamma = g\mu_B/\hbar$ is the gyromagnetic ratio, g is the Landé g-factor and $\hbar$ is reduced Planck's constant.

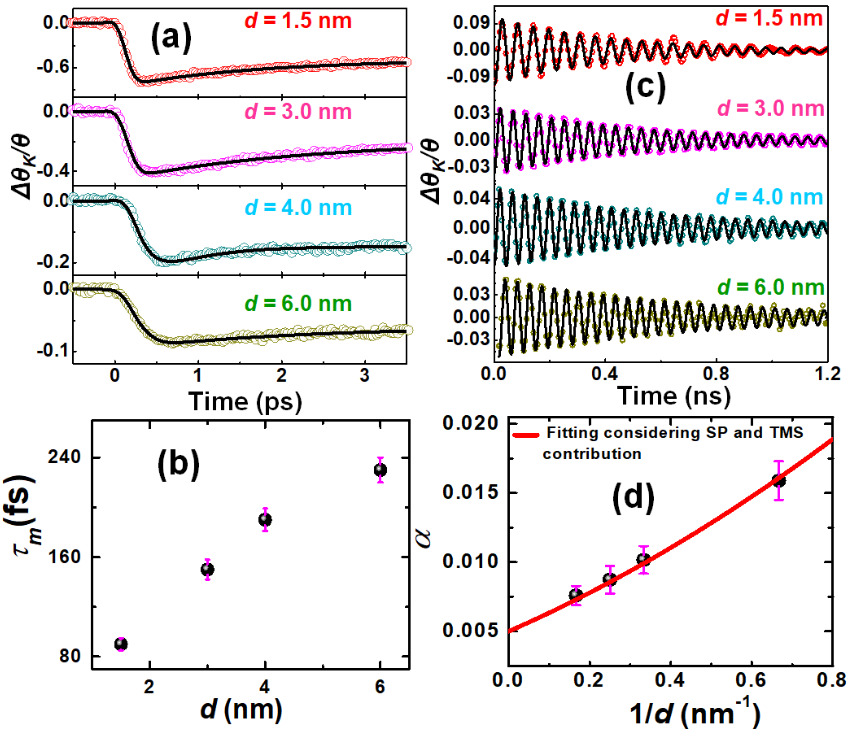

Figure 6.4: (a) Ultrafast demagnetization for SLG/CoFeB (d) measured using TR-MOKE. Solid lines are fits using equation (6.1). (b) Evolution of ultrafast demagnetization time (τ_m) with CoFeB thickness (d) in presence of SLG underlayer. (c) Precessional oscillations obtained for SLG/CoFeB (d) at a bias

magnetic field of 3.59 kOe. Solid lines are fits using equation (6.4). (d) Evolution of Gilbert damping parameter (α) with $1/d$ in presence of SLG under layer fitted with model equation (6.3) (red solid line).

From the Kittel fit, we extracted M_{eff} and g as the fitting parameters. While g was found to be constant at 2.0 ± 0.1 for all samples, M_{eff} increased with CoFeB thickness (Shown in Table-6.2). We also extracted the saturation magnetization (M_S) and interfacial magnetic anisotropy energy density (K_s) from the relation $4\pi M_{eff} = 4\pi M_S - 2K_S/M_s d$ to be 1327 ± 46 emu/cc and 0.655 ± 0.02 erg/cm^2, respectively, in the reference CoFeB films, while in presence of SLG, M_s decreased to 1220 ± 34 emu/cc but K_s increased slightly to 0.667 ± 0.01 erg/cm^2. This decrease in M_s can be attributed to charge transfer across the SLG/CoFeB interface [19, 64-66] and induced hybridization between graphene π-band and d-band of Co/Fe. We have not observed any uniaxial magnetic anisotropy in our samples as observed in CoFeB thin film grown on soft substrates like polyimide [67] because we have grown our CoFeB films on rigid substrates without any stain. However, the CoFeB layers still show some surface anisotropy that arises due to the presence of interfaces which affect the orbital motion of electrons due to symmetry breaking [68].

After extracting relaxation time τ and M_{eff}, we estimated α using the expression [69]:

$$\alpha = \frac{1}{\gamma\tau(H+2\pi M_{eff})} \tag{6.6}$$

Figure 6.4(c) shows the precessional dynamics of Sub/SLG/CoFeB (d)/SiO$_2$ (2 nm) samples by varying CoFeB layer thickness in the range 1.5 nm $\leq d \leq$ 6 nm at H = 3.59 kOe. We extracted α using equation (6. 6) which shows a decrease with the increase in CoFeB thickness. The variation of α with the inverse of CoFeB layer thickness in Figure 6.4(d) is fitted using equation (6.3), where the value of G_{eff} and β_{TMS} are found to be (1.24 ± 0.10) × 10^{15} cm^{-2} and (5.67 ± 0.07) × 10^{-17} cm^2, respectively. The obtained value of G_{eff} is on the higher side of the regularly used high-SOC strength materials [70] like Pt, Ta, W etc.

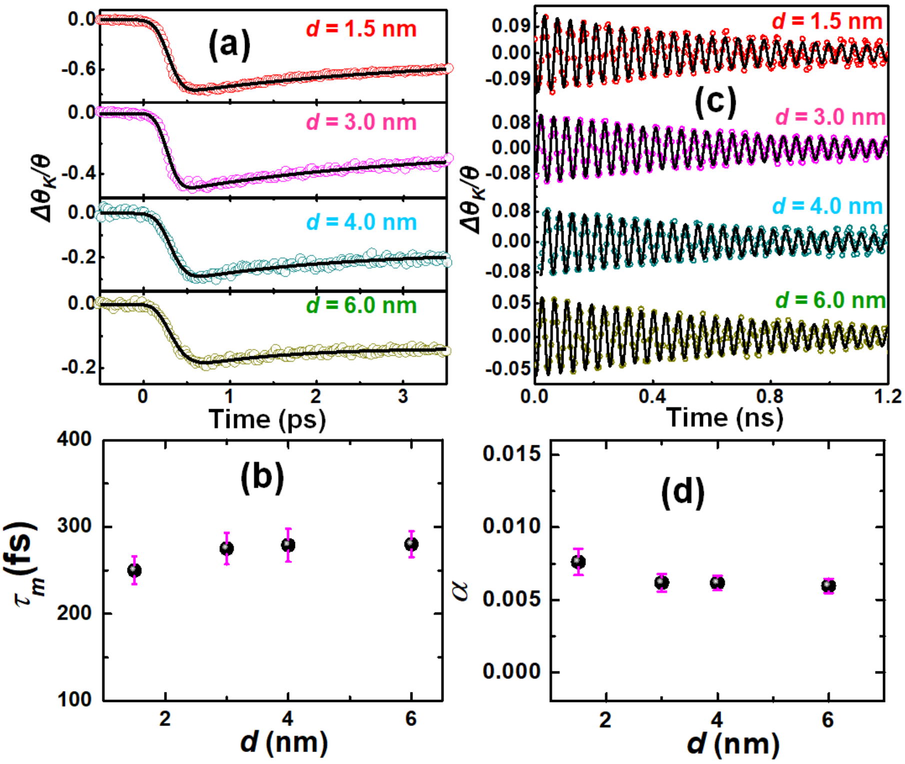

Figure 6.5: (a) Ultrafast demagnetization for CoFeB (*d*) measured using TR-MOKE. Solid lines are fits using equation (6.1). (b) Evolution of ultrafast demagnetization time (τ_m) with CoFeB thickness (*d*) in absence of SLG underlayer. (c) Precessional oscillations obtained for CoFeB (*d*) at a bias magnetic field of 3.59 kOe. Solid lines are fits using equation (6.4). (d) Evolution of Gilbert damping parameter (α) with *d* in absence of SLG under layer.

To underpin the effect of SLG, we also investigated the magnetization dynamics for the reference samples Sub/CoFeB (*d*)/SiO_2 (2 nm) in the same thickness range and measurement configuration. Figure 6.5(a) shows the laser-induced ultrafast demagnetization obtained for different CoFeB thicknesses in Sub/CoFeB (*d*)/SiO_2 (2 nm) samples. Variation of τ_m in the absence of SLG is plotted in Figure 6.5(b) which shows a value of about 280 ± 10 fs independent of CoFeB thickness. Figure 6.5(c) shows the precessional dynamics for the reference samples. Variation of α in the absence of SLG is plotted in Figure 6.5(d) which shows a nearly constant value of 0.006 ± 0.0005 independent of CoFeB thickness.

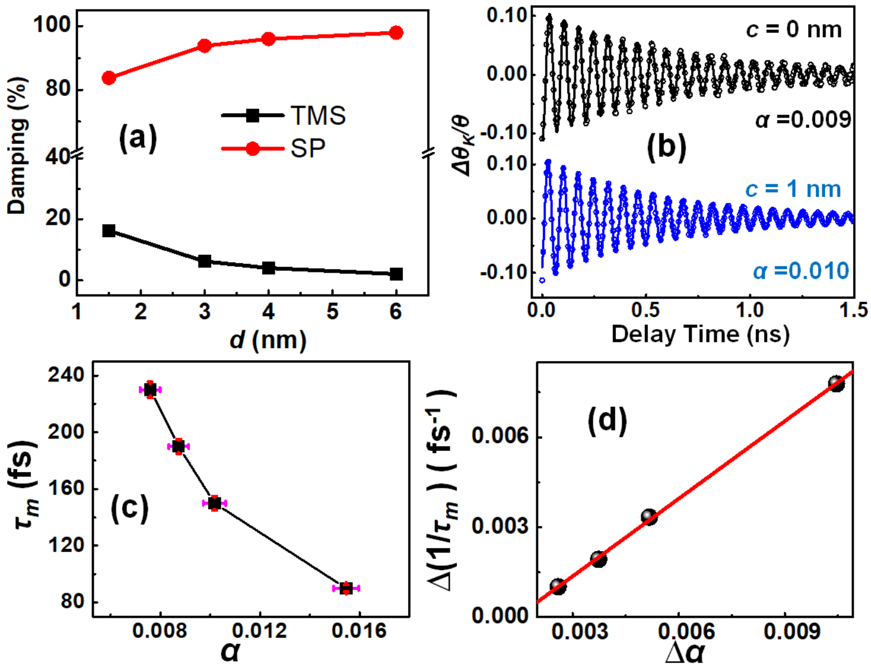

Figure 6.6: (a) Contributions of spin pumping (SP) and TMS to the Gilbert damping modulation in SLG/CoFeB (d). (b) TR-MOKE trace showing precessional oscillations for Sub/SLG/Cu (c)/CoFeB (3 nm)/SiO$_2$ (2 nm) at a bias magnetic field of 3.59 kOe. (c) Ultrafast demagnetization time (τ_m) as a function of Gilbert damping parameter (α). Solid line is a guide to the eye. (d) The variation of ultrafast demagnetization rate ($\Delta\frac{1}{\tau_m}$) as a function enhancement of Gilbert damping ($\Delta\alpha$). The red line indicates the fitting using equation (6.7).

We have plotted the percentage contribution of both TMS and spin pumping to damping modulation in Figure 6.6(a) which shows the contribution of TMS to damping modulation ($\beta_{TMS}d^{-2}$) is about 10 times smaller than the spin pumping contribution. At lower thickness, TMS contribution becomes slightly higher (but remains much lower than spin pumping contribution) which is due to higher roughness in lower thickness films as confirmed by AFM and XRR results. We have found α to be marginally high at the lower field and constant at higher field values. Recent studies have suggested that the extrinsic contributions to damping arising from defects and inhomogeneities can be suppressed effectively by applying a high enough external magnetic field [45, 71]. The intrinsic Gilbert damping is independent of the external field, while the extrinsic contributions arising from the defects are magnetic field dependent [45,72]. Thus, the field-independent damping at higher magnetic field values in our case rules out any extrinsic contributions to the magnetization dynamics in this field regime. We have also correlated the CoFeB-thickness-dependent α and τ_m at H = 3.59 kOe where defect-induced contributions have little or no role to play.

We have subsequently introduced a thin copper spacer layer of 1 nm thickness between the SLG and CoFeB layers to investigate the presence of other possible interfacial effects like spin memory loss

(SML) in SLG/CoFeB thin films. The time-resolved Kerr rotation data in the presence and absence of the copper spacer layer are presented in Figure 6.6(b) at H = 3.59 kOe. No significant damping modulation is observed with the introduction of the copper spacer layer, confirming that other possible interface effects like SML, which could affect the damping modulation, is absent in SLG/CoFeB heterostructures. By plotting τ_m vs α for our SLG/CoFeB system in Figure 6.6(c), we have observed a decrease in τ_m with α. As spin pumping-induced pure spin current transport from CoFeB to SLG is the dominant contribution to α, this spin current at the femtosecond time scale may give rise to a lowering of the demagnetization time by contributing an additional dissipation channel. An approximately linear relationship between the change of the ultrafast demagnetization rate ($\Delta\frac{1}{\tau_m}$) and Gilbert damping modulation ($\Delta\alpha = \alpha - \alpha_0$) is confirmed and shown in Figure 6.6(d), which can be fitted using the following equation [45]:

$$\Delta\frac{1}{\tau_m} = \frac{\mu_s}{\hbar}(\alpha - \alpha_0), \text{ where } \quad \Delta\frac{1}{\tau_m} = {}^{1}\!/_{(\tau_m)_{SLG/CoFeB}} - {}^{1}\!/_{(\tau_m)_{CoFeB}} \qquad (6.7)$$

Here $(\tau_m)_{CoFeB}$ is the values of τ_m in absence of SLG and and μ_s is the spin chemical potential proportional to spin accumulations at the SLG/CoFeB interface. According to the laser-induced ultrafast super-diffusive spin transport model, μ_s largely contributes to the ultrafast demagnetization process [43]. Taking the value of $(\tau_m)_{CoFeB}$ and α_0 as 280 fs and 0.006 respectively, we have obtained a reasonable value of $\mu_s \approx 0.56$ eV from the fit. From this, we can conclude that τ_m in the CoFeB layer was accelerated and the α was enhanced with the insertion of the SLG layer via spin pumping-induced interfacial spin accumulations.

6.4 Conclusions

In short, we have investigated the effect of SLG on the τ_m and α of SLG/CoFeB thin films using an all-optical TR-MOKE magnetometry. By varying the CoFeB thickness (d) from 1.0 to 6.0 nm in presence of SLG, we found the τ_m to increase with d. By analyzing the variation of α with d, we have extracted the value of G_{eff} and β_{TMS} at the SLG/CoFeB interface to be (1.24 ± 0.10) × 10^{15} cm^{-2} and (5.67 ± 0.07) × 10^{-17} cm^{2}, respectively. We have isolated the contribution of TMS from spin pumping, which shows spin pumping to be the dominant contributor to α-modulation. Negligible modulation of α with the insertion of Cu spacer confirms the absence of other interface effects in SLG/CoFeB. We have established an inverse relationship between τ_m and α in SLG/CoFeB heterostructures due to the dominance of the interfacial spin accumulation and pure spin currents transport via spin pumping mechanism to the ultrafast demagnetization process. Therefore, our study has enlightened a new path for a qualitative understanding of ultrafast demagnetization and damping in graphene-based heterostructures, which may lead a step forward towards graphene-based ultrafast spin-based devices.

References

1. K. S. Novoselov, A. K. Geim, S. V. Morozov, D. Jiang, Y. Zhang, S. V. Dubonos, I. V. Grigorieva and A. A. Firsov, Science **306**, 666-669 (2004).
2. W. Han, R. K. Kawakami, M. Gmitra and J. Fabian, Nat. Nanotechnol. **9**, 794-807 (2014).
3. N. Tombros, C. Jozsa, M. Popinciuc, H. T. Jonkman and B. J. V. Wees, Nature **448**, 571-574 (2007).
4. J. Panda, M. Ramu, O. Karis, T. Sarkar and M. V. Kamalakar, ACS Nano **14**, 12771−12780 (2020).
5. M. V. Kamalakar, C. Groenveld, A. Dankert and S. P. Dash, Nat. Commun. **6**, 6766 (2015).
6. T. Y. Yang, J. Balakrishnan, F. Volmer, A. Avsar, M. Jaiswal, J. Samm, S. R. Ali, A. Pachoud, M. Zeng, M. Popinciuc, G. Güntherodt, B. Beschoten and B. Özyilmaz, Phys. Rev. Lett. **107**, 047206 (2011).
7. D. Huertas-Hernando, F. Guinea and A. Brataas, Phys. Rev. B **74**, 155426 (2006).
8. A. K. Geim and K. S. Novoselov, Nat. Mater. **6**, 183-191 (2007).
9. P. Avouris, Z. Chen and V. Perebeinos, Nat. Nanotechnol. **2**, 605-615 (2007) .
10. Z. H. Ni, H. M. Wang, J. Kasim, H. M. Fan, T. Yu, Y. H. Wu, Y. P. Feng and Z. X. Shen, Nano Lett. **7**, 2758-2763 (2007).
11. S. D. Sarma, S. Adam, E. H. Hwang and E. Rossi, Rev. Mod. Phys. **83**, 407-470 (2011).
12. S. Sinha, S. Pan, S. Choudhury, J. Sinha and A. Barman, J. Phys. Chem. C **121**, 17442-17449 (2017).
13. V. V. Cheianov and V. I. Fal'ko, Phys. Rev. Lett. **97**, 226801 (2006).
14. M. Fuchs, J. Schliemann and B. Trauzettel, Phys. Rev. B **88**, 245441 (2013).
15. J. Fischer, B. Trauzettel and D. Loss, Phys. Rev. B **80**, 155401 (2009).
16. N.D. Mermin, Phys. Rev. **176**, 250-254 (1968).
17. S. Deng and V. Berry, Mater. Today **19**, 197-212 (2016).
18. A. H. Castro Neto and F. Guinea, Phys. Rev. Lett. **103**, 026804 (2009).
19. T. Abtew, B. C. Shih, S. Banerjee and P. Zhang, Nanoscale **5**, 1902-1909 (2013).
20. G. Bertoni, L. Calmels, A. Altibelli and V. Serin, Phys. Rev. B **71**, 075402 (2005).
21. Y. Matsumoto, S. Entani, A. Koide, M. Ohtomo, P.V. Avramov, H. Naramoto, K. Amemiya, T. Fujikawa and S. Sakai, J. Mat. Chem. C **1**, 5533-5537 (2013).
22. S. Achilli, S. Tognolini, E. Fava, S. Ponzoni, G. Drera, C. Cepek, L. L. Patera, C. Africh, E. D. Castillo, M. I. Trioni and S. Pagliara, New J. Phys. **20**, 103039 (2018).
23. A. Avsar, J. Y. Tan, T. Taychatanapat, J. Balakrishnan, G. K. W. Koon, Y. Yeo, J. Lahiri, A. Carvalho, A. S. Rodin, E. C. T. O'Farrell, G. Eda, A. H. Castro Neto and B. Özyilmaz, Nat. Commun. **5**, 4875 (2014).
24. Z. Tang, E. Shikoh, H. Ago, K. Kawahara, Y. Ando, T. Shinjo and M. Shiraishi, Phys. Rev. B **87**, 140401 (2013).
25. A. K. Patra, S. Singh, B. Barin, Y. Lee, J. H. Ahn, E. D. Barco, E. R. Mucciolo and B. Özyilmaz, Appl. Phys. Lett. **101**, 162407 (2012).
26. Z. Wang, C. Tang, R. Sachs, Y. Barlas and J. Shi, Phys. Rev. Lett. **114**, 016603 (2015) .

27. G. Schmidt, D. Ferrand, L. W. Molenkamp, A. T. Filip and B. J. V. Wees, Phys. Rev. B **62**, 4790 (R) (2000).
28. W. Han, K. M. McCreary, K. Pi, W. H. Wang, Y. Li, H. Wen, J. R. Chen and R. K. Kawakami, J. Magn. Magn. Mater. **324**, 369-381 (2012).
29. Y. Tserkovnyak, A. Brataas and G.E.W. Bauer, Phys. Rev. Lett. **88**, 117601 (2002).
30. Y. Tserkovnyak, A. Brataas and G.E.W. Bauer, Phys. Rev. B **66**, 224403 (2002).
31. A. J. Berger, W. Amamou, S. P. White, R. Adur, Y. Pu, R. K. Kawakami and P. C. Hammel, J. Appl. Phys. **115**, 17C510 (2014).
32. C. H. Back, R. Allenspach, W. Weber, S. S. P. Parkin, D. Weller, E. L. Garwin and H. C. Siegmann, Science **285**, 864-867 (1999).
33. C. H. Back and D. Pescia, Nature **428**, 808-809 (2004).
34. T. Devoldera, C. Chappert and P. Crozat, Appl. Phys. Lett. **86**, 062505 (2005).
35. M. Nakayamaa, T. Kai, N. Shimomura, M. Amano, E. Kitagawa, T. Nagase, M. Yoshikawa, T. Kishi, S. Ikegawa and H. Yoda, J. App. Phys. **103**, 07A710 (2008) .
36. C. D. Stanciu, F. Hansteen, A.V. Kimel, A. Kirilyuk, A. Tsukamoto, A. Itoh and Th. Rasing, Phys. Rev. Lett. **99**, 047601 (2007).
37. E. Beaurepaire, J. C. Merle, A. Daunois and J. Y. Bigot, Phys. Rev. Lett. **76**, 4250-4253 (1996).
38. F. Siegrist, J. A. Gessner, M. Ossiander, C. Denker, Y. P. Chang, M. C. Schröder, A. Guggenmos, Y. Cui, J. Walowski, U. Martens, J. K. Dewhurst, U. Kleineberg, M. Münzenberg, S. Sharma and M. Schultze, Nature **571**, 240 (2019).
39. B. Koopmans, G. Malinowski, F. Dalla Longa, D. Steiauf, M. Fähnle, T. Roth, M. Cinchetti and M. Aeschlimann, Nat. Mater. **9**, 259-65 (2010).
40. J. Y. Bigot, M. Vomir and E. Beaurepaire, Nat. Phys. **5**, 515–520 (2009).
41. M. Krauß, T. Roth, S. Alebrand, D. Steil, M. Cinchetti, M. Aeschlimann and H.C. Schneider, Phys. Rev. B **80**, 180407 (2009).
42. U. Atxitia, O. Chubykalo-Fesenko, J. Walowski, A. Mann and M. Münzenberg, Phys. Rev. B **81**, 174401 (2010).
43. M. Battiato, K. Carva and P.M. Oppeneer, Phys. Rev. Lett. **105**, 027203 (2010).
44. W. Zhang, W. He, X. Q. Zhang, Z. H. Cheng, J. Teng and M. Fähnle, Phys. Rev. B **96**, 220415 (2017).
45. W. Zhang, Q. Liu, Z. Yuan, K. Xia, W. He, Q. F. Zhan, X. Q. Zhang and Z. H. Cheng, Phys. Rev. B **100**, 104412 (2019).
46. S. N. Panda, S. Mondal, J. Sinha, S. Choudhury and A. Barman, Sci. Adv. **5**, eaav7200 (2019).
47. A.C. Ferrari and D.M. Basko, Nat. Nanotechnol. **8**, 235-246 (2013).
48. P**.** Venezuela, M. Lazzeri and F. Mauri, Phys. Rev. B **84**, 035433 (2011).
49. A. C. Ferrari, Solid State Commun. **143**, 47 (2007).
50. T. Mashoff, D. Convertino, V. Miseikis, C. Coletti, V. Piazza, V. Tozzini, F. Beltram and S. Heun, Appl. Phys. Lett. **106**, 083901 (2015).
51. L. G. Cançado, K. Takai, T. Enoki, M. Endo, Y. A. Kim, H. Mizusaki, A. Jorio, L. N. Coelho, R. Magalhães-Paniago and M.A. Pimenta, Appl. Phys. Lett. **88**, 163106 (2006).
52. A. K. Chaurasiya, A. Kumar, R. Gupta, S. Chaudhary, P. K. Muduli and A. Barman, Phys.Rev. B **99**, 035402 (2019).
53. S.H. Mohameda, F.M. El-Hossarya, G.A. Gamalb and M.M. Kahlid, Acta Physica Polonica A **115**, 704 (2009).

54. Y. Cao and C. Zhou, J. Magn. Magn. Mater. **333**, 1–7 (2013).
55. L. Zhou, L. Fox, M. Włodek, L. Islas, A. Slastanova, E. Robles, O. Bikondoa, R. Harniman, N. Fox, M. Cattelan and W. H. Briscoe, Carbon **136**, 255-261 (2018).
56. M. van Kampen, C. Jozsa, J. T. Kohlhepp, P. LeClair, L. Lagae, W. J. M. de Jonge and B. Koopmans, Phys. Rev. Lett. **88**, 227201 (2002).
57. A. Barman and J. Sinha, Spin Dynamics and Damping in Ferromagnetic Thin Films and Nanostructures (Springer: Switzerland, 2018).
58. F. Dalla Longa, J. T. Kohlhepp, W.J.M. De Jonge and B. Koopmans, Phys. Rev. B **75** , 224431 (2007).
59. G. Malinowski, F. Dalla Longa, J. H. H. Rietjens, P. V. Paluskar, R. Huijink, H. J. M. Swagten and B. Koopmans, Nat. Phys. **4**, 855-858 (2008).
60. C. Weeks, J. Hu, J. Alicea, M. Franz and R. Wu, Phys. Rev. X **1**, 021001 (2011).
61. D. Ma, Z. Li and Z. Yang, Carbon **50**, 297 – 305 (2012).
62. J. M. Shaw, H. T. Nembach and T. J. Silva, Phys. Rev. B **85**, 054412 (2012).
63. L. Zhu, D.C. Ralph and R. A. Buhrman, Phys. Rev. Lett. **123**, 057203 (2019).
64. G. Wu, Y. Ren, X. He, Y. Zhang, H. Xue, Z. Ji, Q. Y. Jin and Z. Zhang, Phys. Rev. Appl. **13**, 024027 (2020).
65. T. Aizawa, R. Souda, Y. Ishizawa, H. Hirano, T. Yamada, K.I. Tanaka and C. Oshima, Surf. Sci. **237**, 194 (1990).
66. K. Yamamoto, M. Fukushima, T. Osaka and C. Oshima, Phys. Rev. B **45**, 11358 (1992).
67. H. Zhang, Y. Li, M. Yang, B. Zhang, G. Yang, S.Wang and K. Wang, Chin. Phys. B **24**, 077501 (2015).
68. A. Stupakiewicz, A. Kirilyuk, A. Fleurence, R. Gieniusz, T. Maroutian, P. Beauvillain, A. Maziewski and Th. Rasing, Phys. Rev. B **80**, 094423 (2009).
69. J. Walowski, M. D. Kaufmann, B. Lenk, C. Hamann, J. McCord and M. Münzenberg, J. Phys. D: Appl. Phys. **41**, 164016 (2008).
70. S. N. Panda, S. Majumder, A. Bhattacharyya, S. Dutta, S. Choudhury and A. Barman, ACS Appl. Mater. Interfaces **17**, 20875–20884 (2021).
71. Y. Fan, X. Ma, F. Fang, J. Zhu, Q. Li, T. P. Ma, Y. Z. Wu, Z. H. Chen, H. B. Zhao and G. Lüpke, Phys. Rev. B **89**, 094428 (2014).
72. G. Woltersdorf, M. Buess, B. Heinrich and C. H. Back, Phys. Rev. Lett. **95**, 037401 (2005).

Chapter-7

Role of spin-orbit coupling on ultrafast spin dynamics in nonmagnetic/ferromagnetic heterostructures

7.1 Introduction

The pioneering work by Beaurepaire *et al.* in 1996 on femtosecond laser-induced demagnetization opened up a new avenue towards the ultrafast manipulation of magnetization in magnetic materials [1]. This work demonstrated that when a femtosecond pulsed laser interacts with a ferromagnetic material, the magnetic moment is rapidly quenched within a sub-picosecond time scale followed by fast recovery of magnetization (fast remagnetization) within tens of picoseconds. Following that, many theoretical and experimental studies were performed on various magnetic materials and their heterostructures to investigate the underlying mechanisms behind ultrafast demagnetization [2-7]. On one hand, these studies have been driven by the thirst to understand the fundamental interactions among the photons, spins, electrons and lattices in magnetic materials on ultrafast time scale. On the other hand, faster demagnetization and remagnetization times promise for the development of ultrafast storage and memory devices as ultrafast demagnetization is believed to be one of the key phenomena involved in all-optical switching (AOS), which can revolutionize modern data storage and memory industries through the optical manipulation of magnetic bits [8-11]. Despite these studies over the last three decades, a clear understanding of the microscopic mechanism behind ultrafast demagnetization remained highly debatable. Researchers claimed that the ultrafast demagnetization is originated from the direct interaction of FM materials with the laser field, where various spin-flip scattering (SFS) processes such as Elliott-Yafet (EY)-like electron-phonon scattering [2], relativistic spin-flip scattering [3], Coulomb scattering [4] and electron-magnon scattering [5] are expected to be involved. It was argued that ultrafast demagnetization is a cooperative effect of the laser field and the SOC of magnetic material [6].

The NM/FM heterostructures are promising as the backbone for future spin-orbitronic devices due to the presence of various SOC-driven physical phenomena such as direct and inverse spin Hall effect [12,13], Rashba-Edelstein effect [14,15] and so on. Hence, the interest in studying ultrafast demagnetization phenomena in NM/FM heterostructures has grown very recently. It was theoretically formulated and experimentally demonstrated that the super-diffusive spin current transport also plays a dominant role behind the ultrafast demagnetization in NM/FM heterostructures [7, 16-18]. In super-diffusive spin current transport, the laser-induced hot electrons travel tens of nanometres inside the material with high velocities. These hot electrons-mediated transport phenomena open up additional spin dissipation channels to accelerate the ultrafast demagnetization process.

It is known that the first contribution, i.e., direct interaction of laser field with FM material to the ultrafast demagnetization, can be controlled by choosing suitable FM materials having different scattering probabilities and SOC strengths [19]. On the other hand, the second contribution, i.e., super-diffusive spin current transport, depends upon the excitation rates, the ratio of excited spin up and spin down electrons and spin-dependent inelastic lifetimes and velocities. The presence of an adjacent NM layer can cause transmission of spin angular momentum in the NM layer and a corresponding spin backflow creating a minority spin accumulation in the FM layer, causing a stronger demagnetization. Therefore, the SOC strengths of NM materials and spin chemical potential at the interface will also play an essential role in demagnetizing such heterostructures. The latter method is more beneficial from a technological point of view. It allows one to optimize demagnetization time only by choosing a suitable NM layer without changing the FM layer. In contrast to ultrafast demagnetization, fast remagnetization is a well-understood phenomenon where heat diffusion from hot electron and spin system to lattice through electron-phonon interaction plays a dominant role [20]. The fast remagnetization process also can be controlled by varying the parameters like electron-phonon coupling strength, specific heat, magnetocrystalline anisotropy, heat diffusion process, the density of laser excitation, etc. [20-23]

The Gilbert damping constant α is another important parameter of FM materials that also controls the performance of many spintronic and magnonic devices. Therefore, controlling α is of paramount importance for optimizing the performance of such devices. For instance, magnetic materials with lower α-value are useful in magnetic read-heads due to their small write-current, while higher α-value materials are useful for faster decay of precessional motion during data writing in magnetic memory and storage devices. Notably, the damping also has two major contributions in NM/FM heterostructures. The first contribution comes from the spin-flip scattering within FM itself, whereas the other comes from the flow of spin angular momentum in the form of spin current out of the FM system due to nonlocal effects like spin pumping [24]. Although the timescale of ultrafast demagnetization (in femtoseconds) and magnetic damping (in pico and nanoseconds) differ by orders of magnitude, the fundamental underlying mechanisms involved in these two phenomena appear to be similar and interconnected [16-18, 25, 26]. Modulation of SOC strength of the NM materials in NM/FM heterostructures has already been proven to be an efficient way to control α by changing the nonlocal spin current flow contribution in the system [27]. This also indicates the possibility of controlling the ultrafast demagnetization time (τ_m) by controlling the SOC strengths of NM materials.

Tveten *et al*. theoretically predicted the possibility of explaining ultrafast demagnetization time in terms of spin current-induced damping in NM/FM heterostructures based on electron-magnon scattering theory [28]. This was later argued and experimentally demonstrated in different systems [17, 18, 29]. The femtosecond laser-induced spin current is very short-lived (sub-picosecond), while spin pumping-induced spin current can live for nanoseconds. However, despite occurring on different timescales their physical natures are similar. The femtosecond spin current causes a lowering of the demagnetization time, while the spin pumping-induced spin current leads to a lowering of the precessional relaxation time (i.e. increased damping). Therefore, ultrafast demagnetization time and Gilbert damping parameter become inversely proportional when spin current dominates. Recently, Malik *et al.* have shown that the remagnetization process of a FM material can also be controlled by tuning α using external means [30]. They have established an inverse relationship between fast remagnetization time (τ_e) and α due to the dominant contribution of magnon dynamics to the remagnetization process. Despite some efforts [16-18, 25, 29, 31, 32], a systematic study on various effects of SOC of NM materials on the ultrafast demagnetization and fast remagnetization in NM/FM heterostructures have not been performed so far. In particular, the relationship among the τ_m, τ_e and α with the SOC strength of NM in NM/FM heterostructures has never been experimentally demonstrated or theoretically formulated. In fact, investigating the correlation between τ_m and α could be a powerful method to detect the dominant mechanisms involved in the ultrafast demagnetization process. An inverse relationship between τ_m and α would validate the nonlocal spin transport as the dominant microscopic mechanism. In contrast, a direct relationship or a deviation from the inverse relationship would point towards spin-flip scattering as the major contribution to ultrafast demagnetization.

The CoFeB films are known to be promising FM material from the application point of view in spintronics devices due to the presence of several compelling properties like high tunnel magnetoresistance, low Gilbert damping, negligible magnetocrystalline anisotropy and large spin polarization [33]. Therefore, we have chosen CoFeB as the FM material deposited on various NM underlayers such as Cu, Ta, W, Pt, Ta/Ru/Ta (TRT hereafter) and Si/SiO_2 (no underlayer), that span a wide range in SOC strength. Our results show that despite having different timescales, the key dynamic parameters: τ_m, τ_e and α are systematically modulated with the SOC strength of the NM underlayer, which indicates the dominant role of spin current inside the NM material in determining those. Stronger SOC of NM underlayer is found to generate more efficient spin current transport through the NM/FM interface, leading to faster demagnetization and remagnetization time and higher damping parameter. Our study demonstrates a dramatic reduction of τ_m (~ 58%) and τ_e (~ 91%) and a giant increment of α (~ 500%) when W underlayer is deposited adjacent to the CoFeB film. We propose a way to further reduce the demagnetization and remagnetization time and discuss the possibility of controlling those parameters by an electric field, which will help to develop electric field-controlled ultrafast spintronics devices.

7.2 Experimental details

The multilayer stacks for our study were deposited on Si (001)/SiO_2 (700 nm) substrates by radio frequency (RF) sputtering at room temperature at a base pressure of about 10^{-8} Torr. The multilayer stacks consist of the following layers from bottom: Si/SiO_2/NM (10)/CoFeB (5)/MgO (2)/Al_2O_3 (10), where the numbers in parentheses are the nominal thicknesses of corresponding layers in nanometres and NM stands for the nonmagnetic materials, such as Cu, Ta, W, Pt. Two reference multilayer stacks: Si/SiO_2/Ta (5)/Ru (20)/Ta (5)/CoFeB (5)/MgO (2)/Al_2O_3 (10) and Si/SiO_2/CoFeB (5)/MgO (2)/Al_2O_3 (10) were also prepared at the same deposition conditions. Here, Al_2O_3 serves as a capping or protecting layer, which stops the degradation of MgO layer and hence the CoFeB film with time. The sputter-deposited films were annealed at 280 °C in vacuum under a perpendicular magnetic field of 600 mT for about 1 hour. The annealing in vacuum ensures smooth defect-free interfaces with uniform lateral distribution of magnetic properties. In this study, we intentionally chose 5-nm-thick CoFeB film, so that its quality (i.e. roughness) and magnetic properties become independent of underlayer materials. This enabled us to investigate the effect of SOC strength of underlayer NM materials on the dynamic parameters of CoFeB while ensuring other magnetic parameters are almost identical.

The surface topography of the samples was investigated using AFM. The electron density, thickness and interface roughness of individual layers were determined by XRR measurement. XRD technique was used to detect the crystal structure and orientation of the nonmagnetic underlayers. Room temperature VSM measurements were performed by a physical property measurement system (PPMS) to estimate the static magnetic properties like saturation magnetization (M_s), saturation field (H_s) and coercive field (H_c) of these samples.

For studying ultrafast magnetization dynamics, a home-built TR-MOKE magnetometer based on a non-collinear optical pump-probe technique was used. The second-harmonic laser beam (wavelength = 400 nm, repetition rate = 1 kHz, pulse width > 35 fs) of an amplified laser system (Libra, Coherent) was used to excite the magnetization of the sample, which is termed as the pump beam. A time-delayed fundamental laser beam (wavelength = 800 nm, repetition rate = 1 kHz, pulse width ~ 35 fs) called the probe beam was used to detect this excitation. The pump beam was focused onto the sample to a spot size of about 300 μm with an oblique incidence (~ 30° with the surface normal). The probe beam was focused onto the sample to a spot size of about 100 µm with normal incidence on the sample, by maintaining an excellent spatial overlap with the pump spot. At first, a large enough magnetic field was applied at a small elevation angle (~ 10°) from the sample plane to saturate the sample magnetization along that direction before the pump pulse excitation. This magnetic field configuration ensures a finite value of the demagnetizing field along the direction of the pump pulse that helps to develop a favourable condition to induce magnetization precession in the sample. The dynamic polar Kerr signal was collected by a specially designed photodetector connected to a lock-in amplifier. All the experiments were conducted under ambient conditions and at room temperature.

7.3 Results and discussions

Static Characterization: AFM-image for Ta/CoFeB sample is shown in Figure 7.1(a). The topographical roughness (R_a) values showed negligible variation when measured at various regions of the same film stack. The average roughness obtained for all the films are listed in Table 7.1. Overall, the R_a values are found to be very small in the order of 0.11-0.17 nm for all the films, which is presumably the imprint of the interfacial roughness due to the minimal thickness of our multilayers. We thus conclude that the average interfacial roughness in these heterostructures is negligibly small and similar in all samples.

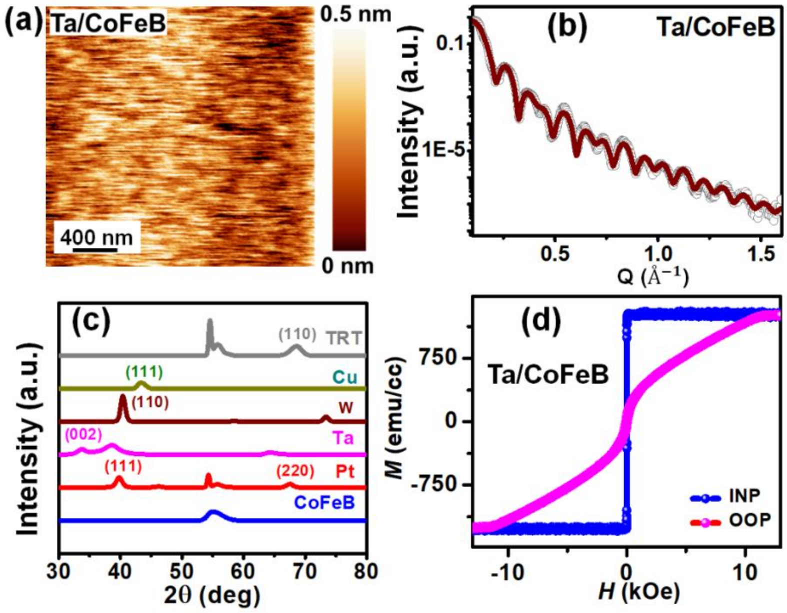

Figure 7.1: (a) Two-dimensional AFM image for Ta/CoFeB. (b) XRR-spectra (black symbols) for Ta (10 nm)/CoFeB (5 nm) sample fitted using GenX (solid red lines). (c) GI-XRD spectra for substrate and different underlayers at a grazing angle of 1°. Peaks corresponding to different crystal orientations are marked. (d) Room temperature in-plane (INP) and out-of-plane (OOP) VSM-loops for Ta (10 nm)/CoFeB (5 nm) sample.

Figure 7.1(b) shows the XRR-spectra of the Ta/CoFeB sample measured using a 1.54 Å Cu-Kα X-ray source. XRR-spectra exhibit well-defined oscillations up to a scattering vector of 1.2 $Å^{-1}$ signifying their uniform deposition. GenX software is used to analyze these spectra from where we have extracted the electron density, average interface roughness and thickness of different layers. The values of layer thicknesses obtained from the fitting are close to the nominal thickness values. Interfacial roughness and electron densities of different underlayers obtained from the fitting are tabulated in Table 7.1. The average interfacial roughness of NM/CoFeB is small and almost constant at 0.10-0.14 nm irrespective of NM underlayer similar to that obtained from AFM measurements.

Table 7.1: The topographical roughness values from AFM and parameter values obtained from fitting of XRR spectra using GenX.

Parameter	Si/SiO$_2$	Cu	TRT	Ta	Pt	W
R_a (nm) from AFM	0.13	0.12	0.17	0.15	0.11	0.11
R_a (nm) from XRR	0.12	0.14	0.10	0.11	0.14	0.12
E_d (10^{-5} × $Å^{-2}$) from XRR	2.0 (For SiO$_2$)	5.62	10.66 (For Ru)	14.10	14.38	16.8

Figure 7.1(c) shows the XRD-spectra of NM/CoFeB films at the glancing angle of 1°. Different underlayer materials show different XRD peaks corresponding to their crystal orientation as marked in the graphs. Room temperature magnetic hysteresis loops are measured in both in-plane (INP) and out-of-plane (OOP) orientation using VSM (Quantum Design PPMS). Figure 7.1(d) shows the INP and OOP hysteresis loops of Ta/CoFeB film. The values of H_s in INP and OOP configurations for this film are about 0.044 kOe and 11.4 kOe respectively, which reveals that these films have an in-plane easy axis of magnetization with negligible out-of-plane anisotropy. The values of M_s, H_c and H_s for in-plane hysteresis loops of the samples are tabulated in Table 7.2. For all these films, M_s values are obtained to be about 1150 ± 83 emu/cc. Also, these films exhibit small in-plane H_c (~ 0.026 ± 0.003 kOe) which reveals their soft-ferromagnetic nature. We do not expect significant effects of doping or intermixing of NM elements in the FM layer because we have not observed any significant modification in the structural and static magnetic properties of the samples due to the insertion of different NM underlayers adjacent to the CoFeB layer [34-36].

Investigation of Ultrafast Magnetization Dynamics: In the optical pump-probe experiment using TR-MOKE, a pump pulse perturbs the magnetic system under investigation, following which a probe pulse arrives at a pre-set delay time to detect the excited magnetic state. By scanning the delay time, the full temporal evolution of the magnet state after its initial perturbation can be followed. Several processes occur when femtosecond pump laser pulses interact with a magnetic material in an external magnetic field. First of all, the magnetization of the system is partially or fully lost within hundreds of femtoseconds [1]. This phenomenon is known as ultrafast demagnetization. Following this demagnetization process, magnetization starts to relax within a few picoseconds timescale, which results in a fast remagnetization process. This is followed by a slow remagnetization superposed with coherent precession of magnetization. In a much longer timescale of a few nanoseconds, the magnetization returns to its initial equilibrium, referred to as the damping of the precessional oscillation [37, 38].

Figure 7.2(a) shows the sample structure and experimental geometry of the TR-MOKE measurement and Figure 7.2(b) shows a representative TR-MOKE trace obtained from Ta/CoFeB sample at pump and probe fluence of 5 mJ cm^{-2} and 1 mJ cm^{-2} at a bias field of 2.80 kOe. The time-resolved Kerr rotation trace shows three-temporal regions: ultrafast demagnetization, fast remagnetization and slow remagnetization superposed with damped coherent precession. To extract the values of ultrafast demagnetization and fast remagnetization times, we use a simplified expression based on a phenomenological thermodynamic model, known as the three-temperature model, where the transient change in magnetization can be expressed as [39, 40]

$$-\frac{\Delta M_z}{M_z} = \left[\left\{\frac{A_1}{(t/\tau_0+1)^{\frac{1}{2}}} + \frac{A_1\tau_m - A_2\tau_e}{\tau_e - \tau_m} e^{-t/\tau_m} + \frac{A_2\tau_e - A_1\tau_e}{\tau_e - \tau_m} e^{-t/\tau_e}\right\} H(t) + A_3\delta(t)\right] \otimes G\,(t) \qquad (7.1)$$

This simplified expression is based on the model that a magnetic system has three coupled subsystems: electron, spin and lattice. Upon femtosecond laser excitation temperature of the electronic system rapidly increases populating hot electrons above the Fermi level. These hot electrons excite their spin degrees of freedom by electron-magnon interaction, resulting in an instantaneous system magnetization quenching. In due course, the distribution of energy between the three coupled subsystems results in a fast relaxation of quenched magnetization. In equation (7.1), A_1 is proportional to magnetization amplitude after fast relaxation, A_2 represents the maximum electron temperature rise, while A_3 stands for the magnitude of state filling effects. The τ_0 represents the cooling time through heat diffusion. $H(t)$, $\delta(t)$ and $G(t)$ are the Heaviside step function, Dirac-delta function and a Gaussian function corresponding to the laser pulse. The ultrafast demagnetization time τ_m mirrors the timescale of magnetization loss and τ_e the fast remagnetization time, represents the timescale of electron-phonon interaction.

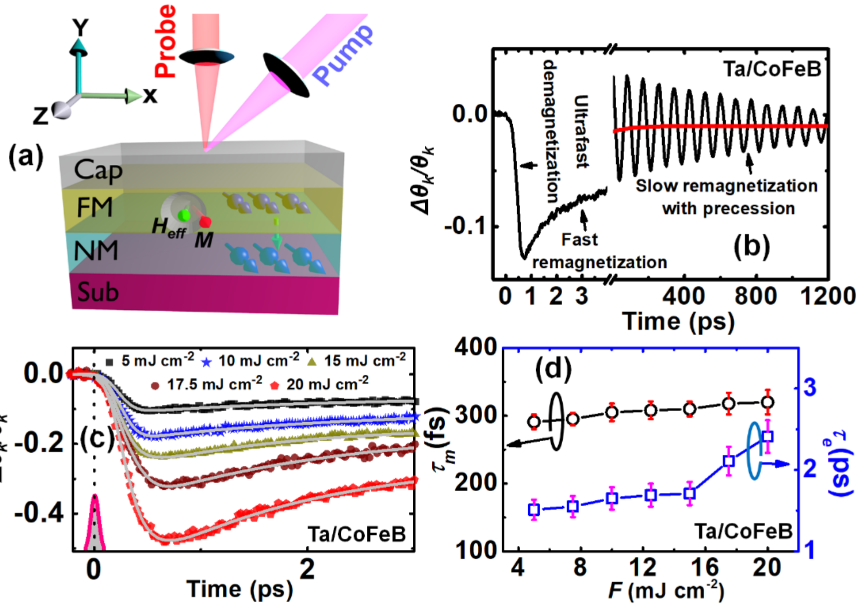

Figure 7.2: (a) Sample structure and experimental geometry. (b) Typical TR-MOKE signal obtained from the Ta (10 nm)/CoFeB (5 nm) heterostructure where different temporal regions are marked. The solid red line shows the biexponential slow remagnetization background. (c) Laser fluence-dependent ultrafast demagnetization curves for Ta (10 nm)/CoFeB (5 nm) heterostructure (symbols). The solid lines represent the fitted curves using equation (7.1). (d) Variation of ultrafast demagnetization time (τ_m) and fast relaxation time (τ_e) with laser fluence.

Figure 7.2(c) shows the ultrafast demagnetization obtained for different pump fluence values for Ta/CoFeB. We have fitted the demagnetization curves using equation (7.1) to extract the values of τ_m and τ_e. A minor increment in τ_m and τ_e with the pump fluence is observed (shown in Figure 7.2(d)). The increase in τ_m with pump fluence is mainly due to the enhanced spin fluctuations at the more elevated temperature of the spin system and the corresponding increment in dynamic longitudinal susceptibility and decrement in exchange interaction strength [21]. An increase in τ_e with pump fluence can be explained by the fact that higher fluence causes a rise in electron temperature followed by spin temperature. Hence, magnetization takes longer for its recovery to its initial equilibrium condition [22]. We have also observed a small time delay between the arrival of the pump pulse (zero delay) and the onset of the demagnetization, i.e., a time smearing effect. This 'delay of demagnetization' becomes shorter with an increase in the pump fluence (as shown in Figure 7.2c). A plausible explanation for this is the dependence of the delay on the electron-thermalization time, which is eventually proportional to the electron density or the pump fluence [41]. Liu *et al*. [42] have shown that delay in demagnetization after pump pulse excitation is a fraction of the laser pulse width, which is much shorter than the demagnetization time and remagnetization time obtained from the theoretical fit. Moreover, to avoid this time smearing effect, we have maintained a constant pump and probe fluences of 5 mJ cm^{-2} and 1 mJ cm^{-2}, respectively, for all comparative measurements and kept all the measurement conditions identical.

Spin Pumping in NM/FM Heterostructure and Extraction of α: During the dynamic measurements, a large static magnetic field is applied at a small angle (θ_c) with respect to the sample plane. Since θ_c is very small, the dominant component of this field is in the in-plane direction and we considered that in-plane component as the bias magnetic field (H). This tilt of magnetization from the sample plane ensures a finite demagnetizing field along the direction of the pump pulse, which is subsequently modified by the pump pulse to result in a change of the equilibrium orientation from θ_c to θ_c', triggering an initial precession of the magnetization in the sample around its new equilibrium orientation [37]. This is routinely used to induce coherent precessional motion of magnetization in ferromagnetic thin films and nanostructures using the all-optical TR-MOKE technique [38]. In an NM/FM heterostructure, there are two significant contributions to damping. The first contribution comes from the local spin-flip scattering that is unavoidable and causes energy dissipation within the FM layer itself. Another contribution arises due to the energy dissipation from the FM to NM, which is nonlocal and controllable. In the presence of coherent magnetization precession of the FM layer, a spin accumulation at NM/FM interface occurs and then gradually dissipates in the adjacent NM layer by a generation of the pure spin current leading to an enhancement of the α of the NM/FM heterostructure. This effect is widely known as spin pumping. In spin pumping, the flow of spins through the NM/FM interface is determined by the electronic conductance properties of the spin channels at the interfaces, which can be parametrized by G_{eff} [43]. Using spin pumping formalism, G_{eff} can be expressed as [44]:

$$G_{eff} = \frac{4\pi t_{FM} M_{eff}}{g\mu_B}(\alpha - \alpha_0) \tag{7.2}$$

Here M_{eff} is the effective magnetization, t_{FM} is ferromagnetic layer thickness, α is the Gilbert damping parameter in the presence of a NM underlayer and α_0 denotes intrinsic Gilbert damping parameter in the absence of any NM underlayer.

The damping constant α can be extracted from the time-resolved Kerr rotation as shown in Figure 7.2(b), which contains the biexponential slow relaxation background superimposed with damped precessional oscillation. First, we subtract the bi-exponential background and fit the background-subtracted data using a damped harmonic function given as [41]:

$$\theta(t) = \theta(0)e^{-\left(\frac{t}{\tau}\right)}\sin(2\pi f t) \tag{7.3}$$

Here $\theta(0)$ is the initial amplitude of magnetization precession, τ is the precessional relaxation time obtained as a fitting parameter and f is the frequency of oscillation that can be directly extracted from the fast Fourier transform (FFT) of the precessional oscillation. To extract M_{eff} of a sample, we fit the bias magnetic field (H) dependent f by using the Kittel formula expressed as [45]:

$$f = \frac{\gamma}{2\pi} \left(H\left(H + 4\pi M_{eff}\right)\right)^{1/2} \tag{7.4}$$

Here, γ ($= g\mu_B/\hbar$) represents the gyromagnetic ratio, g is the Lande g-factor, μ_B is the Bohr magneton and $\hbar$ is reduced Planck's constant. We extract M_{eff} and g as the fitting parameters from the Kittel fit. After extracting τ and M_{eff}, we can estimate α using the following expression [46]:

$$\alpha = \frac{1}{\gamma\tau\left(H + 2\pi M_{eff}\right)} \tag{7.5}$$

Here γ value is taken to be 1.76×10^7 Hz/Oe [44]. From the laser pump fluence-dependent precessional dynamics, we have observed that τ decreases and α increases by a small amount with the pump fluence in the range of 10-20 mJ cm^{-2}, but remains almost unchanged below 10 mJ cm^{-2}. Hence, to avoid any laser-induced heating effect, all the comparative measurements were performed at a low enough pump and probe fluence of 5 mJ cm^{-2} and 1 mJ cm^{-2}, respectively.

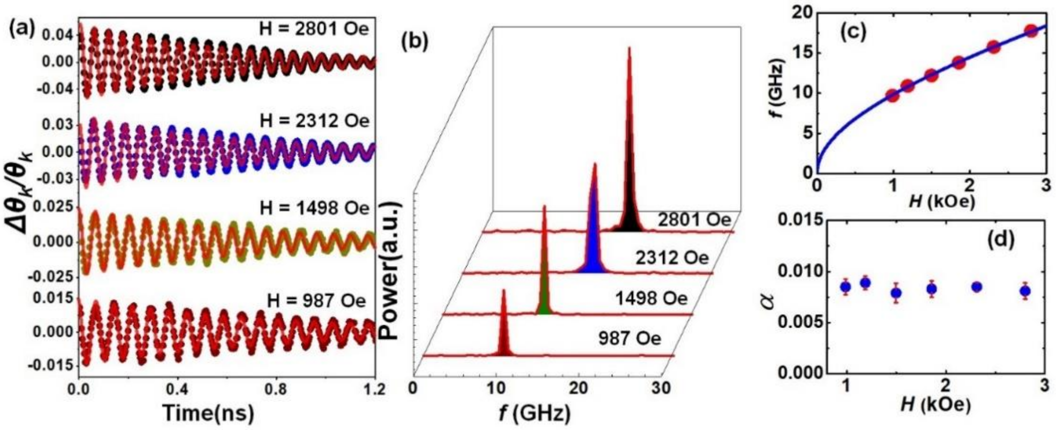

Figure 7.3: (a) Bias magnetic field (H) dependent time-resolved magnetization precession for Ta (10 nm)/CoFeB (5 nm) heterostructure. The symbols represent experimental data points and the solid lines represent fits with a damped sinusoidal function. (b) Corresponding FFT power spectra of the precessional oscillations. (c) H-dependence of precessional frequency (f) for Ta (10 nm)/CoFeB (5 nm) heterostructure and the corresponding Kittel fit (solid line). (d) H-dependence of Gilbert damping parameter (α) as for Ta (10 nm)/CoFeB (5 nm) heterostructure.

Figure 7.3(a) shows the bias field-dependent precessional oscillation for Ta/CoFeB film fitted with equation (7.3). In contrast, Figures 7.3(b) and 7.3(c) show the corresponding FFT spectra and dependence of f on H fitted with the Kittel formula (equation (7.4)). We have obtained the value of g to be 2.0 ± 0.05 from the fit. The values of M_{eff} for our film stacks are tabulated in Table 7.2. The average value of M_{eff} for our films is obtained to be 997 ± 57 emu cc^{-1}, which is slightly lower than the

M_s value obtained from VSM indicating the presence of a small interfacial anisotropy in our heterostructures, which is not surprising for a 5-nm-thick CoFeB film. Here, the extracted value of α is independent of H (Figure 7.3(d)). Recent studies show that in the presence of extrinsic contributions like two-magnon scattering [47], α increases with H, while effects like spin dephasing [48] cause a decrease in α with the rise of H. An H-independent behaviour of α indicates a negligible contribution from those extrinsic sources in our samples.

Table 7.2: Values of saturation magnetization (M_s), coercivity (H_c), saturation field (H_s) (obtained from in-plane VSM loops using PPMS) and effective magnetization (M_{eff}) (obtained from analyzing TR-MOKE data).

Underlayer	M_s (emu cc^{-1})	H_c (Oe)	H_s (Oe)	M_{eff} (emu cc^{-1})
Si/SiO$_2$	1278	25	40	1075
Cu	1095	24.5	45	920
TRT	1028	24.4	46.8	952
Ta	1182	25	44	1018
Pt	1174	27	44.4	1037
W	1046	33	57	984

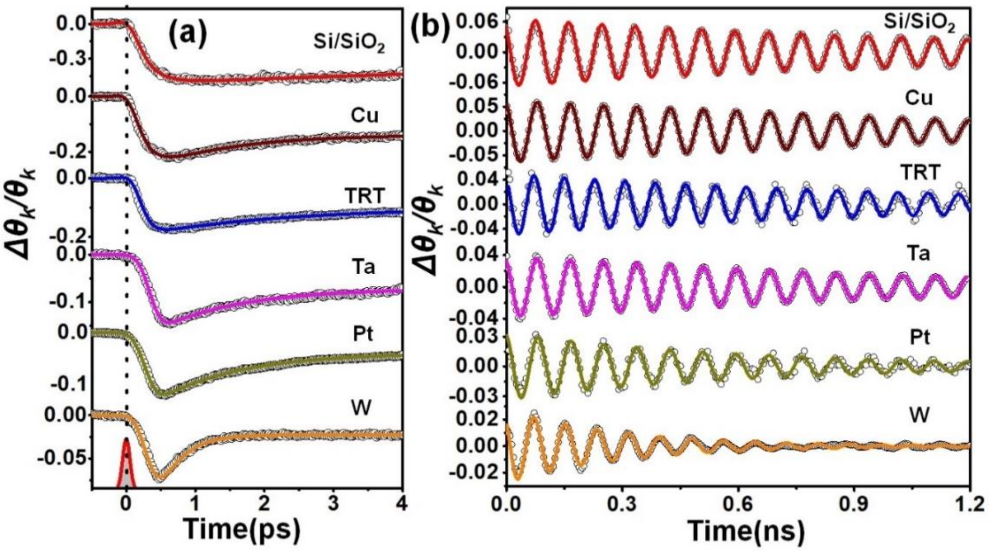

Figure 7.4: (a) Ultrafast demagnetization curves for (Ta, Pt, W, Cu, TRT)/CoFeB heterostructures in comparison with reference CoFeB thin film without any underlayer (denoted by Si/SiO$_2$). (b) Time-resolved magnetization precession for (Ta, Pt, W, Cu, TRT, Si/SiO$_2$)/CoFeB heterostructures at H = 2.80 kOe.

SOC-dependent Modulation of Magnetization Dynamics: Figures 7.4(a) and 7.4(b) show the ultrafast demagnetization and precessional oscillation for NM/CoFeB thin films with different NM underlayers. Before discussing the variation of τ_m and τ_e with NM material's SOC strength, we first must determine their SOC strength. There are some proposals based on simple hydrogen atom model that the SOC strength should scale with Z^4 (Z = atomic number). However further studies on this inferred that for actual atoms this assumption severely overestimates the value of SOC strength [49, 50]. Although our experimental method does not allow us to determine the quantitative values of SOC strength directly, we can still get some qualitative measure of the SOC strength. First, the modulation of α from its intrinsic value in the NM/CoFeB heterostructures can be considered as a measure of the SOC strength of the NM layer as all other external conditions (*i.e.,* laser fluence, interfacial roughness, film thicknesses, etc.) that may affect α are nearly invariant throughout our measurement. Second, the spin-mixing conductance G_{eff}, which is a measure of the efficiency of spin current transport across the NM/CoFeB interface, can also be considered as a measure of the SOC strength of the NM material under the condition that the interfacial roughness (which also determines spin transparency across the interface) is identical for all NM/CoFeB layers. We have extracted the values of α by fitting the time-varying precessional oscillation presented in Figure 7.4(b) with equation (7.3) and subsequently using equation (7.5). The G_{eff} values for different NM/CoFeB interfaces are extracted using spin pumping formalism as given in equation (7.2). The variation of G_{eff} with α is plotted in Figure 7.5(a), which shows their linear relationship. This also indicates huge increments in α (from 0.006 to 0.025) and G_{eff} (from 0.4×10^{15} cm^{-2} to 6.5×10^{15} cm^{-2}) as the underlayer is changed from Cu to W. This also signifies that Cu has the lowest SOC strength and the value gradually increases with TRT, Ta, Pt and W. We also note here that the CoFeB film with no underlayer (i.e., directly deposited on the Si/SiO$_2$ substrate) has the lowest value of α (0.005±0.0003).

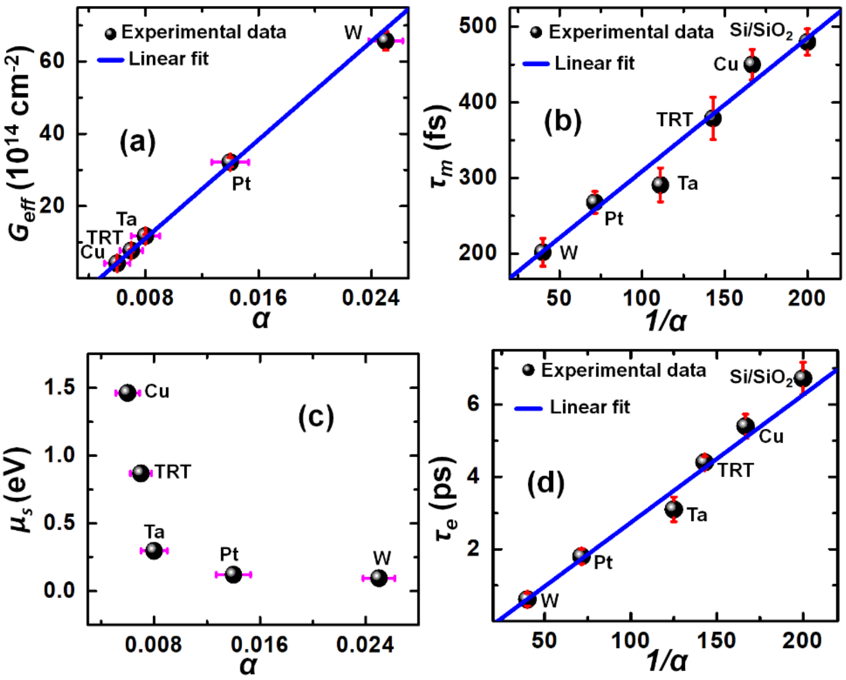

Figure 7.5: (a) Effective spin-mixing conductance (G_{eff}) as a function of α. (b) Ultrafast demagnetization time (τ_m) as a function of the inverse of Gilbert damping parameter ($1/\alpha$). (c) Variation in spin accumulation-driven chemical potential as a function of α. (d) Fast relaxation time (τ_e) as a function of $1/\alpha$.

Figure 7.5(b) represents the plot of demagnetization time τ_m as a function of the inverse of damping constant, i.e., $1/\alpha$, where we observe a linear relationship between τ_m and $1/\alpha$. This means by introducing a NM underlayer and changing its SOC strength, we can tune the τ_m by about 58% from 480 ± 17 fs (in the absence of NM underlayer) to 202 ± 8 fs (lowest with W underlayer). This also signifies that spin pumping-induced pure spin current transport from ferromagnetic CoFeB to NM layer creates an additional dissipation channel to make ultrafast demagnetization faster while increasing the α and G_{eff} values significantly. We can extract the spin accumulation-driven chemical potential (μ_s) for different NM/FM interfaces using the equation [18]:

$$\frac{1}{\tau_m} = \frac{\mu_s}{\hbar}(\alpha - \alpha_0) \tag{7.6}$$

where α_0 is the intrinsic Gilbert damping parameter in the absence of any NM underlayers (~ 0.005 for our case). The variation of μ_s with α is plotted in Figure 7.5(c), which shows that μ_s decreases from 1.46 to 0.09 eV as the underlayer is changed from Cu to W. This indicates that with an increase in the SOC strength of underlayers, interfacial spin accumulation decreases. This is also supported by the fact that high-SOC NMs will absorb more accumulated spins and generate more pure spin current leading to a decrease in the unabsorbed spins at the interface. Although, the value of μ_s for Cu/CoFeB interface (1.46 eV) is on the higher side but studies have shown that for transition metals μ_s-value can be of the order of ~ 1eV, which is similar to their spin splitting [18]. The variation of τ_e with $1/\alpha$ is plotted in Figure 7.5(d), which shows a linear relationship between τ_e and $1/\alpha$, indicating that larger damping corresponds to faster remagnetization dynamics. This suggests that magnon dynamics strongly influences the remagnetization process of an NM/FM heterostructure in a picosecond timescale [23, 30]. This also means that by introducing a NM underlayer with varying SOC strength, we can efficiently tune the τ_e by order of magnitude, i.e., from 0.61 ps to 6.70 ps.

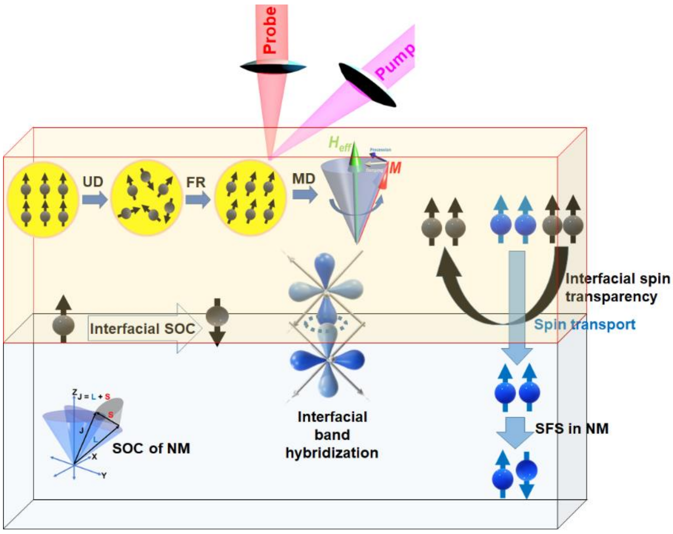

Figure 7.6: A schematic showing the processes involved in ultrafast demagnetization (UD), fast relaxation (FR) and magnetic damping (MD) of ferromagnetic/nonmagnetic heterostructure led by different bulk and interfacial mechanisms.

Recent studies on different NM/FM heterostructures have predicted that other than bulk SOC, there is some finite contribution from interfacial SOC [51] and interfacial band hybridization [52] to spin transport (schematically shown in Figure 7.6). According to the theoretical prediction by Liu *et al.* [53] and Chen *et al.* [54], interfacial SOC has a significant contribution to spin pumping-induced spin transport that can lead to large damping modulation due to interfacial spin flipping and spin memory loss. However, an experimental study by Caminale *et al.* [55] in Py/Pt and Py/Pd systems proved that interfacial SOC-dependent Gilbert damping modulation shows a linear NM thickness dependence with a sharp cut-off thickness (≤ 5 nm). It is non-trivial to quantify the precise contributions of bulk and interfacial SOC to the damping modulation. Still, NM layer thickness of 10 nm (well above the cut-off thickness) in our study ensures that the interfacial SOC will have a minor contribution to the magnetization dynamics. Furthermore, interfacial band hybridization between the electronic band of FM and NM leads to an induced magnetism in very few layers of NM in proximity to the FM, which may also affect the interfacial spin transport. However, Gupta *et al.* [56] and Zhu *et al.* [57] have argued this has a minor or no effect on the interface parameters and spin transport efficiency and therefore can be neglected. Through this systematic investigation, we have established a relationship between the process of ultrafast demagnetization, fast relaxation and magnetic damping bridged by the SOC strength of the NM underlayer. Higher SOC of underlayers leads to more efficient spin current transport, resulting in higher α and faster τ_m and τ_e values in NM/FM thin film heterostructures. We have shown that the τ_m and τ_e of CoFeB can drop down to 202 fs and 0.61 ps, respectively, for W underlayer, which would be very promising for future applications. Nevertheless, this is not the fundamental limit as it can be further reduced by choosing appropriate underlayer material with even higher SOC strength and decreasing FM layer thickness.

Our study can open new avenues in the development of ultrafast spintronics devices, for instance, AOS-device, where switching time can be significantly influenced by τ_m and τ_e. To our understanding, the reduction of FM layer thickness can induce various interfacial SOC phenomena, which may open up more dissipation channels to ultrafast demagnetization similar to damping coefficient and thereby speed up the demagnetization and remagnetization processes further. Besides, this may open a novel way to control the ultrafast demagnetization process by electric field or strain applied at NM/FM interface, which may externally control the SOC similar to what has been done to control the damping coefficient [58-60]. This may eventually help to build up the electric field or strain-controlled ultrafast memory devices. Therefore, we believe that our study underpins the underlying mechanism of ultrafast demagnetization, fast remagnetization and Gilbert damping in NM/FM heterostructures and leads towards the possibility to construct electric field and strain-controlled ultrafast memory devices by material engineering, which may revolutionize future spintronics devices.

7.4 Conclusions

In summary, we have systematically investigated the effects of SOC strength of NM underlayer on the ultrafast spin dynamics in NM/CoFeB heterostructures by using an all-optical time-resolved magneto-optical Kerr magnetometry. As a general rule, the ultrafast demagnetization time (τ_m) and fast relaxation time (τ_e) are found to decrease monotonically, whereas the interfacial spin transparency, i.e., the spin-mixing conductance (G_{eff}) and Gilbert damping parameter (α) increase monotonically with the increment of the SOC strength of the NM layer. We have established an inverse relationship of τ_m and τ_e with α in NM/CoFeB thin film heterostructures with different SOC strengths. The major contribution to ultrafast demagnetization originated from the spin pumping-induced pure spin current transport. We have observed a large modulation in τ_m (2.4 times) and τ_e (11.0 times) with the variation in the NM layer from W to Si/SiO$_2$. Consequently, the α and G_{eff} have also increased by 500% and 1584%, respectively, which, we believe, would be very promising for future applications. This study opens an avenue for further tunability of the ultrafast demagnetization, fast remagnetization time and Gilbert damping by electric field or strain, which will be very useful for developing electric field or strain-controlled ultrafast spintronics devices.

References

1. E. Beaurepaire, J. C. Merle, A. Daunois and J. Y. Bigot, Phys. Rev. Lett. **76**, 4250-4253 (1996).
2. B. Koopmans, G. Malinowski, F. Dalla Longa, D. Steiauf, M. Fähnle, T. Roth, M. Cinchetti and M. Aeschlimann, Nat. Mater. **9**, 259-65 (2010).
3. J. Y. Bigot, M. Vomir and E. Beaurepaire, Nat. Phys. **5**, 515-520 (2009).
4. M. Krauß, T. Roth, S. Alebrand, D. Steil, M. Cinchetti, M. Aeschlimann and H. C. Schneider, Phys. Rev. B **80**, 180407 (2009).
5. G. P. Zhang, W. Hübner, G. Lefkidis, Y. Bai and T. F. George, Nat. Phys. **5**, 499-502 (2009).
6. G. P. Zhang and W. Hübner, Phys. Rev. Lett. **85**, 3025-3028 (2000).
7. M. Battiato, K. Carva and P. M. Oppeneer, Phys. Rev. Lett. **105**, 027203 (2010).
8. C. D. Stanciu, F. Hansteen, A. V. Kimel, A. Kirilyuk, A. Tsukamoto, A. Itoh and T. Rasing, Phys. Rev. Lett. **99**, 047601 (2007).
9. A. Hassdenteufel, B. Hebler, C. Schubert, A. Liebig, M. Teich, M. Helm, M. Aeschlimann, M. Albrecht and R. Bratschitsch, Adv. Mater. **25**, 3122−3128 (2013).
10. C. H. Lambert, S. Mangin, B. S. D. C. S. Varaprasad, Y. K. Takahashi, M. Hehn, M. Cinchetti, G. Malinowski, K. Hono, Y. Fainman, M. Aeschlimann and E. E. Fullerton, Science **345**, 1337−1340 (2014).
11. J. Igarashi, Q. Remy, S. Iihama, G. Malinowski, M. Hehn, J. Gorchon, J. Hohlfeld, S. Fukami, H. Ohno and S. Mangin, Nano Lett. **20**, 8654−8660 (2020).
12. L. Liu, C. F. Pai, Y. Li, H. W. Tseng, D. C. Ralph and R. A. Buhrman, Science **336**, 555–558 (2012).
13. J. Sinova, S. O. Valenzuela, J. Wunderlich, C. H. Back and T. Jungwirth, Rev. Mod. Phys. **87**, 1213–1259 (2015).
14. J. C. Rojas Sánchez, L. Vila, G. Desfonds, S. Gambarelli, J. P. Attané, J. M. De Teresa, C. Magén and A. Fert, Nat. Commun. **4**, 2944 (2013).
15. Y. A. Bychkov and É. I. Rashba, JETP Lett. **39**, 78–81 (1984).
16. M. Fähnle, J. Seib and C. Illg, Phys. Rev. B **82**, 144405 (2010).
17. W. Zhang, W. He, X. Q. Zhang, Z. H. Cheng, J. Teng and M. Fähnle, Phys. Rev. B **96**, 220415 (2017).
18. W. Zhang, Q. Liu, Z. Yuan, K. Xia, W. He, Q. F. Zhan, X. Q. Zhang and Z. H. Cheng, Phys. Rev. B **100**, 104412 (2019).
19. A. Kirilyuk, A. V. Kimel and T. Rasing, Rev. Mod. Phys. **82**, 2731 (2010).
20. J.Y. Bigot, M. Vomir, L.H.F. Andrade and E. Beaurepaire, Chem. Phys. **318**, 137–146 (2005).
21. U. Atxitia, O. Chubykalo-Fesenko, J. Walowski, A. Mann and M. Münzenberg, Phys. Rev. B **81**, 174401 (2010).

22. J. Mendil, P. Nieves, O. Chubykalo-Fesenko, J. Walowski, T. Santos, S. Pisana and M. Münzenberg, Sci. Rep. **4**, 3980 (2014).
23. C. V. K. Schmising, M Giovannella, D Weder, S Schaffert, J. L. Webb and S. Eisebitt, New J. Phys. **17**, 033047 (2015).
24. Y. Tserkovnyak, A. Brataas and G. E. W. Bauer, Phys. Rev. Lett. **88**, 117601 (2002).
25. B. Koopmans, J. J. M. Ruigrok, F. Dalla Longa and W. J. M. De Jonge, Phys. Rev. Lett. **95**, 267207 (2005).
26. J. Walowski, G. Muller, M. Djordjevic, M. Münzenberg, M. Klaui, C. A. F. Vaz and J. A. C. Bland, Phys. Rev. Lett. **101**, 237401 (2008).
27. H. L. Wang, C. H. Du, Y. Pu, R. Adur, P. C. Hammel and F. Y. Yang, Phys. Rev. Lett. **112**, 197201 (2014).
28. E. G. Tveten, A. Brataas and Y. Tserkovnyak, Phys. Rev. B **92**, 180412 (2015).
29. S. N. Panda, S. Majumder, S. Choudhury, A. Bhattacharya, S. Sinha and A. Barman, Nanoscale **13**, 13709-13718 (2021).
30. R. S. Malik, E. K. Delczeg-Czirjak, R. Knut, D. Thonig, I. Vaskivskyi, D. Phuyal, R. Gupta, S. Jana, R. Stefanuik, Y. O. Kvashnin, S. Husain, A. Kumar, P. Svedlindh, J. Söderström, O. Eriksson and O. Karis, Phys. Rev. B **104**, L100408 (2021).
31. C. Guillemard, W. Zhang, G. Malinowski, C. de Melo, J. Gorchon, S. Petit-Watelot, J. Ghanbaja, S. Mangin, P. Le Fèvre, F. Bertran and S. Andrieu, Adv. Mater. **32**, 1908357 (2020).
32. M. R. Karim, A. Adhikari, S. N. Panda, P. Sharangi, S. Kayal, G. Manna, P. S. A. Kumar, S. Bedanta, A. Barman and I. Sarkar, J. Phys. Chem. C **125**, 10483-10492 (2021).
33. S. X. Huang, T. Y. Chen and C. L. Chien, Appl. Phys. Lett. **92**, 242509 (2008).
34. D. Gao, J. Zhang, G. Yang, J. Zhang, Z. Shi, J. Qi, Z. Zhang and D. Xue, J. Phys. Chem. C **114**, 13477–13481 (2010).
35. C. Gómez-Poloa, S. Larumbe and J. M. Pastor, J. Appl. Phys. **113**, 17B511 (2013).
36. M. Cecot, L. Karwacki, W. Skowroński, J. Kanak, J. Wrona, A. Żywczak, L. Yao, S. van Dijken, J. Barnaś and T. Stobiecki, Sci. Rep. **7**, 968 (2017).
37. M. van Kampen, C. Jozsa, J. T. Kohlhepp, P. LeClair, L. Lagae, W. J. M. de Jonge and B. Koopmans, Phys. Rev. Lett. **88**, 227201 (2002).
38. A. Barman and J. Sinha, Spin Dynamics and Damping in Ferromagnetic Thin Films and Nanostructures (Springer: Switzerland, 2018).
39. F. Dalla Longa, J. T. Kohlhepp, W. J. M. de Jonge and B. Koopmans, Phys. Rev. B **75**, 224431 (2007).
40. G. Malinowski, F. Dalla Longa, J. H. H. Rietjens, P. V. Paluskar, R. Huijink, H. J. M. Swagten and B. Koopmans, Nat. Phys. **4**, 855-858 (2008).
41. S. Mondal, A. Barman, Phys. Rev. Appl. **10**, 054037 (2018).
42. X. Liu, Z. Xu, R. Gao, H. Hu, Z. Chen, Z. Wang, J. Du, S. Zhou and T. Lai, Appl. Phys. Lett. **92**, 232501 (2008).
43. L. Zhu, D. C. Ralph and R. A. Buhrman, Phys. Rev. Lett. **123**, 057203 (2019).
44. S. N. Panda, S. Majumder, A. Bhattacharyya, S. Dutta, S. Choudhury and A. Barman, ACS Appl. Mater. Interfaces **13**, 20875-20884 (2021).
45. C. Kittel, Phys. Rev. **73**. 155–161 (1948).
46. J. Walowski, M. D. Kaufmann, B. Lenk, C. Hamann, J. McCord and M. Münzenberg, J. Phys. D: Appl. Phys. **41**, 164016 (2008).

47. G. Woltersdorf, M. Buess, B. Heinrich and C. H. Back, Phys. Rev. Lett. **95**, 037401 (2005).
48. Y. Fan, X. Ma, F. Fang, J. Zhu, Q. Li, T. P. Ma, Y. Z. Wu, Z. H. Chen, H. B. Zhao and G. Lüpke, Phys. Rev. B **89**, 094428 (2014).
49. F. Herman and S. Skillman, Atomic Structure Calculations (Prentice-Hall, New Jersey, 1963).
50. K. V. Shanavas, Z. S. Popovic and S. Satpathy, Phys. Rev. B **90**, 165108 (2014).
51. V. Amin and M. Stiles, Phys. Rev. B **94**,104419 (2016).
52. N. Nakajima, T. Koide, T. Shidara, H. Miyauchi, H. Fukutani, A. Fujimori, K. Iio, T. Katayama, M. Nyvlt and Y. Suzuki, Phys. Rev. Lett. **81**, 5229 (1998).
53. Y. Liu, Z. Yuan, R. J. H. Wesselink, A. A. Starikov and P. J. Kelly, Phys. Rev. Lett. **113**, 207202 (2014).
54. K. Chen and S. Zhang, Phys. Rev. Lett. **114**, 126602 (2015).
55. M. Caminale, A. Ghosh, S. Auffret, U. Ebels, K. Ollefs, F. Wilhelm, A. Rogalev and W. E. Bailey, Phys. Rev. B **94**, 014414 (2016).
56. K. Gupta, R. J. H. Wesselink, R. Liu, Z. Yuan and P. J. Kelly, Phys. Rev. Lett. **124**, 087702 (2020).
57. L. J. Zhu, D. C. Ralph and R. A. Buhrman, Phys. Rev. B **98**, 134406 (2018).
58. A. Okada, S. Kanai, M. Yamanouchi, S. Ikeda, F. Matsukura and H. Ohno, Appl. Phys. Lett. **105**, 052415 (2014).
59. B. Rana, C. A. Akosa, K. Miura, H. Takahashi,G. Tatara and Y. Otani, Phys. Rev. Appl. **14**, 014037 (2020).
60. Z. Zhang, E. Liu, X. Lu, W. Zhang, Y. You, G. Xu, Z. Xu, P. K. J. Wong, Y. Wang, B. Liu, X. Yu, J. Wu, Y. Xu, A. T. S. Wee and F. Xu, Adv. Funct. Mater. **31**, 2007211 (2021).

Chapter-8

Fluence-dependent ultrafast magnetization dynamics in permalloy thin films with different thicknesses

8.1 Introduction

The demand for manufacturing energy-efficient, cost-effective and high-speed magnetic memory and storage devices has reinforced an upsurge in the fundamental research related to ultrafast magnetization dynamics in magnetic thin films, heterostructures and nanostructures [1, 2]. Continuous development in this field makes the clock speed of the processors to enter the sub-GHz range while increasing the storage capacity in the spin-based devices [3, 4]. However, this development hits a bottleneck due to the constraints imposed by the relaxation processes involved in the magnetization dynamics which eventually limit the data transfer rate in the device. Precessional magnetization dynamics of ferromagnetic material follow the Landau-Lifshitz-Gilbert equation where the rate of energy dissipation from spin wave modes to adjacent thermal baths can be expressed by the Gilbert damping parameter (α) which is analogous to the Rayleigh energy dissipation function [5, 6]. There is both intrinsic and extrinsic contribution to α. Intrinsic contribution originates from the spin-flip scattering from phonons inside the ferromagnetic system which can not be reduced to zero [7]. Extrinsic contribution to α comes from additional magnon-phonon and magnon-magnon scatterings introduced to the system by doping, capping, perturbation from spin current, eddy current loss and external temperature [8-12]. Controlling α is of paramount importance as a low α-value helps to reduce write-current in some applications like spin transfer torque magnetoresistive random-access memory (STT-MRAM). On the other hand, a high α-value is necessary to eliminate ‘ringing’ in magnetization precession during the data writing process in storage and memory devices.

On a shorter timescale, ultrafast demagnetization is one of the fastest spin manipulation mechanisms which can revolutionize the field of spintronics by decreasing the switching time by many orders [13]. However, the true microscopic mechanisms responsible for this ultrafast loss of magnetization remain highly debatable to date. Substantial experimental and theoretical research over the last two decades have unravelled the existence of two predominant mechanisms. The first one involves the spin-flip scattering (SFS) process, such as Elliott-Yafet (EY)-like electron-phonon scattering [14], relativistic spin-flip scattering [15], Coulomb scattering [16] and electron-magnon scattering [17] etc., due to the direct light-matter interaction. The other presiding contribution comes from the laser-excited hot electrons through the transportation of spin current [18]. Although the timescales of ultrafast demagnetization and precessional dynamics differ by orders of magnitude, recent developments in this direction have established a correlation between these two fundamental phenomena [19]. The correlation between the ultrafast demagnetization time (τ_m) and α provides insights for identifying the dominant microscopic contribution to the ultrafast demagnetization [20,21]. A proportional relation manifests dominant local spin-flip scattering contribution, while an inverse dependence signifies the contribution from spin transport in the system. Interestingly, this correlation also helps to determine the major microscopic contribution to damping [22]. A linear relationship between τ_m and α, points to the dominance of intra-band conductivity-like contribution whereas an inverse relationship indicates the inter-band resistivity-like contribution.

In this article, we have investigated the effects of pump fluence (F) on the τ_m, fast remagnetization time (τ_e) and α of 50 nm- and 100 nm-thick $Ni_{80}Fe_{20}$ (Py) films using the TR-MOKE magnetometry [23]. TR-MOKE offers several advantages over other electrical detection techniques like spin Hall magnetoresistance and ST-FMR for the investigation of spin pumping. This technique is free from the need for delicate micro-fabrication and broad area averaging. It eliminates inhomogeneous area broadening and prevents the overestimation of α. Furthermore, this pump-probe-based technique is one of its kind for direct time-domain detection of ultrafast demagnetization on femtosecond timescales from a single measurement, which is currently not possible in any other technique [24]. Being a low coercive magnet with negligible magnetostriction and magnetic anisotropy Py is a preferred material for magnetic recording head sensors, high-frequency transformers and several other device applications [25]. Our experimental results on the ultrafast demagnetization supported by three-temperature modelling have revealed a monotonic increase of τ_m and τ_e with laser pump fluence. From the picosecond precessional dynamics, we have observed that α of both Kittel and perpendicular standing spin wave (PSSW) modes remain invariant with the external magnetic field strength, however, it exhibits strong enhancement with laser pump fluence. Instantaneous increase of system temperature and subsequent dissipation of heat from the probed area results in a temporal chirping of the oscillatory Kerr signal with modified precessional frequency for both Kittel and PSSW modes. A direct correlation between τ_m and α indicates that spin-flip scattering can be the dominant microscopic mechanism for ultrafast demagnetization and a major intra-band conductivity-like contribution to α. This comprehensive study of magnetization dynamics over a broad timescale and its control by pump fluence will provide a firm base to integrate various magnetic phenomena on a single on-chip device.

8.2 Experimental details

Py films having thicknesses of 50 nm and 100 nm were deposited using a DC magnetron sputtering system (Base pressure = 3×10^{-7} Torr, Argon pressure = 0.5 mTorr and Deposition rate = 0.2 Å/sec) over 8 mm × 8 mm silicon (100) wafers having 285 nm-thick SiO_2 coating. Thereafter, SiO_2 capping layers of 5 nm were deposited over the Py layer using RF magnetron sputtering. Very slow deposition rates were chosen for achieving uniform thicknesses of the films. Py was deposited at a DC voltage of 430 V and current of 0.06 mA, while SiO_2 was deposited at average RF power of 60 watts. All the other deposition conditions were carefully optimized and kept almost identical for both samples.

The static magnetic properties like coercive field (H_c), saturation field (H_s) and saturation magnetization (M_s) of the two films were characterized using VSM. The GI-XRD technique was used to obtain the crystal structure. The thickness, surface roughness and electron density of different layers were determined by XRR measurement. The surface topography of the films was measured using AFM. TR-MOKE magnetometry was used to study the magnetization dynamics from femtosecond to nanosecond timescale. The second-harmonic of the amplified femtosecond laser pulse (repetition rate = 1 kHz, pulse width ~ 35 fs) generated from a regenerative amplifier system was used to excite the dynamics while the fundamental laser beam of 800 nm was utilized to probe the time-dependent Kerr rotation in polar geometry. Pump and probe beams have spot sizes of about 200 µm and 100 µm, respectively. Before laser pulse excitation, a strong bias magnetic field (H) was applied at a small angle (~ 15°) to the sample plane which ensures a finite demagnetizing field component along the pump pulse direction and helps to induce precessional dynamics in the sample upon optical excitation. The back-reflected probe beam was fed to a set of an analyzer and a photodiode. The polar Kerr signal was finally detected using a lock-in amplifier in a phase-sensitive manner. Throughout the measurement, probe fluence is kept fixed at 2 mJ/cm^2 while pump fluence is varied over a broad range from 12 mJ/cm^2 to 62 mJ/cm^2. All the measurements were performed at room temperature under ambient conditions.

8.3 Results and discussions

Static characterizations: We have measured the in-plane (INP) and out-of-plane (OOP) magnetic hysteresis loops using VSM at room temperature for Sub/Py (50, 100 nm)/SiO_2 (5 nm) as shown in Figure 8.1(a). The value of H_s in INP and OOP configurations for these films are about 50 Oe and 10.6 kOe, which reveal that these films are in-plane magnetized with negligible out-of-plane anisotropy. M_s is obtained to be about 800 emu/cc for both films. Also, these films exhibit small H_c (~ 15 Oe) which reveal their soft-ferromagnetic nature.

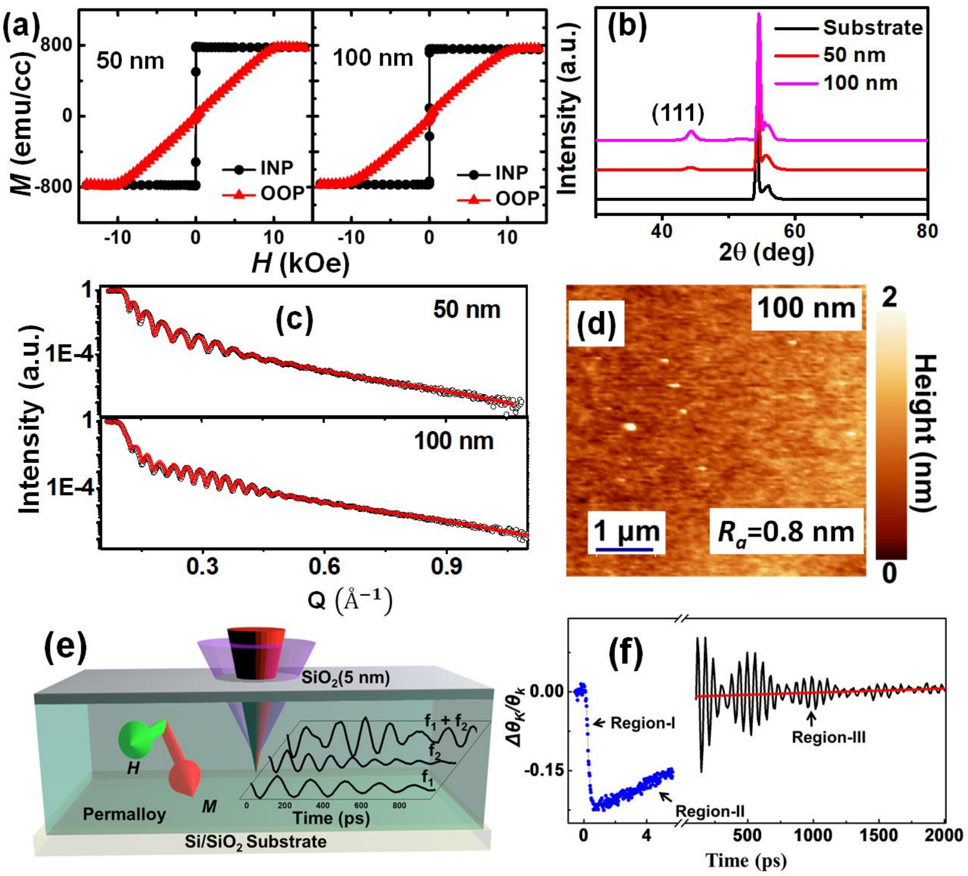

Figure 8.1: (a) VSM loops for Sub/Py (50, 100 nm)/SiO$_2$ (5 nm) samples (b) XRD spectra measured at 2° grazing incidence angle from bare Si/SiO$_2$ substrate and Sub/Py (50, 100 nm)/SiO$_2$ (5 nm) samples. (c) XRR spectra (symbols) for Sub/Py (50, 100nm)/SiO$_2$ (5nm) samples fitted using GenX (solid red lines). (d) The two-dimensional AFM image for Sub/Py (100 nm)/SiO$_2$ (5 nm) sample. (e) A schematic of sample structure and experimental geometry, (f) Representative TR-MOKE data for Sub/Py (50 nm)/SiO$_2$ (5 nm) sample at an applied magnetic field of 2.40 kOe and pump fluence of 25 mJ/cm^2 with three different temporal regimes marked in the figure. The solid red line indicates the exponential background.

Figure 8.1(b) displays the GI-XRD spectra obtained from bare Si/SiO$_2$ substrate and Sub/Py (50, 100 nm)/SiO$_2$ (5 nm) thin films at a glancing angle of 2°. In this plot, the peaks corresponding to the 2θ angle of ~ 44.43° primarily correspond to the (111) orientation of Py signifying its face-centred cubic (fcc) crystal structure. The other high-intense peaks correspond to 2θ angles of ~ 54.57° and ~ 55.53° appear from the substrate.

To obtain information about the interfacial roughness, thickness and average electron density of different sub-layers of Sub/Py (50, 100 nm)/SiO$_2$ (5 nm) thin films, we have measured the XRR-spectra using an 8 KeV X-ray source (as shown in Figure 8.1(c)) and analyzed the spectra using GenX software. The values of thickness obtained from the fit are close to the nominal thickness values. Average surface roughness obtained from the fit for 50 nm- and 100 nm-thick films are 0.62 nm and

0.55 nm, respectively. Electron densities of Py and SiO_2 are found to be 7.1×10^{-5} Å^{-2} and 2.0×10^{-5} Å^{-2}, respectively, in both films.

We have also measured the surface topography of the films using AFM in dynamic tapping mode by taking scans over 5 µm × 5 µm area (as shown in Figure 8.1(d) for 100 nm-thick-Py). Due to the thin capping layer, the interfacial roughness reflects its imprint on the topographical roughness. We have analyzed the AFM images using WSxM software. It is verified that variation in surface roughness is very small when measured at different regions of the same sample. Topographical roughness of 50 nm- and 100 nm-thick films are found to be 0.86 nm and 0.80 nm, respectively, which are slightly higher than the values obtained from the XRR analyses possibly due to large area averaging.

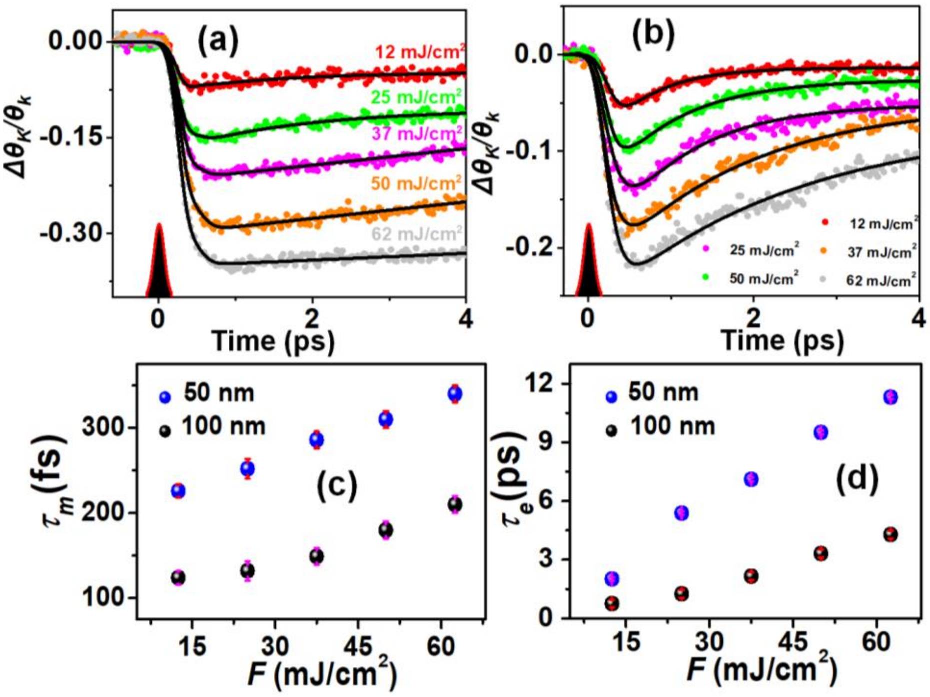

Figure 8.2: Time-resolved Kerr rotation showing ultrafast demagnetization for (a) 50 nm (b) 100 nm thick Py films at different pump fluences. The symbols denote experimental data points and the solid lines represent the fitted curves using equation (8.4). Fluence-dependent variation of (c) ultrafast demagnetization time (τ_m) and (d) fast relaxation time (τ_e) that obtained as fitting parameters.

Magnetization dynamics at different timescales: When a saturated ferromagnetic material is excited by a femtosecond laser pulse, its magnetization is partially or fully lost in sub-picosecond timescale, which is known as ultrafast demagnetization. This instantaneous quenching of system magnetization is followed by a faster recovery within a few picoseconds and a slower recovery within hundreds of picoseconds, known as the fast and slow remagnetizations. The slow remagnetization is accompanied by a damped sinusoidal precession in presence of an external magnetic field triggered by an instantaneous change in the demagnetizing field of the sample. The schematic of experimental geometry is shown in Figure 8.1(e). A representative TR-MOKE data obtained from the 50 nm-thick Py film for H = 2.40 kOe and F = 25 mJ/cm^2 is shown in Figure 8.1(f), which has three different temporal regions, *i.e.*, ultrafast demagnetization (region-I), fast remagnetization (region-II) and slow remagnetization with precession (region-III). The red solid line in Figure 8.1(f) is a fit to the exponential background originating from the heat diffusion during the slow relaxation process from the system to the surroundings.

Laser-induced ultrafast demagnetization: Since the discovery of ultrafast demagnetization in Ni thin film by Bearepaire *et al.* in 1996 [13], several models have been proposed to interpret its origin [26-28]. Among those, the phenomenological three-temperature (3T) model has been widely used which deals with the energy exchange between the three-temperature baths, *i.e.*, electron, spin and lattice. Upon laser excitation, electron temperature increases instantaneously to create a hot electron population above the Fermi level, which then triggers the quenching of magnetization in the spin subsystem by electron-magnon interaction. Subsequently, the energy rebalancing between these three subsystems ensures the quenched magnetization relaxes back into its original equilibrium position. The temporal evolution of these three subsystems can be described by the following coupled differential equations [13]:

$$C_E(T_E)\frac{dT_E}{dt} = -G_{EL}(T_E - T_L) - G_{ES}(T_E - T_S) + P(t) \qquad (8.1)$$

$$C_S(T_S)\frac{dT_S}{dt} = -G_{ES}(T_S - T_E) - G_{SL}(T_S - T_L) \qquad (8.2)$$

$$C_L(T_L)\frac{dT_L}{dt} = -G_{EL}(T_L - T_E) - G_{SL}(T_L - T_S) \qquad (8.3)$$

Where, the temperatures of the electron, spin and lattice baths are denoted by T_E, T_S and T_L respectively. C_E, C_S and C_L are the electron, spin and lattice specific heats. G_{EL}, G_{ES} and G_{SL} are the electron-lattice, electron-spin and spin-lattice coupling constants, respectively. $P(t)$ is the laser excitation term which is generally Gaussian in nature. Solving equations (8.1-8.3) and subsequently by using mean-field theory, the magnetization of the system at any particular time can be extracted. The experimentally measured demagnetization curves can also be fitted with the following expression to extract the τ_m and τ_e [29, 30] directly:

$$-\frac{\Delta M_z}{M_z} = \left[\left\{\frac{A_1}{(t/\tau_0+1)^{\frac{1}{2}}} + \frac{A_1\tau_m - A_2\tau_e}{\tau_e - \tau_m}e^{-t/\tau_m} + \frac{A_2\tau_e - A_1\tau_e}{\tau_e - \tau_m}e^{-t/\tau_e}\right\}H(t) + A_3\delta(t)\right] \otimes G\,(t) \qquad (8.4)$$

In the above expression, A_1 represents the value of magnetization after equilibrium between electron, spin and lattice; A_2 is proportional to the maximum rise in the electron temperature and A_3 represents the magnitude of state filling effect during pump-probe temporal overlap, well described by a Dirac-delta function ($\delta(t)$). The cooling time by heat diffusion is described by τ_0 representing the timescale of electron-phonon interactions. $H(t)$ and $G(t)$ are the Heaviside step function and Gaussian function. The latter corresponds to the profile of the laser pulse. The two exponential terms in the above equation mirror the timescale of magnetization loss by the ultrafast demagnetization and the timescale of electron-phonon interaction by fast remagnetization of magnetization. The temporal changes of Kerr rotation ($\Delta\theta_k(t)$) for all the measurements are normalized by the total Kerr rotation(θ_k) and then fitted with equation (8.4). Figure 8.2(a) and 8.2(b) show the laser-induced ultrafast demagnetization obtained at different laser pump fluence for Py thicknesses of 50 and 100 nm, respectively. We observe a monotonic increase in τ_m and τ_e with pump fluence for both films (Figure 8.2(c) and 8.2(d)). The enhancement in τ_m is an indication of enhanced spin fluctuations at an elevated temperature of the spin system which may be due to an increase in dynamic longitudinal susceptibility and a decrease in exchange interaction strength [31]. The increase in τ_e with pump fluence can be explained by the fact that higher fluence causes a greater rise in electron temperature followed by spin temperature [32] and hence, magnetization takes more time for recovering to its initial equilibrium. Also, we have observed that there is a continuous increase in A_1 and A_2 with pump fluence in these thin films due to higher quenching and longer thermal-relaxation time.

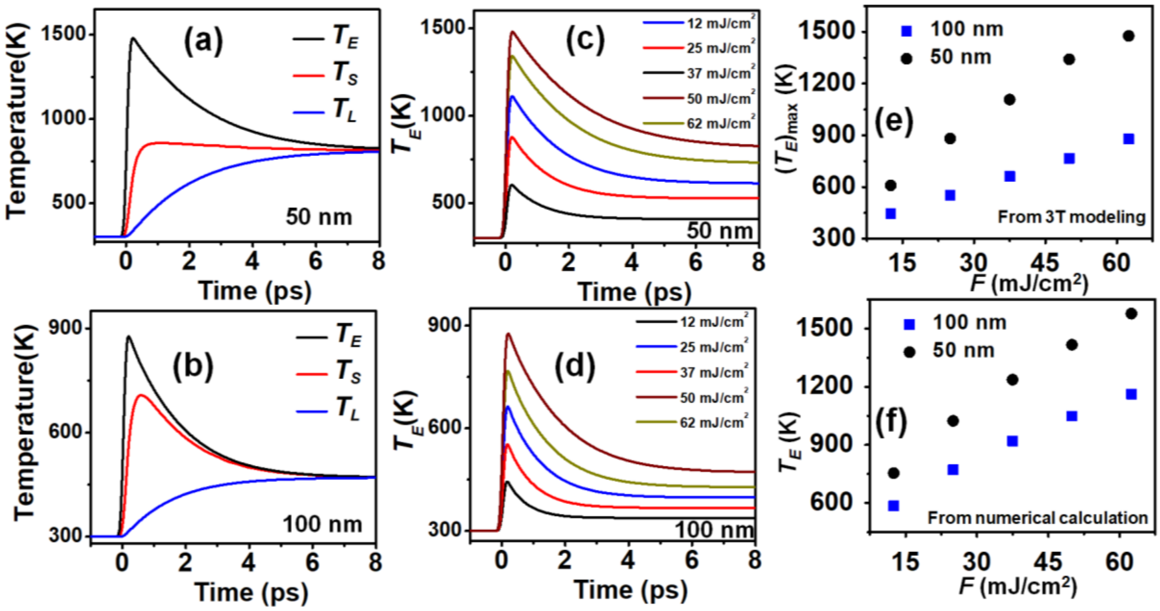

Figure 8.3: Temporal evolution of electron temperature (T_E), spin temperature (T_S) and lattice temperature (T_L) for (a) 50 nm and (b) 100 nm Py film for pump fluence of 62 mJ/cm^2. Variation of T_E as a function of time delay at different laser pump fluence for (c) 50 nm and (d) 100 nm Py film. (e) Maximum electronic temperature rise ($(T_E)_{\max}$) at different laser pump fluences obtained from 3T-modelling. (f) T_E at different laser pump fluences calculated numerically using equation (8.5).

Table 8.1:Parameters obtained from 3T-modelling for 50 nm and 100 nm Py film.

Py thickness	γ (10^3 $\mathrm{Jm^{-3}K^{-2}}$)	C_L (10^6 $\mathrm{Jm^{-3}K^{-1}}$)	C_S (10^5 $\mathrm{Jm^{-3}K^{-1}}$)	G_{EL} (10^{17} $\mathrm{Wm^{-3}K^{-1}}$)	G_{ES} (10^{17} $\mathrm{Wm^{-3}K^{-1}}$)	G_{SL} (10^{17} $\mathrm{Wm^{-3}K^{-1}}$)
50 nm	5.05 ± 0.15	4.10 ± 0.10	2.23 ± 0.10	7.5 ± 2.0	6.0 ± 2.0	5.2 ± 1.3
100 nm	5.05 ± 0.20	6.60 ± 0.09	2.16 ± 0.10	16.0 ± 7.0	14.0 ± 6.0	8.6 ± 1.0

To explore the underlying physics involved in the ultrafast demagnetization process we have modelled the experimental demagnetization data using equations (8.1-8.3). In our calculation, we have considered a linear contribution of the electronic specific heat, *i.e.*, $C_E = \gamma T_E$, where γ is determined by the electron density of states around the Fermi level. Figures 8.3(a) and 8.3(b), shows the temporal evolution of T_E, T_S and T_L for 50 nm- and 100 nm-thick Py films at F = 62 mJ/cm^2. The values of specific heats and coupling constants for 50 and 100 nm films are tabulated in Table 8.1. The 100 nm-thick film has slightly higher C_L in comparison with the thinner film satisfying the Debye-Einstein approximation [33]. The 50 nm-thick Py film possesses lower values of G_{EL}, G_{ES} and G_{SL} in comparison with 100 nm-thick Py. This observation corroborates with higher τ_m and τ_e values and indicates an easier energy dissipation in the thicker sample. This, in turn, signifies a larger increase in system temperature in thinner film in comparison with the thicker film within a comparable fluence range. Figures 8.3(c) and 8.3(d), show the temporal evolution of T_E for 50 nm- and 100 nm-thick Py films at different laser pump fluences. Variation in maximum electronic temperature rise ($(T_E)_{max}$) from this modelling is plotted in Figure 8.3(e) which confirms the continuous increase in electronic temperature with laser fluence. We will now compare this electronic temperature rise with some theoretical arguments, where the T_E is related to the absorbed laser energy per unit volume (E_a) by the following relation [34]:

$$T_E = \sqrt{\frac{2E_a}{\gamma} + T_0^2} \quad \text{where } E_a = \left[1 - e^{-d/\lambda}\right]\frac{F(1-R)}{d} \tag{8.5}$$

where d is the film thickness, λ is the optical penetration depth (~ 17 nm), R is the reflectivity of the sample (~ 0.5), T_0 is the ambient temperature (~ 300 K for room temperature) and F is the laser pump fluence. Variation in T_E with laser pump fluence for both the films using the expression in equation (8.5) is plotted in Figure 8.3(f). T_E derived from the numerical calculation shows qualitative agreement with that obtained using the 3T-modelling.

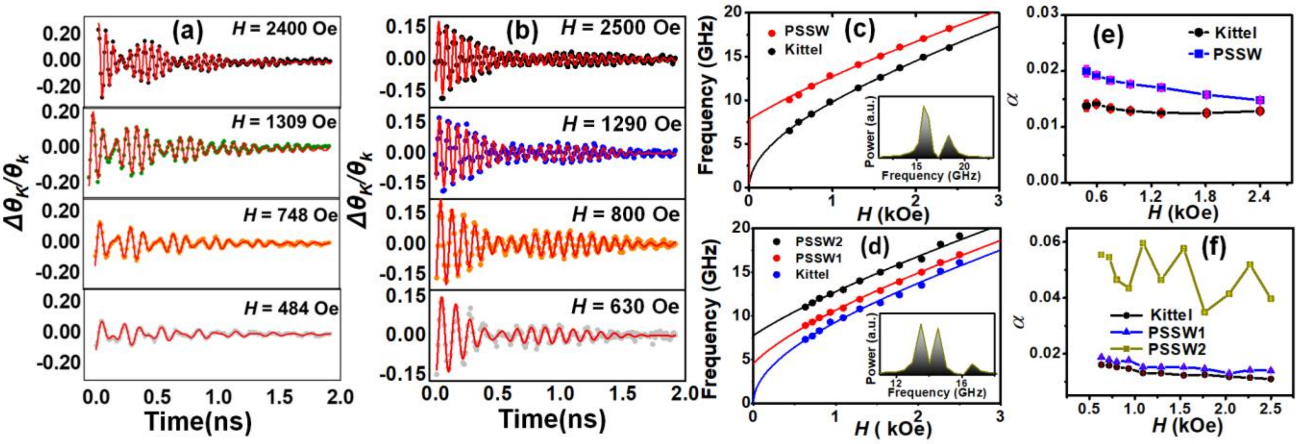

Figure 8.4: Background subtracted time-resolved Kerr rotation data showing precessional oscillations at different bias magnetic field(H) values for (a) 50 nm and (b) 100 nm thick Py film. The symbols represent experimental data points and the solid lines represent the fit using equation (8.6). Precessional frequency as a function of H (symbols) and the corresponding Kittel fit (solid line) for (c) 50 nm and (d) 100 nm thick Py film is shown. (Insets show the fast Fourier transformation power spectra at the highest field which clearly shows (c) two modes for 50 nm thick Py film and (d) three modes for 100 nm thick Py film). Variation of damping constant(α) with applied bias field for (e) 50 nm and (f) 100 nm thick Py film.

Laser-induced modulation of precessional dynamics: The precession of magnetization around an effective magnetic field appears as a damped sinusoidal oscillation in the time-resolved Kerr rotation data in the picosecond to nanosecond timescale. We have extracted the precessional relaxation time (τ) by fitting the background-subtracted Kerr oscillations using the following expression [35, 36]:

$$M(t) = \sum_i A_i e^{-\left(\frac{t}{\tau_i}\right)} \sin(2\pi\,(f_i + b_i t)t + \phi_i) \tag{8.6}$$

Where A_i, τ_i, f_i, ϕ_i and b_i is the precessional amplitude, relaxation time, precessional frequency, initial phase and temporal chirp parameter for i^{th} mode. For all these samples we have investigated the precessional dynamics at various H values. The fast Fourier transformation (FFT) of the oscillations provides f_i for different values of H. The field dispersion of frequency (f) is fitted using the following form of the Kittel formula [37]:

$$f = \frac{\gamma}{4\pi}\sqrt{\left(H + \frac{2A}{M_s}\left(\frac{n\pi}{d}\right)^2\right)\left(H + \frac{2A}{M_s}\left(\frac{n\pi}{d}\right)^2 + 4\pi M_{eff}\right)} \tag{8.7}$$

Where, M_{eff} is effective magnetization and γ $(= g\mu_B/\hbar)$ is the gyromagnetic ratio. g and $\hbar$ are the Landé g-factor and reduced Planck's constant, respectively. Here, A, n and d, are the exchange stiffness constant, order of PSSW mode and thickness of the film, respectively. For uniform Kittel mode $n = 0$ while $n = 1$ and 2 stand for first- and second-order PSSW mode. The A value is taken as 1.3×10^{-6}

erg/cm for Py. M_{eff} and g are determined as the fitting parameters here. After finding τ and M_{eff}, we have estimated α using the following expression [38]:

$$\alpha = \frac{1}{\gamma\tau(H+2\pi M_{eff})} \tag{8.8}$$

Where, the value of γ is 1.76 × 10^7 Hz/Oe. Figure 8.4(a) and 8.4(b) show the time-resolved Kerr oscillations for different bias magnetic fields at F = 25 mJ/cm^2 for the 50 nm- and 100 nm-thick Py film, respectively. Figures 8.4(c) and 8.4(d) show the f vs. H plot fitted with the Kittel formula in equation (8.7) for 50 nm- and 100 nm-thick Py film, respectively. There are two modes for the 50 nm-thick film(as shown in the inset of Figure 8.4(c)): one corresponding to the uniform Kittel mode and the other corresponding to 1st order PSSW mode, whereas three clear modes appear for the 100 nm-thick film(as shown in the inset of Figure 8.4(d)): a low-frequency uniform Kittel mode and 1st and 2nd order PSSW modes. From the Kittel fit, we have obtained $M_{eff} \approx 790 \pm 10$ emu/cc and g = 2.0 ± 0.1 for Kittel and PSSW modes of both Py films which are close to the values obtained from VSM (~ 800 emu/cc). The amplitude of precession is found to increase with H which can be attributed to the enhancement of the in-plane magnetization component with increasing magnetic field strength. α is found to be independent of H (as shown in Figures 8.4(e) and 8.4(f)). The literature shows that in the presence of extrinsic effects like two-magnon scattering, α decreases with the applied magnetic field due to the increased degeneracy of SWs while it should increase in presence of inhomogeneous surface anisotropy [21]. A field-independent nature of α rules out any such extrinsic contributions present in these systems.

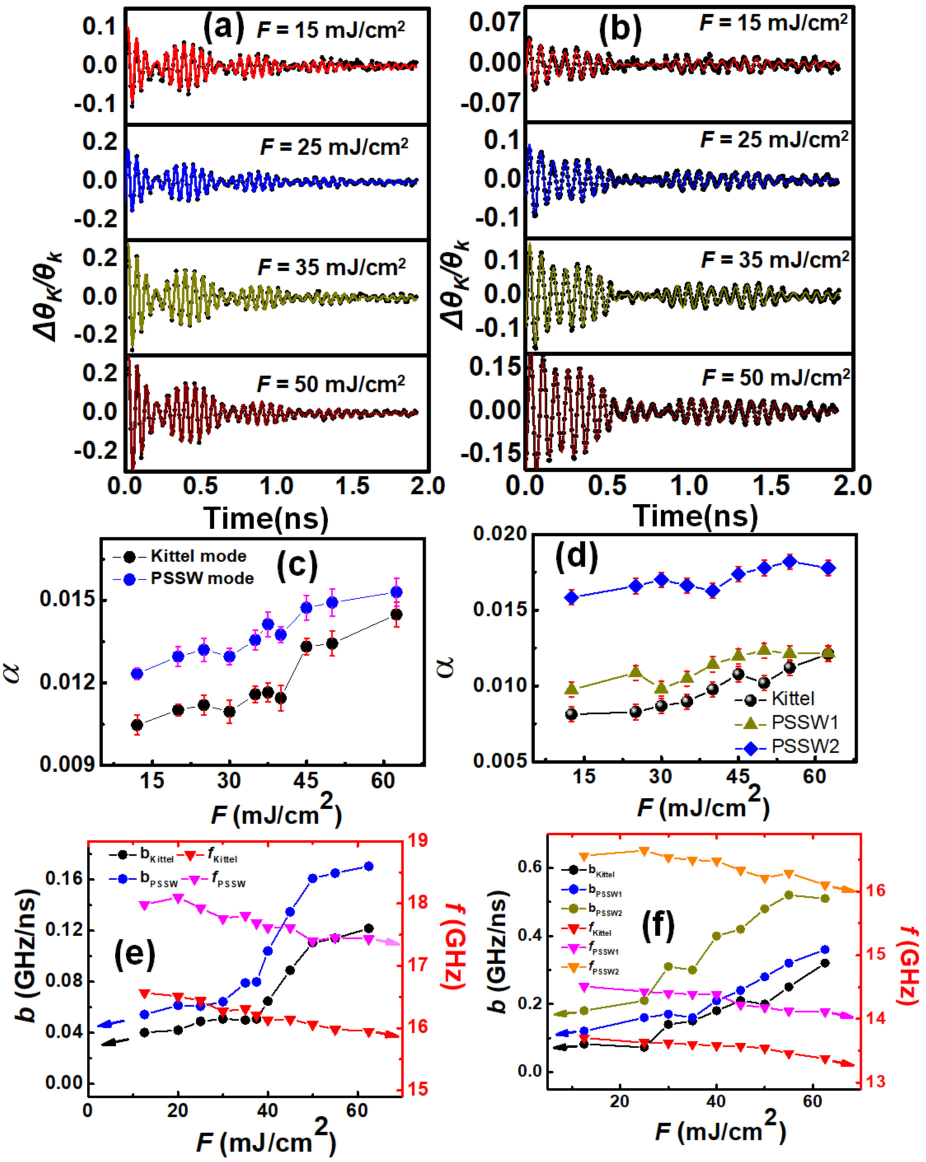

Figure 8.5: Background subtracted time-resolved Kerr rotation data showing precessional dynamics at different laser pump fluences for the (a) 50 nm and (b) 100 nm Py film. The symbols represent experimental data points and the solid lines represent the fit using equation (8.6). Variation of Gilbert damping parameter (α) with laser fluence for (c) 50 nm and (d) 100 nm Py film. Precessional frequency and temporal chirp parameter as a function of laser fluence for (e) 50 nm and (f) 100 nm Py film.

To study the effect of laser pump fluence (F) on precessional dynamics, we have varied F from 12 mJ/cm^2 to 62 mJ/cm^2 at H = 2.4 kOe. The precessional data at different pump fluences for 50 nm- and 100 nm-thick Py are plotted in Figures 8.5(a) and 8.5(b), respectively. The amplitude of precession increases with F due to the stronger modulation of magnetization and the effective field. The variation of α with F is plotted in Figures 8.5(c) and 8.5(d) for 50 nm- and 100 nm-thick Py films which shows damping increases significantly from its intrinsic value for both Kittel and PSSW modes within this fluence range. Although there is a finite possibility of laser fluence-induced damping enhancement due to the eddy current and nonlocal contribution from the propagation of magnetostatic spin waves, recent studies show that eddy current contribution in Py films below 100 nm is negligible [39] and nonlocal contribution to damping is more significant when the excitation area is below 10 µm [40]. Throughout the measurement we have carefully maintained the overlap between the probe and pump beams and the Kerr signal is collected from the uniformly excited region with a 100 µm spot size. Thus, the introduction of any nonlocal effects is very unlikely. Among various other mechanisms responsible for laser fluence-induced damping, the spin-lattice interaction mechanism can be a dominant one. In the presence of this mechanism, energy density deposited in the probed volume increases with laser fluence which causes an enhancement in the energy dissipation from the spin system to lattice and hence, accelerates the decay of spin waves. We have observed that lattice temperatures (extracted from 3T-modelling) for the 50 nm- and 100 nm-thick films increase from approximately 408 K to 818 K and 337 K to 472 K within the experimental fluence range (as shown in Table 8.2). As α is proportional to the susceptibility of the sample, which is a function of the lattice temperature, any change in lattice temperature with laser fluence will affect α. According to the Landau-Lifshitz-Bloch model, during laser-induced magnetization dynamics, spin-flips occur mainly due to electron scattering and an increase in laser fluence will increase the ratio between the system temperature and Curie temperature which induces electron-impurity led spin-dependent scattering and causes the enhancement of α [41].

Table 8.2: Lattice temperature (T_L) obtained from three-temperature modelling.

Fluence (mJ/cm^2)	12	25	37	50	62
$(T_L)_{50\ \mathrm{nm}}$ (in Kelvin)	408	526	610	722	817
$(T_L)_{100\ \mathrm{nm}}$ (in Kelvin)	337	367	396	432	471

With an increase in the pump fluence, precessional frequencies of both Kittel and PSSW modes show considerable redshift (as shown in Figure 8.5(e) and 8.5(f), respectively). The frequencies of Kittel and 1st order PSSW modes in the 50 nm-thick film are reduced by 3.41% and 4.60%. For the 100 nm-thick film, the frequencies of Kittel, 1st and 2nd order PSSW modes are reduced by 2.33%, 2.78% and 3.24%, respectively. This decrease in frequency is mainly due to a change in the local magnetic properties by rapid accumulation and dissipation of thermal energy in the probed volume, which introduces temporal chirping. Chirping appears in a time-dependent Kerr oscillation signal because with time magnetization of the sample acquires an equilibrium state but the precessional frequency is unable to attain a stable equilibrium state and keeps on changing. The temporal chirp parameter (b)

shows almost four times enhancement with the pump fluence for both 50 nm- and 100 nm-thick films as shown in Figures 8.5(e) and 8.5(f), respectively. Enhancement in b for PSSW modes is higher in comparison with the uniform Kittel mode which implies higher frequency modulation of these bulk modes due to the non-uniform distribution of heat.

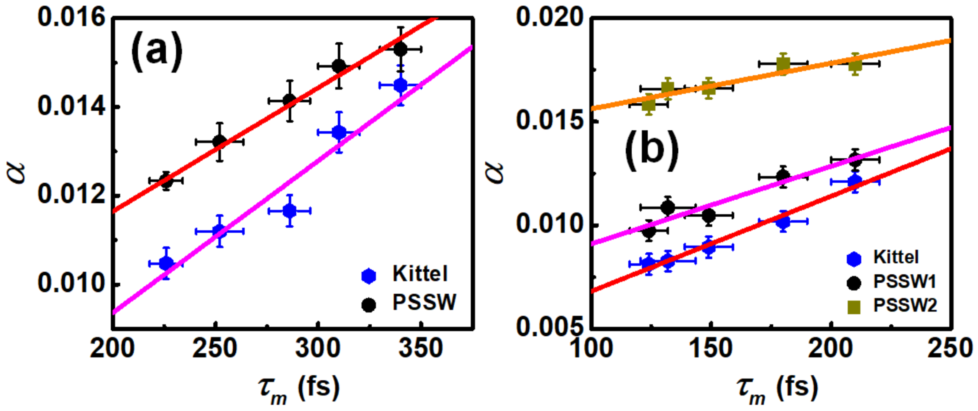

Figure 8.6: Gilbert damping parameter (α) as a function of ultrafast demagnetization time (τ_m) for (a) 50 and (b) 100 nm Py thin films. The solid line is a linear fit to the data.

The correlation between τ_m and α is of significant interest in recent times, as it is an effective method to detect the governing microscopic contribution to ultrafast demagnetization and damping [19-22, 42, 43]. According to this, a proportional relation between the τ_m and α indicates that the local spin-flip scattering mechanism dominates the demagnetization process. However, an inverse dependence implies that the nonlocal spin transport mechanism dominates the demagnetization process. By plotting τ_m with α for 50 nm- and 100 nm-thick Py films obtained at different pump fluences in Figures 8.6(a) and 8.6(b), we have observed an increase in τ_m with α. This proportional relationship signifies that spin-flip scattering is the dominant microscopic mechanism for ultrafast demagnetization in our system. Also, the correlation between τ_m and α helps to determine the major microscopic contribution to damping. A linear relationship points to the dominance of intra-band conductivity-like contribution whereas an inverse relationship indicates the inter-band resistivity-like contribution. Hence, the observed linear relationship between τ_m and α signifies that intra-band conductivity-like contribution dominates the damping process in our samples.

8.4 Conclusions

An extensive and systematic study of ultrafast magnetization dynamics is presented for 50 nm- and 100 nm-thick Py thin films at different pump fluences and bias magnetic field by an all-optical TR-MOKE technique. A strong correlation between ultrafast demagnetization time and fast remagnetization time with the pump fluence is observed. The Gilbert damping parameter for both Kittel and perpendicular standing spin wave (PSSW) modes remains independent of applied bias magnetic field while showing significant enhancement from intrinsic value with an increase in the pump fluence. The precessional frequencies experience a noticeable redshift with pump fluence due to a change in the accumulation and dissipation of thermal energy leading to a temporal chirping. An inverse relationship between τ_m and α is established due to the dominant spin-flip scattering contribution to ultrafast demagnetization and intra-band conductivity-like contribution to damping for Py thick films. This elaborative study will enlighten the understanding of the modulation of magnetization dynamics in ferromagnetic systems in the presence of different external conditions and helps in optimizing parameters for spin-based devices in accordance with external conditions.

References

1. Zutic, J. Fabian and S. Das Sharma, Rev. Mod. Phys. **76**, 323-401 (2004).
2. S. A.Wolf , D. D. Awschalom, R. A. Buhrman, J. M. Daughton, S. von Molnar, M. L. Roukes, A. Y. Chtchelkanova and D. M. Treger, Science **294**, 1488-1495 (2001).
3. A. Hoffmann and S. D. Bader, Phys. Rev. Appl. **4**, 047001 (2015).
4. S. D. Bader, S. S. P. Parkin, Spintronics, Annu. Rev. Cond. Matter Phys. **1**, 71 (2010).
5. L. Landau and E. Lifshits, Phys. Zeitsch. der Sow. **8**, 153 (1935).
6. T. L. Gilbert, IEEE Trans. Magn. **40**, 6 (2004).
7. P. He, X. Ma, J. W. Zhang, H. B. Zhao, G. Lupke, Z. Shi and S. M. Zhou, Phys. Rev. Lett. **110**, 077203 (2013).
8. P. Krivosik, N. Mo, S. Kalarickal and C. E. Patton, J. Appl. Phys. **101**, 083901 (2007).
9. J. O. Rantschler, R. D. McMichael, A. Castillo, A. J. Shapiro, W. F. Egelhoff, B. B. Maranville, D. Pulugurtha, A. P. Chen and L. M. Connors, J. Appl. Phys. **101**, 033911 (2007).
10. Y. Tserkovnyak, A. Brataas and G. E. W. Bauer, Phys. Rev. B **66**, 224403 (2002).
11. Y. Zhao, Q. Song, S. H. Yang, T. Su, W. Yuan, S. S. P. Parkin, J. Shi and W. Han, Sci. Rep. **6**, 22890 (2016).
12. A. Ganguly, R. M. Rowan-Robinson, A. Haldar, S. Jaiswal, J. Sinha, A. T. Hindmarch, D. A. Atkinson and A. Barman, Appl. Phys. Lett. **105**, 112409 (2014).
13. E. Beaurepaire, J. C. Merle, A. Daunois, J. Y. Bigot, Phys. Rev. Lett. **76**, 4250-4253 (1996).
14. B. Koopmans, G. Malinowski, F. Dalla Longa, D. Steiauf, M. Fähnle, T. Roth, M. Cinchetti and M. Aeschlimann, Nat. Mater. **9**, 259-65 (2010).
15. J. Y. Bigot, M. Vomir, and E. Beaurepaire, Nat. Phys. **5**, 515–520 (2009).
16. M. Krauß, T. Roth, S. Alebrand, D. Steil, M. Cinchetti, M. Aeschlimann and H. C. Schneider, Phys. Rev. B **80**, 180407 (2009).
17. G. P. Zhang, W. Hubner, G. Lefkidis, Y. Bai and T. F. George, Nat. Phys. **5**, 499–502 (2009).
18. M. Battiato, K. Carva and P.M. Oppeneer, Phys. Rev. Lett. **105**, 027203 (2010).
19. B. Koopmans, J. J. M. Ruigrok, F. Dalla Longa and W. J. M. De Jonge, Phys. Rev. Lett. **95**, 267207 (2005).

20. W. Zhang, W. He, X. Q. Zhang, Z. H. Cheng, J. Teng and M. Fähnle, Phys. Rev. B **96**, 220415 (2017).
21. W. Zhang, Q. Liu, Z. Yuan, K. Xia, W. He, Q. F. Zhan, X. Q. Zhang and Z. H. Cheng, Phys. Rev. B **100**, 104412 (2019).
22. M. Fähnle, J. Seib and C. Illg, Phys. Rev. B **82**, 144405 (2010).
23. S. N. Panda, S. Mondal, J. Sinha, S. Choudhury and A. Barman, Sci. Adv. **5**, eaav7200 (2019).
24. A. Kirilyuk, A. V. Kimel and T. Rasing, Rev. Mod. Phys. **82**, 2731 (2010).
25. H. D. Arnold and G. W. Elmen, Bell Syst. Tech. J. **2**, 101-111 (1923).
26. B. Koopmans, H. H. J. E. Kicken, M. van Kampen and W.J.M. de Jonge, J. Mag. Mag. Mat. **286**, 271-275 (2005).
27. A. Mekonnen, A. R. Khorsand, M. Cormier, A. V. Kimel, A. Kirilyuk, A. Hrabec, L. Ranno, A. Tsukamoto, A. Itoh and Th. Rasing, Phys. Rev. B **87**.180406 (2013).
28. S. I. Anisimov, B. L. Kapeliovitch and T. L. Perel’man, Zh. Eksp. Teor. Fis. **66**, 776 (1974).
29. F. Dalla Longa, J. T. Kohlhepp, W. J. M. de Jonge and B. Koopmans, Phys. Rev. B **75**, 224431 (2007).
30. G. Malinowski, F. Dalla Longa, J. H. H. Rietjens, P. V. Paluskar, R. Huijink, H. J. M. Swagten and B. Koopmans, Nat. Phys. **4**, 855-858 (2008).
31. J. Mendil, P. Nieves, O. Chubykalo-Fesenko, J. Walowski, T. Santos, S. Pisana and M. Munzenberg, Sci. Rep. **4**, 3980 (2014).
32. U. Atxitia, O. Chubykalo-Fesenko, J. Walowski, A. Mann and M. Münzenberg, Phys. Rev. B **81**, 174401 (2010).
33. A. K. Alassafee and M.S. Omar, J. Tai. Uni. Sci. **11**, 1226–1231 (2017).
34. E. Carpene, E. Mancini, C. Dallera, M. Brenna, E. Puppin and S. De Silvestri, Phys. Rev. B **78**, 174422 (2008).
35. S. Mondal and A. Barman, Phys. Rev. Appl. **10**, 054037 (2018).
36. S. Mondal, A. Talapatra, J. A. Chelvane, J. R. Mohanty and A. Barman, Phys. Rev. B **100**, 054436 (2019).
37. C. Banerjee, A. K. Chaurasiya, S. Saha, J. Sinha and A. Barman, J. Phys. D: Appl. Phys. **48**, 395001 (2015).
38. J. Walowski, M. D. Kaufmann, B. Lenk, C. Hamann, J. McCord and M. Münzenberg, J. Phys. D: Appl. Phys. **41**, 164016 (2008).
39. B. Heinrich and J. A. C. Bland, Spin relaxation in magnetic metallic layers and multilayers, in Ultrathin magnetic structures: fundamentals of nanomagnetism (Springer: New York, 2005).
40. J. Wu, N. D. Hughes, J. R. Moore and R. J. Hicken, J. Magn. Magn. Mater. **241**, 96 (2002).
41. P. Nieves, D. Serantes, U. Atxitia and O. ChubykaloFesenko, Phys. Rev. B **90**, 104428 (2014).
42. J. Walowski, G. Muller, M. Djordjevic, M. Münzenberg, M. Klaui, C. A. F. Vaz and J. A. C. Bland, Phys. Rev. Lett. **101**, 237401 (2008).
43. Y. Ren, Y. L. Zuo, M. S. Si, Z. Z. Zhang, Q. Y. Jin and S. M. Zhou, IEEE Trans. Magn. **49**, 3159-3162 (2013).

Chapter-9

Summary and future perspective

9.1 Summary

In summary, we have investigated the magnetization dynamics in different spintronic materials from femtosecond to nanosecond timescale. We have studied different phenomena like ultrafast demagnetization, fast relaxation, magnetization precession and damping in FM thin films, NM/FM heterostructures and SLG/FM heterostructures. All the samples used in this thesis were prepared by RF/DC magnetron sputtering system. The initial characterizations of the samples were done by the AFM, XRD, XRR and micro-Raman spectroscopy analysis techniques. The static magnetic properties were measured by the static MOKE magnetometer and VSM. We have employed a custom-built non-collinear TR-MOKE magnetometer for studying the magnetization dynamics from femtosecond to nanosecond timescale.

For the sake of energy-efficient spintronic device fabrication based on pure spin current, the NM/FM interfaces must have a high spin transmission probability, which is parametrized by interfacial spin transparency (T). In this thesis, we have reliably probed spin pumping and quantified T in sputter-deposited β-Ta/CoFeB thin film heterostructures using an all-optical TR-MOKE magnetometry from the modulation of the Gilbert damping parameter. The non-monotonic variation in Gilbert damping parameter in β-Ta(t)/CoFeB(3 nm) samples with varying Ta thickness is modelled using spin pumping formalism to extract the spin diffusion length of β-Ta and intrinsic spin-mixing conductance of β-Ta/CoFeB interface. The effective spin-mixing conductance is extracted from the variation of the Gilbert damping parameter with the CoFeB layer thickness. According to the spin Hall magnetoresistance model, T is a function of effective spin-mixing conductance and spin diffusion length, which is obtained to be 0.50 ± 0.03 for the β-Ta/CoFeB interface. We have further done controlled experiments by inserting a Cu spacer layer of varying thickness between the β-Ta and CoFeB layer to eliminate the alternative interfacial effects contributing to the variation of damping, namely interfacial band hybridization, spin memory loss (SML), two magnon scattering (TMS) and Rashba effect. The invariance of the Gilbert damping parameter with the Cu layer thickness confirms the dominance of the spin pumping effect with negligible presence of other interfacial effects. From this study, we have observed low damping and high effective spin-mixing conductance with moderately high T of the β-Ta/CoFeB bilayer system promoting it as a key material for spin-orbit torque-based devices.

W is another heavy metal with strong SOC and it shows a large spin-charge conversion. However, it also shows a thickness-dependent structural phase transition, which may affect the interface quality and the ensuing spin-orbit effect. We have investigated the variation in the Gilbert damping parameter by including the SML and TMS contributions to spin pumping and extracted the SML conductance and coefficient of TMS for the W/CoFeB interface. The effective spin-mixing conductance shows a small decrease in consonance with the thickness-dependent phase transition, while the spin pumping contribution significantly dominates over the SML and TMS for our studied samples. Two different models, i.e., the spin Hall magnetoresistance model and spin transfer torque-based model, are used to extract the value of T. The T-values obtained from the spin transfer torque-based model are slightly higher than the values obtained from the spin Hall magnetoresistance model. However, we consider the values of T obtained from the spin Hall magnetoresistance model to be more accurate as it includes the mandatory contribution of spin current backflow from the W layer into the CoFeB layer. The value of T is found to depend strongly on the crystal structure of W. This structural phase-dependent T value will offer important guidelines for the selection of the material phase for spin-orbitronic applications.

Graphene is a promising spin channel material owing to the achievement of room-temperature spin transport in it with a spin-diffusion length of tens of micrometres owing to its low intrinsic spin-orbit coupling and weak hyperfine coupling. Graphene/FM heterostructures have attracted attention due to their unusual interface properties and spin-orbit effects. We have studied the time-resolved spin dynamics in SLG/CoFeB bilayer samples, where CoFeB (d; 1.5 nm $\leq d \leq$ 6 nm)/SiO_2 (2 nm) layers have been deposited over the CVD-grown SLG. For reference, CoFeB (d; 1.5 nm $\leq d \leq$ 6 nm)/ SiO_2 (2 nm) layers of the same thicknesses were deposited on Si/SiO_2 (300 nm) under identical conditions. In the presence of an SLG underlayer, we have observed a slight decrease in average crystallite size and defect density with an increase in CoFeB thickness. Moreover, in presence of an SLG underlayer, these films exhibit higher coercivity due to increased defect density and lower saturation magnetization due to interfacial band hybridization. In SLG/CoFeB, we have established an inverse relationship between ultrafast demagnetization time and Gilbert damping parameter induced by interfacial spin accumulation and pure spin currents transport via spin pumping mechanism. We have modelled the variation of the Gilbert damping parameter with the CoFeB thickness and estimated the individual contribution of spin pumping and TMS for the SLG/CoFeB heterostructures. This modelling reveals spin pumping as the dominant contributor to the modulation of the Gilbert damping parameter for the SLG/CoFeB heterostructures. This systematic study on SLG/CoFeB heterostructures may open up new pathways for understanding and controlling the ultrafast magnetization dynamics in 2D materials and leads to graphene-based spintronics applications.

SOC arises due to the interaction between spin and orbital angular momentum of an electron and is a key factor to control magnetization. It is also central to designing spin-based devices with low-energy dissipation and faster switching speed. Higher SOC helps in faster spin-flip scattering that leads to efficient generation of spin current through effects like the spin Hall effect, while smaller SOC helps in long-distance transfer of information in spintronics devices. Here, we have systematically investigated magnetization dynamics of CoFeB thin films grown by sputtering over copper (Cu), tantalum (Ta), tungsten (W), platinum (Pt), Ta/Ru/Ta (TRT) underlayers, that differ in SOC strength. For reference, we have also deposited CoFeB thin film of identical thickness without having any underlayer. The ultrafast demagnetization time and fast relaxation time are found to decrease monotonically, whereas the effective spin-mixing conductance and Gilbert damping parameter increase monotonically with the increment of the SOC strength of the NM layer. We have established an inverse relationship between ultrafast demagnetization time and fast relaxation time with the Gilbert damping parameter in NM/CoFeB thin film heterostructures having NM with different SOC strengths. The major contribution to ultrafast demagnetization originated from the spin pumping-induced pure spin current transport. We have observed a large modulation in ultrafast demagnetization time (2.4 times) and fast relaxation time (11.0 times) with the variation in the NM layer from W to no underlayer. Consequently, the Gilbert damping parameter and effective spin-mixing conductance have increased by 500% and 1584%, while spin chemical potential decreased by 1622%. Such a wide range of tuning of important parameters like ultrafast demagnetization time, fast relaxation time, Gilbert damping parameter, effective spin-mixing conductance and spin chemical potential can provide a promising route for designing energy-efficient spintronics devices with nanometer bit-size and ultralow error rate.

Finally, we have studied pump fluence-dependent ultrafast magnetization dynamics in Py thin films having different thicknesses by using TR-MOKE magnetometry. The effect of increasing laser pump fluence on various dynamical entities, such as ultrafast demagnetization time, remagnetization time, electron temperature, spin temperature, lattice temperature, Gilbert damping parameter, precessional frequency and temporal chirping have been comprehensively studied. We found an increment in ultrafast demagnetization time, remagnetization time and temperature of the electron, spin and lattice baths with pump fluence. A substantial enhancement in the Gilbert damping parameter with pump fluence is observed for both Kittel and PSSW modes. With an increase in pump fluence, precessional frequencies of both Kittel and PSSW modes show considerable redshift due to the change in the local magnetic properties by rapid accumulation and dissipation of thermal energy in the probed volume which introduced a temporal chirping. We have established that spin-flip scattering is the possible mechanism behind ultrafast demagnetization and a dominant intra-band conductivity-like contribution behind the damping here for both uniform Kittel and bulk PSSW modes. This comprehensive study of magnetization dynamics over a broad timescale and its control by pump fluence will provide a firm base to integrate various magnetic phenomena on a single on-chip device.

9.2 Future perspective

The fundamental research on exploring the field of spin-based data storage, memory, transistor, logic and other on-chip communication devices is expanding rapidly since these spin-based analogues of conventional charge-based devices are smaller, faster, more cost-effective, thermally stable and possess inherent anisotropy and non-reciprocity. Ferromagnetic thin films are the bedrock for these spin-based device applications due to their highly superior and controlled spin transport and spin dynamics properties. Therefore, an in-depth scientific understanding of ultrafast spin dynamics and control over different spin-related effects in these ferromagnetic thin films is one of the most crucial aspects of modern magnetism research. Ultrafast demagnetization is one of the pioneer processes involved in ultrafast spin dynamics. Despite many efforts to understand the underlying mechanisms behind this phenomenon, many questions have remained unanswered. Both spin-flip scattering and spin current transport have been shown to contribute to the demagnetization process of a magnetic material. Although recent literature including ours shows that in potentially important NM/FM or SLG/FM thin film heterostructures spin current transport can be the dominant contribution to the ultrafast demagnetization, one needs to perform more extensive experimental study and theoretical modelling on different types of materials to investigate their coexistence and quantitative contribution to the demagnetization process. Recently, a new mechanism named optical inter-site spin transfer (OISTR) has been proposed to describe the unusual sub-10 femtosecond loss in magnetic moments in multi-sublattice/multi-component materials. This OISTR effect may also be extended to understand the two-step demagnetization process in multi-sublattice rare-earth alloys.

In this doctoral thesis, we have correlated ultrafast demagnetization time with the Gilbert damping parameter to underpin the dominant microscopic mechanism behind the ultrafast demagnetization process. Similar unification of phenomena over a broad time scale can also be extended to other materials for drawing a universal understanding of ultrafast magnetization dynamics. An important young subfield of spintronics, namely spin-orbitronics has also emerged with the focus on efficient generation, transport and utilization of pure spin current. This sub-field has remarkably transformed the new generation of memory and storage technology. In this thesis, we have used the spin pumping effect to generate pure spin current in NM/FM thin film heterostructures and explained the role of interface for the efficient transfer of pure spin current for utilization in devices. This efficiency of spin current transport is parametrized by interfacial spin transparency that depends upon both intrinsic and extrinsic parameters, such as electronic band structure mismatch, interfacial defects etc. However, there can be many other combinations of heterostructures whose interfacial spin transparency values are still unknown and need to be explored. Also, the effects of different deposition conditions such as annealing temperature, argon pressure, doping of material etc. on the interfacial spin transparency are still rare in the literature, which will be important fields of research in the near future.

Laser-induced modification of different static and dynamic properties of magnetic thin films and heterostructures has offered an external stimulus to this research area. In magnetic memory and storage devices, it is crucial to maintain the non-volatility of the stored information. The advantage of laser-induced magnetic modulation is that both static and dynamic magnetic parameters can be controlled and even reversed via rapid heating and cooling processes. This type of laser-induced study using the TR-MOKE technique can be performed at varying temperatures and pressures. Different magneto-caloric effects, the variation of ultrafast demagnetization time, fast remagnetization time and Gilbert damping parameter with ambient temperature can be extensively studied. Also, these dynamic parameters can be studied in different thin film heterostructures by varying the penetration depth using different laser wavelengths generated by an optical parametric amplifier. In this thesis, we have investigated the effects of bulk spin-orbit coupling of nonmagnetic underlayers on the magnetization dynamics of NM/FM heterostructures. However, there are several other effects like interfacial spin-orbit coupling, proximity effect and perpendicular magnetic anisotropy that can affect the different dynamic parameters. Besides, one can also control the ultrafast spin dynamics by electric field or strain applied at the NM/FM interface, which may externally control the SOC. This may eventually help to build up the electric field or strain-controlled ultrafast memory devices by material engineering.

Appendix I

List of abbreviations

AFM: Atomic force microscopy

AO-HDS: All-optical helicity-dependent magnetization switching

AOS: All-optical switching

BBO: Barium Beta-borate

BWD: Band-width detector

CG: Compressor grating

CM: Compressor mirror

CPA: Chirped pulse amplification

CVD: Chemical vapor deposition

DC: Direct current

emf: Electromotive force

FI: Faraday isolator

FM: Ferromagnetic material

fs: Femtosecond

GMR: Giant magnetoresistance

GVD: Group velocity dispersion

HAMR: Heat-assisted magnetic recording

HDD: Hard disk drive

INP: In-plane

LBO: Lithium tri-borate

LCP: Left circular polarized

LL: Landau and Lifshitz

LLG: Landau-Lifshitz-Gilbert

MOKE: Magneto-optical Kerr effect

MRAM: Magneto-resistive random-access memory

NM: Nonmagnetic material

ns: Nanosecond

OISTR: Optical inter-site spin transfer

OBD: Optical bridge detector
OOP: Out-of-plane
PC: Pockels cell
PEM: Photo elastic modulator
PMA: Perpendicular magnetic anisotropy
ps: Picosecond
PPMS: Physical property measurement system
PSSW: Perpendicular standing spin-wave
PMMA: Poly-methyl methacrylate
PZT: Piezoelectric transducer
RA: Regenerative amplification
RF: Radio frequency
RI: Regan iris
RP: Regan polarizer
RTS: Regan Ti: Sapphire crystal
RWP: Regan waveplate
RM: Regan mirror
SLG: Single layer graphene
SOC: Spin-orbit coupling
ST-FMR: Spin-torque ferromagnetic resonance
S-MOKE: Static magneto-optical Kerr effect
SHE: Spin Hall effect
SPM: Self-phase modulation
SDG: Synchronization and delay generator
SHG: Second-harmonic generator
SM: Stretcher mirror
SBS: Stretcher beam splitter
SG: Stretcher grating
TMR: Tunnel magnetoresistance
TR-MOKE: Time-resolved magneto-optical Kerr effect
TMS: Two-magnon scattering
VSM: Vibrating sample magnetometer

VPUF: Verdi-pumped ultrafast laser
XRD: X-ray diffraction
XRR: X-ray reflectivity
2D: Two-dimensional
μs: Microsecond
2T: Two temperature
3T: Three-temperature

Appendix II

List of tables

Appendix III

List of figures